

# **Computational Modelling Study of Yttria-stabilized Zirconia**

Thesis submitted for the degree of Doctor of Philosophy

**Xin Xia**

Department of Chemistry  
University College London

2010



## Abstract

Interatomic potential and quantum mechanical simulation techniques have been applied to both the bulk and surfaces of yttrium-stabilized cubic zirconia (YSZ) with special reference to its role in partial oxidation reaction at high temperature. The stabilities of pure  $\text{ZrO}_2$  phases and surfaces have been examined. The bulk structures of low pressure phases are reproduced with the observed order of stability: monoclinic > tetragonal > cubic zirconia. The relative stability of plane cubic  $\text{ZrO}_2$  surfaces is predicted to be  $(111)_c > (110)_c > (100)_c > (310)_c$ . In addition, the stability of topological surfaces is found to be reduced with the coordination number of Zr ions at the topological sites in the order: plane > step > kink > corner.

The dispersion of defects in YSZ systems has been studied, considering both the dopant content and surface segregation. In the bulk, the yttrium dopants tend to form a pair with two yttrium atoms close to each other and preferentially occupying the 1<sup>st</sup> or 2<sup>nd</sup> nearest neighbour (NN) sites to the compensating oxygen vacancy. At the surface, yttrium segregates to the top layers (up to 4-5 Å) of the dominant (111) surface of YSZ. The composition of the outermost surface of YSZ is predicted to be independent of Y bulk concentration and reach a maximum Y/Zr ratio of 1:1.

In relation to catalytic oxidation, the interaction between oxygen molecules and the (111) surfaces of pure c- $\text{ZrO}_2$  and YSZ have been investigated using quantum-mechanical DFT-GGA methods. The adsorption states of oxygen and the pathways for dissociation have been indentified on the plane and stepped (111) surfaces. In general, the creation of oxygen vacancies by yttrium doping provides an active site for oxygen adsorption. In addition, the low-coordinated Zr cations on the YSZ surfaces can attract strongly reduced oxygen species and the most stable adsorption state of oxygen is adopted to achieve a higher bond saturation of the neighbouring Zr site.



## **List of Abbreviations**

**AIMS:** Atoms in Molecules

**BFGS:** Broyden, Fletcher, Goldfarb and Shanno algorithm

**B1LYP:** Becke's one-parameter method with Lee–Yang–Parr correlation

**B3LYP:** Becke's three-parameter method with Lee–Yang–Parr correlation; Hybrid exchange correlation functional that incorporates 20% of Hartree–Fock exchange.

**CIM:** Compressible Ion Model

**CG:** Conjugate Gradients

**CN:** Coordination Number

**CPOM:** Catalytic Partial Oxidation of Methane

**DFT:** Density Functional Theory.

**EDS:** Energy Dispersive X-ray Analysis

**EELS:** Electron Energy Loss Spectroscopy

**EPR:** Electron Paramagnetic Resonance

**GGA:** Generalised Gradient Approximation in the DFT

**GPES:** Global Potential Energy Surface

**GULP:** General Utility Lattice Program

**HF:** Hartree-Fock

**HRTEM:** High Resolution Transmission Electron Microscopy



**IP:** Interatomic Potentials

**KS:** Kohn–Sham

**LAPW:** Linear Augmented Planewave Method

**LMTO:** Linear Muffin-Tin Orbital

**LDA:** Local Density Approximation in the DFT

**LSD:** Local Spin Density Approximation (LDA with spin polarisation)

**MARVIN:** Minimisation and Relaxations of Vacancies and Interstitials of Neutral Surface

**MEPs:** Minimum Energy Paths

**MD:** Molecular Dynamics

**MO:** Molecular Orbital

**MO-LCAO:** Molecular Orbital-Linear Combination of Atomic Orbitals

**NCPP:** Norm-Conserving Pseudopotential

**NEB:** Nudged Elastic Band

**NN:** Nearest Neighbour

**NNN:** Next Nearest Neighbour

**NPA:** Natural Population Analysis

**PAW:** Projector Augmented Wave

**PBC:** Periodic Boundary Conditions

**PES:** Photoelectron Spectroscopy



**PW91:** Exchange-correlation functional with gradient corrections for DFT calculations, developed by Perdew and Wang.

**QM:** Quantum Mechanics

**RFO:** Rational Function Optimizer

**SCF:** Self-Consistent Field

**SOFC:** Solid Oxide Fuel Cell

**STM:** Scanning Tunnelling Microscopy

**TDGL:** continuum Time-Dependent Ginzburg Landau

**TPD:** Temperature Programmed Desorption

**USPP:** Ultrasoft Pseudopotential

**VASP:** Vienna Ab Initio Simulation Program

**VB:** Valence Band

**VE:** Vacancy Formation Energy

**VUV:** Vacuum Ultraviolet Absorption

**XRD:** X-ray Diffraction

**XPS:** X-ray Photoelectron Spectroscopy



# List of Contents

<b>Chapter 1</b>	Introduction.....	1
<b>Chapter 2</b>	ZrO <sub>2</sub> Structure and Stability.....	3
2.1	Fluorite ZrO <sub>2</sub> and Structural Instability .....	3
2.2	Phase Transitions of ZrO <sub>2</sub> .....	6
2.3	Phase Stabilizations–The Behaviour of Dopants .....	14
2.3.1	Categories of Cation Dopants .....	14
2.3.2	Ytria-stabilized c-ZrO <sub>2</sub> .....	17
2.4	ZrO <sub>2</sub> Surface.....	21
2.4.1	Surface Structure and Morphology .....	21
2.4.2	Surface Segregation .....	24
	References .....	26
<b>Chapter 3</b>	Partial Oxidation Catalysis .....	31
3.1	Syngas and CPOM .....	32
3.2	Ytria-stabilized Zirconia for CPOM .....	36
3.3	Surface Interaction and Oxygen State on the Metal Oxide Catalyst.....	40
3.4	Opportunities for Computational Modelling.....	47
	References.....	48



<b>Chapter 4</b>	<b>Computational Methodology .....</b>	<b>51</b>
4.1	Interatomic Potential Methods .....	52
4.1.1	Born Model Potentials for Ionic Systems .....	52
4.1.1.1	Long Range Potentials .....	52
4.1.1.2	Short Range Potentials .....	55
4.1.2	Ionic Polarization and the Shell Model .....	56
4.1.3	Parameterisation of potentials .....	59
4.1.4	Model Point Defects.....	60
4.1.5	Phonon Modes.....	61
4.1.6	Surface Modelling of a Periodic Lattice .....	62
4.1.6.1	Slab Model .....	63
4.1.6.2	Surface Reconstruction .....	64
4.1.6.3	Surface Energy .....	64
4.2	Quantum Mechanics.....	66
4.2.1	The Schrödinger Equation and Born-Oppenheimer Approximation ....	67
4.2.2	Hartree-Fork Theory .....	68
4.2.3	Density Function Theory.....	70
4.2.3.1	<i>Thomas-Dirac-Fermi</i> .....	71
4.2.3.2	<i>Hohenberg- Kohn Theorem</i> .....	72
4.2.3.3	<i>Kohn-Sham equations</i> .....	74
4.2.4	Exchange-Correlation Functionals (LDA and GGA) .....	76
4.2.4.1	<i>Local Density Approximation</i> .....	76
4.2.4.2	<i>Generalized Density Approximation</i> .....	76
4.2.5	Limitations of DFT .....	79
4.2.5.1	<i>Delocalization Error and Fractional Charges</i> .....	80
4.2.5.2	<i>Static Correlation Error and Fractional Spin</i> .....	80
4.2.6	Electronic Structure in Periodic Solids .....	82
4.2.6.1	<i>Bloch's Theorem</i> .....	82
4.2.6.2	<i>Plane-waves</i> .....	82
4.2.6	Pseudopotentials and Projector Augmented Wave Method.....	84



4.2.6.1	<i>Norm-conserving pseudopotentials</i> .....	85
4.2.6.2	<i>Ultrasoft pseudopotentials</i> .....	86
4.2.6.3	<i>The projector augmented-wave method</i> .....	86
4.3	Charge Population Analysis.....	89
4.3.1	Orbital Based Method: Mulliken Population Analysis .....	89
4.3.2	Electron Density Based Method: Bader Charge Analysis .....	91
4.4	Energy Minimization .....	93
4.3.1	Line Search.....	94
4.3.2	Steepest Search.....	94
4.3.3	Newton Raphson .....	95
4.3.2	Conjugate Gradient .....	97
4.4	Codes and Computers .....	99
	References.....	101
<b>Chapter 5</b>	<b>Interatomic Potential Studies of YSZ</b> .....	106
5.1	Bulk Structures of Pure Zirconia .....	107
5.2	Yttrium Doped ZrO <sub>2</sub> .....	111
5.2.1	Defect Calculations using the Mott-Littleton Method .....	112
5.2.2	Defect Calculations using the Supercell Approach.....	114
5.3	Pure Zirconia Surface.....	117
5.4	Yttrium Segregation on the ZrO <sub>2</sub> Surfaces .....	119
5.5	Conclusions .....	126
	References .....	127
<b>Chapter 6</b>	<b>Quantum Mechanical Studies of YSZ</b> .....	129



6.1	ZrO <sub>2</sub> Phases .....	129
6.2	Defect Structure and Oxygen Vacancy Formation .....	138
6.3	Plane ZrO <sub>2</sub> Surfaces .....	141
6.4	Defects on Plane (111) Surfaces .....	144
6.5	Topologically Complex Surfaces .....	146
6.5.1	Step Models.....	147
6.5.2	Corner Models.....	151
6.5.3	Defect Sites on Stepped Surfaces.....	155
6.6	Conclusions .....	158
	References .....	159
<b>Chapter 7</b>	<b>Quantum Mechanical Studies of Oxygen Adsorption .....</b>	<b>161</b>
7.1	O <sub>2</sub> Adsorption on the Plane (111) Surface of Pure ZrO <sub>2</sub> .....	161
7.1.1	Spin Polarization .....	163
7.1.2	Adsorption Sites .....	165
7.2	O <sub>2</sub> Adsorption on the Plane (111) Surface of YSZ .....	167
7.2.1	Geometries and Energies.....	169
7.2.2	Density of States .....	174
7.3	O <sub>2</sub> Dissociation on the Plane (111) Surface of YSZ .....	177
7.3.1	O <sub>2</sub> Dissociation on the YSZ1 Surface Model .....	177
7.3.2	O <sub>2</sub> Dissociation on the YSZ3 Surface Model .....	184
7.4	Adsorption States of Oxygen on the YSZ (111) Plane Surface .....	191
	References .....	194



<b>Chapter 8</b>	Role of Active Sites Topology on O <sub>2</sub> Adsorption .....	195
8.1	O <sub>2</sub> Adsorption on the Stepped (111) Surfaces .....	195
8.1.1	O <sub>2</sub> Adsorption on the Step Edge Sites of Pure ZrO <sub>2</sub> .....	195
8.1.2	O <sub>2</sub> Adsorption on the Edge Sites of YSZ Step.....	197
8.2	O <sub>2</sub> Dissociation on the Stepped (111) Surface of YSZ .....	199
8.3	Oxygen Adsorption States on the Stepped Surface of YSZ .....	208
	References .....	209
<b>Chapter 9</b>	Conclusions.....	210
9.1	Structural Stability of Zirconia .....	210
9.2	Bulk Dispersion and Surface Segregation of Defects in YSZ .....	210
9.3	Adsorption of Oxygen .....	212
	Outline of Future Works .....	216
	Acknowledgements .....	217



## Chapter 1 Introduction

Over the last decade, our understanding of the structural chemistry of oxide ceramics which are used as refractory structural and functional materials in a wide range of catalyst, dielectric and electronic applications, has benefited extensively from the development of computational modelling techniques. In this context, zirconium dioxide ( $\text{ZrO}_2$ ) is an important technological material that has been exploited both as a solid-state oxygen ion conductor and electrolyte in several key industrial applications including solid-oxide fuel cells (SOFC) and catalysis.

Pure  $\text{ZrO}_2$ , as a polymorphic metal oxide, displays various phases. At ambient pressure, the ground-state  $\text{ZrO}_2$  has a monoclinic structure with Zr cations 7-fold coordinated by oxygen anions. The cubic fluorite phase of zirconia (8-fold) is only thermodynamically stable at temperatures higher than 2650 K since  $\text{Zr}^{4+}$  is too large for an efficiently packed rutile structure and too small to form the 8 fold coordinated fluorite structure. The addition of trivalent cation dopants, e.g. yttrium, stabilizes the cubic phase of zirconia down to room temperature and results in the presence of oxygen vacancies. Yttria-stabilized zirconia (YSZ) substantially improves the mechanical, electrical, and chemical properties of  $\text{ZrO}_2$ . Importantly, the high conductivity of the doped material promotes its functionality as a solid electrolyte and, in addition, YSZ is proving to be a promising material for catalytic partial oxidation of methane (CPOM) to synthesis gas.

The oxygen vacancies in YSZ, in addition to stabilizing  $\text{ZrO}_2$  in its cubic form, are thought to play an important role in high temperature catalytic processes such as direct partial oxidation of methane or steam reforming, which is the intermediary step from hydrocarbon to bulk chemicals and synthetic fuels. The cation dopants and oxygen vacancies on the surface have been proposed as the most likely electronic or structural defects involved as active sites in adsorption and activation of reacting molecules, thereby influencing catalytic activity and selectivity.

The aim of this study is to understand the oxygen adsorption and dissociation mechanisms on the surface of YSZ in relation to catalytic partial oxidation. For this



purpose, computational calculations applying both interatomic potential (IP) and quantum mechanical (QM) simulation techniques have been carried out to investigate:

- the structures and relative stabilities of pure  $\text{ZrO}_2$  phases and surfaces (IP & QM);
- the defect distribution in the YSZ bulk and surface (IP & QM);
- the generation of topological surfaces and relative stabilities (IP & QM);
- the energetically favoured defect configuration on the stepped YSZ surface (IP & QM);
- oxygen adsorption and dissociation on the dominant (111) plane surface of YSZ (QM);
- oxygen adsorption and dissociation on the energetically favourable step surface of YSZ (QM).

Chapter 2 of the thesis discusses the structural stability of zirconia and reviews the related extensive experimental and computational studies; Chapter 3 discusses the reaction mechanisms of catalytic partial oxidation of methane over yttrium stabilized zirconia proposed by previous experimental studies and also summarizes the early research on oxygen adsorption on metal oxide catalysts. The methodologies of interatomic potential (IP) calculation and quantum mechanical (QM) methods based on density function theory (DFT) are presented in Chapter 4. The bulk phase and surface structures of pure  $\text{ZrO}_2$  and YSZ together with study of defect dispersion are calculated by interatomic potential based methods in Chapters 5 and further examined by the quantum mechanical DFT-GGA approach in Chapter 6. A variety of topological surfaces with increasing complexity involving step, corner and kink models are also designed and modelled for pure  $\text{ZrO}_2$  and YSZ in Chapter 6. In Chapter 7,  $\text{O}_2$  adsorption and dissociation pathways are proposed for different plane surface models based on the DFT-GGA calculations. Oxygen adsorption species are identified according to an analysis of the electronic charge density. The effects of low-coordinated Zr and oxygen vacancies as topological active sites are investigated for the stepped YSZ surface in Chapter 8. Finally, the main outcomes regarding the structural stability, yttrium dispersion and surface segregation and oxygen adsorption state on the surfaces are highlighted in Chapter 9 together with an outline of future work to further develop our understanding of this important complex material.



## Chapter 2 ZrO<sub>2</sub> Structure and Stability

*The study of the physical world is a search for structure and not a search for substance.*

*--Eddington, Sir Arthur Stanley*

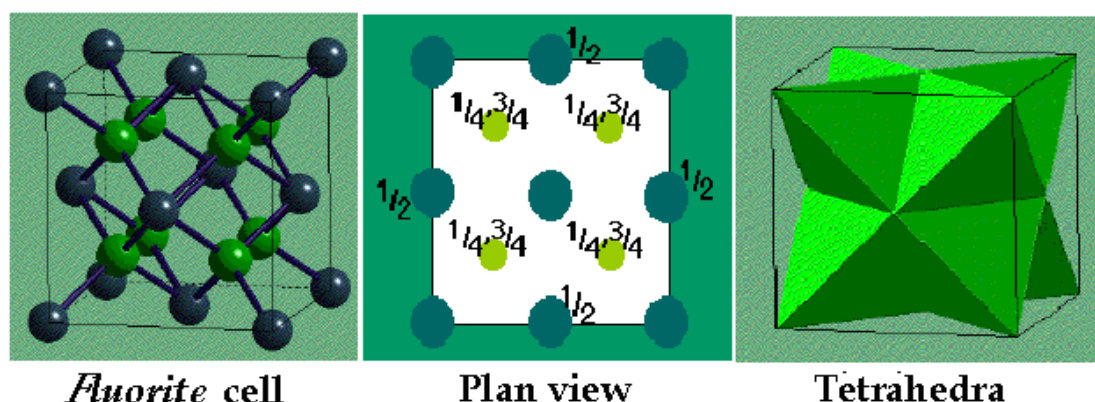
The most commonly occurring natural form of zirconia is baddeleyite with a monoclinic crystalline structure which was first described in 1892 and named after Joseph Baddley.<sup>[1]</sup> As a cubic crystal, zirconia is rarely found in minerals, but can be prepared by several synthetic techniques. Pure zirconia exists in the monoclinic form converting to the tetragonal and cubic phase at a high temperature. However, the transformation is accompanied by a large change in lattice size and in consequence, a large volume expansion on cooling which cause the failure of pure zirconia ceramics fabrication. In order to manufacture zirconia components, it is necessary to 'lock' the material wholly or partially into the cubic form by the use of additives or stabilising agents. The addition of varying amounts of cubic stabilisers such as CaO, MgO, and Y<sub>2</sub>O<sub>3</sub> allows the formation of partially or fully stabilised zirconia, which combined with processing variations, can result in ceramics possessing exceptional properties. In this chapter, the structural transformation and phase stabilization of zirconia are discussed in the light of both experimental and theoretical studies. After that, the surface structure and properties of the pure and stabilized material, which have great importance for catalytic application, are reviewed in relation to the previous computational studies.

### 2.1 Fluorite ZrO<sub>2</sub> and Structural Instability

The cubic fluorite structure is one of the commonest crystal structures for ionic compounds of general formula MX<sub>2</sub>; the term originates from the mineral fluorite



$\text{CaF}_2$ . The basic structure of fluorite can be described as a face centered cubic (*fcc*) sublattice of cations, with anions in all of the tetrahedral holes (4-coordinate). Alternatively, it can be viewed as a simple cubic sublattice of anions with lattice constant  $a/2$  and one half of the subcell centres occupied by cations. Thus, anions are 4-fold coordinated and cations are 8-fold coordinated. The fluorite unit cell comprises of 8 tetrahedra, each with cations at the corners and an anion in the centre. These tetrahedra form a three-dimensional, edge-sharing network as shown in **Figure 2.1**.



**Figure 2.1** Schematic views of fluorite structure: perspective view (Right), plan view (Middle) and tetrahedra view (Left). Green and blue circles denote anions and cations respectively; the green tetrahedras present anions 4-folded by cations. <sup>[1]\*</sup>

According to **Pauling's Rule 1**:

*A coordinated polyhedron of anions is formed about each cation. The cation-anion distance is determined by the radius sums, and the coordination number by the radius ratio. The coordination number is the maximum number consistent with the minimum cation-anion distance.* <sup>[2]</sup>






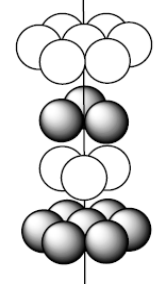
Pauling's model treats the anions and cations of a crystal as hard spheres tightly packed together from which is derived the simple rule that the different types of coordination polyhedra are determined by the radius ratio,  $R^+/R^-$ , of the cation to the anion. However, the radius of a cation depends on its coordination number to a certain extent.

The ideal radius ratios corresponding to the relevant coordination number and crystal geometry have been listed in **Table 2.1**. For a stable coordinated structure, the bonded

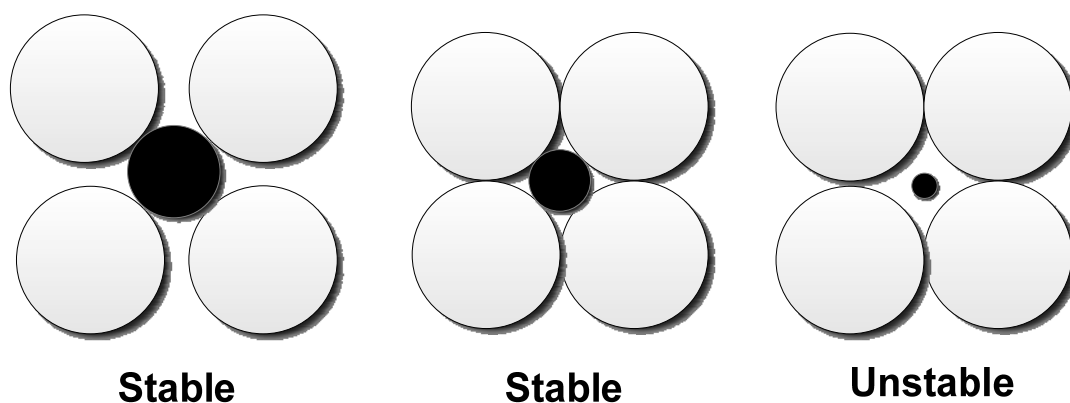


cation and anion must be in contact with each other. If the cation is larger than the ideal radius ratio, the cation and anion are still in contact, but the only the anions are forced apart. The structure can remain stable as shown in **Figure 2.2**. Conversely, if the cation is too small for the site, the structure will distort or reconstruct by adopting a structure with a lower coordination number. Within this criterion, the crystal structures of many ionic compounds can be rationalized in terms of the radius ratio of the ions.

**Table 2.1** Critical radius ratios for various coordination numbers. The most stable structure is usually the maximum coordination number allowed by the radius ratio. (Anion: white sphere; Cation: black sphere)

Type	Coordination No.	Minimum Radius Ratio	Structure <sup>[2]*</sup>
Linear	2	0	
Triangular	3	$2 / \sqrt{3} - 1 = 0.155$	
Tetrahedral	4	$\sqrt{3} / \sqrt{2} - 1 = 0.225$	
Octahedral	6	$\sqrt{2} - 1 = 0.414$	
Body Center Cubic (bcc)	8	$\sqrt{3} - 1 = 0.732$	
Hexagonal or Cubic Closest-Packing (hcp)	12	1	





**Figure 2.2** Schematic of stable and unstable coordinations. (Anion: white circle; Cation: black circle)

To maintain the fluorite structure, the ideal radius ratio of cation and anion ( $R^+/R^-$ ) derived from crystal geometry must be greater than 0.732. A smaller cation to anion radius ratio is expected to result in a lower coordination number. The ionic radii ratio of  $Zr^{4+}$  and  $O^{2-}$  (i.e.  $R_{Zr^{4+}}/R_{O^{2-}} = 0.62$ )<sup>[2]</sup> places  $ZrO_2$  on the border between octahedral array of rutile (as in  $TiO_2$ ), and cubic arrays of fluorite structure (as in  $UO_2$ ). The observed instability of c- $ZrO_2$  at room temperature originates from the close-packed oxygen ions in the fluorite structure, because the ionic radii ratio is too small to be compatible with the eight-fold structure<sup>[3]</sup> as depicted in **Figure 2.2**. However, the large cation of  $Zr^{4+}$  is also too large for a stable six-fold rutile structure which is never observed experimentally in  $ZrO_2$ . Indeed, the simple hard sphere ionic model is inadequate to explain the observed polymorphs of  $ZrO_2$ ; the partial covalent nature of Zr-O bonds has already been postulated<sup>[4]</sup> and is evident from electronic structure calculations based on density functional theory<sup>[5]</sup> as from the calculations reported later in this thesis.

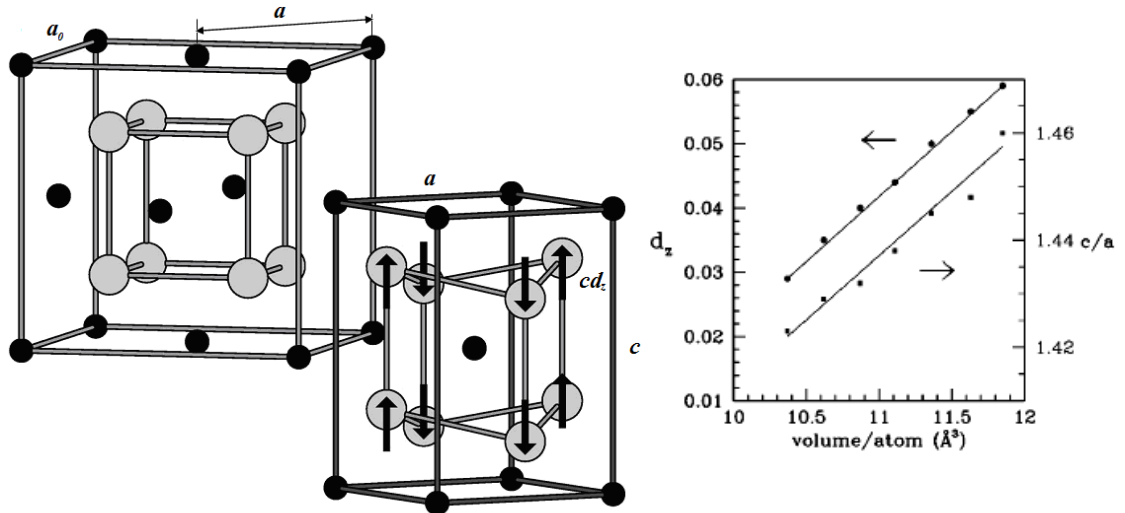
## 2.2 Phase transitions of $ZrO_2$

As discussed above, due to the structural instability caused by the incompatibility of its cation to anion radius ratio,  $ZrO_2$  could adopt various phases in different ranges of temperature and pressure. In particular, the three low pressure phases: cubic(c- $ZrO_2$ ,  $O_h^5$ ,  $Fm3m$ ), tetragonal (t- $ZrO_2$ ,  $D_{4h}^{15}$ ,  $P4_2/nmc$ ), and monoclinic (m- $ZrO_2$ ,  $C_{2h}^5$ ,  $P2_1/c$ ) structures have been extensively studied for both their scientific and



technological importance.<sup>[6-8]</sup> At ambient pressure,  $\text{ZrO}_2$  has a monoclinic structure up to a temperature of  $\sim 1450\text{K}$ <sup>[9]</sup> when the m to t-phase transition occurs accompanied by a decrease in unit cell volume since the 7-fold co-ordination of Zr changes to 8-fold.<sup>[10]</sup> The cubic fluorite phase of zirconia is only thermodynamically stable at temperatures higher than  $2650\text{K}$  prior to melting.<sup>[11]</sup> The phase transition mechanisms have been well understood through modelling studies and experimental observations.

**Figure 2.3** The geometry of cubic and tetragonal phase of zirconia (Left, reproduced from Ref. [13])). Light and dark circles denote oxygen and zirconium atoms, respectively. Note that the unit cell in tetragonal phase is rotated with respect to that in cubic structure.  $a_0$  denotes the lattice parameter of cubic phase.  $a$  and  $c$  represent the lattice parameters of tetragonal zirconia. Arrows represent the structural instability of the oxygen sublattice along  $c$  axis; the displacement is represented by arrows of length  $cd_z$ . The plots of calculated lattice parameters ratio  $c/a$  and internal structural parameter  $d_z$  of the tetragonal phase as a function of volume (Right, from Ref. [14]).

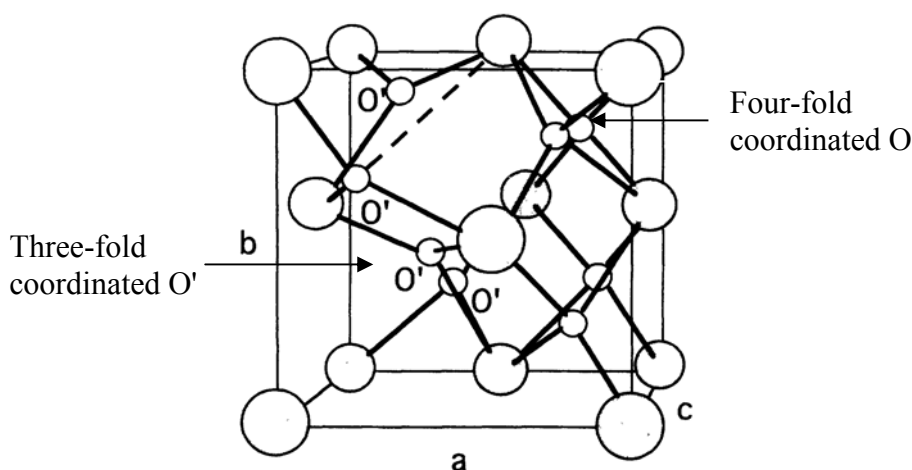


The tetragonal phase can be considered as a distorted cubic structure with displacement of oxygen ions along the  $\langle 001 \rangle$  direction ( $c$  axis). As shown in **Figure 2.3**, the c-t phase transition is driven by shifting the oxygen sub-lattice along this direction ( $c$  axis) and increasing the  $c/a$  from  $\sqrt{2}$  to  $\sim 1.45$ .<sup>[12]</sup> The displacement of oxygen atoms can be described by the internal parameter  $d_z$ , where the position of oxygen atoms is  $Z_0 = (0.25 \pm d_z) c$ .<sup>[13]</sup> According to previous *ab initio* studies of the tetragonal phase,  $d_z$  is a function of cell volume.<sup>[14]</sup>



Unlike the t-c transition, the m-t phase transition is usually described as a first order displacive martensitic (shear) phase transition, which means crystal undergoes shear because of the substantial difference in crystal structure between the two phases. To accommodate the extensive strain induced by such a transformation, both elastic and plastic strain of the surrounding material is necessary. The metastable tetragonal crystal can be restrained from undergoing the martensitic transformation by the constraint imposed by the matrix.<sup>[6]</sup> The m- to t-phase transition is accompanied with a decrease in lattice parameters and an increase in density of 4%. A key difference between m-ZrO<sub>2</sub> and the two more symmetric phases is that in m-ZrO<sub>2</sub>, Zr adopts 7-fold co-ordination by oxygen instead of 8-fold and the oxygen sublattice of m-ZrO<sub>2</sub> is split into two non-equivalent families: 4-fold coordinated and 3-fold as in **Figure 2.4**.

**Figure 2.4** Monoclinic crystal structure. Larger spheres, Zr<sup>4+</sup>; small sphere O<sup>2-</sup>. (From Ref. [5]) Small circles represent the oxygen atoms; large circles represent the zirconium atoms. *a*, *b* and *c* indicate the crystal line axes. O and are four and three coordinated oxygen atoms, respectively. The Zr-O' bond which is shown by a dashed line is broken. Note that the unit cell is rotated with respect to that in tetragonal cell.



In addition to the three low pressure equilibrium ZrO<sub>2</sub> phases, there are two orthorhombic (*Pbca*) high pressure phases which are designated as O<sub>I</sub> and O<sub>II</sub>. The transformation from m-ZrO<sub>2</sub> to the O<sub>I</sub> phase occurs between 3 and 11 GPa and a second pressure induced transition occur to form the O<sub>II</sub> phase with distorted cotunnite (PbCl<sub>2</sub>) structure<sup>[10]</sup> at ~22GPa<sup>[15-19]</sup>. Pressure increases the Zr<sup>4+</sup> coordination number from 7 to 9.



In computational modelling, the classical empirical models of zirconia are based on the assumption of its ionicity. Empirical approaches like the shell model or the rigid ion model described the structural,<sup>[20]</sup> dynamical,<sup>[21-22]</sup> and transport<sup>[23-25]</sup> properties of the  $\text{ZrO}_2$  phases on which they were parameterized, but failed to predict the absolute stability of the  $m$  structure. There have been several attempts to derive a transferable atomistic model describing the properties of zirconia at all temperature and pressures. Cohen *et al.*<sup>[26]</sup> constructed the potential ion breathing (PIB) model to derive elastic constants and equations of state for several  $\text{ZrO}_2$  polymorphs. Their results show significant discrepancies with experiment which have been attributed to the effect of non-spherical charge relaxation which is not included in the PIB approach. Boyer and Klein<sup>[27]</sup> derived a simple rigid-ion potential from linear muffin-tin orbital (LMTO) *ab initio* calculations. The resulting potential model gives the cubic fluorite structure as the ground state, implying that polarization effects need to be included which will act to lower the energy of the lower symmetry structures compared to the highly symmetric fluorite polymorph. Recent theoretical studies by Wilson, Schönberger, and Finnis have extended the ionic model to include compressible and polarizable oxygen ions. This compressible ion model (CIM) provided an explanation of the relative stability of the  $\text{ZrO}_2$  phases at 0 K, in particular, the occurrence of the monoclinic phase as the ground state which can be attribute to the dipole and quadrupole polarizabilities of the  $\text{O}^{2-}$  ion which induce the symmetry breaking distortions of the lattice.<sup>[10][28]</sup> However, the calculated lattice energies are still significantly higher than the experimental values and also failed to generate the “double well” energy landscape for the distortion of the cubic to the tetragonal structure.

The experience gained with the CIM model suggests that a successful empirical model of zirconia should describe the effects of the atomic polarization, but should also go beyond a purely ionic description of the bonding. The semiempirical method gives a less satisfactory representation of the partial covalent character of zirconia. Stefanovich, Shlunger and Catlow<sup>[5]</sup> presented a mix of calculation techniques including *ab initio* Hartree-Fock, semiempirical Hartree-Fock, and atomistic relaxation with classical potentials to study the electronic and geometrical structures of pure and doped  $\text{ZrO}_2$  phases. The three low pressure phases (monoclinic, tetragonal, and cubic) were qualitatively reproduced by the semiempirical Hartree-Fock and full

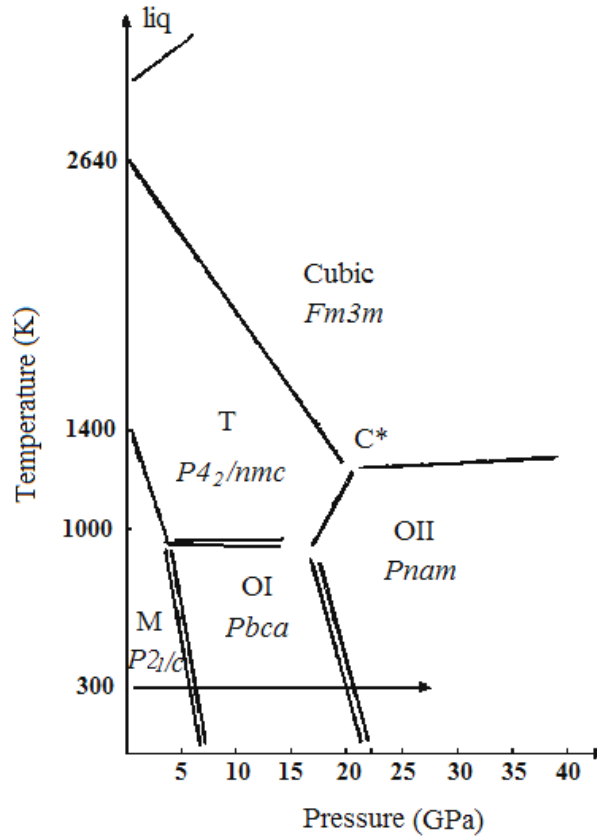


Hartree-Fock techniques. The classical potentials predicted an orthorhombic phase in disagreement with the two other approaches. Despite the different methods used for both the electronic structure calculation and the charge determination, a decrease of ionicity for lower symmetry phases has been generally found. Since smaller ionicity (high covalency) favors structures with lower coordination numbers,<sup>[29-31]</sup> the Zr-O covalent bonding is considered as one of the major factors influencing the stability of the low symmetry structures of zirconia. However, the comparison with experimental data shows that the energy differences between the three phases are underestimated even in the *ab initio* Hartree-Fock techniques. Only the very recent Hartree-Fock<sup>[12]</sup> and DFT calculations studies<sup>[14][32-33]</sup> consistently reproduce the relative energetics of the zirconia polymorphs including the monoclinic ground state and the high pressure orthorhombic phases.

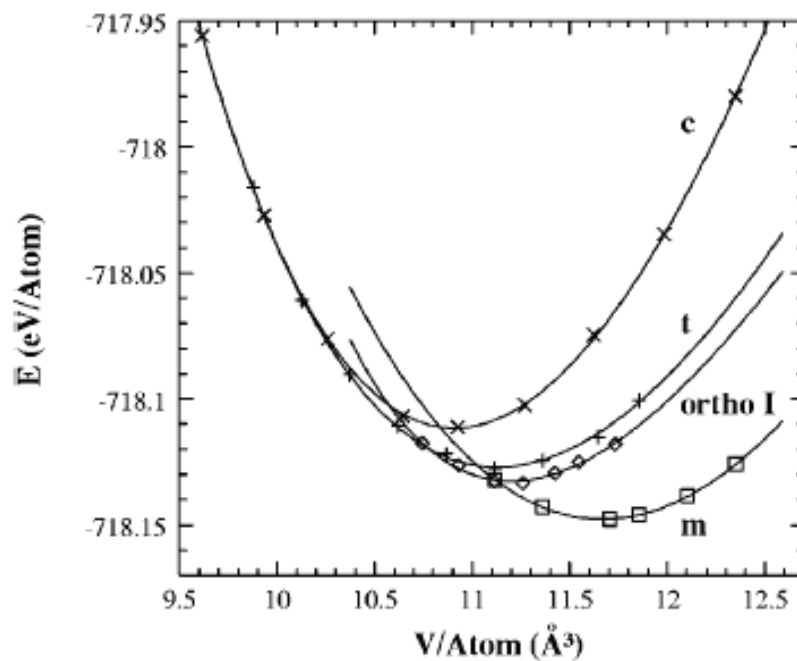
To summarize previous experimental and theoretical studies, first, in **Figure 2.5** we display the pressure-temperature phase transition diagram of pure ZrO<sub>2</sub> which was generated by Bouvier *et al.*<sup>[18]</sup> The relevant lattice parameters for the observed phases of ZrO<sub>2</sub> are summarized in **Table 2.2**. **Figure 2.6** plots the computed energy versus volume at zero temperature by Stapper *et al.*<sup>[14]</sup> and the unit cell structures of three low pressure phases are presented in **Figure 2.7**. These data provide a reasonable starting point for modelling bulk ZrO<sub>2</sub>.



**Figure 2.5** Pressure-temperature phase diagram of zirconia. The lower arrow corresponds to an experimental excursion performed using Raman spectrometry on pure monoclinic zirconia. (From Ref. [18])



**Figure 2.6** Computed energy versus volume data fitted by a Murnaghan equation of state for monoclinic (m), tetragonal (t), cubic (c), and orthorhombic brookite (orthoI) phases. (From Ref [14])





**Table 2.2** Lattice parameters of the phases of ZrO<sub>2</sub>.

(a) Lattice parameter for the Low-Pressure phases. (The tetragonal phases t' and t'' for Y<sub>2</sub>O<sub>3</sub> doped ZrO<sub>2</sub> are discussed in section 2.3)

	<b>m</b>	<b>t</b>	<b>t'</b>	<b>t''</b>	<b>c</b>
Space Group	$P2_1/c$	$P4_2/nmc$	$P4_2/nmc$	$P4_2/nmc$	$Fm3m$
a Å	5.156	3.64	~3.5984	5.094	5.07
b Å	5.191				
c Å	5.304	5.27	~5.1520	5.177	
c/a		1.448	~1.432	1.016	1
$\beta$	98.9°	90°	90°	90°	90°
coordination	7	8	~8	~8	8
ZrO <sub>2</sub> per unit cell	4	2	2	4	4
Density gm cm <sup>-3</sup>	5.830			6.100 (calc)	6.090 (calc)
Reference	34	35	36	37	38

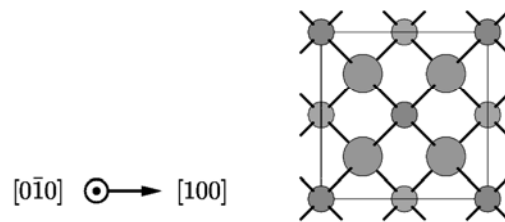
(b) Lattice parameters for the High-Pressure phases

	<b>m</b>	<b>O<sub>I</sub></b>
Space Group	$P2_1/c$	$P bca$
coordination	7	9
Wyckoff	Zr (0.2754, 0.0395, 0.2083)	Zr (0.8843, 0.0332, 0.2558)
Coordinates	O <sub>I</sub> (0.0700, 0.3317, 0.3447)	O <sub>I</sub> (0.7911, 0.3713, 0.1310)
	O <sub>II</sub> (0.4496, 0.7569, 0.4792)	O <sub>II</sub> (0.9779, 0.7477, 0.4948)
Reference	39	40



**Figure 2.7** Unit cells of the observed bulk structures of  $\text{ZrO}_2$ : a) Cubic, b) Tetragonal and c) Monoclinic. The cubic and tetragonal unit cells chosen correspond to the  $\text{CaF}_2$  unit cell. Crystalline directions are indicated by arrows at the lower right of each panel. Zr ions are small and O ions are large. Ions in the foreground are shaded darker than ions in the background. (From Ref. [19])

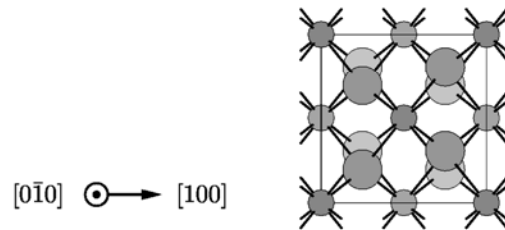
- a) Cubic (space group :  $\text{Fm}\bar{3}\text{m}$ )  
stable :  $2370^\circ\text{C} < T < 2600^\circ\text{C}$



Inequivalent directions :

$[100]$   
 $[110]$   
 $[111]$

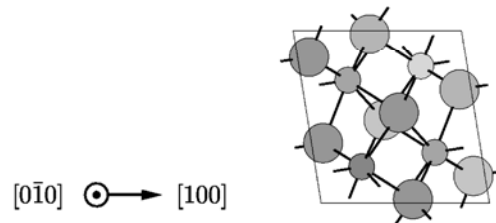
- b) Tetragonal (space group :  $\text{P } 4_2/\text{n m c}$ )  
stable :  $1180^\circ\text{C} < T < 2370^\circ\text{C}$



Inequivalent directions :

$[001]$   
 $[100]$   
 $[110]$   
 $[101]$   
 $[111]$

- c) Monoclinic (space group :  $\text{P } 2_1/\text{c}$ )  
stable :  $0^\circ\text{C} < T < 1180^\circ\text{C}$



Inequivalent directions :

$[001]$   $[011]$   
 $[010]$   $[\bar{1}01]$   
 $[100]$   $[111]$   
 $[110]$   $[\bar{1}\bar{1}1]$   
 $[101]$



## 2.3 Phase Stabilization - The Behavior of Dopants

The cubic phase of  $\text{ZrO}_2$  is only stable at high temperature; the volume expansion caused by the c-t or to t-m transformation induces very large stresses, and will cause pure  $\text{ZrO}_2$  to crack upon cooling. Stabilization of zirconia can be achieved by addition of larger cations to expand the lattice or by doping with a lower valence cation to create oxygen anion vacancies (e.g. Y), or a combination of the two effects. The creation of oxygen vacancies serves to reduce the average co-ordination number and facilitates relaxation of the oxygen sub-lattice towards cubic symmetry; this mechanism can be considered more effective than expanding the lattice. Four groups of cation dopants are discussed in the following section. In addition, undoped t- $\text{ZrO}_2$  can also be stabilized at room temperature as small particles typically less than 20 nm in diameter, by using solution phase precipitation preparation processes. This effect stems from the dominance of surface tension (surface energy) in controlling morphology and crystal structure. However, on heating to temperatures above  $800^\circ\text{C}$ , sintering occurs and the material transforms to m- $\text{ZrO}_2$ .<sup>[18][41]</sup>

### 2.3.1 Categories of Cation Dopants

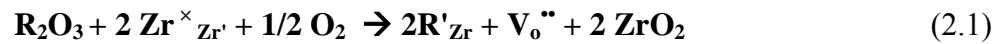
#### a) Tetravalent Cations

Since tetravalent cations stabilize the cubic phase by expanding the  $\text{ZrO}_2$  lattice, the dopant size must be greater than that of  $\text{Zr}^{4+}$  (0.84 Å). Practically, due to factors relating to cost and toxicity, the choice is limited to  $\text{Ce}^{4+}$  (0.97 Å) and normally,  $\text{CeO}_2$  must be added at high mole fractions to achieve cubic stability. Formation of a cubic-like phase (t"/c), i.e.  $c/a$  equal to unity requires a high content level of  $\text{CeO}_2$  ~70%. Tetragonal stabilization (t') can be achieved at ~30%.<sup>[42]</sup> However, using lower dopant levels, stabilization has been claimed for small crystallite sizes.<sup>[43]</sup> Besides expanding the  $\text{ZrO}_2$  lattice, Ce can also be preserved as  $\text{Ce}^{3+}$  through the facile  $\text{Ce}^{4+}/\text{Ce}^{3+}$  redox reaction which creates oxygen vacancies in  $\text{ZrO}_2$ <sup>[44]</sup> as discussed below for  $\text{Y}^{3+}$ .

#### b) Rare Earth Trivalent Cations



Rare earth trivalent cations operate to stabilize the fluorite structure through creation of oxygen vacancies according to the following reaction:



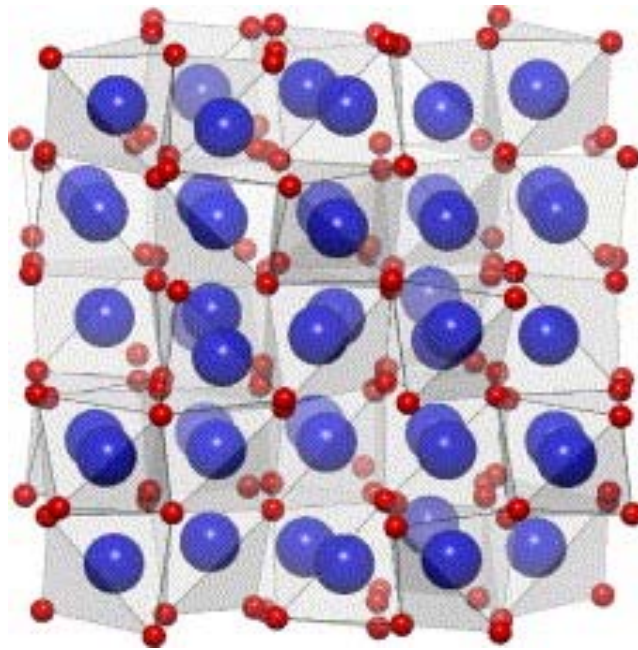
The solubilities of trivalent cations in  $\text{ZrO}_2$  depend on the match of cation ionic radii, and also the similarity of the cation and oxygen anion sub-lattices between the sesquioxide cubic (C)  $\text{R}_2\text{O}_3$  structure, which is adopted by the  $\text{Y}_2\text{O}_3$  and several of the rare earth oxides, and c- $\text{ZrO}_2$ .

The structure of the rare earth oxides vary with the cation radius. Under ambient conditions, the hexagonal A-form is the stable structure for the larger cations,  $\text{R} = \text{La}$ ,  $\text{Ce}$ ,  $\text{Pr}$ ,  $\text{Nd}$ , while  $\text{Sm}_2\text{O}_3$ ,  $\text{Eu}_2\text{O}_3$ , and  $\text{Gd}_2\text{O}_3$  with smaller cations have both the monoclinic B- and cubic C-form. <sup>[45]</sup> The solubilities of those cations in  $\text{ZrO}_2$  and cubic stabilization are not straightforward. For Instance, the largest rare earth cation  $\text{La}^{3+}$  (1.16 Å), has a strong tendency to segregate as the pyrochlore  $\text{La}_2\text{Zr}_2\text{O}_7$ . <sup>[46]</sup> For the second largest,  $\text{Pr}^{3+}$  (1.126 Å), experimental work has suggested that mixtures of tetragonal phases are present at dopant levels above 15 mol%. <sup>[41]</sup> In the case of the rare earths, a temperature limit ( $T_L$ ) has been defined, above which there is a continuous evolution of the structure from tetragonal to cubic and the biphasic domain of c- and t- $\text{ZrO}_2$  co-exist. <sup>[47]</sup> For  $\text{Nd}^{3+}$  (1.109 Å) and  $\text{Sm}^{3+}$  (1.079 Å),  $T_L$  lies close to the melting point, while for  $\text{Gd}$  (1.053 Å),  $T_L$  occurs significantly below the melting point. X-Ray Diffraction has also indicated considerable crystal distortion for  $\text{Nd}$  and  $\text{Sm}$  doped  $\text{ZrO}_2$  compared to the smaller  $\text{Gd}$ . <sup>[48]</sup>

The C-type  $\text{R}_2\text{O}_3$  structure is characteristic for  $\text{R} = \text{Tb}$ ,  $\text{Dy}$ ,  $\text{Ho}$ ,  $\text{Er}$ ,  $\text{Tm}$ ,  $\text{Yb}$ ,  $\text{Lu}$ ,  $\text{Y}$ , and  $\text{Sc}$  as presented in **Figure 2.8**. <sup>[45]</sup> In essence, the C-type sesquioxides can be derived from the face centred cubic fluorite phase by removal of  $1/4$  of the oxygen anions with the remainder having a small displacement resulting in reduction of the symmetry from  $C_1$  to  $D_{5d}$  type. In this process, the eight cations in the  $\text{R}_2\text{O}_3$  unit cell do not change their position, while the oxygen anions are subject to more significant displacement but remain approximately within the same locations as in the symmetric c- $\text{ZrO}_2$  phase. The anion framework occupies a second, larger, body centred cubic super-cell with lattice parameter ( $a_i$ )  $\sim 10$  Å, i.e. twice the unit cell parameter for c- $\text{ZrO}_2$  ( $a_F$ )  $\sim 5$  Å. <sup>[49]</sup> Due to this structural similarity, these small rare earth cations have



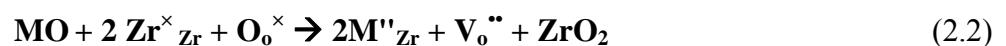
been shown to be effective in phase stabilization of c-ZrO<sub>2</sub> with little crystal distortion.<sup>[50]</sup> In terms of cost effectiveness, Y<sup>3+</sup> (1.019 Å) is practically the best option to stabilize c-ZrO<sub>2</sub> for high temperature applications. The behaviour of Y stabilized ZrO<sub>2</sub> is discussed in more detail in Section 2.3.2. The smallest rare earth cation Sc<sup>3+</sup> (0.87 Å) is also of considerable interest in fuel cell applications since it gives higher ionic conductivity.<sup>[51-55]</sup> However, for Sc<sup>3+</sup>, there is a strong tendency for segregation of a rhombohedral β phase above 10 mole% Sc<sub>2</sub>O<sub>3</sub>.



**Figure 2.8** The polyhedral representation of the cubic C-type structure of R<sub>2</sub>O<sub>3</sub>. The large and small spheres are R and O atoms, respectively. (From Ref. [45])

c) Divalent Alkaline Earths- Mg<sup>2+</sup>; Ca<sup>2+</sup> ;

Doping ZrO<sub>2</sub> with the alkaline divalent cations can be represented by the Kröger-Vink notation:



From the equation above, the divalent alkaline earths are twice as efficient per cation in creating anion vacancies as trivalent dopants. However, the dopant charge mismatch of 2+ in itself could generate structural instability and there is evidence of



phase segregation (e.g.  $\text{CaZr}_4\text{O}_9$ ) in its use at high temperature. This group of dopants is therefore only employed in the manufacture of partially stabilized zirconia (PSZ) [6].

#### d) Transition Metals and $\text{Al}^{3+}$

In addition to  $\text{Sc}^{3+}$  discussed above, a number of  $\text{M}^{3+}$  first row transition metals have been doped into zirconia. Also,  $2+$  and  $4+$  species have been investigated. As an example, for small amounts of  $\text{Mn}^{3+}$  doping into yttria partially stabilized zirconia (Y-PSZ), the tetragonal (t') phase can be further stabilized to the cubic phase. [54] In contrast, substitution by  $\text{Ti}^{4+}$  in Y-PSZ causes formation of m- $\text{ZrO}_2$ , i.e. destabilization, which has been suggested may due to  $\text{Ti}^{4+}$  occupying interstitial sites and removal of oxygen anion vacancies according to the equation [59]:



$\text{Al}^{3+}$ ,  $\text{Fe}^{3+}$ ;  $\text{Cu}^{2+}$  and  $\text{Ni}^{2+}$  have all been reported to be stable in  $\text{ZrO}_2$ , but on calcination to above  $800^\circ\text{C}$ , phase segregation occurs and m- $\text{ZrO}_2$  is formed on cooling. [55-58]

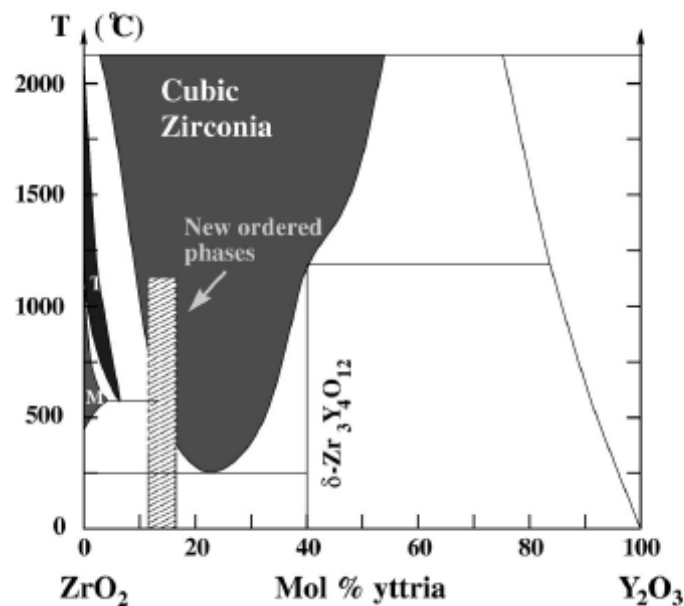
#### 2.3.2. Yttria-stabilized c- $\text{ZrO}_2$

In practice, the c-type  $\text{Y}_2\text{O}_3$ , which would be stable up to  $1800^\circ\text{C}$  in air, [45] is the most commonly used stabilizer for zirconia. Yttria-stabilized zirconia (YSZ) is a solid solution in the cubic fluorite lattice with yttrium and zirconium on a face-centered-cubic cation lattice and oxygen and vacancies on a simple cubic anion lattice. In the cubic fluorite structure, each cation is in the center of a cube of eight anions and each oxygen ion or oxygen vacancy is in the centre of a cation tetrahedron. The introduction of yttria creates charge compensating oxygen vacancies that become mobile at high temperatures, and hence increases the conductivity; an oxygen ion can hop across an edge of a tetrahedron between two cations. [59] YSZ is an attractive electrolyte for solid oxide full cell (SOFC) because it exhibits good oxide ion conductivity over a wide range of oxygen partial pressures, is stable under oxidizing and reducing conditions, and has good elevated temperature mechanical properties [3].



In the case of Y doped  $\text{ZrO}_2$ , the work reported by Yashima *et al.* [50] indicates that there are actually three tetragonal phases t, t' and t''- $\text{ZrO}_2$ . All these phases belong to the  $P4_2/nmc$  space group as shown in **Table 2.2(a)**. Pure t- $\text{ZrO}_2$ , which is transformable directly to m- $\text{ZrO}_2$  and stable only at high temperature, appears as a tetragonal phase in the equilibrium or stable phase diagram. Doping of cations at a low content level can stabilize the tetragonal phases at room temperature. The doped t'-form ( $c/a > 1$ ) is metastable even at high temperature and does not transform to the m- $\text{ZrO}_2$  phase. t'' is unstable in relation to the mixture of dopant stabilized c- $\text{ZrO}_2$  or t'. The t'' phase, which contains a higher dopant level than t', is defined as a tetragonal form without tetragonality, i.e.  $c/a = 1$ , but the oxygen atoms are displaced all along the c axis from the ideal sites in the fluorite cubic phase. t''- $\text{ZrO}_2$  is, however, also metastable. [41][42]

**Figure 2.9** Schematic illustration of the  $\text{Y}_2\text{O}_3$ - $\text{ZrO}_2$  composition temperature phase diagram. (Taken from Ref. [60-61])



**Table 2.3** Ytria dopant composition range for metastability.

$\text{YO}_{1.5}$ Mole %	m	t'	t''	c
Minimum Dopant Level	-	5	16	20
Dopant Range	0-5	2-16	12-20	$\geq 20$



According to previous experimental studies, various phases can be generated from the solid solution depending on the composition of  $\text{Y}_2\text{O}_3\text{-ZrO}_2$  system. **Figure 2.9** presents the  $\text{Y}_2\text{O}_3\text{-ZrO}_2$  phase diagram<sup>[60][61]</sup>, in which the formation of m- $\text{ZrO}_2$  is confined to a small region of the phase diagram  $\leq 3$  mol%  $\text{Y}_2\text{O}_3$  (6 % Y) as suggested by Schusterius *et al.*<sup>[62]</sup> In the region of 2-6 mol% yttria content, the partially stabilized zirconia (PSZ) is produced with a tetragonal phase t'. The fully stabilized zirconia (FSZ) is shown to occur at an yttria content above approximately 8 mol%. However, around 8 mol % yttria content, the presence of a cubic like t'' phase ( $a/c$  is equal to unity), which can not be distinguished from the cubic phase by XRD, have also been identified from Laser Raman spectroscopy and electron diffraction studies by Yashima *et al.*<sup>[50]</sup> According to Pascual and Durán,<sup>[63]</sup> for an yttria content higher than 40 mol %, the system crystallizes as  $\text{Y}_4\text{Zr}_3\text{O}_{12}$ . Mixtures of the cubic Y doped  $\text{ZrO}_2$  solid solution and segregated microdomains of  $\text{Y}_4\text{Zr}_3\text{O}_{12}$  were also proposed for an yttria content between 15-40 mol%. **Table 2.3** generalises the stable phase behaviour as a function of the trivalent cation concentration.

For applications in catalysis and as solid oxide anion conductors, zirconia stabilised at 8-10 mol%  $\text{Y}_2\text{O}_3$  is employed, since the ionic conductivity of YSZ exhibits several intriguing features. It increases with the dopant concentration up to about 8-9 mol%  $\text{Y}_2\text{O}_3$  and then decreases with the addition of more yttria, despite the presence of more vacancies that could aid oxygen diffusion.<sup>[64][65]</sup> The decrease in conductivity has been attributed to defect interactions, clustering effects and the tendency of ordering but the origin is not yet clear. Generally, two mechanisms have been postulated by several previous studies: more yttria increases the number of randomly distributed high-energy Y-Y pathways, making oxygen diffusion less favorable, and the addition of yttria introduces more vacancies that form ordered arrangements and inhibit the diffusion of oxygen into vacant sites.<sup>[66-70]</sup> The study of ordering in the  $\text{ZrO}_2\text{-Y}_2\text{O}_3$  system is, thus, a subject that has generated much interest.

A number of computational studies of have been carried out concerning the composition and ordering of bulk yttrium stabilised zirconia. For example, Katamura and Sakuma<sup>[71]</sup> have investigated the microstructural evolution during the cubic-to-tetragonal transition by using the continuum time-dependent Ginzburg Landau (TDGL) kinetic model, in which, the free energy of  $\text{ZrO}_2\text{-Y}_2\text{O}_3$  system at a constant



temperature is calculated to be a surface varying with both yttria composition and structure tetragonality (i.e.  $a/c$ , defined as order parameter by the authors). Their simulation work also predicts that the anti-phase domain boundary has a cubic-like structure ( $t''$ ) in agreement with the experimental studies by Yashima *et al.*

Several computational studies also have been carried out to examine the ordered ground-state structures in  $\text{ZrO}_2\text{-Y}_2\text{O}_3$ . Bogicevic *et al.* [60] using DFT method established the model of the experimentally identified compound  $\delta\text{-Zr}_3\text{Y}_4\text{O}_{12}$  (i.e.  $\sim 43\%$  Y substitution), and several metastable zirconia-rich ordered phases were predicted in which the anion vacancies repel each other at short separations, but show an energetic tendency to align as third-nearest neighbors ( $3^{\text{rd}}$  NN) along  $\langle 111 \rangle$  directions. Moreover, Predith *et al.* [59] predict a stable ground-state of  $\text{Zr}_4\text{Y}_2\text{O}_{11}$  by DFT calculations at 33 mol%  $\text{YO}_{1.5}$  content. The  $\text{Zr}_4\text{Y}_2\text{O}_{11}$  structure contains several features of the stability found in YSZ: yttrium with oxygen vacancies at the second nearest neighbor sites ( $2^{\text{nd}}$  NN or NNN), relaxation of Zr-O bond lengths, and seven fold coordination of zirconium by oxygen as in monoclinic  $\text{ZrO}_2$ . The discovery of metastable ordered structures at 25% and 29% mole  $\text{YO}_{1.5}$  content of YSZ suggests that short-range order at these compositions may be expected at nonzero temperatures.

While some reports have focused on the structures of YSZ and the evidence for short range ordering, others have focused on elucidating the driving forces for stability. Three major driving forces for stability in the system are considered to be: (i) the electrostatic interaction of ions and vacancies; (ii) the preference for 7-fold coordinated zirconium; and (iii) the relaxation of ions away from idealized cubic fluorite sites driven by vacancy relaxation and by the size difference between  $\text{Y}^{3+}$  and  $\text{Zr}^{4+}$ , regarding which, the effect of relaxation has been extensively discussed. [72]

Numerous experimental studies have measured the direction of relaxation of oxygen, Zr, and Y away from cubic fluorite sites. [14][74-80] In contrast, some computational studies of ordered structures show that the elastic and electrostatic interactions push the structure in opposite directions. [72-73] The elastic component of the energy tends to move the ions away from cubic fluorite sites. In particular, Zacate *et al.* [81] using interatomic potential approach found that oxygen ions relax toward a vacancy when a dopant cation smaller than Zr is the nearest neighbour (NN) to the vacancy. If the



dopant located at the NN position is larger than Zr (eg. Y), only some of the oxygen ions relax in position. The dopant-vacancy pair has the highest binding energy in the case of the larger dopant move to a next nearest neighbor (NNN) site to the vacancy. With respect to yttrium dispersion, Li and Hafskjold <sup>[82]</sup> concluded that the oxygen vacancy prefers Y as its nearest neighbour, consistent with early X-ray absorption spectroscopy studies <sup>[78][79]</sup>. A recent simulation by Kilo et al <sup>[67]</sup> found that oxygen vacancies in YSZ have no energetic preference between Zr and Y as first neighbors (NN). However, several simulations <sup>[75][80][82–84]</sup> and experiments, <sup>[60][80]</sup> indicate that oxygen vacancies tend to be located at the second nearest neighbor position with respect to  $Y^{3+}$ .

## 2.4 ZrO<sub>2</sub> Surfaces

Surfaces impart crucially important properties to the performance of a material, especially, in applications to catalysis. Both experimental techniques and computational modelling have been applied to investigate surface structure and properties. In this section, previous studies for pure and yttrium stabilized zirconia are reviewed with respect to surface structure and morphology and yttrium segregation.

### 2.4.1 Surface Structure and Morphology

In experimental studies, the low index surfaces of Y-stabilized t-ZrO<sub>2</sub> and m-ZrO<sub>2</sub> have been examined by Auger, photoelectron, and vibrational spectroscopy as well as high resolution transition electron microscopy (HRTEM) and X-ray diffraction. However, these techniques have mostly provided indirect and incomplete information about the detailed surface atomic structure. From HRTEM studies at lower calcination temperatures (600°C), Morterra *et al.* <sup>[85]</sup> show that Y stabilized t-ZrO<sub>2</sub> appears to display small coin-like morphology with the (111) surface favoured. At higher calcination temperatures, the morphology changes to pebble-like crystals with (101) as a prominent surface. In monoclinic ZrO<sub>2</sub>, the study found the material tends to form coin-like particles and have a strong preference for (111) and ( $\bar{1}11$ ) surfaces. Moreover, some very recent experimental studies proposed that the corrugated surfaces



containing a high density of steps may be stable relative to flat YSZ surfaces or kinetically inhibited from annealing.<sup>[86-88]</sup>

Several computational modelling studies on zirconia surface properties have been reported. Christensen and Carter<sup>[19]</sup> carried out a systematic density functional study on the principal surfaces of zirconia for all experimentally observed bulk phases. The monoclinic ( $\bar{1}11$ ) and tetragonal (101) surfaces are predicted to be the most stable. Both exhibit a rather small relaxation, confined to the near surface ions. (NOTE: The tetragonal (101) surface was characterised as (111) and tetragonal (001) was considered as (110) due to using the coordinate system of cubic zirconia.) Haase and Sauer<sup>[89]</sup> have carried out another density functional study for the (pure) tetragonal phase. The authors conclude that the (101) surface is more stable than (001) which in turn is more stable than (111). This is in accord with experimental results by Morterra *et al.* on Y stabilized t-ZrO<sub>2</sub>.<sup>[85]</sup>

For cubic ZrO<sub>2</sub>, according to the previous computational studies, the (011) and (111) surfaces are predicted as the most thermodynamically stable surfaces. Overall, the calculations confirm that the (111) surface is more stable than (011). The results from the atomistic simulations<sup>[90]</sup> in terms of relaxed surface structure and energy are very similar to the more computationally demanding quantum mechanical (QM) calculations<sup>[91]</sup>. The Hartree-Fock studies carried out by Genard *et al.*<sup>[92]</sup> show that in the relaxed (011) surface, Zr reduces to 6-fold co-ordination and O becomes three-fold. The surface can be described as being constructed from repeated O-metal-O platelets separated by rows of vacant interstitial sites in the O sub-lattice. On relaxation, columns of cations move up or down in a concerted way with the oxygen ions ‘rolling’ round the cations keeping the Zr-O distance roughly constant. These QM studies also suggest that surface Zr ions have a higher electron density than those in the subsurface layers and in the bulk indicating the increased covalent nature of Zr-O bonds at the surface where the Coulomb field is less favourable to formally charged Zr<sup>4+</sup>/O<sup>2-</sup>. The increased electron density of surface cations is orientated perpendicular to the surfaces. Likewise, the surface oxygen ions show pronounced deviations from spherical symmetry.



Turning to the surface structure, the (111) surface can be imagined as a stepped (011) surface in which the O-metal-O platelets partially overlap those in the layer below. The overall effect is a rumpled surface with highly exposed terminal oxygen ions, O is three-fold coordinated and Zr is 7-fold coordinated, similar to the bulk m-ZrO<sub>2</sub>. Slight oxygen displacements  $\sim 0.05$  Å, were found. Besides these two low index surface, Balducci *et al.* <sup>[90]</sup> have studied the (310) surface of cubic fluorite structure ZrO<sub>2</sub> atomistically. Following extensive relaxation, the (310) surface becomes energetically comparable to the (110) surface, but still less stable than the (111) surface.

Overall, the results of experimental and computational morphology studies for the studies for the phases of zirconia can be summarized as below in **Table 2.4**.

**Table 2.4** Surface morphologies for the phases of zirconia.

Stability	Cubic <sup>a</sup>	Tetragonal <sup>b</sup>	Y-Stabilized Tetragonal <sup>c</sup>	Monoclinic <sup>cd</sup>
↑	(111)	(101)	(101) **	(111)
	(110)	(001)	(111) *	( $\bar{1}11$ )
	(310)	(111)		

a computational modelling [90-91]

b computational modelling [89][92]

c HRTEM measurements [85]

d computational modelling [19]

\* Low temperature calcination – 600°C \*\* High temperature calcination  $\geq 800^\circ\text{C}$

The previous computational works discussed above related to surfaces modelled as terraces. However, the more complicated topology of the relevant cubic structures such as MgO and CeO<sub>2</sub> have also been investigated by recent modelling work. For simple rock-salt structure MgO, DFT molecular modelling was carried out by Pawel Stelmachowski *et al.* <sup>[93]</sup> to elucidate the role of topological irregularities such as corners, steps and edges in dry and wet environment. In the case of the fluorite structure, However, Branda *et al.* <sup>[94]</sup> have built a variety of stoichiometric and nonstoichiometric step models for the (111) surface of c-CeO<sub>2</sub> with varying Ce



coordination number. According to their DFT calculation, a more stable step model has been established as the realistic model for steps which can serve as a basis for the further adsorption studies in computational heterogeneous catalysis. However,  $\text{ZrO}_2$  is expected to behave differently from  $\text{CeO}_2$  due to its different structural and redox properties, a set of step models for  $\text{ZrO}_2$  has been separately developed and examined in this thesis.

### 2.4.2 Yttrium Surface Segregation

There is an accumulation of experimental and computational evidence that Y in stabilized t- and c- $\text{ZrO}_2$  does indeed segregate to the surface. The X-ray photoelectron spectroscopy (XPS) studies by Morterra *et al.*,<sup>[85]</sup> indicate that Y segregation in t- $\text{ZrO}_2$  is favoured under conditions of marginal stabilization (low levels of yttria content ~2 mol %  $\text{Y}_2\text{O}_3$ ). For PSZ or FSZ with 3-10 mol %  $\text{Y}_2\text{O}_3$ , Y segregation has also been confirmed by low energy ion scattering, which indicated that there is a high enrichment of yttrium on YSZ surface monolayers.<sup>[95][96]</sup> Bernasik's study of the surface segregation in yttria-stabilized zirconia by XPS data shows an Y level at the surface in excess of the bulk concentration, but only slightly.<sup>[91]</sup> Moreover, a concentration limit of yttrium at the surface of YSZ has been observed by Zhu *et al.*<sup>[97]</sup> They also suggested that the surface composition is independent of Y concentration in the bulk due to segregation of  $\text{Y}_2\text{O}_3$ .

Ballabio *et al.*,<sup>[98]</sup> have performed DFT calculations for the main surfaces (111), (110) and (100) of YSZ. They reported yttrium segregation as well. From another *ab initio* study by Eicher and Kresse<sup>[99]</sup>, in Y stabilized t- $\text{ZrO}_2$ , the (101)<sub>t</sub> surface becomes more stable if the dopants are located close to the surface which indicates a driving force for Y surface segregation. In contrast, for the (001)<sub>t</sub> surface, there is no significant driving force for Y surface segregation. (Note: The tetragonal (101)<sub>t</sub> is equivalent to the (111)<sub>c</sub> c- $\text{ZrO}_2$  surface and (001)<sub>t</sub> surface is equivalent to the (110)<sub>c</sub> surface). This study also suggested that the (stoichiometric) oxygen (O) terminated phase is more stable than the Zr or O-O terminations, independent of the specific orientation of the surface. Atomistic simulation techniques also have been used to predict the preferential segregation of yttrium to the low index surface of the t- $\text{ZrO}_2$ . According to the recent study by Stanek *et al.*,<sup>[100]</sup> since surface orientation dependence caused significant



variation in concentration of yttrium at different surfaces, properties that are a function of defect concentration and distribution are also surface dependent.

The accompanying surface segregation of the charge compensating oxygen anion vacancies in YSZ would have a substantial effect on surface chemistry in relation to defining the nature of the active sites influencing catalyst behaviour.



---

## References

---

- [1] S. A. Heimstra, *Amer. Mineral.* **40**, 275, 1955.
- [2] L. Pauling, *The Nature of the Chemical Bond and the Structure of Molecules and Crystals: An Introduction to Modern Structural Chemistry*, Cornell University Press, Ithaca, NY, 1960; L. Pauling, *J. Am. Ceram. Soc.* **51**, 1010, 1929.
- [3] T. H. Etsell and S. N. Flengas, *Chem. Rev.* **70**, 339, 1970
- [4] S. M. Ho, *Mater. Sci. Eng.* **54**, 23, 1982.
- [5] E. V. Stefanovich, A. L. Shluger, and C. R. A. Catlow, *Phys. Rev. B* **49**, 11560, 1994.
- [6] *Science and Technology of Zirconia, Advances in Ceramics, Vol. 3*, edited by A. H. Heuer and L. W. Hobbs, The American Ceramics Society, Westerville, OH, 1981.
- [7] F. F. Lange, *J. Mater. Sci.* **17**, 240, 1992.
- [8] G. Teufer, *Acta Cryst.* **15**, 1187, 1962.
- [9] J. D. McCullough and K. N. Trueblood, *Acta Cryst.* **12**, 507, 1959.
- [10] M. Wilson, U. Schönberger, and M. W. Finnis, *Phys. Rev. B.* **54**, 9147, 1996-I
- [11] O. Ruff and F. Ebert, *Z. Anorg. Allg. Chem.* **180**, 19, 1929.
- [12] R. Orlando, C. Pisani, C. Poetti, E. Stefanovich *Phys. Rev. B* **45**, 596, 1992.
- [13] S. Fabris, A. T. Paxton, and M. W. Finnis, *Phys. Rev. B* **61**, 6617, 2000.
- [14] G. Stapper, M. Bernasconi, N. Nicoloso, and M. Parrinello, *Phys. Rev. B* **59**, 797, 1999.
- [15] O. Ohtaka, T. Yamanaka, S. Kume, E. Ito and A. Navrotsky, *J. Am. Ceram. Soc.* **74**, 505, 1991.
- [16] O. Ohtaka, T. Yamanaka, S. Kume, N. Hara, H. Asano, and F. Izumi, *J. Am. Ceram. Soc.* **78**, 233, 1995.
- [17] C. J. Howard, E. H. Kisi, and O. Ohtaka, *J. Am. Ceram. Soc.* **74**, 2321, 1991.
- [18] P. Bouvier, E. Djurado, and G. Lucazeau, T. Le Bihan, *Phys. Rev. B* **62**, 8731, 2000.
- [19] A. Christensen and Emily A. Carter, *Phys. Rev. B* **58**, 8050, 1998.
- [20] A. Dwivedi and A. N. Cormack, *Philos. Mag. A* **61**, 1, 1990.
- [21] A. P. Mirgorodsky, M. B. Smirnov, and P. E. Quintard, *Phys. Rev. B* **55**, 19, 1997.
- [22] A. Cormack and S. C. Parker, *J. Am. Ceram. Soc.* **73**, 3220, 1990.
- [23] X. Li and B. Hafskjold, *J. Phys.: Condens. Matter* **7**, 1255, 1995.



- 
- [24] F. Shimojo, T. Okabe, F. Tachibana, M. Kobayashi, and H. Okazaki, *J. Phys. Soc. Jpn.* **61**, 2848, 1992.
- [25] F. Shimojo and H. Okazaki, *J. Phys. Soc. Jpn.* **61**, 4106, 1992.
- [26] R. E. Cohen, M. J. Mehl, and L. L. Boyer, *Physica B* **150**, 1, 1988.
- [27] L. L. Boyer and B. M. Klein, *J. Am. Ceram. Soc.* **68**, 278, 1985.
- [28] M. W. Finnis and A. T. Paxton, M. Methfessel, M. van Schilfgaarde, *Phys. Rev. Lett.* **81**, 23, 1998.
- [29] J. A. Van Vechten, *Phys. Rev.* **187**, 1007, 1969.
- [30] J. C. Phillips, *Phys. Today* **23** (2), 23, 1970.
- [31] A. Garcia and M. L. Cohen, *Phys. Rev. B* **47**, 4215, 1993; **47**, 4221, 1993.
- [32] B. Králik, E. K. Chang, and S. G. Louie, *Phys. Rev. B* **43**, 7027, 1998.
- [33] G. Jomard, T. Petit, A. Pasturel, L. Magaud, G. Kresse, and J. Hafner, *Phys. Rev. B* **59**, 4044, 1999.
- [34] JCPDS Pattern 37-1484
- [35] JCPDS pattern NO. 42-1164 for t-ZrO<sub>2</sub> at 1250°C.
- [36] JCPDS pattern NO. 50-1089 for metastable t-ZrO<sub>2</sub> stabilized at room temperature as an oxygen deficient structure
- [37] Unit cell parameter derived assuming a cubic approximation.
- [38] C. R. A. Catlow, *J. Chem. Soc., Faraday Trans.* **86**, 1167, 1990.
- [39] C. J. Howard, R. J. Hill, and B. E. Reichert, *Acta Cryst. Sect. B: Struct. Sci.* **44**, 116, 1988
- [40] O. Ohtaka, T. Yamanaka, S. Kume, N. Hara, H. Asano, and F. Izumi, *Proc. Jpn. Acad., Ser. B: Phys. Biol. Sci.* **66**, 193, 1990.
- [41] A. B. Corradi, F. Bondioli and A. M. Ferrari, *Chem. Mater.* **13**, 4450, 2001.
- [42] M. Yashima, K. Morimoto, N. Ishizawa and M. J. Yoshimura. *J. Am. Ceram. Soc.* **76**, 1745, 1993
- [43] A. P. Bechepeche, O. Treu, E. Longo, C. O. Paiva-Santos and J.A. Varela. *J. Mat. Sci.* **34**, 2751, 1999
- [44] G. Balducci, J. Kaspar, P. Fornasiero, and M. Graziani, M. S. Islam and J. D. Gale, *J. Phys. Chem. B* **101**, 1750, 1997.
- [45] M. Zinkevich, *Prog. Mater. Sci.* **52**, 597, 2007.
- [46] M. Fowles and P. Ingram. Syntex/MEL results. 2002
- [47] J. Lefevre. *Ann. Chim.* **8**, 117, 1963



- 
- [48] D. K. Hohnke, *J. Phys. Chem. Solids* **41**, 777, 1980
- [49] A. F. Wells, *Structural Inorganic Chemistry* 4<sup>th</sup> Ed, Clarendon Press, Oxford. 1975
- [50] M. Yashima, H. Takanashi, K. Ohtake, T. Hirose. M. Kakihana, H. Arashi and M. J. Yoshimura. *J. Am. Ceram. Soc.* **57**, 289, 1996
- [51] I. Kobayashi, I. Takahashi, Mshiono and M. Dokiya, *Sol State Ionics* **152-153**, 591, 2002.
- [52] Z Cai, T. N. Lan, S. Wang and M. Dokiya, *Sol State Ionics* **152-153**, 583, 2002.
- [53] I. Kobayashi, H. U. Anderson, Y. Mizutani and K. Ukai, *Sol State Ionics*. **152-153**, 431, 2002.
- [54] T. Raming, L. Winnubst and H. Verweij, *J. Mater. Chem.* **12**, 3705, 2002.
- [55] V. V. Srdic and M. Winterer, *Chem, Mater.* **15**, 2668, 2003.
- [56] A. Mondal and S. Ram, *Sol. State Ionics* **160**, 169, 2003.
- [57] P-C Yang, X-H Cai and Y-C Xie, *Acta Phys Chim Sin.* **19**, 714, 2003.
- [58] X. J. Huang and W. Wieppner, *J. Chem. Soc, Faraday Trans.* **92**, 2173, 1996.
- [59] A. Predith,<sup>1</sup> G. Ceder,<sup>1</sup> C. Wolverton,<sup>2</sup> K. Persson,<sup>1</sup> and T. Mueller, *Phys. Rev. B* **77**, 144104, 2008.
- [60] A. Bogicevic, C. Wolverton, G. M. Crosbie, and E. B. Stechel, *Phys. Rev. B* **64**, 014106, 2001.
- [61] V. S. Stubican, J. R. Hellmann, and S. P. Ray, *Mater. Sci.* **10**, 257, 1982.
- [62] C. Schusterius and N. N. Padurow, *Ber, Dtsch, Keram. Ges.* **30**, 235, 1953.
- [63] C. Pascual and P. Durán, *J. Am. Ceram. Soc.* **66**, 22, 1983.
- [64] A. I. Ioffe, D.S. Rutman, S.V. Karpachov, *Electro. chim. Acta* **23**, 141, 1978.
- [65] S. P. S. Badwal, *Solid State Ionics* **52**, 23, 1992.
- [66] M. Khan, M. Islam, and D. Bates, *J. Mater. Chem.* **8**, 2299, 1998.
- [67] M. Kilo, R. Jackson, and G. Borshardt, *Philos. Mag.* **83**, 3309, 2003.
- [68] V. Zavodinsky, *Phys. Solid State* **46**, 453, 2004.
- [69] R. Krishnamurthy, Y. Yoon, D. Srolovitz, and R. Car, *J. Am. Ceram. Soc.* **87**, 1821, 2004.
- [70] M. Martin, *Z. Phys. Chem.* 219, 105, 2005.
- [71] J. Katamura and T. Sakuma, *Acta. Mater.* **46(5)**, 1569, 1998.
- [72] A. Bogicevic and C. Wolverton, *Phys. Rev. B* **67**, 024106, 2003
- [73] A. Bogicevic and C. Wolverton, *Europhys. Lett.* **56**, 393, 2001.
- [74] F. Frey, H. Boysen, and I. Kaiser-Bischoff, *Z. Kristallogr.* **220**, 1017, 2005.



- 
- [75] C. Catlow, A. Chadwick, G. N. Greaves, and L. Moroney, *J. Am. Ceram. Soc.* **69**, 272, 1986.
- [76] D. Steele and B. Fender, *J. Phys. C* **7**, 1, 1974.
- [77] D. Argyriou, M. Elcombe, and A. Larson, *J. Phys. Chem. Solids* **57**, 183, 1996.
- [78] K. McClellan, S-Q. Xiao, K. Lagerlof, and A. Heuer, *Philos. Mag. A* **70**, 185, 1994.
- [79] S. Suzuki, M. Tanaka, and M. Ishigame, *J. Phys. C* **20**, 2963, 1987.
- [80] T. Welberry, R. Withers, J. Thompson, and B. Butler, *J. Solid State Chem.* **100**, 71, 1992.
- [81] M. Zacate, L. Minervini, D. Bradfield, R. Grimes, and K. Sickafus, *Solid State Ionics* **128**, 243, 2000.
- [82] P. Li, I. Chen, and J. Penner-Hahn, *J. Am. Ceram. Soc.* **77**, 118, 1994.
- [83] A. Gallardo-Lopez, J. Martinez-Fernandez, and A. Dominguez-Rodriguez, *Philos. Mag. A* **81**, 1675, 2001.
- [84] A. Gallardo-Lopez, J. Martinez-Fernandez, and A. Dominguez- Rodriguez, *J. Eur. Ceram. Soc.* **22**, 2821, 2002.
- [85] C. Morterra, G. Cerrato, L. Ferroni and L. Montanara. *Mat. Chem. and Phys.* **37**, 243, 1994.
- [86] T. Thome, L.P. Van, J. Cousty, *J. Euro. Ceram. Soc.* **24**, 841, 2004.
- [87] J. Lahiri, A. D. Mayernick, S. L. Morrow, B. E. Koel, A. C. T. van Duin, M. J. Janik, . Batzill, *J. Phys. Chem. C* **114(13)**, 5990, 2010.
- [88] S. L. Morrow, T. Luttrell, A. Carter, M. Batzill, *Surf. Sci.* **603**, L78, 2009.
- [89] F. Haase and J. Sauer, *J. Am. Chem Soc.* **120**, 13503, 1998
- [90] G. Balducci, J. Kaspar, P. Fornasiero and M. Graziani M. S. Islam, *J. Phys. Chem. B* **102**, 557, 1998.
- [91] A. Bernasik, K. Kowalski, and A. Sadowski, *J. Phys. Chem. Solids* **63**, 233, 2002
- [92] S. Gernnard, F. Cora, and C. R. A.Catlow, *J. Phys. Chem. B* **103**, 10158, 1999.
- [93] P. Stelmachowski, F. Zasada, W. Pjskorz, A. Kotarba, J. Paul and Z. Sojka, *Catal. Today* **137**, 423, 2008.
- [94] M. M. Branda, C. Loshchen, K. M. Neynan, and F. Illas, *J. Phys. Chem. C* **112**, 17643, 2008
- [95] M. de Ridder, R. G. van Welzenis, H. H. Brongersma and U. Kreissig. *Sol. State. Ionics* **156**, 255, 2003.



- [96] M. de Ridder, H. H. Brongersma and U. Kreissig, *Sol. State. Ionics* **158**, 67, 2003.
- [97] J. Zhu, J. G. van Ommen, J. Henny, M. Bouwmeester, L. J. Lefferts, *Catal.* **233**, 434, 2005.
- [98] G. Ballabio, M. Bernasconi, F. Pietrucci, and S. Serra, *Phys. Rev. B.* **70**, 075417, 2004.
- [99] Andreas Eichler and Georg Kresse, *Phys. Rev. B.* **69**, 045402, 2004
- [100] C. R. Stanek, R. W. Grimes, M. J. D. Rushton, K. J. McClellan, R. D. Rawlings, *Philos. Mag. Lett.* **85**, 445, 2006.

### **\* Internet Resources**

- [1]\* [http://www.chem.ox.ac.uk/icl/heyess/structure\\_of\\_solids/Strucsol.html](http://www.chem.ox.ac.uk/icl/heyess/structure_of_solids/Strucsol.html)
- [2]\* <http://positron.physik.uni-halle.de/talks/CERAMIC1.pdf>



## Chapter 3 Partial Oxidation Catalysis

*It is certain that substances ... have the property of exerting an effect... quite different from ordinary chemical affinity, in that they promote the conversion ... without necessarily participating in the process with their own component parts....*

*-- Jöns Jakob Berzelius*

The study of catalysis dates back to the mystery of the philosopher's stone in medieval time. The term *catalyst* was defined by Jöns Jakob Berzelius in 1836 as a material which changes the rate of establishing chemical equilibrium without itself being changed or consumed.<sup>[1]</sup> Catalysis can be regarded as providing an alternative pathway for a chemical reaction which gives selectivity towards the formation of the preferred product.

Natural gas (predominantly methane), as a raw material for organic chemical products, is forecast to outlast oil by a significant margin.<sup>[2]</sup> Partial oxidation is a process in which the quantity of oxidizer is less than that stoichiometrically required for the complete combustion of a hydrocarbon fuel. The product of the partial oxidation of methane is called synthesis gas (syngas) and consists of a gas mixture composed primarily of hydrogen and carbon monoxide. Such mixtures represent the intermediary step from hydrocarbons to bulk chemicals (including methanol, dimethyl ether, ammonia, acetic acid, oxo-alcohols, isocyanates) and synthetic fuels (synthetic Diesel)<sup>[3]</sup>.

YSZ, due to its elevated ionic conductivity and good environmental resistance, is widely used as a catalyst for the partial oxidation of methane at high temperature.<sup>[4]</sup> In this chapter, catalytic partial oxidation of methane (CPOM) over yttria-stabilized zirconia, a typical heterogeneous catalytic reaction occurring at the gas-solid interface is reviewed. The interaction of oxygen with the surface of oxide catalysts as well as the oxygen state at the surface is discussed with reference to the previous literature and the challenges which can be met by computational modeling of YSZ are identified.



### 3.1 Catalytic Partial Oxidation of Methane

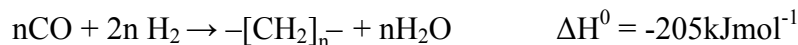
#### 3.1.1 Applications of Syngas

Syngas, a mixture of carbon monoxide and hydrogen, generated by a variety of partial oxidation processes from natural gas, is very important in two major industrial applications: methanol synthesis and the Fischer-Tropsch reaction which converts synthesis gas into a large range of linear hydrocarbons. <sup>[3]</sup> The main reactions are represented shown as below.

Methanol: <sup>[5-6]</sup>



Fischer-Tropsch: <sup>[3]</sup>



Syngas is also a major source of hydrogen for hydrogenation reactions and hydrogen fuel cells. The hydrogen content in syngas reaction can be enhanced by the water gas shift reaction: <sup>[7]</sup>



Therefore, the production of syngas represents a key method of harnessing natural gas (methane) or other hydrocarbons for large scale chemical synthesis.

#### 3.1.2 Mechanism

The three processes that attract greatest industrial interest are methane steam reforming, methane dry reforming with carbon dioxide, and methane partial oxidation with oxygen, together with the associated water gas shift reaction. There is also



considerable attention given to the use of attractive substitutes to methane, for example, steam reforming of ethanol derived from fermentation.<sup>[8-9]</sup>

The most established method of producing syngas by partial oxidation of methane is steam reforming. This process involves the following reaction:



An important factor in catalyst deactivation is carbon deposition via the Boudouard reaction (Eq. 3.3), which is also accelerated by the supported metal catalysts used for steam reforming, typically Ni on alumina.



To avoid the Boudouard reaction, steam is normally added well in excess of the stoichiometric requirement of reaction in Eq. 3.1, so that the reaction equilibrium moves towards more CO<sub>2</sub> production rather than CO, which is achieved by the associated water-gas shift reaction (Eq. 3.1). The overall reaction is highly endothermic and is normally carried out at temperatures above 800°C.<sup>[10]</sup> Such high temperature can lead to metal sintering and hence a reduction in catalyst lifetime.

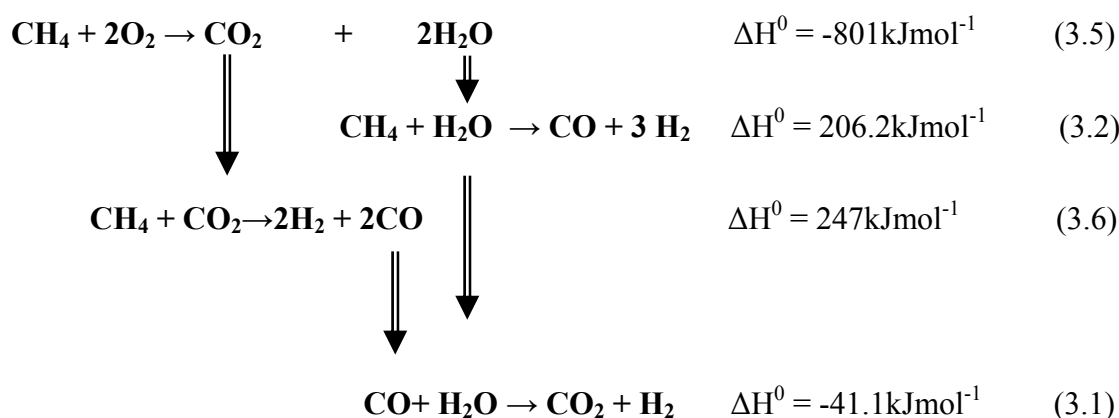
In order to increase the rate of oxidation of methane to syngas and mitigate the problems of coke deposit, selective catalytic partial oxidation of methane has been developed more recently. This reaction has attracted attention due to its moderate exothermicity, as expressed in Eq. 3.4 and favourable H<sub>2</sub>/CO ratio (2:1) for downstream methanol synthesis.<sup>[11]</sup>



However, selective CPOM has a fatal disadvantage that, unlike steam reforming, the hydrogen produced is derived only from methane, and hydrogen in inexpensive water can not be utilized. Also, pure oxygen resulting in additive expense is required. Moreover, the complete oxidation of methane to H<sub>2</sub>O and CO<sub>2</sub> competes with CPOM, especially at higher conversion levels, causing decrease in selectivity to H<sub>2</sub>, which is also a common problem in methane oxidative coupling to synthesis C<sub>2</sub> compounds.<sup>[12]</sup>



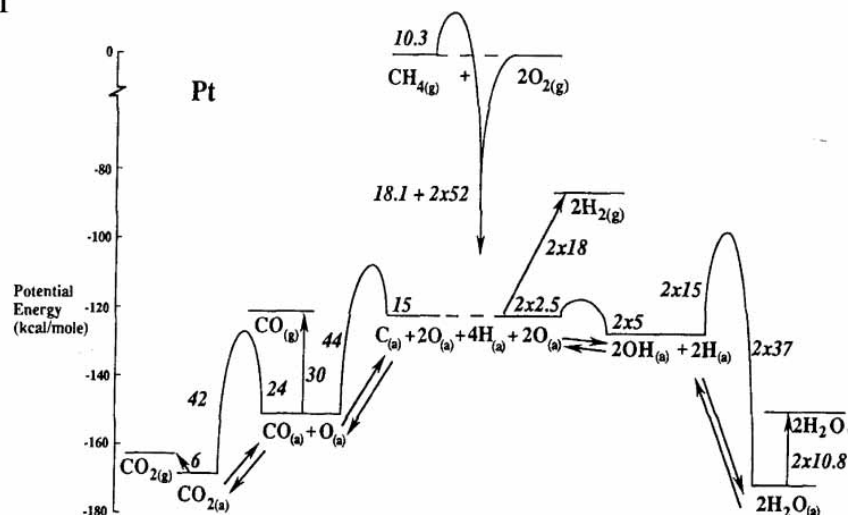
Since the work of Green and co-workers rekindled interest in the partial oxidation reaction, <sup>[13,14,15]</sup> extensive experimental work has been devoted to the elucidation of the mechanism. In general, there are two mechanisms proposed to account for the catalytic conversion of methane and oxygen to synthesis gas: a combustion reforming pathway, or a pyrolysis pathway (in which CO is formed by the pyrolysis of methane,  $\text{CH}_4 \rightarrow \text{CH}_x + (2-x/2) \text{H}_2$ , followed by the oxidation of carbon containing species). The combustion reforming pathway which was first proposed by Prettre *et al.* <sup>[16]</sup> is currently the more widely accepted mechanism. In this pathway, a highly exothermic step, the complete combustion of methane (Eq. 3.5), <sup>[4]</sup> is followed by two possible endothermic steps which are the steam reforming processes (Eq. 3.2) or  $\text{CO}_2$  reforming (Eq. 3.6) and the water gas shift reaction (Eq. 3.1) to give synthesis gas.



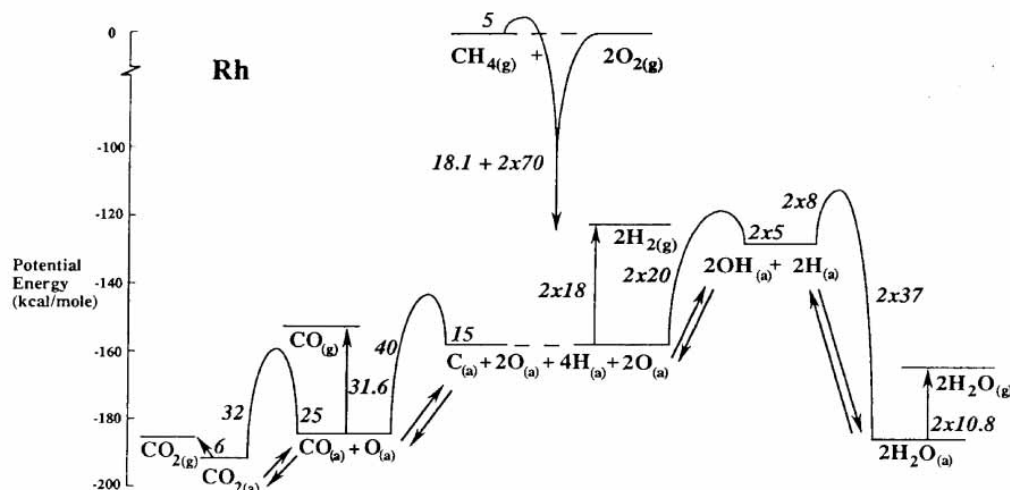
CO and  $\text{H}_2$  are the secondary products in this mechanistic scheme. Equation 3.6, involving  $\text{CO}_2$  reacting with methane, is the basis of a third partial oxidation catalytic process under investigation known as dry reforming. As an example, **Figure 3.1** displays the energetic pathway of reactants and intermediates during CPOM over Pt and Rh as catalysts.



## (a) Platinum



## (b) Rhodium



**Figure 3.1** Energy level diagrams for O, C, and H species on Pt and Rh at low coverage. (From Ref. [17])

Industrially, oxide supported metal catalysts are used to activate the partial oxidation reaction. The first row transition metals (Ni, Co) and noble metals (Fe, Ru, Rh, Pd, Pt, and Ir) have been reported as active catalysts for CPOM. <sup>[18]</sup> However, as mentioned above, most of these metals are also good catalysts for CH<sub>4</sub> decomposition to carbon. Exceptionally, Ru and Rh are very active catalysts for CPOM and show very high resistance to carbon deposition (in this case attributed to the very low solubility of carbon in these metals). <sup>[17]</sup> However, the high costs and limited availability of these noble metals have limited their application. Ideally, the choice for catalyst should take into account such issues as activity, selectivity, surface area, and carbon resistance as

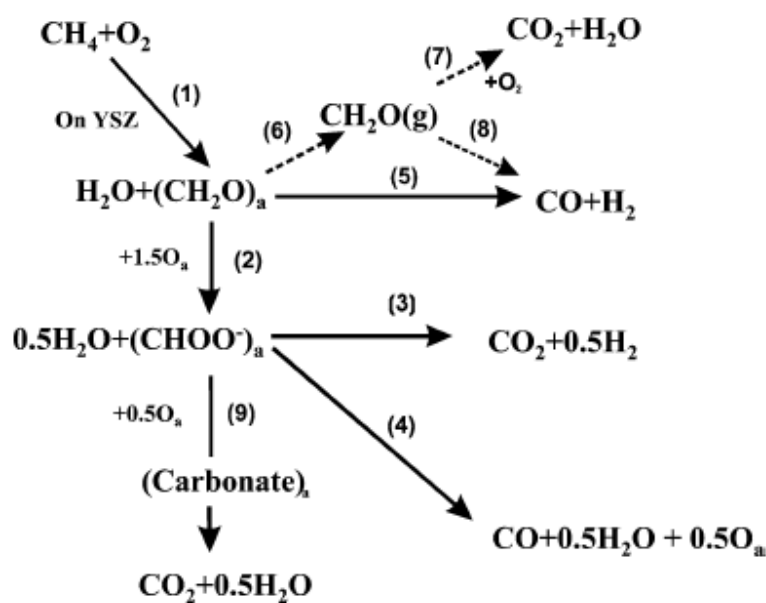


well as the need for thermal stability and control of metal sintering in the operating environment. Recent studies have focused on developing a highly active and stable catalyst for CPOM with a thermally smooth reaction pathway. In this respect, some irreducible metal oxides such as  $\text{Y}_2\text{O}_3$ ,  $\text{MgO}$ ,  $\text{TiO}_2$ ,  $\text{La}_2\text{O}_3$ , and  $\text{ZrO}_2$  have been studied as catalysts. [19][20] Among these materials, Yttria-stabilized zirconia (YSZ) demonstrated a superior stability and the best catalytic performance. [11]

### 3.2 Yttrium Stabilized Zirconia for CPOM

Extensive studies on the use of pure  $\text{ZrO}_2$  (monoclinic) and YSZ (tetragonal/cubic) for catalytic partial oxidation of methane to produce syngas have been carried out by Zhu *et al.* applying the dual bed approach. [21] The primary products of CPOM over YSZ in the first bed are  $\text{CO}$ ,  $\text{H}_2$ ,  $\text{CO}_2$ , and  $\text{H}_2\text{O}$ . Besides these four major products, traces of hydrocarbons, formaldehyde and formic acid were observed in the product mixture at high reaction temperatures. The reaction scheme for CPOM over YSZ is proposed as in Figure 3.2.

**Figure 3.2** The reaction pathways of CPOM on YSZ. (From Ref. [21])



The relative importance of the competing pathways is strongly influenced by temperature. Above  $600^\circ\text{C}$ , activation of methane (Reaction 1) is the rate-determining step at higher temperatures. Selectivity to synthesis gas depends strongly on the



relative rates of three dominating reactions, reactions 3, 4, and 5. CO and H<sub>2</sub> are formed via decomposition of both adsorbed formaldehyde and formate (Reactions 5 and 3), while CO<sub>2</sub> is produced via decomposition of formate mainly (Reaction 3). The relative rates as a function of temperature for the various product forming reactions in **Figure 3.2** are shown as below:

$$R_3 (40\%) \sim R_4 (37\%) > R_5 (20\%) \gg R_9 (2\%)$$

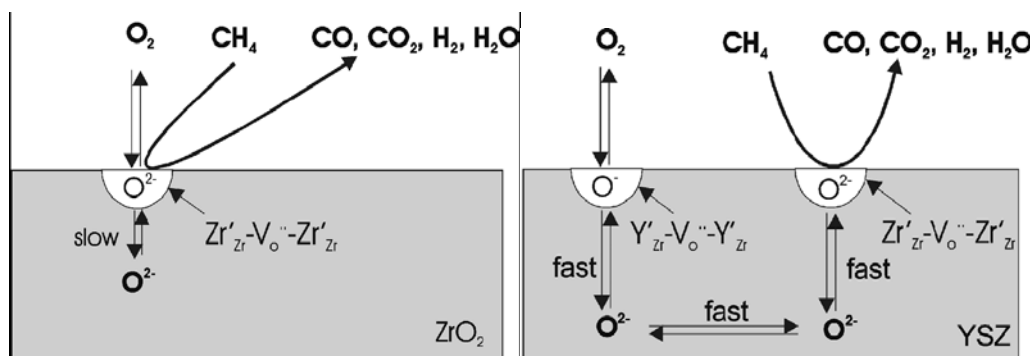
where  $R_n \% = (R_n / \sum R_n) \times 100\%$

Overall, since the oxidation of CH<sub>2</sub>O (Reaction 2) on the surface of oxide catalysts, the challenge is to accelerate CH<sub>2</sub>O decomposition (Reaction 5) or prevent oxidation to improve selectivity.<sup>[21]</sup>

In their catalyst testing experiments, Zhu *et al.*<sup>[22]</sup> have shown that the catalytic activity of YSZ is considerably greater than that of the undoped ZrO<sub>2</sub>, indicating the importance of Y doping. The authors have investigated the role of Y in a further series of experiments involving <sup>18</sup>O isotope exchange and pulsed CH<sub>4</sub> and O<sub>2</sub> studies. Results have shown faster <sup>18</sup>O exchange above 600°C for YSZ than in ZrO<sub>2</sub>. A likely explanation is that O anion vacancies, created as compensating defects due to the presence of Y<sup>3+</sup> in Zr<sup>4+</sup> sites, are important in the exchange process and therefore also in catalysis. The vacancies enhance anion mobility, which relates directly to the high ion conductivity of YSZ. Zhu *et al.* have also carried out temperature programmed oxidation on used catalysts to study the surface carbon formation – a major catalyst deactivation mode. The results indicate that the oxygen vacancies in YSZ are also important in reduction of carbon deposition, probably due to more effective active oxygen supply. However, experimental results have shown that for both m-ZrO<sub>2</sub> and YSZ, oxygen can be extracted from the catalyst surface in the absence of gas phase O<sub>2</sub>. Quantitatively, it has been estimated that 13.6% and 8.5% of oxygen ions in the surface monolayer are available from m-ZrO<sub>2</sub> and YSZ respectively.<sup>[22]</sup>



**Figure 3.3** The reaction models proposed for CPOM over  $\text{ZrO}_2$  and YSZ catalysts. (From Ref. [22])

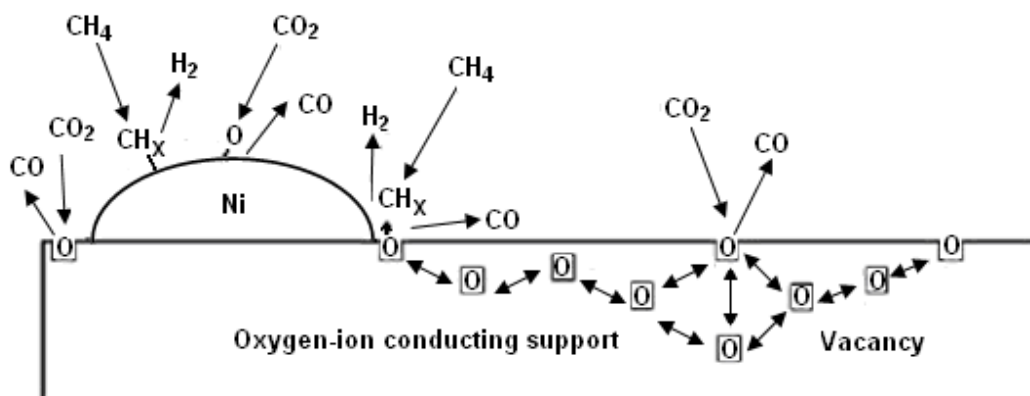


The apparent conflict between the availability of surface oxygen for oxidation, which is greater for  $\text{m-ZrO}_2$ , and the catalyst activity and  $^{18}\text{O}$  exchange behavior, which are higher for YSZ, have been rationalized in terms of the reaction model proposed in **Figure 3.3**. Pure  $\text{m-ZrO}_2$  has a complete surface lattice and thus more oxygen can be abstracted. In contrast, YSZ has oxygen vacancies which mean higher oxygen mobility but less oxygen at the surface. In both cases,  $\text{CH}_4$  is selectively oxidized at surface lattice oxygen vacancies. For  $\text{m-ZrO}_2$ , oxygen replenishment occurs by direct activation of  $\text{O}_2$  at these vacancies. The extrinsic vacancies in YSZ allow a second route, lattice diffusion, which facilitates rapid replenishment and higher activity.

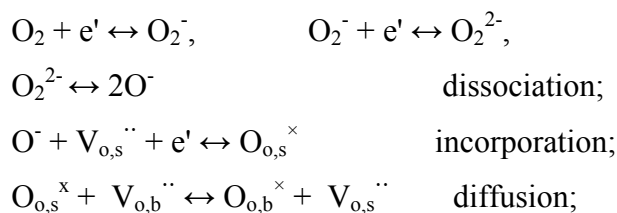
The importance of oxygen vacancies has also been discussed in relation to researches on steam reforming over Ni supported on a variety of perovskites, eg.  $\text{SrTiO}_3$ , by Urasak *et al.* [23] and dry reforming over Ni on  $\text{Sm}^{3+}$  and  $\text{Gd}^{3+}$  doped  $\text{CeO}_2$  by Huang *et al.* [24] The model in **Figure 3.4** for doped  $\text{CeO}_2$  indicates three sites for activation of  $\text{CO}_2$ : the surface of Ni, the Ni/oxide interface and oxygen vacancies in the oxide surface. Also shown in **Figure 3.4** is the transport of oxygen ions through the lattice following regeneration of lattice oxygen by decomposition of  $\text{CO}_2$  and the enhanced availability of lattice oxygen for oxidation of adsorbed  $\text{CH}_4$  fragments. The process for steam forming is considered to be similar.



**Figure 3.4** A schematic diagram of production, transport, and reaction of the mobile oxygen species for CO<sub>2</sub> reforming of CH<sub>4</sub> over doped-ceria supported Ni catalyst. (Reproduced from Ref. [24])



The process of oxygen capture, surface incorporation and lattice transport in **Figure 3.4** can be formalized in a set of equations: <sup>[25][ 26]</sup>



The Kröger-Vink notation is used for lattice defects:  $\text{V}_{\text{o}}^{\cdot\cdot}$  denotes an oxygen vacancy,  $\text{O}_{\text{o}}^{\times}$  a regular lattice oxygen ion, and  $\text{e}'$  an electron. The subscripts s and b refer to surface and bulk, respectively. In principle, each of the indicated reaction steps may be rate-determining.

The above equations are similar to those proposed by Petrolekas *et al.* in their ion redox model for high temperature oxidation, e.g. combustion, over perovskites such as LaCoO<sub>3</sub>.<sup>[27]</sup> It should be noted that the defect chemistry of LaCoO<sub>3</sub> in relation to high temperature oxidation processes is now well understood both theoretically and experimentally.<sup>[28]</sup> Also, it is important to remember, unlike Zr or Y, Co in LaCoO<sub>3</sub> shows facile redox behavior in relation to the electronic processes depicted in **Figure 3.4** and indicated in the above equations.

Experimental work has raised a number of issues concerning the factors which control the overall activity and selectivity of the reaction scheme depicted in **Figure 3.2**, specifically those which determine the alternative reaction pathways to partial



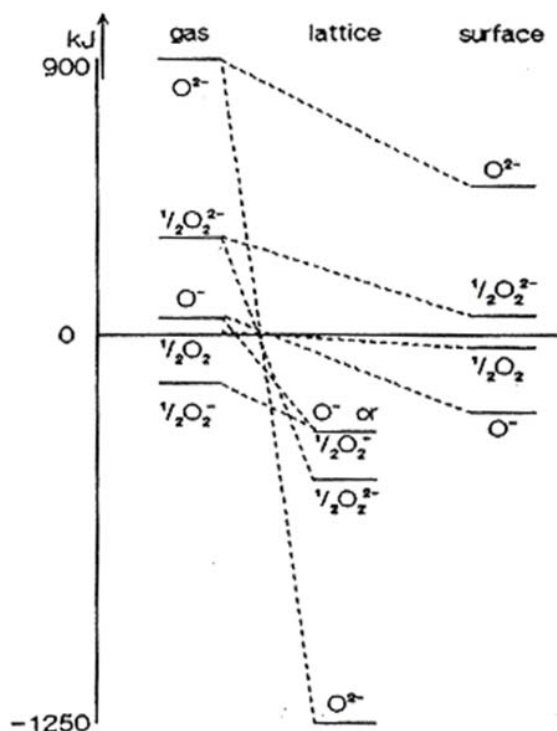
oxidation (syngas) or total oxidation (combustion). Other possible pathways over catalytic oxides can lead to methanol (selective oxidation) or formation of carbon-carbon bonds (oxidative coupling).<sup>[11]</sup> Potentially important factors in this context are the modes of activation of methane and oxygen, the nature of the resulting surface species and the roles of oxygen vacancies and specific cations. In this thesis, our focus is on gaining a better understanding of the oxygen activation process and the identity of active oxygen species.

### 3.3 Surface Interaction and Oxygen States on Metal Oxide Catalysts

As discussed in the above section, several different types of oxygen adsorbed species, including  $O_2$  (adsorbed molecule),  $O$  (adsorbed neutral atom),  $O_2^-$  (superoxide),  $O_2^{2-}$  (peroxide) and  $O^-$  (adsorbed atomic ion) can occur as intermediates for the reduction of molecular oxygen on the catalyst surface. The energies for different oxygen states in the gas, lattice and surface phases have been estimated by Beilanski and Haber<sup>[29]</sup> as shown in **Figure 3.5**. The stability of these different oxygen ions is evaluated by the published dissociation energy of oxygen and the electron affinity of various oxygen ions in the gas phase combined with assumptions about the stabilization energies in the lattice and at the surface.

According to their well known work, the superoxide ion ( $O_2^-$ ) is the only stable ion in the gas phase. Thus it has been commonly seen as an adsorbed oxygen species at the surface.  $O^-$  has also been observed as a surface species since it only takes 10 kJ to create two  $O^-$  ions from one molecule of  $O_2$  (and two electrons). These two ions,  $O_2^-$  and  $O^-$ , have been implicated in low temperature suprafacial and high temperature intrafacial oxidation catalysis respectively over perovskites.<sup>[30]</sup> The  $O^{2-}$  is highly unstable in the gas phase having an electron affinity estimate to be  $\sim 9\text{eV}$ . The oxide ion  $O^{2-}$  can only be stabilised in the crystal lattice by the electric field created by the neighbouring cations. Indeed, this stabilising Madelung energy is sufficient to make the oxide ion the most stable form of oxygen in the lattice.<sup>[29]</sup>

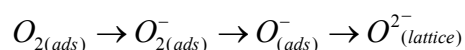




**Figure 3.5** Different oxygen species occurring in catalysis over oxides. (From Ref. [29])

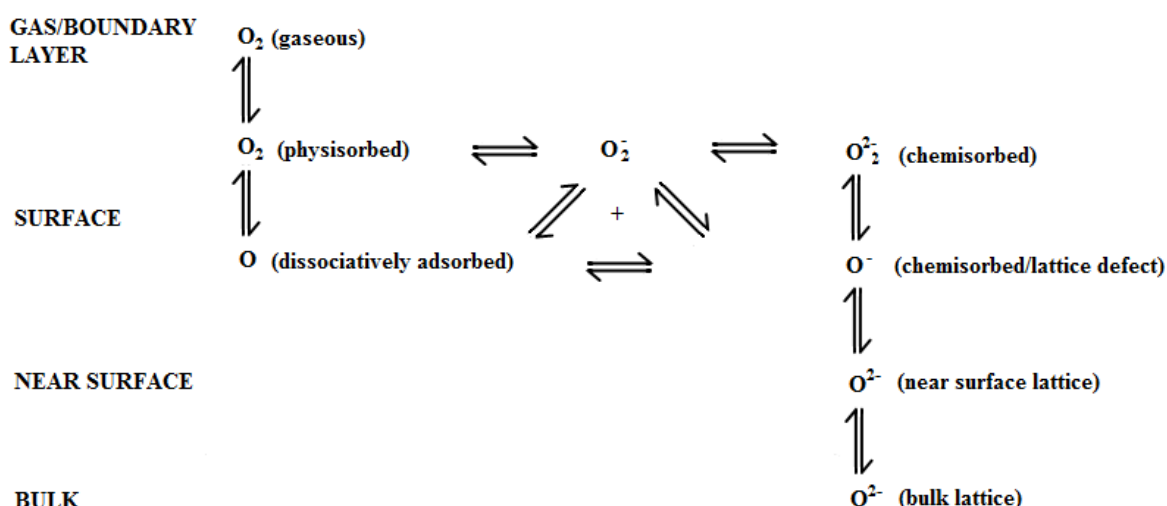
Charged oxygen species on the surface also require stabilization energy. It is assumed that the stabilization energy at the surface relative to that in the lattice is roughly proportional to the number of cations coordinated to each oxide ion. As the coordination number of oxide ions in the surface is less than in the lattice, the stabilization energy of  $O^{2-}$  at the surface would be lower as well, so it is not a stable surface species.

More recently, the transformation of the oxygen species at the surface has been considered as a stepwise process: [32]



where the oxygen gradually becomes richer in electrons. **Figure 3.6** presents a schematic diagram for the different oxygen states as a function of depth from the surface. [31][32]





**Figure 3.6** Schematic diagram for the different oxygen states.

The direct experimental evidence identifying different states of oxygen on the surface of YSZ is limited due to the difficulty in carrying out *in-situ* experiments. However, some clues to the adsorbed oxygen states can be obtained from surface science studies of other materials. For example, X-ray photoelectron spectroscopy (XPS) has detected two  $O\ 1s$  peaks on the  $LaCoO_3$  perovskite surface, a sharper, lower binding energy ( $BE$ ) peak interpreted as near surface lattice oxygen  $O^{2-}$  and a broader, higher  $BE$  peak interpreted as a mixture of less electron rich adsorbed oxygen species such as  $O^-$ ,  $O_2^-$  and  $OH^-$ .<sup>[33]</sup> Also for  $LaCoO_3$ , temperature programmed desorption (TPD) has detected as many as three oxygen adsorption peaks. The lowest temperature peak,  $\alpha_1$ , is assumed to be loosely bound, adsorbed oxygen while the higher temperature,  $\alpha_2$ , peak may be due to loss of surface lattice oxygen or  $O_2^-$  adsorbed in oxygen vacancies. Finally, the highest temperature peak,  $\beta$ , is clearly due to loss of lattice oxygen since it is accompanied by reduction of  $Co^{3+}$  to  $Co^{2+}$ .<sup>[34][35]</sup>

Electron paramagnetic resonance (EPR) has been applied to identify oxygen states on some simple ionic oxides. For example, in an early review, Che *et al.*<sup>[36]</sup> have concluded that there is firm evidences for  $O^-$  and the superoxide ion  $O_2^-$  on several oxides and weak evidence for the peroxide ion  $O_2^{2-}$ . In addition, Zhang *et al.*<sup>[37]</sup> and Soria *et al.*<sup>[38]</sup> have detected  $O_2^-$  on  $CeO_2$ . Iwamoto *et al.* detected  $O^-$ ,  $O_2^-$  and  $O_3^-$  on  $MgO$  and have proposed an order of activity  $O^- > O_3^- > O_2^-$ .<sup>[39]</sup> Finally, in a recent



review on oxidation reactions over solid solution oxides, Cimino *et al.* discuss reaction mechanisms in terms of high and low coordinate  $O^{2-}$  ions.<sup>[40]</sup>

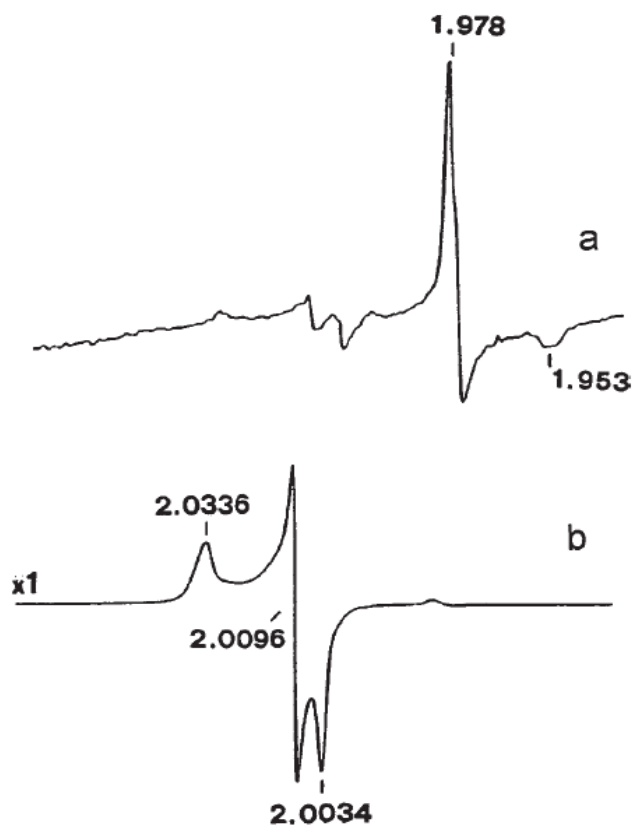
Ayame *et al.*<sup>[41]</sup> have studied the oxygen adsorption on a silver catalyst supported on  $\alpha\text{-Al}_2\text{O}_3$  during the course of the partial oxidation of ethylene. The coverage by molecular oxygen has been estimated to be thousands of times bigger than that of oxygen adatoms. These results indicated that the first dissociative adsorption on a vacant active centre was much slower than the second dissociative oxygen adsorption on a pre-adsorbed adatom. They also suggested that the adatom seemed likely to act as an active centre for the second oxygen adsorption. Selectivity to ethylene oxide increased almost linearly with the increase in the coverage of oxygen admolecules.

Among the various oxygen species reported in the literature, the superoxide radical  $O_2^-$  has been more widely investigated because, being paramagnetic, the EPR technique provides a great deal of information on its structure, location, stability, surface mobility and on-site dynamics.<sup>[42]</sup> Since the EPR features depend on the local positive field felt by the negative anion and the  $O_2^-$  ion is usually stabilized on positive ions at the solid surface, the adsorbed superoxide  $O_2^-$  also constitutes a particularly useful probe of the electric field at the surface of ionic solids, particularly of oxides. The features of the superoxide species formed during a catalytic process yield information on the nature of the active sites. In particular, Anpo *et al.*<sup>[43]</sup> illustrates the main circumstances under which stable superoxide anions are formed at surfaces: (i) direct surface-dioxygen electron transfer; (ii) photo-induced electron transfer; (iii) surface intermolecular electron transfer; (iv) decomposition of hydrogen peroxide.

Specifically, for  $\text{ZrO}_2$  systems, EPR studies have been carried out on samples of vacuum-activated monoclinic  $\text{ZrO}_2$  containing coordinatively unsaturated (cus) Zr ions (claimed to be  $\text{Zr}^{3+}$  by the authors) at the surface as defective centres.<sup>[43-44]</sup> The results of experiments indicated that electron transfer to dioxygen molecule did not occur at room temperature. Anpo *et al.* compared the EPR spectra of activated  $\text{ZrO}_2$  before and after  $\text{O}_2$  adsorption in their work. As presented in **Figure 3.7**, the intensity of the superoxide species (**Figure 3.7-b**) overwhelms that of the  $\text{Zr}^{3+}$  signal in the starting sample (**Figure 3.7-a**). However, the  $\text{Zr}^{3+}$  signal does not completely



disappear after superoxide formation (**Figure 3.7-b**). This indicates that the majority of the oxygen molecules are not reduced by  $\text{Zr}^{3+}$  ions and that the reducing centres, if localized, are not paramagnetic. They also suggested the electrons transferred to the surface adsorbed dioxygen are, in the partially reduced solid, delocalized over the conduction band due to its semiconducting properties. <sup>[43]</sup>



**Figure 3.7** EPR spectra of: (a) activated  $\text{ZrO}_2$  containing surface  $\text{Zr}^{3+}$  ions; (b) the same sample after contact with  $\text{O}_2$  and surface adsorbed superoxide formation. (From Ref. [43])

Several recent experiments aimed to identify the activation sites for the oxidants  $\text{O}_2$ ,  $\text{NO}$  and  $\text{N}_2\text{O}$  during CPOM. Il'ichev *et al* have studied  $\text{O}_2^-$  radical anion formation during  $\text{NO} + \text{O}_2$  and  $\text{O}_2$  absorption on  $\text{ZrO}_2$  by EPR. <sup>[45]</sup> The influence of both preliminary thermal treatment of  $\text{ZrO}_2$  in different atmospheres and surface compositions created by  $\text{O}_2$ ,  $\text{CO}$ ,  $\text{H}_2$ ,  $\text{NH}_3$ , and  $\text{CH}_3\text{OH}$  gases over  $\text{MoO}_3$  supported on  $\text{ZrO}_2$  have been investigated. During adsorption of an  $\text{NO} + \text{O}_2$  mixture on  $\text{ZrO}_2$ , the formation of  $\text{O}_2^-$  occurs on the  $\text{Zr}^{4+}$  and  $\text{O}^{2-}$  Lewis sites. The radical  $\text{O}_2^-$  anions were localized in the coordination spheres of the coordinately unsaturated  $\text{Zr}$  ions. As in the



case of  $O_2$  absorption on reduced (0.1–2.0) %  $MoO_3/ZrO_2$  samples,  $O_2^-$  radical anions were formed during the interaction of  $O_2$  with the  $Mo^{5+}$  ions in an octahedral configuration. A change in the  $MoO_3$  content of the samples from 0.1 to 0.5% led to an increase in the amount of  $O_2^-$ , whereas a change from 0.5 to 2.0% led to a decrease in  $O_2^-$  due to the screening of the  $Zr^{4+}$  ions by oxo complexes and polymolybdates.

Miller and Grassian <sup>[46-47]</sup> have studied  $N_2O$  adsorption and decomposition on  $ZrO_2$  by FT-IR spectroscopy. Results from their experiments indicate that  $N_2O$  adsorbs on Lewis acid sites  $Zr^{4+}$  and  $Zr^{3+}$ . In particular,  $Zr^{4+}$  cations are the site responsible for molecular adsorption of  $N_2O$ , whereas  $Zr^{3+}$  sites are active towards dissociative adsorption of  $N_2O$  at room temperature. Moreover, Zhu *et al.* <sup>[48-49]</sup> investigated the activation of both  $O_2$  and  $N_2O$  on YSZ by TPD. They concluded that different sites are responsible for  $N_2O$  and  $O_2$  dissociation: molecular  $O_2$  is dissociatively activated at Y-induced oxygen vacancies sites to form a  $\beta$ -O type of oxygen species, i.e. the type of surface lattice oxygen species which can be extracted by reaction with methane during CPOM. In contrast, both the intrinsic oxygen vacancies and the unsaturated Zr sites at corners, edges, steps and kinks can activate the  $N_2O$  molecule. Accordingly, two types of oxygen species ( $\alpha$ -O and  $\beta$ -O) have been identified respectively. However, CPOM with  $O_2$  over YSZ gives much higher reaction rates than with  $N_2O$ .

Computational modelling has also been applied to study some simple oxides. Kantorovich *et al.* using Density Functional Theory (DFT) slab configuration calculations have predicted favourable formation of the peroxide ion  $O_2^{2-}$  by adsorption of atomic oxygen at a lattice oxygen site in MgO. <sup>[50]</sup> Islam *et al.* have carried out interatomic potential based calculations to examine the formation of  $O^-$  and  $O_2^{2-}$  species on  $La_2O_3$  and have considered the interaction of molecular oxygen with oxygen vacancies to form hole species ( $2O^-$  or  $O_2^{2-}$ ). <sup>[51]</sup>

In the case of more covalent oxides, e.g. vanadium oxides, DFT cluster calculations have indicated that molecular oxygen is strongly adsorbed at oxygen vacancies. <sup>[52]</sup> The adsorbed molecular oxygen is extensively polarised leading to dissociation and activation. From experimental work on this type of oxide, Haber *et al.* have postulated that catalytic oxidation of an organic molecule can proceed via an electrophilic



mechanism in the case of  $O_2$ ,  $O_2^-$  or  $O^-$  active species leading to total oxidation, i.e. combustion, or via nucleophilic attack for  $O^{2-}$  (lattice oxygen) giving high partial oxidative selectivity, e.g.  $\alpha$ -alcohol synthesis .<sup>[53]</sup>

In addition, the ab initio calculations of silicon oxidation by Szymanski *et al.*<sup>[54]</sup> are of note. Their DFT calculations were carried out based on the assumption that the electrons responsible for the charged oxygen states come from the silicon conduction band. Also the charged unit cells were treated by employing a neutralising background and Makov-Payne monopole-monopole energy correction.<sup>[55]</sup> In this brief paper, the role of charged and neutral oxidising species in silicon oxidation has been discussed with the conclusion that: (i) molecular oxygen species are energetically preferable over atomic ones; (ii) charged oxygen species are energetically more favourable than neutral ones; (iii) the diffusion of atomic species ( $O$ ,  $O^-$ ,  $O^{2-}$ ) will result in oxygen exchange, whereas the diffusion of molecular species ( $O_2$ ,  $O_2^-$ ,  $O^{2-}$ ) is not likely to lead to a significant exchange with the lattice. Overall, the charged species have been predicted to play the key role in silicon oxidation.

Finally, interesting conclusions has been drawn from studies of oxygen adsorption on a series of metals. From a combination of UV and X-ray photoelectron spectroscopy (PES) and scanning tunnelling microscopy (STM) data for co-adsorption studies of ammonia oxidation, Carley *et al.*<sup>[56]</sup> have proposed that when oxygen adsorption is highly exothermic, as in the case for Mg, Al, Ni, and Cu metals, a transient  $O^\delta$  state is formed. For weak oxygen adsorption, such as on Ag and Zn,  $O_2^\delta$  has been identified. The authors have concluded that the adsorption oxygen with greater the electron enrichment gives a higher probability of dissociation.

Overall, since the oxygen states on metal oxide catalysts such as  $Y_2O_3/ZrO_2$  are difficult to examine by experimental approaches, particularly *in-situ*, and conclusions remain ambiguous from other materials, there is a strong interest in applying computational modelling to identify the most likely stable oxygen species.



### 3.4 Opportunities for Computational Modelling

Although YSZ may be one of the most extensively studied materials, there are still several areas of incomplete understanding not easily investigated by experiment so presenting a considerable opportunity for computational modelling, in particular:

- Modelling can provide a more precise picture of the bulk structures and the factors affecting stability across the temperature range, which are complex owing to the polymorphic nature of  $\text{ZrO}_2$  and the complicated phase transition processes.
- Since catalysis is a surface process, modelling can better understand the topography and chemistry of the surface with particular reference to segregation of yttrium and creation of oxygen vacancies.
- In relation to partial oxidation of methane, modelling can identify the nature of the active sites for the adsorption of gaseous reactants and in particular, study the activation of oxygen and its electronic and molecular state at the surface of yttrium stabilized  $\text{ZrO}_2$ .

The studies presented in this thesis are dedicated to provide further understanding of these issues.



## References

- 
- [1] M. W. Roberts, *Catalysis Letters* **67** (1), 1, 2000.
- [2] S. Cornot-Gandolphe, *Energy Exploration & Exploitation*, **13**, 3, 1995.
- [3] T. S. Christensen and I. I. Primdahl, *Hydrocarbon Processing* **3**, 9, 1994.
- [4] J. Zhu, M. S. Rahuman, J. G. van Ommen, L. Lefferts, *Appl. Catal. A* **259**, 95, 2004; J. Zhu, J. G. van Ommen, L. Lefferts, *J. Catal.*, **225**, 388, 2004; J. Zhu, J. G. van Ommen, A. Knoester, L. Lefferts, *J. Catal.* **230**, 291, 2005,
- [5] J. C. Bart and R. P. A. Sneed, *Catal. Today* **2**, 1, 1987; D. L. Trimm and M.S. Wainwright, *Catal. Today* **6**, 261, 1990
- [6] G. Chichen, P. J. Denny, J. R. Jennings, M. S. Spencer, and K.C. Waugh, *Appl. Catal.*, **36**, 1, 1988.
- [7] C. Ratnasamy and J. P. Wagner, *Catal. Rev.* **51**, 325, 2009.
- [8] S. Cavallaro, S. Freni, *Int. J. Hydrogen Energy* **21** (6) 465, 1996.
- [9] A. N. Fatsikostas, X. E. Verykios, *J. Catal.* **225** (4), 439, 2004.
- [10] S. H. Clare, Andrew L. Dicks, Kevin Pointon, Thomas A. Smith, Angie Swann, *Catal. Today*, **38**, 411, 1997
- [11] J. Zhu, J. G. van Ommen, A. Knoester, L. Lefferts. *J. Catal.* **291**, 230, 2005
- [12] J. J. Spivey, *Catalysis*, **16**, 143, 1993
- [13] A. T. Ashcroft, A. K. Cheetham, J. S. Foord, M. L. H. Green C. P. Grey, A. J. Murrell, P. D. F. Vernon, *Nature*, **344**, 319, 1990.
- [14] P. D. F. Vernon, M. L. H. Green, A. K. Cheetham, and A. T. Ashcroft, *Catal. Lett.* **6**, 181, 1990.
- [15] A. T. Ashcroft, A. K. Cheetham, M. L. H. Green, P. D. F. Vernon, *Nature*, **352**, 225, 1991.
- [16] M. Prettre, C. H. Eichner and M. Perrin, *Trans. Faraday Soc.* **43**, 335, 1946.
- [17] D. A. Hickmann, and L.D.Schmidt, *AIChE J.*, **39**, 1164, 1993; D. A. Hickmann, E. A. Hauptfear, and L. D. Schmidt, *Catal. Lett.* **17**, 223, 1993.
- [18] A. P. E. York, T. Xiao, M. L.H. Green, *Topic. Catal.* **22**, 345, 2003
- [19] A. Santos, M. Menendez, A. Monzon, J. Santamaria, E.E. Miro, E.A. Lombardo, *J. Catal.*, **158**, 83, 1996.
- [20] A. G. Steghuis, J. G. van Ommenm, J. A. Lercher, *Catal. Today* **46**, 91, 1998.
- [21] J. Zhu, J. G. van Ommen, and L. Lefferts, *J. Catal.* **225**, 388, 2004.



- 
- [22] J. Zhu, J. G. van Ommen, Henny J.M. Bouwmeester, L. Lefferts, *J. Catal.* **233**, 434, 2005.
- [23] K. Urasaki, *Appl. Cat. A Gen* **286**, 23, 2005
- [24] T-J Huang, H-J Lin, and T-Ch Yu, *Catal. Lett.* **105**, 239, 2005
- [25] R. Merkle, J. Marier, *Phys. Chem. Chem. Phys.* **4**, 4140, 2002.
- [26] B.A. Boukamp, B.A. van Hassel, I.C. Vinke, K.L. de Vries, A.J. Burgraaf, *Electrochem. Acta* **38**, 1817, 1993.
- [27] P. D. Petrolekas; I.S.Metcalf, *J. Catal.* **152**, 147, 1995.
- [28] S. Khan, R. J. Oldman, F. Cora, C. R. A. Catlow, S. A. French, S.A. Axon. *Phys. Chem. Chem. Phys.* **8**, 5207, 2006.
- [29] A. Beilanski, J. Haber, *Catal. Reviews-Science and Engineering*, **19(1)**, 1, 1979.
- [30] R. J. H. Voorhoeve, J. P. Remieka, L.G. Trimble, *N. Y. Ann. Acad. Sci.*, **3**, 272, 1976
- [31] R. J. Oldman. *Synetix Report No 10*, 2002.
- [32] Y. Wu, B. Dou, C. Wang; X. Xie. Z. Yu, S. Fa, Z. Fan, L. Wang, *J. Catal.* **88**, 120, 1989
- [33] M. O. Connel; A. K. Norman; C. F. Hutterman; M. A. Morris, *Catal. Today* **47**, 123, 1999.
- [34] J. M. D. Tascon, J. L. G. Fierro, L. G. Tejuca, "*Properties and Applications of Perovskite Oxides*", Chapter 8, *Infrared Spectroscopy and Temperature Programme Desorption*; Marcel Dekker, 1992.
- [35] S. Royer, D. Duprez, S. Kaliaguine, *J. Catal.* **234**, 364, 2005
- [36] M. Che and A.J. Tench, *Adv. Catal.* **31** (1982) 77; M. Che and A. J. Tench, *Adv. Catal.* **32**, 1, 1983.
- [37] X. Zhang; K.J.Klabunde. *Inorg. Chem.* **31**, 1706, 1992.
- [38] J. Soria, A. Martínez-Arias, and J.C. Conesa, *J. Chem. Soc. Faraday Trans.* **91**, 1669 (1995).
- [39] M. Iwamoto, J. H. Lunsford, *J. Phys. Chem.* **84**, 3079, 1980.
- [40] A. Cimino, F. S. Stone, *Adv. Catal.* **47**, 141, 2002.
- [41] A. Ayame, Y. Uchida, H. Ono, M. Miyamoto, T. Sato, and H. Hayasaka, *Appl. Catal. A* **244**, 59, 2003.
- [42] M. Che and E. Giamello, *Stud. Surf. Sci. Catal.* **57 B** (1990) 265.



- 
- [43] M. Anpo, M. Che, B. Fubini, E. Garrone, E. Giamello and M. C. Paganini. *Topic. Catal.* **8**, 189, 1999.
- [44] C. Morterra, E. Giamello, L. Orio and M. Volante, *J. Phys. Chem.* **94**, 3111, 1990.
- [45] A. N. Il'ichev; M. D. Shibonova; V. N. Korchak. *Kinetic and Catalysis*, **45(1)**, 114, 2004.
- [46] T. M. Miller and V. H. Grassian, *J. Am. Chem. Soc.* **117**, 10969, 1995.
- [47] T. M. Miller and V. H. Grassian, *Catalysis Letters* **46**.213, 1997.
- [48] J. Zhu, S. Albertsma, J. G. van Ommen, L. Lefferts , *J. Phys. Chem.* **109**, 9950, 2005.
- [49] J. Zhu, J. G. van Ommen, L. Lefferts , *Catal. Today*. **112**, 82, 2006
- [50] L. N. Kantorovich, A. L. Shluger, J. Gunster, P. Stracke, D. W. Goodman, V. Kempter, *Faraday Disc.* **114**, 173, 1999.
- [51] M. S. Islam, D. J. Ilett, S. C. Parker, *J. Phys. Chem.* **98**, 9637, 1994.
- [52] I. Czekaj, K. Hermann, M. Witko, *Surf. Sci.* **545(1-2)**, 85, 2003.
- [53] J. Haber, M. Witko, *Catal. Lett.* **9(3-4)**, 297, 1991.
- [54] M. A. Szymanski, A.M. Stoneham, A. Shluger, *Microelectronic Reliability*, **40**, 567, 2000.
- [55] V. Makov, M. C. Payne, *Phys. Rev. B*, **51**, 4014, 1995.
- [56] A. F. Carley, P. R. Davies, M.W.Roberts. *Catal. Lett.* **80(1-2)**, 25, 2002.



## Chapter 4 Computational Methodology

*The fundamental laws necessary for the mathematical treatment of large parts of physics and the whole of chemistry are thus fully known, and the difficulty lies only in the fact that application of these laws leads to equations that are too complex to be solved.*

*--Paul Adrien Maurice Dirac*

Over the past decades, computer modelling, which is increasingly integrated with experimental synthetic and characterization studies, has developed into a valuable tool for prediction and understanding of chemistry and physics. The techniques for modelling at the atomic and molecular level can be divided into two categories: force-field methods based on parameterized interatomic potentials and electronic structure methods which attempt to solve the Schrödinger equation at some level of approximation. There is also growing use of hybrid methods which describe part of the system quantum mechanically and the remainder using interatomic potential methods. <sup>[1]</sup> All methods involve evaluation of an expression for the energy of a given geometric arrangement of atoms. An equilibrium structure is obtained by variation of the atomic position to minimize the energy expression i.e. energy minimization to achieve the global minimum on the Potential Energy Surface. Calculation of forces may allow dynamical effect to be modeled.

This chapter provides a general introduction to the methods of computer modelling which are employed to generate the results in the rest of the thesis. The interatomic potential simulation codes GULP (General Utility Lattice Program) <sup>[2]</sup> and MARVIN (Minimisation and Relaxations of Vacancies and Interstitials of Neutral Surface) <sup>[3]</sup> were chosen to investigate the bulk defect and surface properties of pure and yttria doped zirconia. In addition, the plane-wave code VASP (Vienna Ab Initio Simulation Program) <sup>[4]</sup> has been used to check their electron structures quantum mechanically and identify oxygen states during the process of O<sub>2</sub> adsorption. The background as basis of these codes is presented.



## 4.1 Interatomic Potential Methods

For strongly ionic solids, these simulation methods are based on the use of Born Model employing interatomic potentials (IP) to describe the interaction between atoms. Ionic polarization may be included most commonly by the shell model which is discussed later. Such simulations are relatively less time consuming than calculations using *ab initio* methods and allow modeling of large scale systems containing  $10^4 \sim 10^6$  atoms. As a result, they have been widely applied to identify the geometrical structures and properties for periodic solid systems especially ionic materials.

### 4.1.1 Born Model for Ionic Systems

In most formulations of the Born Model, the potential energy function  $U(r_1 \dots r_N)$ , which express the energy of an assembly of  $N$  atoms or ions as a function of the nuclear coordinates  $r_1 \dots r_N$ , can be approximated by including only the two body components.<sup>[5]</sup> These two-body terms can be further decomposed into the long range electrostatic or Coulombic interactions, where the energy is calculated using the Ewald summation, and the short range dispersive force, i.e. non-Coulombic terms including overlap repulsion and van der Waals attraction between electron charge clouds.<sup>[6]</sup>

#### 4.1.1.1 Long Range Potentials

The electrostatic Coulombic contribution ( $U_{el}$ ) is a function of the charges on the non-bonded atoms and their interatomic distance, written as:

$$U_{el} = \frac{1}{2} \sum_A \sum_B \frac{q_A q_B}{r} \quad (4.1)$$

where  $r$  is the separation between the atoms  $A$  and  $B$ , and  $q_A$ ,  $q_B$  are the charge valences on the corresponding atoms. If part of the system, e.g. a solvent, is not modelled by an explicit atomistic approach, then a dielectric constant  $\epsilon$  may be included in the denominator.<sup>[6]</sup> According to the above equation, the potential energy



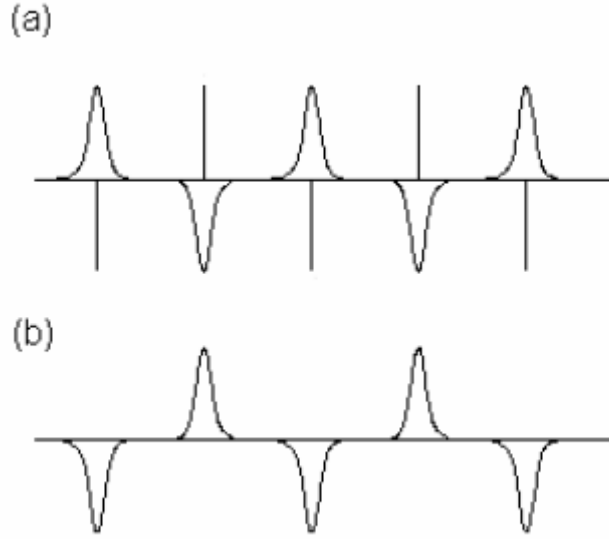
between ions falls off as to  $1/r$ ; however, the number of interacting ions increases with the surface area of sphere given by  $4\pi r^2$ . The interaction energy increases with the growth of the number interacting ions faster than the energy decays with increasing distance. Hence the electrostatic sum give in Eq. 4.1 converges only conditionally, which means that it is not possible to evaluate the electrostatic energy of the lattice by simply increasing the radius of the interacting spheres. Therefore an alternative procedure, first proposed by Paul Peter Ewald (1921), has been widely implemented to achieve a high degree of convergence. <sup>[2][7]</sup>.

The long-range interaction energy is the sum of interaction energies between the charges of a central unit cell and all the charges of the lattice. Hence, it can be represented as a double integral over two charge density fields representing the fields of the unit cell and the crystal lattice. The Ewald summation, which can sum the Coulombic interactions to infinity in a periodic system, transforms the total Coulombic contribution into two convergent series, one in the real space and one in the reciprocal space, each of which converges rapidly. <sup>[7-8]</sup> A cutoff radius is chosen such that the number of terms used in each summation is minimized. The first contribution can be visualised as resulting from the interactions in a system in which each point charge is surrounded by a Gaussian charge distribution of equal magnitude and opposite sign, centred on the point charge, as shown in **Figure 4.1-a**. These Gaussian charge distributions screen the point charges they are surrounding, thus lowering the interactions between them. The real electrostatic energy of the sum of the point charges plus the screening Gaussian densities is written in the form:

$$U_{el}^{real} = \frac{1}{2} \sum_{A,B} \frac{q_A q_B}{r} \operatorname{erfc}(-\alpha r) \quad (4.2)$$

where  $\operatorname{erfc}(x) = \frac{2}{\sqrt{\pi}} \int_x^\infty e^{-t^2} dt$  is the complementary error function. This is a rapidly convergent series which can be evaluated and truncated in real space.





**Figure 4.1** Charge distributions in the Ewald sum: (a) point charges screening by spurious Gaussian charge distributions; (b) compensating Gaussian charge distributions to (a).

Another Gaussian charge distribution must be added in order to maintain the neutrality of charges (**Figure 4.1-b**). This second distribution gives an electrostatic energy that is easier to calculate in reciprocal space:

$$U_{el}^{reciprocal} = \frac{1}{2} \sum_{k \neq 0} \sum_{A,B} \frac{4\pi q_A q_B}{V_{cell} k^2} \exp\left(-\frac{k^2}{4\alpha^2}\right) \cos(k \cdot r) \quad (4.3)$$

where  $k$  are the reciprocal vectors and  $V_{cell}$  is the volume of the unit cell of the crystal.

Moreover, we must correct for the spurious interaction of each Gaussian density with itself, which is included in the real space sum:

$$U_{el}^{self} = \left(\frac{\alpha}{\pi}\right)^{\frac{1}{2}} \sum_A q_A^2 \quad (4.4)$$

The reciprocal space summation in effect calculates the energy due to a system with a Gaussian distribution of charge placed at the lattice point with signs the same as the charges at those points. The effect of the Gaussian charge distributions is then removed by calculating the energy of a system where Gaussian charge distributions are superimposed on each of the lattice points, with opposite sign to the charge at



those points which are summed in real space. How rapidly these two sums converge is controlled by a factor  $\alpha$ , which effectively defines the width of the Gaussian distributions. The total electrostatic energy per unit cell can then be calculated as:

$$U_{el} = U_{el}^{real} + U_{el}^{reciprocal} - U_{el}^{self} \quad (4.5)$$

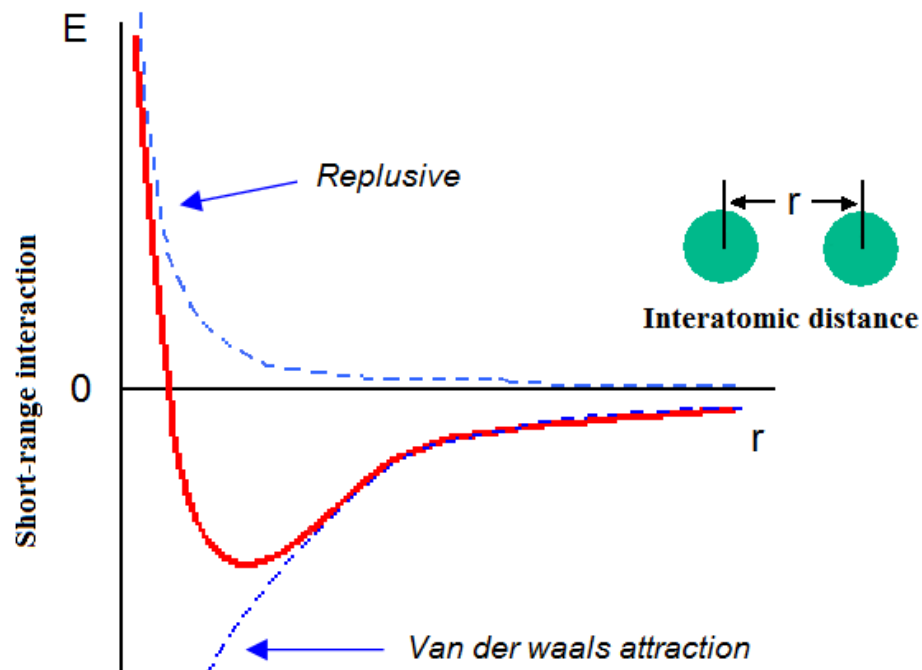
using equations 4.2, 4.3 and 4.4.

#### 4.1.1.2 Short Range Potentials

A general functional form for the non-electrostatic interaction is given by:

$$U^{short-range}(R_1, \dots, R_M) = \sum_{A,B} U_{AB}(R_A, R_B) + \sum_{A,B,C} U_{ABC}(R_A + R_B + R_C) + \dots \quad (4.6)$$

where the first term  $U_{AB}$  refers to two-body potentials, gives the most contribution to the short-range interactions. **Figure 4.2** displays the non-Coulombic energy change with interatomic distance.



**Figure 4.2** The non-Coulombic interaction including the attractive and repulsive components as a function of ion separation.



The short range potentials are usually handled approximately by analytical functions which comprise both an attractive and a repulsive term. The repulsive term describes the Pauli repulsion due to overlap of the closed shell electron configurations. The van der Waals attraction, i.e. the attractive term, arises at close interatomic separations due to an induced-dipole interaction and covalence effects. <sup>[6][9]</sup> It is also called the “London force” or dispersive interaction.

Several available functions in GULP code are shown in **Table 4.1**. However, the Buckingham function ( $E_{Buck}$ ) is widely used as an analytical expression for the short-range energy in the study of ionic and semi-ionic solids. Assuming the electron density falls exponentially with distance from the nucleus, <sup>[2]</sup> the Buckingham potential models repulsive the effects of the overlap of the electron wave functions supplemented by van de Waals attraction. It can be written as:

$$U_{AB}^{Buck} = A \exp\left(-\frac{r}{\rho}\right) - \frac{C}{r^6} \quad (4.7)$$

where  $A$ ,  $\rho$  and  $C$  are constants and  $r$  is the interatomic distance. This is the most commonly applied expression in ionic systems. <sup>[5]</sup>

Overall, the effective potentials describing the interatomic forces are represented by ionic, pair-wise potentials of the form <sup>[5]</sup>

$$\phi_{AB}(r) = \frac{q_A q_B}{r} + A \exp\left(-\frac{r}{\rho_{AB}}\right) - \frac{C}{r^6} \quad (4.8)$$

The calculation of a three-dimensional system involves the evaluation of interactions between all species within the unit cell and their periodic replications to infinity. For short-range interaction, some finite cut-off must be placed on computation of the interactions. <sup>[2]</sup> These can normally be safely set to zero at distances beyond  $\sim 10 \text{ \AA}$ . However, the Coulombic interactions fall-off as  $1/r$  (Eq. 4.1), so the electrostatic energy is not negligible even at considerable distances and it is never safe to truncate the Coulombic summation which must be summed to infinity as described above. <sup>[7]</sup>

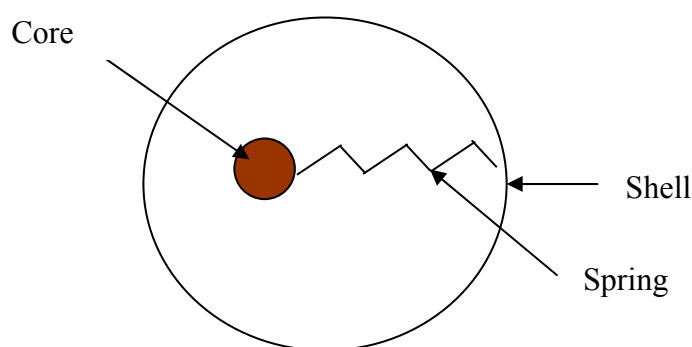


### 4.1.2 Ionic Polarization and the Shell Model

The Born Model discussed above is formulated treating ions as point charges. For complex oxides, ions and defects will polarize other ions in the lattice. Polarisability relates to the tendency of the electron cloud of an atom to be distorted from its normal shape by the presence of an electric field. In computer modelling, simple point dipole models are inadequate for ionic crystal as they lead to over estimate of the polarization energy. As an alternative way, the ionic polarization can be incorporated into the potential model via the shell model.<sup>[10]</sup>

The shell model, which was developed by Dick and Overhauser in 1958,<sup>[11]</sup> treats each ion as a core and shell. The core represents the nucleus and the core electrons, while the shell models the valence electrons and is coupled to the core with an harmonic spring as illustrated in **Figure 4.3**. The sum of the core and shell charges is the total ion charge. The free ion polarisability ( $\alpha$ ) is related to the shell charge ( $Y$ ) and the spring constant ( $k$ ) according to the equation:<sup>[12]</sup>

$$\alpha = \frac{Y^2}{k} \quad (4.9)$$



**Figure 4.3** Model of a polarisable ion showing the core connecting to the shell by a spring. (Note that in the implementation of the model both core and shell are point entities. Reproduced from Ref. [11])

The shell model provides a simple description of polarization effects and has also proven to be effective in simulating the dielectric properties of ceramic oxides. Short-range interaction act through the shells which serve to dampen excessive polarization.



**Table 4.1** Functional forms for interatomic potentials incorporated into GULP [From Ref. [2]]

potential name	formula	units for input
Buckingham	$A \exp(-r/\rho) - C r^{-6}$	$A$ in eV, $\rho$ in Å, $C$ in eV Å <sup>6</sup>
Lennard-Jones	$A r^{-m} - B r^{-n}$	$A$ in eV Å <sup>m</sup> , $B$ in eV Å <sup>n</sup>
(combination rules permitted)	or $\varepsilon [c_1(\sigma/r)^m - c_2(\sigma/r)^n]$ $c_1 = [n/(m-n)] * (m/n) ** [m/(m-n)]$ $c_2 = [m/(m-n)] * (m/n) ** [n/(m-n)]$	$\varepsilon$ in eV, $\sigma$ in Å
harmonic ( $k_3/k_4$ optional)	$1/2 k_2(r - r_0)^2 +$ $1/6 k_3(r - r_0)^3 +$ $1/12 k_4(r - r_0)^4$	$k_2$ in eV Å <sup>-2</sup> , $r_0$ in Å $k_3$ in eV Å <sup>-3</sup> $k_4$ in eV Å <sup>-4</sup>
Morse	$D\{1 - \exp[-a(r - r_0)^2]\}^2 - 1$	$D$ in eV, $a$ in Å <sup>-2</sup> , $r_0$ in Å
Spring (core-shell)	$1/2 k_2 r^2 + 1/24 k_4 r^4$	$k_2$ in eV Å <sup>-2</sup> , $k_4$ in eV Å <sup>-4</sup>
general	$A \exp(-r/\rho) r^{-m} - C r^{-n}$	$A$ in eV Å <sup>m</sup> , $\rho$ in Å, $C$ in eV Å <sup>n</sup>
Stillinger-Weber (2-body)	$A \exp[\rho/(r - r_{\max})] (B r^{-4} - 1)$	$A$ in eV, $\rho$ in Å, $B$ in Å <sup>4</sup>
Stillinger-Weber (3-body)	$K \exp[\rho/(r_{12} - r_{\max}) + \rho/(r_{13} - r_{\max})]$ $[\cos(\theta_{213}) - \cos(\theta_0)]^2$	$K$ in eV, $\rho$ in Å
three-body harmonic	$1/2 k_2(\theta - \theta_0)^2 +$ $1/6 k_3(\theta - \theta_0)^3 +$ $1/12 k_4(\theta - \theta_0)^4$	$k_2$ in eV rad <sup>-2</sup> , $\theta_0$ in degrees $k_3$ in eV rad <sup>-3</sup> $k_4$ in eV rad <sup>-4</sup>
three-body harmonic + exponential	$1/2 k_2(\theta_{213} - \theta_0)^2 \times$ $\exp(-r_{12}/\rho) \exp(-r_{13}/\rho)$	$k_2$ in eV rad <sup>-2</sup> , $\theta_0$ in degrees, $\rho$ in Å
Axilrod-Teller	$K(1 + 3 \cos \theta_{213} \cos \theta_{123}$ $\cos \theta_{132}) / (r_{12} r_{13} r_{23})^3$	$K$ in eV Å <sup>9</sup>
three-body exponential	$A \exp(-r_{12}/\rho) \exp(-r_{13}/\rho) \exp(-r_{23}/\rho)$	$A$ in eV, $\rho$ in Å
Urey-Bradley	$1/2 k(r_{23} - r_0)^2$	$k$ in eV Å <sup>-2</sup> , $r_0$ in Å
four-body	$k[1 + \cos(n\phi - \phi_0)]$	$k$ in eV, $\phi_0$ in degrees
Ryckaert-Bellemans	$\sum k_n(\cos \phi)^n$	$k_n$ in eV

$r$  represents the distance between two atoms  $i$  and  $j$ ,  $\theta_{ijk}$  represents the angle between the two interatomic vectors  $i-j$  and  $j-k$  and  $\phi_{ijkl}$  is the torsional angle between the planes  $ijk$  and  $jkl$ .



### 4.1.3 Parameterisation of Potentials

Having established the overall framework of the potential model, the variable parameters must be determined either by fitting to experimental data or the results of more theoretical studies such as *ab initio* calculations. <sup>[11, 13, 14]</sup>

The potential parameters used in this thesis for atomistic calculation were transferred directly from the previous studies of  $\text{ZrO}_2$  <sup>[15]</sup> and tabulated in **Table 4.1** (i). **Table 4.1** (ii) shows the Shell model parameters employed for the oxygen and zirconium ions. The parameters derived for the Zr-O potential were adjusted by a least-squares fitting routine to achieve the concordance between the calculated properties of  $\text{ZrO}_2$  and the experimental crystal properties, in this case the structural parameters and the dielectric constants of cubic phase and the lower symmetry tetragonal phase. <sup>[15]</sup> The O-O interaction was taken from the earlier work of Lewis and Catlow for oxides. <sup>[16]</sup>

**Table 4.1** Interatomic potential for  $\text{ZrO}_2$ .

(i) Short-range

Interaction	$A/\text{eV}$	$\rho/\text{\AA}$	$C/\text{eV \AA}^6$	Cut-off $\text{\AA}$
$\text{Zr}^{4+} \dots \text{O}^{2-}$	985.869	0.3760	0.0	10
$\text{O}^{2-} \dots \text{O}^{2-}$	22764.0	0.1490	27.880	12
$\text{Y}^{3+} \dots \text{O}^{2-}$	1345.1	0.3491	0.0	10

(ii) Shell-model

Species	$Y/e$	$k/\text{eV \AA}^{-2}$
$\text{O}^{2-}$	-2.077	27.290
$\text{Zr}^{4+}$	1.35	169.617



#### 4.1.4 Modelling Point Defects

Two contrasting approaches may be used to model point defects i.e. the periodic supercell and aperiodic Mott-Littleton methods. The details of these two approaches are discussed in detail in the following section.

The supercell method, which applies 3-D Periodic Boundary Conditions (PBC), is a simple procedure for calculating the formation energy of defect structures. PBC refers to simulations in a periodic lattice of identical sub units. The large defect supercell is periodically repeated to form an infinite lattice.<sup>[5]</sup> The supercell method is preferred when the calculation is carried out at a higher concentration of defects. The defect concentration can then be varied by varying the supercell size.

To evaluate the defect formation energy ( $E_{DEF}$ ), results for the defect doped lattice are compared with the perfect lattice. In the case of  $ZrO_2$ ,  $E_{DEF}$  is the energy difference between the defect containing  $ZrO_2$  structure e.g. YSZ and non-doped  $ZrO_2$  lattice.

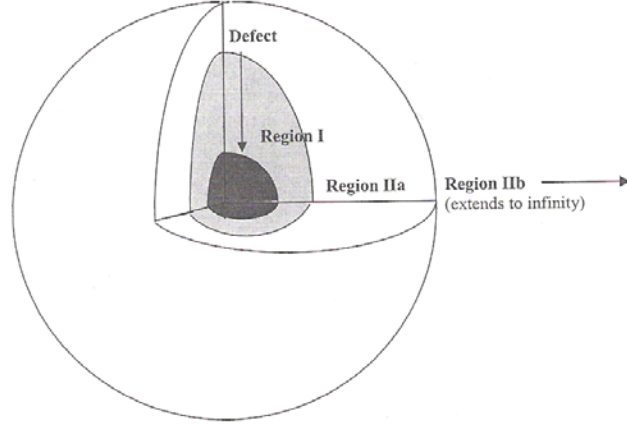
$$E_{DEF} = E[YSZ] - E[ZrO_2] \quad (4.10)$$

In the supercell calculation, the system must be neutralised, i.e. a uniform background of charge density is needed to compensate for the net charge of the cell. Otherwise, the Coulombic summation would diverge.

The calculation of defect energies for bulk solids can also be performed using the Mott-Littleton approach.<sup>[17]</sup> In this procedure, the isolated defect or defect cluster is embedded in the crystal which extends to infinity. The volume around the defect is divided into three spherical regions I, IIa and IIb as shown in **Figure 4.4**.

In the inner region I, the ions are allowed to relax freely in response to the forces arising from the defect until the system achieves equilibrium (zero net force on all ions). This central region contains typically 100-300 atoms. In the interface region (IIa) where the influence of the defect is relatively weak, the individual ions are assumed to be constrained within a harmonic well. In the outer region (IIb), the polarisation of the sub-lattice is considered via a quasi continuum approximation.<sup>[15]</sup>





**Figure 4.4** Schematic diagram of the Mott-Littleton method dividing the crystal into three regions. (From Ref. [15])

Therefore, the total energy of the system can be expressed as:

$$E = E_1(x) + E_{12}(x, \varsigma) + E_2(\varsigma) \quad (4.11)$$

where vector  $x$  represents the displacement of the ions in region I,  $\varsigma$  represents the displacements of the ions in regions II<sub>a</sub> and II<sub>b</sub>,  $E_1$  and  $E_2$  are the energies of regions I and II<sub>a</sub> and II<sub>b</sub> together respectively, while  $E_{12}$  is the interaction of between them.

The Mott-Littleton calculation can be applied to a charged system as well as a charged neutral model. In addition to defect formation energies, the binding energy of defect clusters,  $E_{\text{bind}}$ , can also be evaluated by the Mott-Littleton approach as in Eq. 4.12 by comparison with isolated defects.

$$E_{\text{bind}} = E_{\text{cluster}} - \left\{ \sum_{\text{component}} E_{\text{isolated defect}} \right\} \quad (4.12)$$

where  $E_{\text{cluster}}$  is the energy of a charge neutral cluster of compensating defects and  $E_{\text{isolated defect}}$  is the energy of an individual defect comprising the clusters.

#### 4.1.5 Phonon Modes

An important requirement in solid state modeling is the calculation of the phonon modes, <sup>[18]</sup> which describe the vibrational motion and provide a criterion for the system stability. An introduction to the concept of phonon is given in Ref. [19]. To



calculate the vibrations or phonons of a system, the starting point is the force constant matrix (as shown in Eq. 4.13), given by the mass-weighted second derivatives with respect to the atoms in Cartesian space. <sup>[15]</sup> In the case of a periodic solid, the dynamical matrix is a function of the reciprocal vector  $k$  chosen from the Brillouin zone.

$$F_{i\alpha j\beta} = \sum_R \left( \frac{\partial^2 U}{\partial \alpha \partial \beta} \right) \exp \left[ ik(r_{ij} + R) \right] \quad (4.13)$$

The Eq. 4.13 presents the force constant matrix for two atoms  $i$  and  $j$  and involves the summation over all lattice vectors  $R$  within the cut-off radius which is then converted to the dynamical matrix by multiplying the inverse square root masses of the ions: <sup>[20]</sup>

$$D_{i\alpha j\beta} = \frac{F_{i\alpha j\beta}}{(m_i m_j)^{1/2}} \quad (4.14)$$

Since the vibrational frequencies are the square roots of eigenvalues of the dynamic matrix, any negative eigenvalues, i.e. imaginary frequencies, imply that a lower energy conformation can be found by some distortion of the crystal lattice.

Dispersion curves, which give vibrational frequency as a function of wave vector, yield important information about the stability of the system. In particular, negative phonon frequencies show that the structure is unstable since these modes lead to a reduction in the energy of the system and show that ions cannot be at a minimum energy position. In this thesis, the phonon dispersion curves have been examined to test for stability of the optimized structures from the minimization calculations since experimental studies have suggested there are displacive phase transitions of  $\text{ZrO}_2$  driven by vibrational modes.

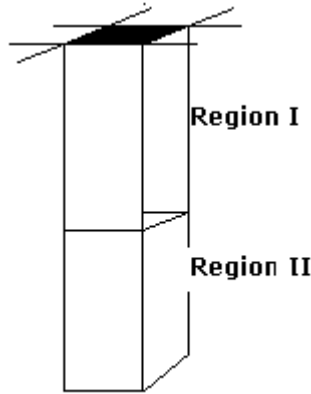
#### 4.1.6 Surface Modelling of a Periodic Lattice

Surface modelling plays an important role in many fields of material science. The computer code MARVIN <sup>[3]</sup> was used in this thesis for modeling surfaces or interfaces employing interatomic potentials. The basic concept of calculations using this code is the use of a slab model, which has planar 2D periodic boundary conditions parallel to the interface.



#### 4.1.6.1 Slab Model

The slab model is based on 2D periodic boundary conditions. The cell consists of one or more blocks, which are split into two regions (I and II) as in **Figure 4.6**. Each region consists of structural units, which may be ions or molecules consisting of one or more atoms. The structure and surface energy of the surface can be obtained by relaxing the ions to their mechanical equilibrium positions using this two-region approach.<sup>[3]</sup>



**Figure 4.6** Schematic diagram of the slab model.

In the surface region I, the atoms are relaxed explicitly to zero force whilst those atoms of region II are kept fixed to reproduce the electrostatic and short-range potential of the bulk lattice on region I. The sizes of the regions I and II are chosen such that the surface energy converges.

The total energy of the system includes all the species in region I, which interact with themselves, all the species in region II and the periodic images of both regions. Concentrating on the two-body terms, the total energy can be expressed as:<sup>[21]</sup>

$$E_{total}^{(2)} = \sum_a^{N_I} \left[ \frac{1}{2} \sum_{l \neq 0} V_{aa}(|l|) + \frac{1}{2} \sum_{b \neq a}^{N_I} \sum_l V_{ab}(|r_{ab} + l|) + \sum_b^{N_{II}} \sum_l V_{ab}(|r_{ab} + l|) \right] \quad (4.15)$$

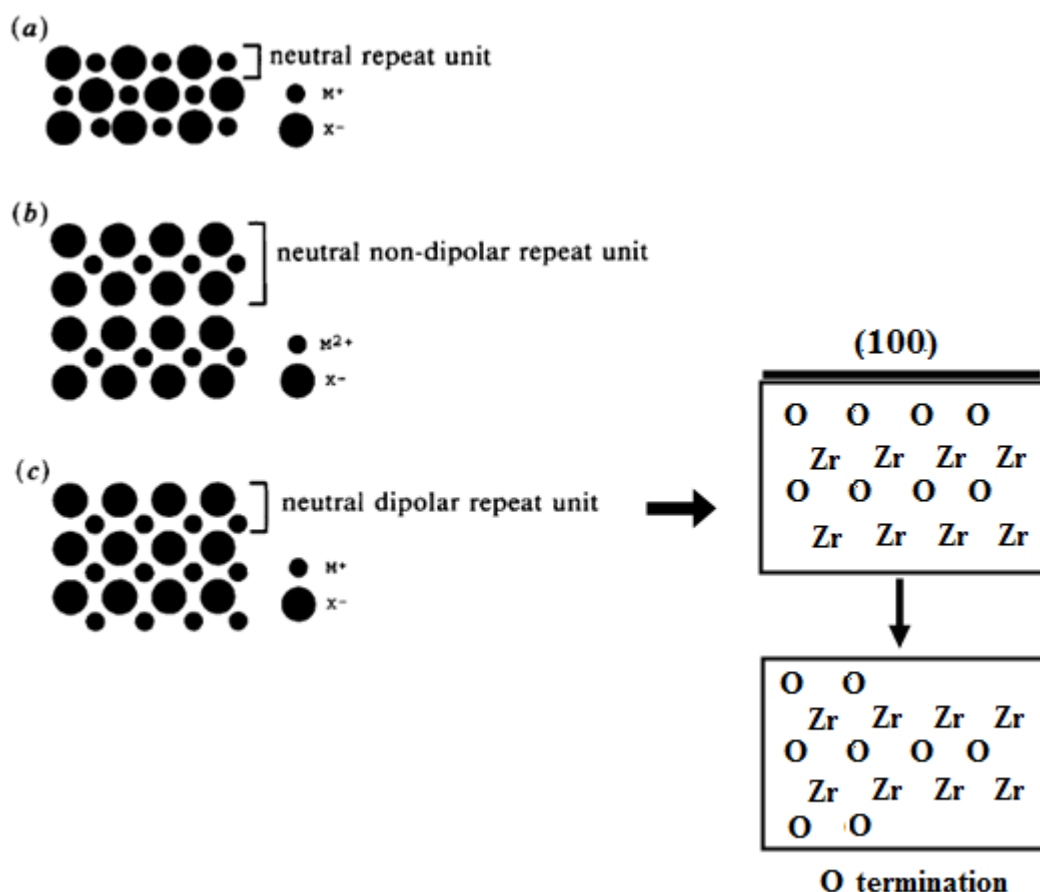
where  $N_I$  is the total number of particles in regions I,  $N_{II}$  is the total number of particles in regions II,  $l$  are the 2D lattice vectors and  $r_{ab}$  is the vector between particle  $a$  and particle  $b$ . The first term inside the brackets describes the interactions between a



particle and its periodic images, the second term describes the interactions between all region I particles and their images, whilst the third term describes the interactions between region I and region II particles. The first two terms are multiplied by a half to account for double counting of interactions. The boundary interaction energy ( $E_{BI}$ ) is defined as half of the third term. <sup>[3]</sup> Similar expressions apply for the three- and four-body interactions.

#### 4.1.6.2 Surface reconstruction

In computational modelling, the surfaces required are created by slicing through the bulk structure along the reciprocal lattice vectors which are denoted by Miller indexes. The low energy and hence the most common surfaces of a crystal are generally those of low Miller index. <sup>[22]</sup>



**Figure 4.7** Schematic representation of (a) type I, (b) type II, (c) type III surfaces (Left, from Ref. [23] ) and the (100) surface reconstruction of  $\text{ZrO}_2$  (Right).



Tasker *et al.* <sup>[23]</sup> identified three different types of stacking sequences for the exposed surface as shown in **Figure 4.7**. Type I surfaces comprise planes containing all component ions in their stoichiometric ratio. Thus cleaving the crystal at any position will yield a non-dipolar repeat. Type II surfaces involve a stack of charged planes with the repeat unit consisting of three planes in a symmetrical configuration and hence there is no dipole moment perpendicular to the surface. Type III surfaces stack the alternating charged planes in sequence with dipoles perpendicular to the surfaces. In such a case, the surface energy would diverge. Type III surfaces are not stable; therefore the dipole must be quenched in the  $z$  direction.

The dipole can be quenched by surface reconstruction which involves removing half the ions at the exposed surface to an infinite distance below the surface. In this project, the low index surfaces (111), (110), (100) and surface (310) of c-ZrO<sub>2</sub> were simulated. The (111), (110) and (310) surfaces are charged neutrally in the  $z$  direction, whilst the Type III (100) surface has a dipole moment perpendicular to the surface repeat unit, which, as shown by Tasker, results in instability. Therefore, the dipole moment was removed by surface reconstruction as presented in **Figure 4.7**.

#### 4.1.6.3 Surface Energy

The stability of a surface structure is determined largely by its surface energy, i.e. the thermodynamic penalty for cleaving a surface from a bulk material. The surface energy ( $\gamma$ ) can be calculated from the difference between the energy of the surface block and the energy for the same number of bulk ions per unit area:

$$\gamma = \frac{(E_{SURF} - E_{BULK})}{A} \quad (4.15)$$

where  $E_{SURF}$  is the energy of surface block and  $E_{BULK}$  is the energy of the corresponding quantity of bulk lattice.  $A$  is the surface area.

However, for the doped surface, the values of  $E_{BULK}$  automatically used in MARVIN calculations are the energies of the perfect lattice, meaning that a correction term ( $\Delta\gamma$ ) is required to obtain the surface energy for the doped surface ( $\gamma_{DEF}$ ), i.e.



$$\gamma_{DEF} = \gamma + \Delta\gamma \quad (4.16)$$

where

$$\Delta\gamma = \frac{(\Delta E_{SURF} - \Delta E_{BULK})}{A} \quad (4.17)$$

$\Delta E_{SURF}$  is the energy difference between the doped and pure surfaces;  $\Delta E_{BULK}$  is the energy difference between the perfect lattice and defect lattice which is defined in the term of defect energy ( $E_{DEF}$ ) and obtained from a super-cell calculation in Chapter 5. Note that in MARVIN simulations, since the energy minimization of the two region model includes the full value of boundary interaction ( $E_{BI}$ ), it is also necessary to correct the calculated total energy for the surface block ( $E_{SURF}^{TOT}$ ) for the boundary interaction energy between the surface and bulk blocks (i.e. region I and II), such that the energy of surface block  $E_{SURF}$  is given by:

$$E_{SURF} = E_{SURF}^{TOT} - 1/2 E_{BI} \quad (4.18)$$

In this thesis, the method described above is used throughout to derive the correction term for the surface energy calculations of yttrium doped  $ZrO_2$  surface.

## 4.2 Quantum Mechanics

As discussed in the above section 4.1, the interatomic potential method relies on a parameterised force-field and is a good starting point towards the understanding of materials properties and behavior; but it does not implicitly model electron and electron states of the solid crystals. Electronic structure methods aim to solve the Schrödinger equation using certain approximations. The intensive growth of computational power makes it now possible to handle the complicated mathematical relations of quantum mechanics for complex solid state systems on a scale up to  $\sim 100$  atoms or more.

### 4.2.1 The Schrödinger Equation and Born-Oppenheimer Approximation

The *Schrödinger equation* formulated by Erwin Schrödinger (1887-1964) in 1926 describes how the quantum state of a physical system changes in time. However, the



time-dependent Schrödinger equation is difficult to solve except for extremely small systems. Most quantum mechanical approaches attempt to solve the time-independent and non-relativistic Schrödinger equation although some progress has been made in dealing with the fully relativistic Dirac equation. The non-relativistic equation can be written as: <sup>[24]</sup>

$$\left[ -\sum_{i=1}^N \frac{1}{2} \nabla_i^2 - \sum_{A=1}^M \frac{1}{2M_A} \nabla_A^2 - \sum_{i=1}^N \sum_{A=1}^M \frac{Z_A}{r_{iA}} + \sum_{i=1}^N \sum_{j>1}^N \frac{1}{r_{ij}} + \sum_{A=1}^M \sum_{B>A}^M \frac{Z_A Z_B}{R_{AB}} \right] \Psi = E \Psi \quad (4.19)$$

where  $\Psi$  is the wavefunction and  $E$  is the energy of the system. The wavefunction itself is not an observable property but  $\psi\psi^*$  gives the corresponding particle density. The indexes  $i$  and  $j$  enumerate the electrons and run from 1 to  $N$ , while the indexes  $A$  and  $B$ , running from 1 to  $M$ , represent the nuclei;  $M_A$  and  $Z_A$  are the mass and the atomic number of the nucleus  $A$ , respectively, and  $r_{iA}$ ,  $r_{ij}$  and  $R_{AB}$  are the electron-nucleus, electron-electron and nucleus-nucleus distances, respectively. The Hamiltonian operator in the bracket acting on the wavefunction  $\Psi$  contains terms representing, in the order shown in Eq. 4.19, the kinetic energy of the electrons, the kinetic energy of the nuclei, the electron-nucleus interactions, the electron-electron interactions and the nucleus-nucleus interactions. This equation can be solved exactly for the one electron system, but for the many electron system, the Schrödinger equation still cannot be solved exactly and approximations are need to derive a solution.

It is usual to invoke the so-called **adiabatic or Born-Oppenheimer approximation** <sup>[25]</sup>. Since the nuclei are much heavier than the electrons ( $M_A \gg M_i$ , the ratio of the electron mass to the nuclei mass  $M_i/M_A$  is less than  $10^{-5}$  for atoms heavier than calcium), the electrons move much faster than the nuclei. Hence, the electrons can be regarded as particles responding instantaneously to the motion of the nuclei without requiring a finite relaxation time. Alternatively, during the time of a cycle of electrons motion, the change in nuclear configuration is negligible. Thus, it can be assumed that the electrons are in the adiabatic equilibrium of their ground state with respect to the position of the nuclei at all times. This approximation makes it possible to separate the electronic and nuclear coordinates in the many-body wave function, reducing the



problem to the solution of the dynamics of the electrons in a frozen configuration of the nuclei:

$$\left[ -\sum_{i=1}^N \frac{1}{2} \nabla_i^2 - \sum_{i=1}^N \sum_{A=1}^M \frac{Z_A}{r_{iA}} + \sum_{i=1}^N \sum_{j>1}^N \frac{1}{r_{ij}} \right] \psi = E\psi \quad (4.20)$$

However, solving this equation is still a formidable task, even for simple atoms or molecules. Further simplifications can be introduced that allow total-energy calculations to be performed accurately and efficiently for most systems of interest. These include the Hartree-Fock (HF) approximation or the Density Functional Theory (DFT) method to model the electron-electron interactions and the pseudopotential theory to deal with electron-ion interactions.

#### 4.2.2 Hartree-Fock Theory

The major complication in the solution of the Schrödinger equation is the coupling introduced by electron-electron interactions. The Hartree-Fock (HF) approximation includes electron interaction with the other electrons in a mean field way and reduces the multi-electronic equation to a mono-electronic problem. <sup>[26]</sup>

The **Hartree-Fock theory** <sup>[27,28]</sup> is based on the assumption that the multi-electron wavefunction  $\Psi(x_1, \dots, x_N)$  can be built from one-electron orbitals  $\varphi_i(x_i)$  in the following way:

$$\psi(x_1, \dots, x_N) = \frac{1}{\sqrt{N!}} \det \begin{pmatrix} \varphi_1(x_1) & \dots & \varphi_N(x_1) \\ \vdots & \ddots & \vdots \\ \varphi_1(x_N) & \dots & \varphi_N(x_N) \end{pmatrix} \quad (4.21)$$

which is called the **Slater determinant**, <sup>[29]</sup> where  $x \equiv \{r, s\}$  is the set of all spatial and spin coordinates of one electron. This form is not arbitrary but it is the simplest form that captures the antisymmetry principle for the wavefunction: when the coordinates of two electrons are exchanged in the wavefunction, the result equals the original wavefunction but with opposite sign. This principle is just a mathematical expression of **Pauli's exclusion principle**, which states that “no two electrons can occupy the



same state at the same time”.<sup>[30]</sup>

By invoking the **Variational Principle** to an *ansatz* (trial wave function) as a product of single-particle functions and minimize the energy of the system:<sup>[31]</sup>

$$E = \langle \psi | \hat{H} | \psi \rangle \quad (4.22)$$

With this constraint for the form of the wavefunction, the differential equations for finding the Hartree-Fock orbitals have the same general form as:<sup>[32]</sup>

$$\hat{f} \varphi_i = \varepsilon_i \varphi_i, \quad (i = 1, 2, \dots, n) \quad (4.23)$$

The solution of these equations yields the Hartree–Fock wave function and energy.  $\varphi_i$  is the  $i^{\text{th}}$  spin-orbital, and the Fock operator  $\hat{f}$  is defined as

$$\hat{f} = -\frac{1}{2} \nabla^2 - \sum_{A=1}^M \frac{Z_A}{|r - R_A|} + \hat{v}_i^{HF} \quad (4.24)$$

where the first term is the kinetic energy of the electron, the second is the interaction of the electron with the nuclei, and the third ( $\hat{v}_i^{HF}$ ) is an operator representing the interaction of the electron with the rest of the electrons in the system. This last operator can be expressed in terms of the same solutions ( $\varphi_i$ ) of the Hartree–Fock equations as a sum of two terms: the classical Coulomb interaction of one electron with the others, and the so-called **exchange interaction**, which does not have a classical equivalence and results from the inclusion of the antisymmetry principle via the Slater determinant.

The key mathematical procedure is to solve one particle effective Hamiltonian in a self-consistent loop: the  $\hat{v}_i^{HF}$  is constructed from an initial guess for the  $N$  occupied orbitals and then the corresponding Fock operator is used to obtain a new set of orbitals by solving the HF equation. A new potential is constructed with the  $N$  orbitals with the lowest energies (occupied orbitals). The process is repeated until convergence has been reached. From the converged orbitals the final multi-electronic wavefunction is built as a Slater determinant and thus the final energy and any other physical property can be obtained from this wavefunction. The Slater form of the wavefunction



is an important constraint for the HF solution. It is not difficult to show that this condition implies that the electrons will be described as more independent than they actually are. The only correlation between the electrons arises from the inclusion of the antisymmetry principle, which ensures that the motion of electrons with parallel spins is correlated in some way but the motion of electrons with opposite spins is not correlated at all. The difference between the exact total energy and the total energy given by the HF method is generally called the correlation energy (despite the fact that some electronic “correlation” is already included in the HF method). Although in some cases the contribution of the correlation energy is small and can be neglected, in many cases it plays an important role, and different post-HF methods have been developed to deal with the discrepancy. Most of these methods are based on relaxing the condition of the Slater form for the wavefunction, which is then expressed as a combination of different determinants including not only the occupied orbitals but also the empty ones.

Parallel to the development of this line in electronic structure theory, Thomas and Fermi proposed that the full electronic density was the fundamental variable of the many-body problem and derived a differential equation for the density without resorting to one-electron orbitals.<sup>[33]</sup> The Thomas-Fermi approximation was too crude because it did not include the exchange and correlation effects and was also unable to sustain bound states because of the approximation used for kinetic energy of the electrons. However, it set up the basis for the later development of density functional theory, which has been the method of choice in many electronic structure calculations in condensed matter physics and widely applied by the quantum chemistry community because of its computational advantages compared to HF-based methods.<sup>[36]</sup>

#### **4.2.3 Density Functional Theory**

The Hartree Fock theory is based on a many electron wavefunction. Density Functional Theory (DFT) replaces the many body electronic wavefunction with the electron density as the basic quantity. Unlike the wavefunction, which is not a physical observable but a purely mathematical construct, electron density is a physical characteristic of all molecules. While wavefunction becomes more complicated



mathematically as the number of electrons increases (spatial and spin variables for each of the  $N$  electrons), the density functional theory depends only on density as the function, which is easier to calculate. And more importantly, DFT methods overcome one of the main disadvantages of Hartree-Fock methods: the complete neglect of electron correlation. As a result, DFT methods significantly improve the calculation accuracy without the additional increase in computing time.

#### 4.2.3.1 Thomas-Dirac-Fermi Theory

Thomas–Fermi model, developed in 1927, was the predecessor to density functional theory, which is a statistical model to approximate the distribution of electrons in an atom. They used the expression for the kinetic, exchange and correlation energies of the homogeneous electron gas to construct the same quantities for the inhomogeneous system. <sup>[34-35]</sup>

In the case of a homogeneous electron gas, the orbitals of the system are by symmetry plane waves. If the electron-electron interaction is approximated by the classical Coulomb potential, the exchange and correlation effects are neglected, and the total energy functional can be readily computed. <sup>[33-34]</sup> Under these conditions, the dependence of the kinetic and exchange energy on the density of the electron gas can be extracted (Dirac <sup>[36]</sup>) and expressed in terms of a local function of density.

For the homogeneous electron gas, the density is related to the Fermi energy  $\varepsilon_F$  by

$$\rho = \frac{1}{3\pi^2} \left( \frac{2m}{\hbar^2} \right)^{3/2} \varepsilon_F^{3/2}, \quad (4.25)$$

and the kinetic energy by  $T = 3\rho\varepsilon_F/5$ , so the total kinetic energy

$$T_{TF}[\rho(r)] = C_k \int \rho^{5/3}(r) dr \quad (4.26)$$

with  $C_k = \frac{3}{10} (3\pi^2)^{2/3} = 2.871$  atomic units.

The next stage is for the inhomogeneous system to be considered as locally



homogeneous on combining with the classical expression for the nuclear-electron attractive potential and the electron-electron repulsive potential, the famous Thomas-Fermi expression for the energy of an atom can be given as:

$$T_{TF}[\rho(r)] = C_k \int \rho^{5/3}(r) dr + \int v(r)\rho(r) dr + \frac{1}{2} \iint \frac{\rho(r)\rho(r')}{|r-r'|} dr dr' \quad (4.27)$$

It can be seen that  $E_{TF}$  depends only on the electronic density. The Thomas-Fermi model may also employ the variational principle. Assuming the ground state of the system is connected to the electron density  $\rho(r)$ , which minimizes the  $E_{TF}[\rho(r)]$ , subject to the constraint on the number of electrons:  $\int \rho(r) dr = N$

The Thomas–Fermi equation's accuracy is limited because the resulting kinetic energy functional is only approximate, and because the method does not attempt to represent the exchange energy although an exchange energy functional was added by Dirac in 1928. <sup>[35]</sup>

However, the Thomas–Fermi–Dirac theory remained rather inaccurate for most applications. The largest source of error was in the representation of the kinetic energy, followed by the errors in the exchange energy, and due to the complete neglect of electron correlation.

#### 4.2.3.2 Hohenberg- Kohn Theorem

In 1964, Hohenberg and Kohn <sup>[37]</sup> stated two fundamental theorems that put the former ideas proposed by Thomas and Fermi on firmer mathematical grounds.

The first Theorem:

*The external potential  $V_{ext}(r)$  is (to within a constant) uniquely determined by the electronic density  $\rho(r)$  i.e.*

$$V_{ext}(r) \Leftrightarrow \rho(r) \quad (4.28)$$

*since, in turn  $V_{ext}(r)$  fixes Hamiltonian operator  $\hat{H}$ , the full many particle ground*



state wave function  $\Psi$  is a unique functional of  $\rho(r)$ .

Therefore, all material properties of a physical system can be computed in principle if  $\rho(r)$  is known. Hohenberg and Kohn gave a straightforward proof of this theorem, and it was generalized to include systems with degenerate states by Levy in 1979.<sup>[38]</sup>

The second theorem is based on the variational principle:

*Given any trial density  $\rho_t(r)$  of a  $N$  electron system in an external potential  $V_{ext}(r)$  i.e.  $\rho_t(r)$  normalized to  $N$ , the total energy calculated with this density will always be larger or equal than the ground state energy  $E_0$ , i.e.*

$$\begin{aligned} E_0 \leq E[\rho_t(r)] &= F[\rho_t(r)] + \int V_{ext}(r)\rho_t(r)dr \\ &= T[\rho_t(r)] + V_{ne}[\rho_t(r)] + V_{ee}[\rho_t(r)] + E_{xc}[\rho_t(r)] \end{aligned} \quad (4.29)$$

For a system comprising nuclei and electrons the external potential  $V_{ext}(r)$  is the Coulombic attraction between electron and nuclei, and  $F[\rho(r)]$  refers to the sum of the kinetic energy and the electron–electron Coulombic, exchange and correlation energies.  $E[\rho(r)]$  equals  $E_0$  only when  $\rho(r)$  is the exact electronic density of the system. Therefore, the minimization of the energy allows the calculation of the electronic density of the ground state of the system.

Combining these two theorems lead to the fundamental expression of density functional theory (DFT):

$$\delta \left\{ E[\rho(r)] - \mu \left( \int \rho(r)dr - N \right) \right\} = 0 \quad (4.30)$$

The ground state energy and density correspond to the minimum of  $E[\rho(r)]$  which subject to the constraint electrons. The Lagrange multiplier  $\mu$  represents the electronic chemical potential:

$$\mu = \frac{\delta E[\rho(r)]}{\delta \rho(r)} = V_{ext}(r) + \frac{\delta F[\rho(r)]}{\delta \rho(r)} \quad (4.31)$$

As a universal functional  $F[\rho(r)]$  does not depend on the external potential but only



on the electronic density. And hence,  $F[\rho(r)]$  implies the solution of the full many body Schrödinger equation.

However, to solve the Schrödinger equation in this direction, the difficulty remains in the calculation of the kinetic and electron-electron terms in Hamiltonian. The density functional theory only became a workable method through the development by Kohn and Sham (1965).

#### 4.2.3.3 Kohn–Sham equations

According to the Hohenberg-Kohn theorems Eq.4.29, the universal functional  $F[\rho(r)]$  can be divided into specific components:

$$F[\rho(r)] = T[\rho(r)] + J[\rho(r)] + E_{xc}[\rho(r)] \quad (4.32)$$

where the individual contribution of the kinetic energy  $T[\rho(r)]$ , the classical electron-electron repulsion, and the non-classical portion  $E_{xc}[\rho(r)]$  due to self-interaction corrections, exchange (i.e. antisymmetry) and electron correlation effects. In this explicit form, the classical Coulombic interaction,  $J[\rho(r)]$ , which is known as Hartree energy, is given by

$$J[\rho(r)] = \frac{1}{2} \iint \frac{\rho(r)\rho(r')}{|r-r'|} dr dr' \quad (4.33)$$

The other parts of the universal functional remained undetermined until Kohn-Sham introduced a method for calculating the kinetic energy in 1965.

The starting point of the Kohn-Sham (KS) method is to replace the real system of interacting electrons with a fictitious system of non-interacting electrons that has the same density and moving in an effective potential  $V_{eff}$ , and from which, an auxiliary set of one-electron orbitals, Kohn-Sham orbitals ( $\phi_i$ ), was postulated.<sup>[39]</sup> By choosing the effective potential  $V_{eff}$ , the electron density resulting from the summation of the moduli of the squared orbitals  $\phi_i$  exactly equals the ground state density of the real system with interacting electrons.



$$\rho_s(r) = \sum_{i=1}^N |\varphi_i|^2 = \rho_0(r) \quad (4.34)$$

where the sum is over all the occupied Kohn-Sham orbitals.

In such a system, the exact kinetic energy of non-interacting fermions is calculated using a Slater determinant composed of orbitals  $\varphi_i$

$$T_{KS}[\rho] = -\frac{1}{2} \sum_{i=1}^N \langle \varphi_i | \nabla^2 | \varphi_i \rangle \quad (4.35)$$

where  $T_{KS}$  describes a main part of the true kinetic energy ( $T_{KS} < T[\rho]$ ). The approach of finding the best kinetic energy for the system is similar to that in the Hartree-Fock theory where a set of orthogonal orbitals is obtained via a self consistent field to achieve the lowest energy for the system. A one electron operator  $\hat{h}_{KS}$  (analogous to Fock operator) is used to build the pseudo-eigenvalue equations known as the Kohn-Sham equation:

$$\hat{h}_{KS} \varphi_i = \varepsilon_i \varphi_i, \quad (4.36)$$

where

$$\hat{h}_{KS} = -\frac{1}{2} \nabla^2 + \sum_{A=1}^M \frac{Z_A}{|r - R_A|} + \int \frac{\rho(r')}{|r - r'|} dr' + V_{xc}(r). \quad (4.37)$$

The first term of the Kohn-Sham operator is the electron and nucleus potential, the second is the electron-electron Coloumb potential and the final term is the exchange correlation potential which is the functional derivative (analogous to a function derivative) of the exchange correlation functional, i.e.

$$V_{xc}(r) = \frac{\delta E_{xc}[\rho(r)]}{\delta \rho(r)} \quad (4.38)$$

The KS equation can be solved iteratively by assuming an initial density from the equation since the KS operator itself depends on the orbitals  $\varphi_i$  of the solution. From this initial density, the effective potential  $V_{eff}$  can be calculated and the KS equation can be solved obtaining a new electron density. From this new electron density an updated effective potential is obtained. The iterative process is repeated until the new



electron density is equal to the previous one. However, the utility of the theory rests on the approximation used for  $E_{xc}[\rho]$ .

#### 4.2.4 Exchange-Correlation Functionals (LDA and GGA)

As discussed above, the Kohn-Sham formalism allows an exact treatment of most contributions to the electronic energy including the major fraction of the kinetic energy. So far, the DFT theory is exact and does not contain any approximations. All remaining uncertainty about the universal functional  $F[\rho]$  are collectively folded into the exchange-correlation functionals  $E_{xc}[\rho]$ . By comparison with the Hartree-Fock effective Hamiltonians, this term must contain the exchange energy, correlation energy and the difference between the kinetic energies of non-interacting and interacting systems. To generate the exchange-correlation functionals, approximations are necessary, which has led to a large and rapidly expanding field of research. Many different functionals have been proposed; two important levels of approximation the local density approximation (LDA) and the generalized gradient approximation (GGA) will be discussed here and employed for the QM studies in the later Chapters.

##### 4.2.4.1 Local Density Approximation

The simple local density approximation (LDA) is based on the Thomas-Fermi-Dirac theorem. This approximation assumes that the charge density varies slowly on the atomic scale and therefore the inhomogeneous electronic systems can be considered as locally homogeneous, or equal, but constant density and the same spin polarization which is known as jellium.<sup>[40]</sup> Thereby, the local exchange correlation energy is written as a function of the local charge density  $\varepsilon_{xc}$  as below:

$$E_{xc}^{LDA}[\rho(r)] = \int \rho(r) \varepsilon_{xc}(\rho(r)) dr, \quad (4.39)$$

where  $\varepsilon_{xc}(n(r))$  is a functional representing the exchange-correlation energy at point  $r$  of a uniform electron gas (Note not a function of  $\rho$ ) as displayed in **Figure 4.8**.  $\varepsilon_{xc}(n(r))$  can be further separated into exchange and correlation contributions:

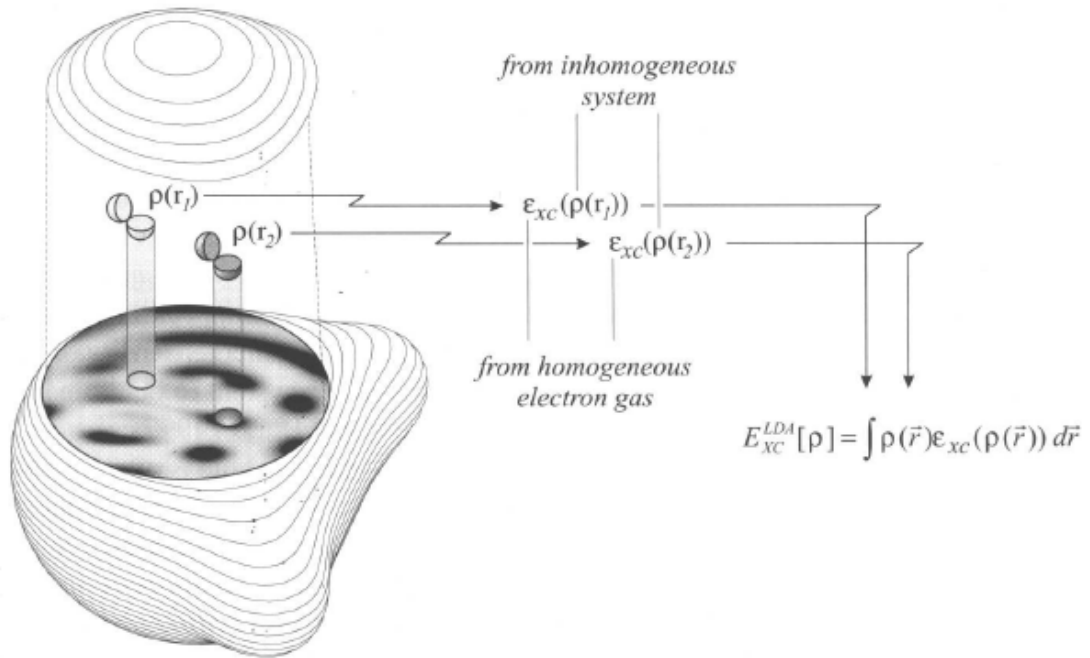


$$\varepsilon_{xc}(\rho(r)) = \varepsilon_x(\rho(r)) + \varepsilon_c(\rho(r)) \quad (4.40)$$

The exchange part, which is originally derived by Bloch and Dirac and equal to Slater exchange of Hartree-Fock calculation, is given by:

$$\varepsilon_x(\rho(r)) = -\frac{3}{4} \left( \frac{3\rho(r)}{\pi} \right)^{1/3} \quad (4.41)$$

Moreover, the exact form of the correlation contribution  $\varepsilon_c(n(r))$  is now well known from highly accurate numerical quantum Monte Carlo simulations by Ceperley and Alder (1980) <sup>[41]</sup> and has been fitted to analytic representations (VWN) <sup>[37, 42]</sup>



**Figure 4.8** The local density approximation. (From Ref. [43])

The LDA is a simple approximation which provides reasonable accuracy for some systems, however, the exchange energy is generally underestimated by ~10% with respect to HF, and the correlation energy is overestimated by around a factor of 2 which leads to oversizing of bond length. Moreover, when the density varies rapidly, the LDA is a poor approximation. The accuracy can be improved by taking the gradient of the local density approximation. This modification is referred to as the generalised gradient approximation (GGA) <sup>[44-45]</sup>.



#### 4.2.4.2 Generalised Density Approximation

In general, the exchange-correlation energy per particle  $\varepsilon_{xc}$  is a functional of the spin densities; and it depends on the values of the spin densities in the whole space and not only for the values at the integration point  $r$ , as in the LDA. The generalised gradient approximation (GGA) improves the LDA technique by considering the system as a non-uniform electron gas and taking account of non-local electron effects in the functional by incorporating a dependence of  $\varepsilon_{xc}$  on the gradients of the spin densities. It can be written as:

$$E_{xc}^{GGA}[\rho(r)] = \int f_{xc}(\rho(r), |\nabla\rho(r)|) dr \quad (4.42)$$

Actually, the GGA is still local in the sense that both the density and the gradients are only evaluated at the integration point  $r$ , but the dependence on the gradients incorporates some information about the density in the vicinity of  $r$ . In practice, the  $E_{xc}^{GGA}$  also splits into exchange and correlation contributions as in LDA (Eq. 4.40) and the approximations for the two parts are sought individually. The exchange term is given by:

$$E_x^{GGA} = E_x^{LDA} - \sum_{\sigma} \int F(s_{\sigma}) \rho_{\sigma}^{4/3}(r) dr, \quad (4.43)$$

where  $s_{\sigma}$  is a local inhomogeneity parameter defined as a function of the reduced gradient for spin  $\sigma$ :

$$s_{\sigma}(r) = \frac{|\nabla\rho_{\sigma}(r)|}{\rho_{\sigma}^{4/3}(r)} \quad (4.44)$$

For the function  $F$ , two main classes of realization have been proposed: the first is based on a GGA exchange functional developed by Becke in 1988 <sup>[46]</sup>; the second class uses a rational function of the reduced density gradient <sup>[42]</sup>. However, the largest error of the GGA arises from the gradient contribution to the correlation term.

GGA exchange correlation employed in this study was developed by Perdew and Wang, which is normally referred to in the literature as PW91. The exchange-correlation functional is constructed using only quantum Monte Carlo data for the



uniform electron gas and exact sum rules. PW91 includes a real space cut-off for the correlation functionals and employs the Becke exchange with only small refinements.<sup>[47]</sup> According to the authors, when the energy functional of the exchange-correlation hole (the depletion of the density of the other electrons at a point  $r+u$ ) surrounding an electron at  $r$  is expanded in a series of increasing derivatives, the zeroth-order term, which corresponds to the LDA, provides a good approximation to both the hole and the cusp at  $u=0$ . If the electron varies slowly over space, the addition of each successive term of higher order improves the description of the hole at small  $u$ , but worsens it at large  $u$ . Starting with the second-order gradient approximation, the spurious large  $u$  contributions are cut off to restore the exact conditions required on the hole.<sup>[48]</sup> This procedure defines a numerical GGA with no empirical input, and the PW91 functional is an analytical fit to this numerical functional.

The results of calculations with the PW91 functional show that it typically reduces exchange energy errors from 10% in LDA to 1% and correlation energy errors from 100% to about 10%.<sup>[39]</sup> PW91 corrects the LDA overestimation of the atomisation energies for molecules and solids, and enlarges equilibrium bond lengths and lattice parameters; it also usually reduces vibrational frequencies and bulk moduli.<sup>[49]</sup> In almost all cases where PW91 has been carefully tested, the results are significantly improved. The PW91 functional is used in the calculations reported in this thesis.

#### 4.2.5 Limitations of DFT

Despite the widespread popularity and success of DFT, its application can still suffer from large pervasive errors that cause qualitative failures in predicted properties. These failures are not breakdowns of the theory itself but are only due to deficiencies of the currently used approximate exchange-correlation functionals. The errors arise from DFT approximate functionals can be described in terms of violations of requirements of the exact functional and divided into delocalization (self-interaction) and static correlation error (strong correlation). The delocalization error originates from the violation of linearity of the energy as a function of fractional charges, and the static correlation error emerges from the violation of constancy of the energy as a function of fractional spins.<sup>[50]</sup>



#### 4.2.5.1 Delocalization Error and Fractional Charges

According to the previous studies, the major problems encountered in DFT including: the calculations tend to underestimate the barriers of chemical reactions, the band gaps of materials and charge transfer excitation energies; They also overestimates the binding energies of charge transfer complexes and the response to an electric field in molecules and materials. All of these diverse issues share the same root of the delocalization error, due to the dominating Coulomb term that pushes electrons apart.<sup>[50]</sup> The electron delocalization, which refers to the tendency of approximate functionals to spread out the electron density artificially, is related to self-interaction in many electron systems.<sup>[51]</sup> The error of self-interaction is induced by the potential computed from the total electron density in DFT. As each individual electron contributes to this total density – an electron interacts with itself.

In chemical reactions, since the transition state has electrons delocalized over more than one center, approximate DFT calculations report significantly lower transition state energies and hence lower reaction barriers than experiment observations. Approximate functionals of DFT can also predict unphysical charge transfer between the molecule and the metal leads in molecular electronic devices, and cause an overestimation of electronic conductance.<sup>[52]</sup> When adding or removing an electron from a system, DFT approximate functionals produce an overly disperse distribution for the added electron or hole. This effect can be magnified in large systems because the delocalization error increases with system size. Thus, the delocalization error may be a particular concern for cluster calculations that attempt to approach the bulk limit.

In contrast with DFT, Hartree-Fock approximation with an orbital functional has the opposite characteristic and suffers from a localization error that saturates with system size.<sup>[51]</sup> Therefore, Hybrid functionals contain both DFT and Hatree-Fock components may benefit from error cancellation in some cases, thus reproducing good band gaps for solids with midsize gaps; however, they do not provide general solutions.

#### 4.2.5.2 Static Correlation Error and Fractional Spin

Another common error of density functional approximation is static correlation error



in strongly correlated systems, characterized by the presence of degeneracy or near degeneracy. These situations can be described within DFT by fractional-spin states that are ensembles of degenerate pure-spin states.<sup>[53]</sup> The constancy condition for the exact functional requires that systems with fractional spins have an energy equal to that of the normal-spin states. However, approximate functionals do not accurately describe the interaction between the degenerate spin-up and spin-down states and have a massive error for these fractional-spin states.<sup>[50]</sup> The violation of the constancy condition for fractional spins gives rise to the static correlation error and explains the difficulty in using the electron density to describe degenerate states.

Static correlation is a pervasive problem in DFT.<sup>[50]</sup> Breaking any chemical bonds leads to failures, with a static correlation error that is proportional to the number of electron pairs involved. For instance, transition metal dimers, which have multiple bonds and hence multiple degeneracies, the static correlation error dominates. As such, DFT calculations cannot accurately describe the chemical bonding in metal dimers. Another example is the calculation of the open-shell boron atom, which has a threefold spatial degeneracy among the  $p$  orbitals. DFT calculations of the spherical density give an excessively high energy because of multiple fractional-spin occupations. In particular for study molecular ions with covalent bond, approximate functionals in DFT severely overestimate the energies upon dissociation. Furthermore, in case of magnetic system, magnetic properties, such as the magnetic coupling constants, rely on the accurate calculation of both singlet and triplet states. However, due to static correlation error, the accurate calculation of closed-shell singlets is not always possible in DFT. This problem has led to the routine use of broken-symmetry open-shell singlets state which avoids fractional spins.

In general, DFT can suffer from large errors that manifest themselves in a wide range of applications. An insight into the errors of functionals arising from fractional charges and fractional spins are of great importance to understand the problems encountered in DFT, and also could illuminate a path for further development. Indeed, new hybrid functionals have been constructed to minimize the delocalization error and improve many related predictions. An example is the approximation known as B3LYP,<sup>[54]</sup> which reproduces better band gaps and magnetic properties. However, the use of such hybrid functional approaches is restricted by its significantly increased



computational cost and will be a further issue for the study of oxygen dissociation.

#### 4.2.6 Electronic Structure in Periodic Solids

In the preceding sections, a many-body problem can be mapped into an effective single-particle problem, and thus avoid the problem of the coupling between electrons. However, there still remains the difficult task of handling an infinite number of non-interacting electrons in the static potential of an infinite number of nuclei in a solid material. In this section, the application of density function theory to the condensed phase is described.

##### 4.2.6.1 Bloch's Theorem

The basic issue in considering condensed phases is the number of electrons involved in the calculation. For crystalline solids, the translational periodicity of the crystal should reduce this problem to the calculation of the electronic structure for one particular unit cell. Symmetry also plays an important role, since the higher symmetry the fewer number of atoms need to be considered.

According to Bloch's Theorem (1928),<sup>[55]</sup> the mono-electronic wavefunction in a regularly repeating lattice (i.e. periodic boundary conditions) can be given by:

$$\psi_k(r) = e^{ik \cdot r} u_k(r) \quad (4.45)$$

where  $e^{ik \cdot r}$  is the phase factor,  $r$  is the position and  $k$  is the wave vector. For any lattice vector  $a_i$  of the simulation cell:

$$\psi_k(r + a_i) = e^{ik \cdot r} \psi_k(r) \quad (4.46)$$

where  $u_k(r)$  has lattice periodicity:  $u(r + a_i) = u(r)$ .

##### 4.2.6.2 Plane-waves

The plane-wave is a mathematical expression of the condensed phase basis sets which



represent waves propagating with a constant frequency and amplitude; and it is perfectly periodic and obeying Bloch's theorem.

The periodic function  $u(r)$  can be expanded as a Fourier series in the form:

$$u_i(r) = \sum_G c_{i,G} e^{iG \cdot r} \quad (4.47)$$

where  $G$  are the reciprocal lattice vectors defined by the condition  $\exp(iG \cdot a_i) = 1$ . ( $i=1,2,3$ ) Hence, the electronic wave-function can be written as:

$$\psi_{i,k}(r) = \sum_G c_{i,k+G} e^{i(k+G) \cdot r} \quad (4.48)$$

According to the above equations, it can be proved that any wavefunction with index  $k+G$  is identical to the wavefunction with index  $k$ . Therefore,  $k$  can be restricted to the first Brillouin zone in the reciprocal space. In practice,  $k$  points on a regular grid for 3D integration are normally used and the grid fineness is a convergence parameter. The number of  $k$  point in one unit cell needed for convergence varies inversely with simulation volume. Usually, a small  $k$  point number is chosen to calculate the wavefunctions, since the wavefunctions and other properties such as Hamiltonian eigenvalues vary smoothly over the Brillouin zone.<sup>[56]</sup> Methods for making efficient choices of  $k$  points have been developed by several authors.<sup>[57]</sup>

The energy cut-off of plane waves is another important convergence parameter. According to the Eq. 4.48, to expand the periodic wavefunction, an infinite summation is required over all possible values of  $G$ . However, the Fourier coefficients  $c_{i,k+G}$  for the plane waves decreases with increasing value of  $|k+G|$ , since the lower kinetic energy are typically more important than those with large kinetic energy. Thus the plane-wave basis set can be truncated to include only plane waves that have kinetic energies that are less than some particular cut-off energy. The point at which to stop the summation is decided by the kinetic energy cut-off which is defined as:

$$\frac{\hbar^2}{2m} |k+G|^2 < E_{cut} \quad (4.49)$$

A higher energy cut-off means more plane waves are included in the summation hence



leading to a better representation of the wavefunction. In QM modelling, this energy cut-off has to be sufficiently high to ensure that the properties of the system are well converged with respect to changes in the values of  $E_{cut}$ .

However, since the steep ionic potential causes rapid oscillations of the wavefunction and the orthogonal condition between different states, large kinetic energies and hence a very large number of plane waves is required to reproduce the wavefunction the region close to the atomic nuclei. The Hamiltonian matrix will be intractably large for systems that contain both valence and core electrons. To solve this problem, the summation is calculated by ignoring core electrons and concentrating on the valence electrons. The potentials of the atomic centers have to be modified and thus pseudopotentials are introduced in such a way which reproduces the properties of the valence electrons accurately. <sup>[58]</sup>

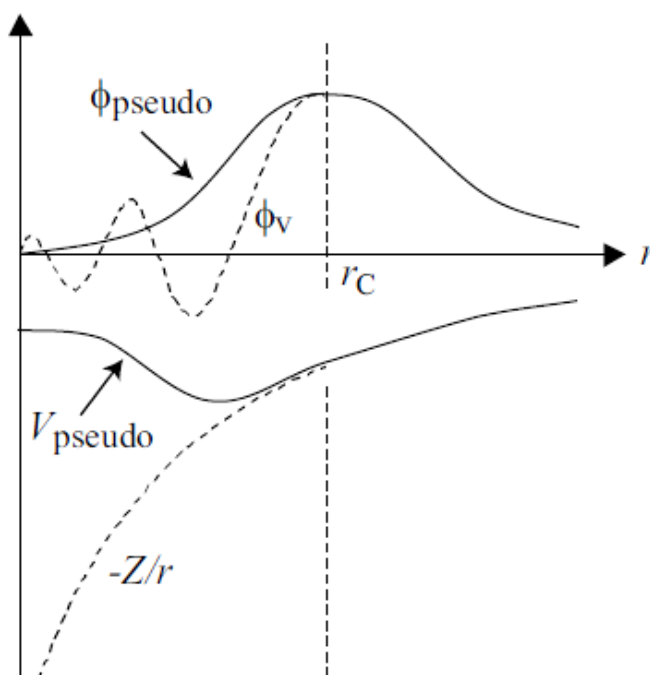
#### 4.2.7 Pseudopotentials and Projector Augmented Wave Method

Since most physical properties of solids are dependent on the valence electrons to a much greater extent than on the core electrons, the pseudopotential approximation assumes that only the valence electrons participate strongly in the interaction between atoms. Thus, the core electron states are considered to be fixed and a pseudopotential can be constructed for each atomic species by replacing the Coulomb potential of the nucleus and the effects of the tightly bound core electrons with an effective ionic potential, which only acts on the valence electrons. <sup>[59, 60]</sup> The pseudopotentials are derived from the all-electron calculations to keep the same energy levels for their wave-functions. The valence electron pseudopotential is required to reproduce the behaviour and properties of the valence electrons in the full calculation. The pseudo-wave-functions corresponding to this modified potential do not exhibit the rapid oscillations of the true wave-functions. And the number of basis functions needed in the calculation can be dramatically reduced without substantial loss of any accuracy in treating the valence shell electrons. <sup>[61]</sup>

A schematic of all-electron potential and corresponding pseudopotential is depicted in **Figure 4.9**. In the region occupied by the core electrons ( $r < r_c$  in the figure) the valence wavefunctions oscillate rapidly due to the strong Coulomb potential in this



region. These oscillations maintain the orthogonality between the core wavefunctions and the valence wavefunctions as required by the exclusion principle.



**Figure 4.9** Schematic illustration of all-electron (dashed lines) and pseudo (solid lines) potentials and their corresponding wavefunctions. The radius at which all electron and pseudopotential values match is  $r_c$ .<sup>[62]</sup>

#### 4.2.7.1 Norm-conserving pseudopotentials

Hamann *et al.* extended the concept of pseudopotential to a norm-conserving pseudopotential (NCPP) approach<sup>[63]</sup> in which the all-electron wavefunction is replaced by a soft nodeless pseudo-wavefunction inside the core radius  $r_c$ , with the crucial restriction that the pseudo-wavefunction must have the same norm (electronic charge) as the all-electron wavefunction within the chosen core radius. For  $r > r_c$  the pseudo and the all-electron wavefunction are identical.

The use of these pseudopotentials allows the electronic wavefunctions to be expanded using far fewer plane waves and also gives a better relative accuracy since the total energy of the valence electron system is much smaller than the energy of the all-electron system. However, the norm-conserving pseudopotentials approach still needs a large number of plane waves for the description of atoms with well-localised



electrons i.e.  $2p$  first-row elements and the  $3d$  transition metals. In the calculation of these elements, although the required cut-off energy can be decreased with increasing radius of  $r_c$ , this increase of radius also reduces the transferability and accuracy of the pseudopotential as good transferability requires a core radius around the outermost maximum of the all-electron wavefunction. Therefore, for these elements it is generally not possible to construct a pseudo wavefunction significantly smoother than the all-electron wavefunction.

#### 4.2.7.2 *Ultrasoft pseudopotentials*

Relaxation of the norm conservation condition leads to Vanderbilt ultrasoft potentials (1990) <sup>[60]</sup> which allow smoother wavefunctions, and hence lower cut-off energies. In this method, the constraint of norm-conservation is removed and localized atom-centered augmentation charges are introduced to compensate the resulting charge deficit. Transferability is guaranteed even for large core radii, by allowing more than one reference energy per quantum state. <sup>[64]</sup> The core radius can then be chosen around half the nearest-neighbour distance, independently of the position of maximum of the all-electron wavefunction. Vanderbilt's scheme enables the construction of "ultrasoft" pseudopotentials requiring no more than 50-100 plane waves per atom, even for the difficult cases of  $2p$  and  $3d$  elements. Taking advantage of the significant reduction in the size of the plane wave basis set, the ultrasoft pseudopotentials (USPP) approach has been implemented in the VASP code by Kresse and Hafner. <sup>[63]</sup>

#### 4.2.7.3 *The projector augmented-wave method*

The pseudopotential projector augmented wave (PAW) method is an all-electron structure method developed by Blöchl in 1994. <sup>[65]</sup> It combines ideas from the pseudopotential method and from the all-electron linear augmented planewave (LAPW) method. <sup>[66]</sup> In this thesis, most of the quantum mechanic calculations used the (PAW) method.

In the PAW formalism, the all-electron wavefunction is constructed by a superposition of different terms: a pseudo wavefunction and atom-like functions localised near the



nuclei. As displayed in **Figure. 4.10**, the pseudo-wavefunction  $|\tilde{\psi}\rangle$  coincides with the wavefunction  $|\psi\rangle$  in the interstitial region. And inside the spheres of augmentation regions ( $\Omega_A$ ), the wavefunction is almost atom-like. Therefore, the solutions  $|\phi_\Lambda\rangle$  of the one-electron Schrödinger's equation for the isolated atom, i.e. partial waves, are used as a basis set for the atomic regions. Here  $\Lambda = \{A, \varepsilon, l, m\}$  is a global index for the atom  $A$ , with quantum numbers  $l$  and  $m$ , and the reference energy  $\varepsilon$  for which Schrödinger's equation is solved.

A set of auxiliary functions  $|\tilde{\phi}_\Lambda\rangle$ , so-called pseudo partial waves, are introduced to link the expansion in the atom-like functions near the nuclei to the pseudo-wavefunction. In the interstitial region, i.e.  $r \notin \Omega_A$ ,  $\tilde{\phi}_\Lambda = \phi_\Lambda$ . The coefficients  $c_\Lambda$  of the wavefunction expansion in partial waves are chosen to eliminate the spurious contribution of the pseudo wavefunction in the augmentation region. For this purpose, the projector functions  $\langle \tilde{p}_\Lambda |$  are introduced to fulfill the condition,

$$\sum_\Lambda |\tilde{\phi}_\Lambda\rangle \langle \tilde{p}_\Lambda| = 1 \quad (4.50)$$

and the expansion coefficients of an arbitrary wavefunction  $\tilde{\psi}$  can be identified with

$$c_\Lambda = \langle \tilde{p}_\Lambda | \tilde{\psi} \rangle \quad (4.51)$$

and therefore, the pseudo and all electron wavefunctions can be reconstructed from the plane-wave expanded pseudo wavefunctions as

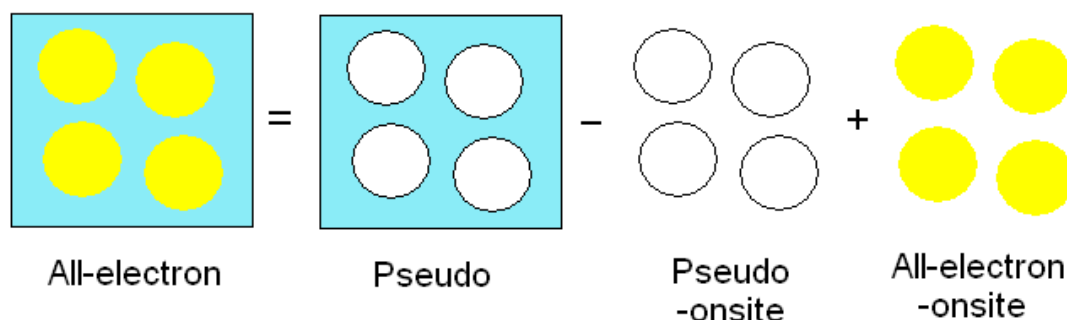
$$\begin{aligned} |\tilde{\psi}\rangle &= \sum_\Lambda |\tilde{\phi}_\Lambda\rangle c_\Lambda & r \in \Omega_A \\ |\psi\rangle &= \sum_\Lambda |\phi_\Lambda\rangle c_\Lambda & r \notin \Omega_A \end{aligned} \quad (4.52)$$

Equation 4.52 results in the bi-orthogonality condition:

$$\langle \tilde{p}_\Lambda | \tilde{\phi}_{\Lambda'} \rangle = \delta_{\Lambda, \Lambda'} \quad (4.53)$$

for the projector functions, which are chosen to be localised within the corresponding augmentation regions.





**Figure 4.10** Decomposition of the all-electron wave-function in the PAW method. Interstitial region (Blue); Atomic sphere (Yellow).

Overall, with these conditions, the wavefunction can be obtained from the pseudo-wavefunction as:

$$|\psi\rangle = |\tilde{\psi}\rangle + \sum_{\Lambda} \left[ |\phi_{\Lambda}\rangle - |\tilde{\phi}_{\Lambda}\rangle \right] \langle \tilde{p}_{\Lambda} | \tilde{\psi} \rangle \quad (4.54)$$

Equation 4.54 holds exactly only for a complete partial wave expansion. In practice, the partial wave expansion is truncated and, as a result, the plane waves also contribute to the true wavefunction inside the atomic regions. This approach has the advantage that the missing terms in a truncated partial wave expansion are partly accounted for by plane waves, which explains the rapid convergence of the partial wave expansion.

Using the transformation of equation 4.54, all the integrals can be evaluated as a combination of integrals of smooth functions extending throughout space plus localized contributions evaluated by radial integration over the augmentation spheres. In the PAW method, the full all-electron wavefunction is kept, although with the core states frozen at the atomic solutions. The access to the full charge and spin density is an important advantage of the PAW method over pseudopotentials, which allows, for example, the calculation of hyperfine parameters.<sup>[67]</sup> Limitations of plane-wave basis to periodic systems can be overcome by making unit cell sufficient large and decoupling the long-range interactions.<sup>[68]</sup> The present method can be used to study molecules, surfaces and solids within the same approach.

The plane wave convergence is more rapid than in norm-conserving pseudopotential



(NCP) and in principle should be equivalent to that of the ultrasoft pseudopotentials (USPP). Compared to the USPP, the PAW method has the advantage that the total energy expression is less complex and therefore is expected to be more efficient. The PAW method has been implemented in VASP by Kresse and Joubert,<sup>[69]</sup> who described the formal relationship between USPP and PAW.

### 4.3 Charge Population Analysis

The properties of chemicals and materials are often described in terms of charge transfer between atoms and the presence of ionic charges or electric multipoles on atoms or molecules. The idea of assigning charge contributions to individual atoms has proved an immensely valuable heuristic tool for chemists. However, atomic charges in molecules or solids are not defined by quantum mechanical theory. The output of quantum mechanical calculations is continuous electronic charge density and it is not clear how one should partition electrons amongst fragments of the system such as atoms or molecules. Many different schemes have been proposed, some based on electronic orbitals (such as Mulliken Population Analysis and the Weinhold-Reed Natural Population Analysis) and others based on only the charge density (e.g. Bader's Atoms in Molecules method and Hirshfeld procedure).

#### 4.3.1 Orbital Based Method: Mulliken Population Analysis

The most commonly used orbital method is the Mulliken analysis based on first-order density functions within the molecular orbital-linear combination of atomic orbitals (MO-LCAO) approach.<sup>[70]</sup> In MO-LCAO theory, the molecular orbital (MO)  $\varphi_i$  is expressed as a linear combination of monoelectronic functions. Thereby, the electron density distribution at a point  $r$  (the probability of finding an electron in a volume element  $dr$ ) can be simply written as a bilinear form:

$$\rho(r) = \sum_{\mu}^N \sum_{\nu}^N P_{\mu\nu} \varphi_{\mu} \varphi_{\nu}, \quad (4.55)$$

where the charge and bond order matrix:  $P = \{P_{\mu\nu}\}$  is defined in terms of the molecular orbital coefficients



$$P_{\mu\nu} = \sum_i \omega_i c_{\mu i} c_{\nu i} \quad (4.56)$$

$c_{\mu i}$  and  $c_{\nu i}$  are the linear coefficients; the parameters  $\omega_i$  are the MO occupation numbers.

Mulliken method apportions the electrons of an  $N$  electron molecule into two parts of net populations and overlap populations. All of the electron density (net populations  $P_{\mu\mu}$ ) in an orbital is allocated to the atom on which  $\phi_\mu$  is located. The remaining electron density is associated with the overlapping population,  $\phi_\mu\phi_\nu$ . If the overlap between two orbitals of  $\phi_\mu$  and  $\phi_\nu$  is written as  $S_{\mu\nu}$  and the basis functions are assumed to be normalised ( $S_{\mu\mu}=1$ ), the total number of electrons in a closed shell system is given by the integral over the electron density as:

$$\int \rho(r) dr = \sum_{\mu}^N \sum_{\nu}^N P_{\mu\nu} S_{\mu\nu} = N \quad (4.57)$$

In the Mulliken scheme, the overlap population is simply shared between the contributing atoms, which lead to the following charge for each basis orbital:

$$q_{\mu} = P_{\mu\mu} + \sum_{\mu \neq \nu} P_{\mu\nu} S_{\mu\nu} \quad (4.58)$$

Summing of the charges in the orbitals associated with each atom gives the atomic charge.

Mulliken Population Analysis is a fast and useful way of determining partial charges on atoms. It can be applied when basis functions centered on atoms are used in the calculation of the electronic wavefunction of the system. The charge associated with the basis functions centered on a particular atom is then assigned to that atom. Mulliken analysis simply divides overlap populations equally between the two atoms of a bond and thus has the advantage of simplicity. However, part of the weakness in the Mulliken approach arises from the fact that it employs a nonorthogonal basis set, and this problem was overcome by Löwdin, who transformed the atomic orbitals to an orthogonal basis set to achieve an improved population analysis (Löwdin charges) <sup>[71]</sup>. Weinhold and co-workers have extended the idea of “natural orbitals”, to yield natural population analysis (NPA) charges. <sup>[72]</sup>



The orbital based method such as Mulliken approach has a major drawback the analysis is sensitive to the choice of basis set. Furthermore, in the limit of an infinite basis, the assignment becomes arbitrary. As an extreme case, a complete basis set can be formed where all the basis functions are centered on just one atom in the system. The Mulliken analysis would then clearly be misleading as it would assign all the electrons in the system to that one atom. Moreover, many calculations are carried out with plane wave basis functions which are not associated with any particular atom in the system. Mulliken analysis is not applicable in such cases.<sup>[73]</sup>

#### 4.2.3.2 Electron Density Based Method: Bader Charge Analysis

An alternate approach to partition electrons between the atoms in molecules is to make use of the charge density distribution. This distribution contains all of the information needed for calculating the properties of the system (i.e., the energy, dipole and higher moments, etc.) and it may be calculated directly via density functional theory without the use of molecular orbital methods.<sup>[74]</sup> The use of the charge density has a natural advantage over other partitioning schemes (such as orbital based Mulliken analysis) in that it is an observable quantity that can be measured experimentally or calculated. Furthermore, in a converged electronic structure calculation, the charge density is insensitive to the basis set used.

One of the earlier electron density methods is Hirshfeld procedure,<sup>[75]</sup> in which a hypothetical “promolecule” is constructed by the superposition of the spherically symmetrized charge density distributions of the isolated atoms. The charge density of the real molecule at each point in space is then divided between the constituent atoms in the same proportions as they contribute charge density to that point in the hypothetical promolecule. The atomic populations are obtained by integrating these charge density contributions over all space. A deficiency of the original Hirshfeld procedure is that the final charges obtained are highly dependent on the initial spherical atomic density. This procedure usually produces atomic charges rather small magnitudes.

A different approach was proposed by Bader in his theory of Atoms in Molecules (AIMS),<sup>[76]</sup> in which, the topology of the charge distribution is used to define atomic



regions. Electron densities are integrated over the volumes (basins) assigned to the individual atoms. Each Bader volume contains a single charge density maximum, and is separated from other volumes by surfaces on which the charge density is a minimum normal to the surface. Typically, there is one charge density maximum at each atomic center and one Bader volume for each atom, but this is not required; there are cases in which Bader volumes do not contain a nucleus. The dividing volumes are assigned in terms of “zero flux surfaces” defined by the gradients of the electronic density function  $\nabla\rho(r_s)$ . For every point  $r_s$  on the surface  $S(r_s)$ , an interatomic surface satisfies the “zero-flux” boundary condition:

$$\nabla\rho(r_s) \bullet n(r_s) = 0 \quad (4.59)$$

where  $n(r_s)$  is the unit vector normal to the surface at  $r_s$ . At a point on a dividing surface the gradient of the electron density has no component normal to the surface.

There are several different approaches to calculating Bader volumes. Early algorithms were implemented for quantum chemistry calculations of small molecules, in which the gradient of the charge density can be calculated from derivatives of an analytic wavefunction.<sup>[76, 77]</sup> These methods first find stationary points in the charge density and then follow trajectories along the density gradient from these points to map out their connectivity and the zero-flux dividing surfaces. With the dividing surfaces represented in this way, the charge in each Bader volume can be integrated from the charge density maximum to the surface. While this approach works for small molecules, a high density of descent trajectories is needed to accurately represent the surface away from the critical points, and the method has been criticized as being computationally expensive for large systems. It was also found to fail for complex bonding geometries and when the radial integration rays have multiple intersection points with the dividing surface.<sup>[78]</sup>

Several improvements to this original approach have been proposed. Most current implementations of Bader’s analysis are based upon a grid of charge density values<sup>[73, 79-80]</sup>. This is particularly important for plane-wave-based DFT calculations, because it allows for the analysis of condensed phase systems with many atoms. The partitioning algorithm follows steepest ascent paths along the charge density gradient from grid point to grid point until a charge density maximum is reached. As the algorithm



assigns grid points to charge density maxima, subsequent paths are terminated when they reach previously assigned grid points. The constraint of ascent trajectories to the grid means that each point need be considered only once. The improved algorithm is highly efficient, scales linearly with system size, and is robust to complex bonding topology found in condensed systems.<sup>[79]</sup>

In this thesis, charge population analysis of the quantum mechanical calculations are carried out by Bader Charge Analysis. The fast grid-based algorithm employed in this analysis code is developed Arnaldsson *et al.* and discussed in details elsewhere.<sup>[73]</sup>

#### 4.4 Energy Minimization Methods

The calculation of free energy is based on the theories of statistical mechanics where microscopic properties of individual atoms or ions are related to macroscopic thermodynamic and other properties of the material.<sup>[81]</sup> The Global Potential Energy Surface (GPES) is a curve or a (multidimensional) hyper surface, which represents the total energy of an atom arrangement with atomic positions as variables. It can be derived from the force field equations or DFT calculations. Several points on the potential energy surface determine the important features of the system, e.g. the global minimum corresponds to the most stable nuclear configuration, saddle points or local maxima correspond to transition states, and local minima correspond to reactive intermediates.<sup>[82]</sup>

In computational modelling, the final structure or the relaxed structure (energy minimum) is achieved by surface relaxation allowing the ions to relax to the point at which they experience a zero net force, i.e. equilibrium positions. Therefore, efficient minimization of the energy on the potential energy surface is an essential part of the simulation of solids as it is a prerequisite for any subsequent evaluation of physical properties and normally represents the computationally most demanding stage. The simplest approach to minimize a structure is to consider an initial conformation and adjust it to give a lower total energy, which can then be further reduced to a minimum value by an iterative method, i.e. to make small changes in the geometry of the structure and check if the energy decreases.<sup>[83]</sup> The resulting minimum will typically be a local minimum on the GPES that the starting coordinates lie closest to. Trying to



locate the global energy minimum is a far more challenging task and one that has no guarantee of success, except for the simplest possible cases. <sup>[18]</sup>

The number of iterations depends on the nature of the minimization algorithm, the form of the energy function, the number of atoms as well as the curvature of potential energy surface. Since a crude search is very time consuming, many efficient algorithms such as the line search, steepest descent, conjugate gradient and Newton Raphson methods have been developed to find the energy minimum. <sup>[65]</sup> If the function had several minima (e.g. double well potential) the method described here would locate the position of the minimum in whose basin of attraction the initial sampling point lies.

#### 4.4.1 Line Search

A line search is the lowest level of sophistication in optimization procedures. The search changes the coordinates of the structure to a new lower energy structure. <sup>[69]</sup> The simplest method for a line search is to consider points in a line from the initial coordinates. The line search determines all the energies along one direction before moving to the next one. The minimum is determined along the line of the tangent point to the energy contour as shown in **Figure 4.11** (Line search). Therefore each line is orthogonal to the previous one. The actual minimum can be determined by successive interactions.

#### 4.4.2 Steepest Descent

Sine the line search is obviously inefficient, derivative methods have been developed to achieve higher search efficiency. The simplest derivative searching procedure is implemented by the steepest descent method <sup>[84]</sup> in which the derivative of the energy function is used to find the direction of the steepest slope. Once the steepest slope has been chosen, the energy can be searched along this direction to find the minimum which become the new energy point to search for the direct of steepest slope. The process continues until the gradient becomes flatter than a predefined cut-off value. This method also employs the line search method (given above) to determine how far the process needs to go to establish the minimum.



Although this method is good for minimizing systems which are far away from the minimum it tends to oscillate around the true minimum and the convergence is slow when it get close to the minimum.

#### 4.4.3 Newton Raphson

The Newton Raphson method uses both the gradient and the curvature (i.e. second derivative) of the potential energy surface.<sup>[69]</sup> The method employs the gradient method to identify the direction of the search and then the curvature of the function (second derivative) can be used to determine where the function passes through a minimum along that direction. It is very effective for minimizing energies. However, calculating the curvature of the potential energy surface may be time consuming so approximations can be applied to speed up the process. One approximation is the Quasi-Newton-Raphson method, which uses the conjugate gradient method and utilizes previous iterations to direct the minimization along a more efficient pathway. This method works well on larger systems. The Broyden, Fletcher, Goldfarb and Shanno (BFGS) algorithm is one example of the Quasi-Newton-Raphson method and has been applied for all the atomistic simulations discussed in Chapter 5. The algorithm spends considerable time on each step but it makes the best step.<sup>[85]</sup>

If the molecular energy surface is harmonic then the minimization can occur in one step but generally energy surfaces are not harmonic so the algorithm must be applied iteratively. The iterative Newton Raphson method can be unstable if the conformation is far away from the local minimum such that the potential energy surface is not quadratic. Therefore this is only the most efficient method to determine the minimum when the structure is close to the minimum compared to the conjugate gradient method, which can be applied when the structure is far away from the minimum.

Several types of standard minimizations are available in GULP. The most commonly used being to optimize at constant pressure, in which all internal and cell variables are included, or at constant volume, where the unit cell remains frozen. A range of other possibilities exist, such as the shell only optimization the shell coordinates and radii vary. This is useful in analyzing the electronic polarisation contribution to the relaxation. Symmetry adapted relaxation, shell only relaxation, breathing only



relaxation, unrestrained relaxation and constraining of internal and cell coordinates can also be employed in GULP calculations. However, the most efficient minimisers are based on the Newton Raphson method, in which the hessian or some approximation is used. The minimization search direction,  $x$ , is then given by:

$$x = -H^{-1}g \quad (4.60)$$

where  $H$  is the Hessian matrix and  $g$  is the corresponding gradient vector. The Hessian is explicitly recalculated when either the energy drops by more than a certain criterion in one step or the angle between the gradient and search vectors becomes too large. At each cycle, a line search is performed to obtain the optimum step length along the search vector. For example, the default minimiser in the GULP code employs the exact second-derivative matrix, calculated analytically, to initialize the Hessian for the minimisation variables and then subsequently updates it using the Broyden-Fletcher-Goldfarb-Shanno (BFGS) algorithms or the Davidon-Fletcher-Powell (DFP).<sup>[86]</sup> In addition, the Rational Function Optimiser (RFO) has been developed to deal with particularly soft modes in the Hessian.<sup>[87]</sup> The use of RFO can lead to rapid convergence in cases where the default minimiser fails. When running very large systems the conjugate gradients approach is used instead of a Hessian based technique as the memory requirements for storing even a lower half triangular second derivative matrix become prohibitive and matrix operations start to dominate the computational expense of the calculations.<sup>[18]</sup>

In a similar way to GULP, the program MARVIN allows a combination of minimization techniques as well. Each minimisation technique is applicable to specific problem types. Other than the hybrid Newton approach realized by the Broyden-Fletcher-Goldfarb-Shanno algorithm, MARVIN also employ the downhill Simplex method and conjugate gradient method.

The simplest downhill Simplex method which requires only function evaluations, not derivatives, is a technique for non-linear optimization. It is very inefficient when the system is near a minimum but is efficient far away from a minimum, a common occurrence at the start of minimisations when molecules and ions are being docked onto a surface. The details of this method are discussed elsewhere in Ref. [88]



#### 4.4.4 Conjugate Gradient

The conjugate gradient method requires both the evaluation of the function and its gradient. The method uses conjugate gradients instead of the local gradient for going down hill. In the case that the potential energy surface has a long, narrow shaped valley the minimum is reached in fewer steps than using the steepest descent method. It also applies line searches to get to the minimum, but information from successive searches is not thrown away as it is for the steepest descent minimization. The data are stored and used to shape the rest of the minimization. This algorithm requires more time but it is more efficient.

In the conjugate gradient method, the first step is the same as in the steepest descent algorithm, but the direction of successive displacements are not necessarily perpendicular to the previous gradient. At each iteration, the new search direction is obtained by incorporating information from the search direction and the gradient in the previous step. It can be written as:

$$R^{m+1} = R^m + b^m S^m \quad (4.61)$$

where the search vector is now the gradient plus a certain contribution from the previous search direction:

$$S^m = F(R^m) + \gamma^m S^{m-1} \quad (4.62)$$

and the scalar coefficient  $\gamma^m$  controlling that contribution is calculated as

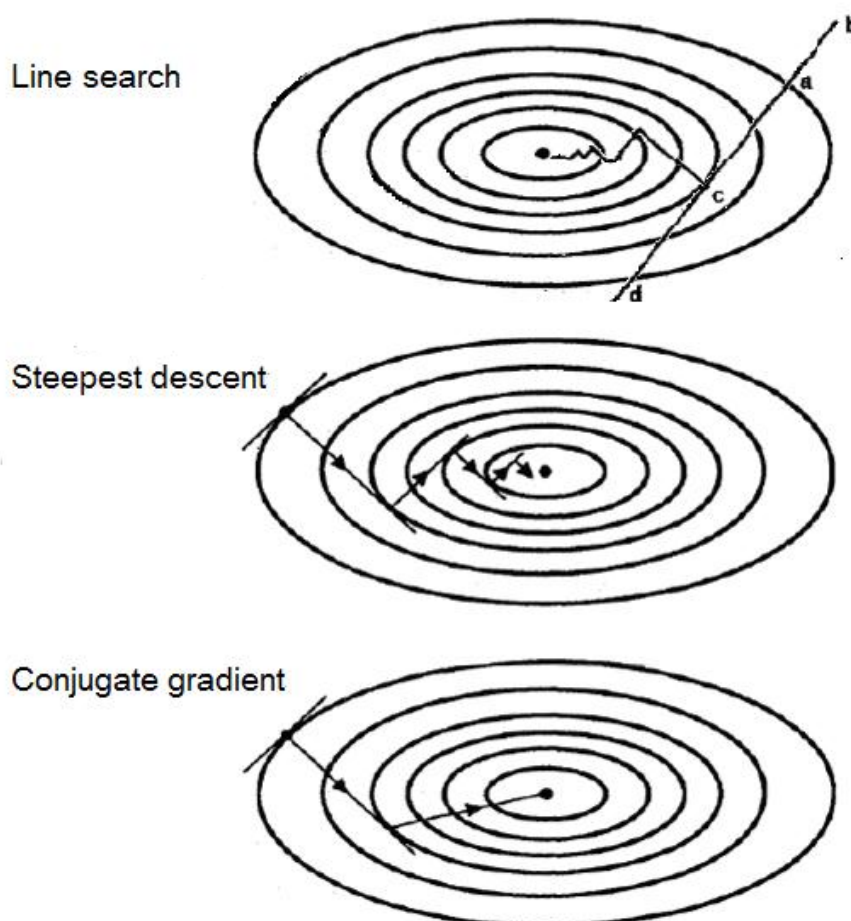
$$\gamma^m = \frac{F(R^m) \cdot F(R^m)}{F(R^{m-1}) \cdot F(R^{m-1})} \quad (4.63)$$

and  $\gamma^1 = 0$ .<sup>[89]</sup> It has been proved that by choosing the search directions in this way, they are optimally independent (or *conjugate*) from each other, which means that for a quadratic function of  $M$  variables the minimum will be reached in  $M$  steps. The number of iterations needed to reach the minimum decreases substantially in comparison with the steepest descent method. The conjugate gradient method, for example, only needs two steps to converge to the minimum in the quadratic function of two variables shown in **Figure 4.11**. This algorithm is very efficient at moderate to close distances from a minimum but has slow convergence when very close to an



energy minimum.

**Figure 4.11** Schematic illustration of the line search, steepest-descent and the conjugate-gradient methods. (Reproduced from Ref. [65])



The conjugate gradient method is also employed in the VASP calculations of Chapters 7 and 8. In the VASP code, the line minimisation at each iteration is performed in several steps: (i) First a trial step into the search direction (scaled gradients) is made, with the length of the trial step controlled by a user-defined parameter, and the energy and the forces are recalculated. (ii) The approximate minimum of the total energy is calculated from a cubic (or quadratic) interpolation taking into account the change of the total energy and the change of the forces. Then a corrector step to the approximate minimum is performed. (iii) After the corrector step the forces and energy are recalculated and it is checked whether the forces contain a significant component parallel to the previous search direction. If this is the case, the line minimization is improved by further corrector steps.



## 4.5 Codes and Computers

Three computer codes are employed for the modeling studies in this thesis. A brief introduction to these codes is given as below.

The interatomic potential simulation codes GULP (General Utility Lattice Program) is a computation program designed by Gale *et al.*<sup>[18]</sup> to perform material simulations of three dimensional solids using boundary conditions. The focus of the code is on analytical solutions, through the use of lattice dynamics, rather than on molecular dynamics. A variety of force fields can be used within GULP spanning the shell model for ionic materials, molecular mechanics for organic systems, the embedded atom model for metals and the reactive REBO potential for hydrocarbons.

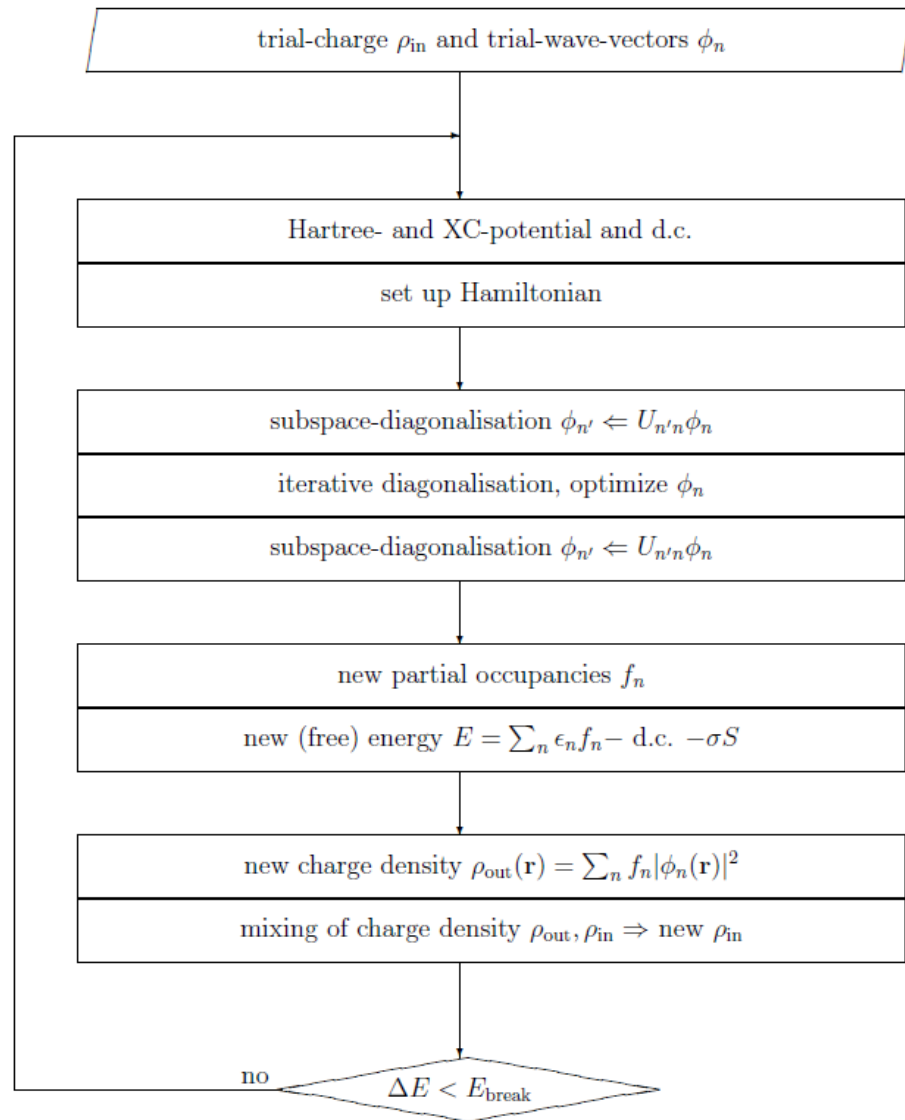
The MARVIN (Minimisation and Relaxations of Vacancies and Interstitials of Neutral Surface) code is developed to study two-dimensional surfaces and interfaces by Gay *et al.*<sup>[3]</sup> As in GULP, the foundation of MARVIN is the Ewald sum. MARVIN is a more flexible program that allows not only the modeling of simple inorganic surfaces and interfaces but also the surface of molecular and molecular ionic systems and the docking of molecules and ions.

The GULP and MARVIN calculations for the bulk defect and surface properties of pure and yttria doped zirconia in this thesis are carried out on the UCL computer clusters Bragg and Faraday.

The VASP package (Vienna Ab Initio Simulation Program) is a density functional code developed by Georg Kresse and Jürgen Furthmüller to perform *ab initio* quantum mechanical molecular dynamics (MD) using pseudopotentials and a plane wave basis set. The approach implemented in VASP is based on a finite-temperature local-density approximation (with the free energy as a variational quantity) and the electronic ground-state is determined by a conjugate gradient algorithm.<sup>[90]</sup> Forces and the full stress tensor can be calculated with VASP and used to relax atoms into their instantaneous ground state. An exact evaluation of the instantaneous electronic ground state at each MD step is obtained via an efficient matrix diagonalization scheme and Pulay mixing.<sup>[91,92]</sup> These techniques avoid all problems occurring in the original



Car-Parrinello method which is based on the simultaneous integration of electronic and ionic equations of motion. The interaction between ions and electrons is described using ultrasoft Vanderbilt pseudopotentials (USPP) or the projector augmented wave method (PAW). Sampling in reciprocal space is carried out at points of Monkhorst-Pack special grids. <sup>[93]</sup> **Figure 4.12** shows a brief flow chart of a single self-consistency cycle in VASP. After determination of the electronic ground-state for a given ionic configuration, the forces on the atoms can be evaluated, leading to the absolute energetic minimum of a system. Thereby it is possible to constrain each cartesian direction of every single ion individually.



**Figure 4.12:** Typical flow-chart of VASP for the selfconsistent determination of the Kohn-Sham ground-state. (From the VASP Guide <sup>[1]\*</sup>) The abbreviation d.c. states for double-counting corrections



## References

- 
- [1] C. R.A. Catlow, R. Bell, F. Cora, S. A. French, B. Slater and A. Sokol, *Annu. Rep. Prog. Chem., Sect. A*, **101**, 513, 2005.
- [2] J. D. Gale, *J. Chem. Soc., Faraday Trans.* **93** (4), 629, 1997.
- [3] D. H. Gay and A.L. Rohl, *J. Chem. Soc. Faraday Trans.* **91**(5), 925, 1995.
- [4] G. Kresse and J. Hafner, *Phys. Rev. B* **47**, 558-561, 1993; G. Kresse and J. Hafner, *Phys. Rev. B* **49**, 14251, 1994a; G. Kresse and J. Furthmüller, *Comput. Mater. Sci.* **6**, 15-50, 1996; and J. Furthmüller, *Phys. Rev. B* **54**, 11169-11186 (1996); Kresse and Furthmüller, *Mater. Sci.* **6**, 15-50, 1996.
- [5] C. R. A. Catlow, E. Kotomin "Computational Materials Science"; IOS Press, 2001.
- [6] F. London, *Z. Phys.* **63**, 245, 1930.
- [7] P. P. Ewald, *Ann. Phys.* **64**, 253, 1921.
- [8] C. Kittel, "Introduction to Solid State Physics", 7th Ed, John Wiley & Sons, Inc., 1996.
- [9] T. L. Hill, *J. Chem. Phys.* **16**, 399, 1948.
- [10] M. S. Khan and D. R. Bates, *J. Mater. Chem.*, **8**(10), 2299, 1998
- [11] B. G. Dick and A. W. Overhauser. "Theory of the dielectric constant of alkali halide crystals." *Phys. Rev.* **112**, 90, 1958.
- [12] C. R. A. Catlow, A. K. Cheetham, P. Day, "Solid State Chemistry: Techniques", Oxford University Press, 1986.
- [13] G. V. Lewis, C. R. A. Catlow, *J. Phys. C Solid state Phys.* **18**, 1149, 1985.
- [14] C. R. A. Catlow, C.M.Freeman, M. S. Islam, R. Jackson, M. Leslie; S. M. Tomlinson. *Phil. Mag. A*. **58**, 123, 1988
- [15] A. Dwivedi and A. N. Cormack, *Philos. Mag. A*, **61**, 1, 1990.
- [16] C. R. A. Catlow, *Proc. R. Soc. A*, **353**, 533, 1977; G. V. Lewis and C. R. A. Catlow, *J. Phys. C*, **18**, 1149, 1985.
- [17] N. Mott, M. Littleton. *Trans. Faraday Soc.* **34**, 485, 1938.
- [18] J. D. Gale and A. L. Rohl, *Molecular Simulation*, 291, **29** (5), 2003
- [19] W. Krauth, "Statistical mechanics: algorithms and computations", Oxford University Press, 2006.
- [20] T. Esaka, H. Sakguchi, S. Kobayashi, *Sol. St. Ionics* **166**, 351, 2004.



- 
- [21] D. C. Sayle, C. R. A. Catlow, J. H. Harding, M. J. F. Healy, S. A. Maicananu, S. C. Parker, B. Slater and G. W. Watson *J. Mater. Chem.*, **10**, 1315, 2000
- [22] S. C. Parker, E. T. Kelsey, P. M. Oliver and James O. Titiloye *Faraday Discuss.*, **95**, 75, 1993.
- [23] P. W. Tasker, E. A. Colbourn and W. C. Mackrodt, *J. Am. Ceram. Soc.*, **68**, 74, 1985.
- [24] E. Schrödinger, *Ann. d. Physik* **79**, 361, 1926.
- [25] M. Born, J. R. Oppenheimer, *Ann. d. Physik* **84**, 457, 1927
- [26] J. Kohanoff and N. I. Gidopoulos, *"Handbook of Molecular Physics and Quantum Chemistry"*, John Wiley & Sons, Ltd, Chichester, 2003
- [27] D. R. Hartree, *Proc. Cambridge. Philos. Soc.*, **24**, 89, 1928.
- [28] V. Fock, *Z. Phys.*, **61**, 126, 1930.
- [29] J. C. Slater, *Phys. Rev.* **35**, 210, 1930.
- [30] F. J. Dyson and A. Lenard, *J. Math. Phys.*, **8**, 423, 1967; *J. Math. Phys.*, **9**, 698, 1968.
- [31] J. M. D. Tason, J. L. G., Fierro, L. G. Tejuca, *Phys. Chem.* **36**, 237, 1989.
- [32] K. Tabara, Y. Hirano, S. Suzuki, *Appl. Catal. A*, **170**, 245, 1998.
- [33] N. H. March, *"Theory of the Inhomogeneous Electron Gas"*, Plenum Publishing, New York, 1983.
- [34] L. H. Thomas, *Proc. Cambridge. Philos. Soc.* **23**, 1927.
- [35] E. Fermi, *Z. Phys.* **48**, 73, 1928.
- [36] P. A. M. Dirac, *Proc. Camb. Phil. Soc.*, **26**, 376, 1930. See also P. Gombás, *"Die statistische Theorie des Atoms und ihre Anwendungen"*, Springer, Wien, 1949.
- [37] P. Hohenberg, and W. Kohn, *Phys. Rev. B*, **136**, 864, 1964.
- [38] M. Levy, *Proc. Nati. Acad. Sc. USA* **76(12)**, 6062, 1979.
- [39] W. Kohn, and L. J. Sham, *Phys. Rev. A* **140**, 1133, 1965.
- [40] J. P. Perdew, and A. Zunger, *Phys. Rev. B* **23**, 5048, 1981.
- [41] D. M. Ceperley and B. J. Alder, *Phys. Rev. Lett.* **45**, 566, 1980.
- [42] S. H. Vosko, L. Wilk, and M. Nussair, *Can. J. Phys.* **58**, 1200, 1980.
- [43] W. Koch and M. C. Holthausen, *"A Chemist's Guide to Density Functional Theory"*, Wiley-Vch, Weinheim, Germany, second edition edition, 2000.
- [44] J. P. Perdew, J. A. Chevary, S. H. Vosko, K. A. Jackson, M. R. Pederson, D. J. Singh and C. Fiolhais, *Phys. Rev. B* **46**, 6671, 1992.



- 
- [45] J. P. Perdew, K. Burke and M. Ernzerhof, *Phys. Rev. Lett.* **77**, 3865, 1996.
- [46] A. D. Becke, *Phys. Rev. A* **38**, 3098, 1988.
- [47] J. P. Perdew and Y. Wang, *Phys. Rev. B* **45**, 13244, 1992; J. P. Perdew, J. A. Chevary, S. H. Vosko, K. A. Jackson, M. R. Pederson, D. J. Singh, and C. Fiolhais, *Phys. Rev. B* **46**, 6671, 1992.
- [48] K. Burke, J. P. Perdew and Y. Wang, *"Electronic Density Functional Theory: Recent Progress and New Directions"*, edited by D. Dobson, G. Vignale and M. P. Das. New York, Plenum, 1997.
- [49] K. Burke, J. P. Perdew and M. Levy, *"Modern Density Functional Theory: A Tool for Chemistry"*, edited by J. M. Seminario and P. Politzer. Amsterdam, Elsevier, 1995.
- [50] A. J. Cohen, P. Mori-Sánchez, W. Yang, *Science* **321**, 792, 2008.
- [51] P. Mori-Sánchez, A. J. Cohen, W. Yang, *Phys. Rev. Lett.* **100**, 146401, 2008
- [52] S.-H. Ke, H. U. Baranger, W. Yang, *J. Chem. Phys.* **126**, 201102, 2007.
- [53] A. J. Cohen, P. Mori-Sánchez, W. Yang, *J. Chem. Phys.* **129**(12), 121104, 2008.
- [54] Becke, A.D. *J. Chem. Phys.*, **107**, 8554 (1997)
- [55] F. Bloch, *Z. Phys.* **52**, 555, 1928.
- [56] L. P. Bouckaert, R. Smoluchowski and E. Wigner, *Phys. Rev.* **50**, 58, 1936.
- [57] H. J. Monkhorst, and J. D. Pack, *Phys. Rev. B* **13**, 5188, 1976.
- [58] J. C. Philips, L. Kleinman, *Phys. Rev.* **136**, 287, 1959.
- [59] M. L. Cohen and V. Heine, *"Pseudopotential Theory of Cohesion and Structure"*, Solid State Physics, **24**, Academic Press, New York, 1970.
- [60] M. T. Yin and M. L. Cohen, *Phys. Rev. B* **25**, 7403, 1982.
- [61] D. Vanderbilt. *Phys. Rev. B* **41**, 7892, 1990.
- [62] M. C. Payne, M. P. Teter, D. C. Allan, T. A. Arias, and J. D. Joannopoulos, *Rev. Mod. Phys.* **64**, 1045, 1992.
- [63] D. R. Hamann, M. Schluter and C. Chiang, *Phys. Rev. Lett.* **43**, 1494, 1979.
- [64] G. Kresse, and J. Hafner, *J. Physics-Condensed Matter.* **6**, 8245, 1994.
- [65] P. E. Blöchl, *Phys. Rev. B* **50**, 17953, 1994.
- [66] O. K. Andersen, *Phys. Rev. B* **12**, 3060, 1975.
- [67] S. Cottenier, V. Vanhoof, D. Torumba, V. Bellini, M. Āakmak and M. Rots, *Hyperfine Interactions* **158**, 9, 2004.
- [68] P. E. Blöchl, *J. Chem. Phys.* **103**, 7422, 1995.



- 
- [69] G. Kresse, and D. Joubert, *Phys. Rev. B* **59**, 1758, 1999.
- [70] R.S. Mulliken and P. Politzer, *J. Chem. Phys.*, 55,5135 (1971); D.D. Grier and A. Streitwieser Jr., *J. Am. Chem. SOC.*, 104,3556 (1982).
- [71] P.-O. Löwdin, *Adv. Quantum. Chem.* **5**, 185, 1970; P.-O. Löwdin, *Phys. Rev.* **97**, 1474, 1955.
- [72] A. E. Reed, R. B. Weinstock and F.A. Weinhold, *J. Chern. Phys.* **83**,735, 1985; A. E. Reed, F. Weinhold and L.A. Curtiss, *Chem. Rev.* **88**, 899, 1988.
- [73] G. Henkelman, A. Arnaldsson and H. Jónsson, *Comput. Mater. Sci.* **36**, 254, 2006.
- [74] K. B. Wiberg and P. R. Rablen, *J. Comput. Chem.* **14**(12), 1504, 1993.
- [75] F. L. Hirshfeld, *Theor. Chim. Acta.* **44**, 129, 1977; J. P. Ritchie, *J. Am. Chem. Soc.* **107**, 1829, 1985; J. P. Ritchie and S. M. Bachrach, *J. Comp. Chem.* **8**, 499, 1987.
- [76] R. F. W. Bader, *"Atoms in Molecules, A Quantum Theory"*, Clarendon Press: Oxford, 1993; R. F. W. Bader, *Acc. Chem. Res.* **18**, 9, 1985.
- [77] B. B. Stefanov and J. Cioslowski, *J. Comput. Chem.* **16**, 1394, 1995.
- [78] B. P. Uberuaga, E. R. Batista and H. Jónsson, *J. Chem. Phys.* **111**, 10664, 1999.
- [79] E. Sanville, S. D. Kenny, R. Smith and G. Henkelman, *J. Comp. Chem.* **28**, 899, 2007.
- [80] W. Tang, E. Sanville, and G. Henkelman, *J. Phys.: Condens. Matter.* **21**, 084204, 2009.
- [81] P. E. Gill, W. Murray and M. H. Wright, *"Practical Optimization"*, London, Adademic, 1981.
- [82] B. J. Garrison and D. Srivastava *Annu. Rev. Phys. Chem.* **46**, 373, 1995.
- [83] Cerius2 *"Forcefield-Based Simulations"*. Molecular Simualtion Inc. **2000**.
- [84] F. Jensen, *"Introduction to Computational Chemistry"*, Johnm Wiley & Sons, 2002.
- [85] R. Fletcher *"Practical Methods of Optimisation"*; Wiley, New York, 1980.
- [86] W. H. Press, S. A. Teukolsky, W. T. Vetterling and B. P. Flannery, *"Numerical Recipes"*, Cambridge University Press, Cambridge, 2nd edn., 1992.
- [87] A. Banerjee, N. Adams, J. Simons and R. Shepard, *J. Phys. Chem.*, **89**, 52,1985.
- [88] S. A. Teukolsky, W. T. Vetterling, B. P. Flannery, William H. Press. *Numerical Recipes in C++: The Art of Scientific Computing*, Pearson Education, 1992.
- [89] R. Fletcher and C. Reeves, *Comput. J.* **7**, 81, 1964.
- [90] P. M. Teter, M. C. Payne, and D. C. Allan, *Phys. Rev. B* **40**, 12255, 1989.



- [91] G. Kresse and J. Furthmüller, *Phys. Rev. B* **54**, 11169, 1996.  
[92] D. M. Wood and A. Zunger, *J. Phys. A: Gen. Phys.* **18**, 1343, 1985.  
[93] H. J. Monkhorst and J. D. Pack, *Phys. Rev. B* **13**, 5188, 1976.

### **\* Internet Resources**

- [1] <http://cms.mpi.univie.ac.at/vasp/vasp/vasp.html>



## Chapter 5 Interatomic Potential Studies of YSZ

*We do not expect an accurate description of chemical binding.*

*--W. Kohn and L. J. Shan*

Since pure  $\text{ZrO}_2$  displays three polymorphs at atmospheric pressure: monoclinic (m-), tetragonal (t-), and cubic (c-) with increasing temperature, phase stabilisation of  $\text{ZrO}_2$  is important in high temperature applications where cycling may occur through the m-t transition during material preparation or use. For example in catalytic steam reforming of methane, the substantial change in unit cell volume leads to mechanical failure of catalyst pellets. As discussed in Chapter 2, stabilization of t- or c- $\text{ZrO}_2$  down to room temperature can be achieved in a number of ways but most commonly by doping with  $\text{Y}^{3+}$ .<sup>[1-2]</sup> In addition to stabilising  $\text{ZrO}_2$  in its cubic form, the created vacancies increase oxygen anion mobility in YSZ and are thought to play a crucial role in high temperature catalytic processes such as direct partial oxidation of methane or steam reforming.

There is extensive experimental data on bulk Y doped  $\text{ZrO}_2$  and a number of surfaces studies have indicated a degree of Y surface segregation. However, the nature of defect ordering, the dispersion of yttrium and compensating oxygen vacancies which defines the active sites in high temperature oxidation catalysis are still not well understood theoretically. To this end, atomistic calculations of Y doped c- $\text{ZrO}_2$  have been carried out in more detail in this thesis, to elucidate the formation, location and orientation of the compensating defect clusters as a function of Y concentration. In this chapter, atomistic interatomic potential based methods are used as they allow us to exploit a wide range of options in terms of concentration and dispersion of the defects. Besides the surface studies, bulk calculation as a function of Y concentration have been performed with particular reference to the phase behaviour of 8-10 mol%



Y<sub>2</sub>O<sub>3</sub> doped ZrO<sub>2</sub>, since material in this region is of considerable technological interest because of its superior mechanical properties in relation to catalytic pellet performance. [3]

## 5.1 Bulk Structures of Pure Zirconia

In this section, the validity of the atomistic potential model reported by Dwivedi and Cormack [4] was first assessed by simulating the three low pressure phases of zirconia at zero temperature. The cubic fluorite ZrO<sub>2</sub> structure was well reproduced by the GULP code. The lattice parameters obtained (**Table 5.1**) show excellent agreement with the experimental results and electronic structure calculations; all the differences are less than 1%. [4-8]

**Table 5.1** Calculated and observed structural parameters of cubic ZrO<sub>2</sub> (a [4]; b [5]; c [6])

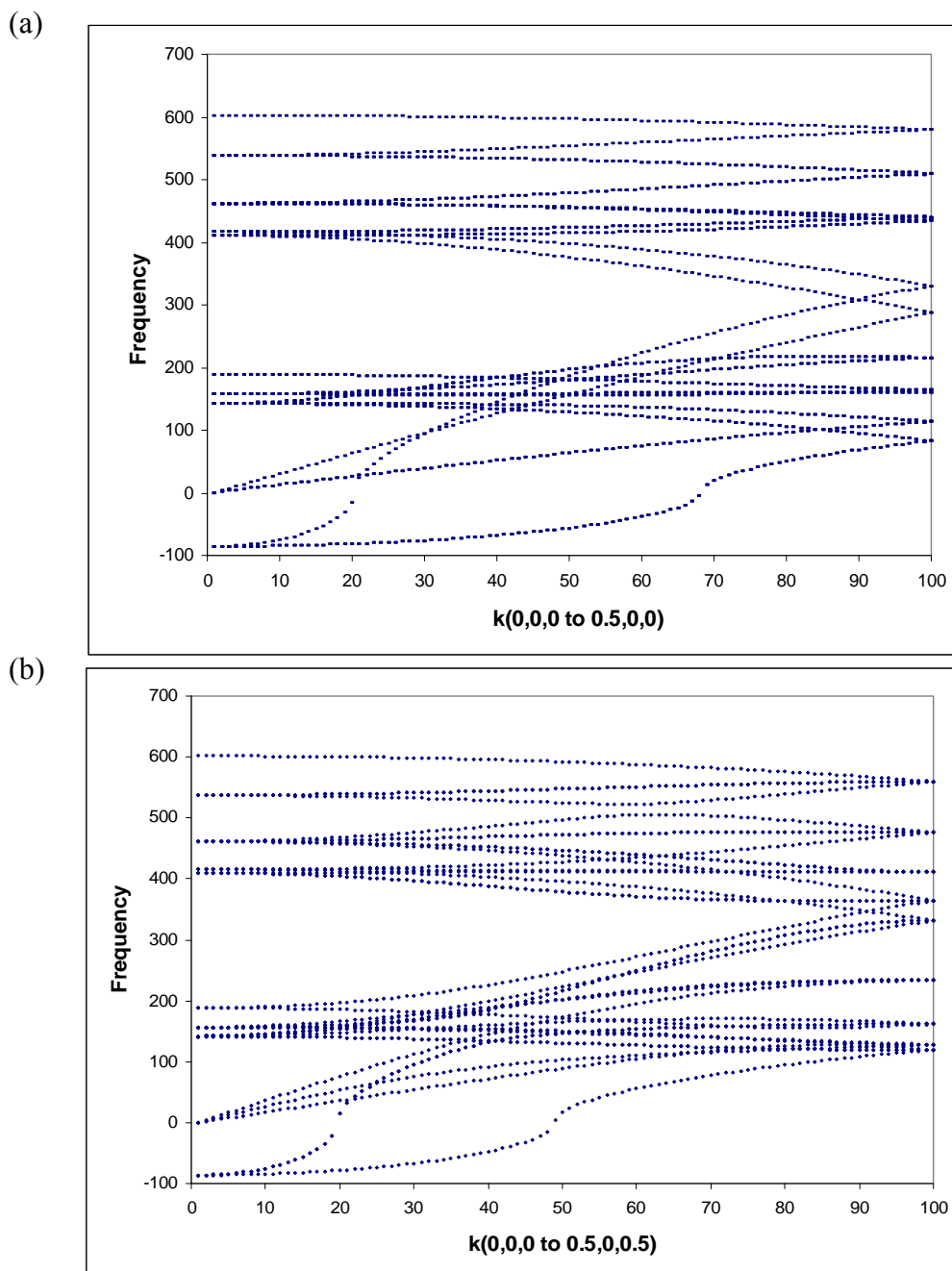
Parameters	$r$ Å (expt.)	$r$ Å (calc.)	$\Delta$ Å	$\Delta\%$
Zr ..... O <sub>I</sub>	2.204 <sup>a</sup>	2.198	-0.006	-0.27
Zr ..... O <sub>II</sub>	2.204 <sup>a</sup>	2.198	-0.006	-0.27
O <sub>I</sub> ..... O <sub>II</sub>	2.563 <sup>a</sup>	2.538	-0.025	-0.97
Zr ..... Zr	3.589 <sup>b</sup>	3.589	—	—
a=b=c	5.070 <sup>c</sup>	5.076	0.006	0.11
$\alpha = \beta = \gamma$	90°	90°	—	—
Lattice Energy Per ZrO <sub>2</sub> (eV)		-109.76		

In order to check whether these structures achieved the true energy minimum, dispersion curves have been calculated using the GULP code from the  $k$  point (0, 0, 0) to  $k$  points: (0.5, 0.0, 0.0); (0.0, 0.5, 0.0); (0.0, 0.0, 0.5); (0.0, 0.5, 0.5); (0.5, 0.5, 0.0); (0.5, 0.0, 0.5) in reciprocal space. **Figure 5.1** depicts phonon dispersion curves obtained for the cubic fluorite structure. Since cubic ZrO<sub>2</sub> has *fcc* symmetry, the dispersion curves derived from six directions are sufficient to assess the stability of the structure. The frequency data all start from negative numbers and gradually go



positive. The negative frequencies presented in the phonon dispersion curves are due to the instability of c-ZrO<sub>2</sub> as discussed in Sections 1.2 and 3.1.5.<sup>[7]</sup> To test the effect of allowing more degrees of freedom in the system, further simulations were run by using much larger supercells. Unsurprisingly, the negative frequencies remained in the cubic array supercell calculations.

**Figure 5.1** Dispersion curves for the 1x1x1 unit cell of c-ZrO<sub>2</sub>. For each curve, 100 points were taken along the direction from initial k points to final k points in reciprocal space. Directions along (a)  $k(0, 0, 0$  to  $0.5, 0, 0)$  and (b)  $k(0, 0, 0$  to  $0.5, 0, 0)$





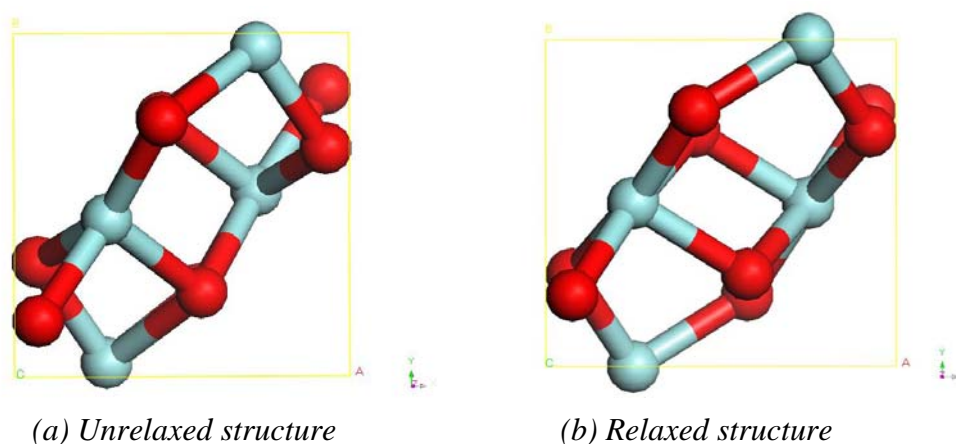
For the tetragonal structure  $\text{ZrO}_2$ , the phonon frequencies start from essentially zero ( $-0.000009 \sim 0.000004$ ) at the  $\Gamma$  point, and are positive throughout the Brillouin Zone, demonstrating the stability of the structure. **Table 5.2** compares the observed and calculated structure parameters for the tetragonal phase. The calculated parameters are in good over all agreement with experiment data <sup>[8]</sup> and similar to the results of previous Hartree-Fock studies by Orlando *et al.* <sup>[9]</sup>

**Table 5.2** Calculated and observed structure parameters of tetragonal  $\text{ZrO}_2$ . (a [8]; b [9])

Parameters	$r$ Å (expt.)	$r$ Å (calc.)	$\Delta$ Å	$\Delta\%$
Zr ..... O <sub>I</sub>	2.065	2.049	-0.016	-0.77
Zr ..... O <sub>II</sub>	2.463	2.416	-0.047	-1.91
O <sub>I</sub> ..... O <sub>II</sub>	2.635	2.663	0.028	1.06
Zr ..... Zr	3.683	3.639	-0.044	-1.19
a	3.640 <sup>a</sup>	3.588	-0.052	-1.43
c	5.270 <sup>a</sup>	5.217	-0.053	-1.01
c/a	1.448 <sup>a</sup>	1.454	0.006	
d <sub>z</sub>	0.065 <sup>b</sup>	0.060	0.005	
$\alpha = \beta = \gamma$	90°	90°	—	—
Lattice Energy		-109.78		
Per $\text{ZrO}_2$ (eV)				

Based on the atomic coordinates derived from the *ab initio* study by Stapper *et al.*, <sup>[10]</sup> simulation of monoclinic  $\text{ZrO}_2$  was attempted using the GULP code. However, an energetically more favorable orthorhombic  $\alpha\text{-PbO}_2$  structure was predicted after relaxation (**Figure 5.2-b** and **Table 5.3**) as suggested by the classical potential calculations of Stefanovich, Shluger, and Catlow. <sup>[7]</sup> And no negative frequency is indicated by the calculations of phonon dispersion for the predicted orthorhombic structure.



**Figure 5.2** Relaxation of monoclinic  $\text{ZrO}_2$ **Table 5.3** Calculated and observed structure parameters of monoclinic  $\text{ZrO}_2$ . (a [10])

Parameters	$r \text{ \AA}$ (expt.)	$r \text{ \AA}$ (calc.)	$\Delta$	$\Delta\%$
<b>a</b>	5.150 <sup>a</sup>	4.778	-0.372	-7.1
<b>b/a</b>	1.012 <sup>a</sup>	1.044	0.032	4.0
<b>c/a</b>	1.032 <sup>a</sup>	1.163	0.131	4.9
<b><math>\alpha = \beta</math></b>	90°	90°	—	9.4
<b><math>\gamma</math></b>	99.23° <sup>a</sup>	-90.01°	9.22°	-9.3
<b>Lattice Energy</b>		-110.34		
<b>Per <math>\text{ZrO}_2</math> (eV)</b>				

In addition, the structure of yttria, which has a sesquioxide cubic lattice, has also been modelled. The lattice parameters ( $a=b=c=10.51 \text{ \AA}$ ) obtained are within 1% of the experimental data ( $10.60 \text{ \AA}$ )<sup>[11]</sup>. The largest deviation of atom positions is less than  $0.01 \text{ \AA}$  and no negative phonon frequency has been observed. The obtained C-type sesquioxide structure of  $\text{Y}_2\text{O}_3$  can be related to the fluorite structure of  $\text{ZrO}_2$  in such a way that, the oxygen anion are still surrounded tetrahedrally by four cations, but the eightfold coordination of Zr cations in fluorite structure is reduced to a lower 6-fold coordination of Y since the ion radius of yttrium is smaller. The Y cations situated at the centres of slightly deformed cubes, in which two of eight corners remain unoccupied. The lattice energy per  $\text{Y}_2\text{O}_3$  unit for the equilibrated structure was calculated as -135.39 eV and is employed in the subsequent calculation of solution energies in the YSZ system.

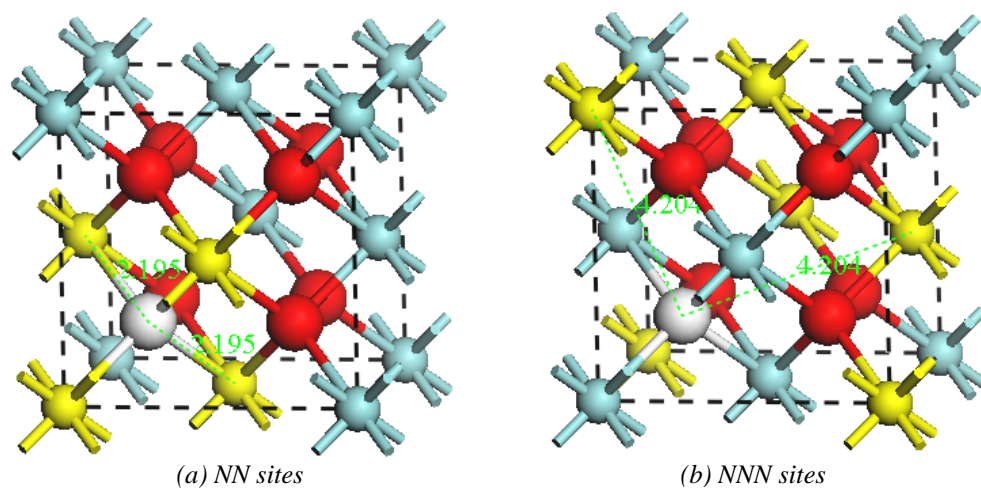


## 5.2 Yttrium Doped ZrO<sub>2</sub>

As discussed in Chapter 1, the instability of the cubic ZrO<sub>2</sub> at room temperature is due to its failure to satisfy the Pauling's Rule: Zr<sup>4+</sup> is too small to allow 8-fold coordination by oxygen in the fluorite structure and too large for octahedral 6 coordination in the rutile structure. By doping with a lower valence cation such as Y<sup>3+</sup>, cubic ZrO<sub>2</sub> can be stabilized. The mechanism is a combination of two effects: the creation of oxygen vacancies as in Eq. (5.1) serves firstly to reduce the average coordination number and secondly facilitates relaxation of the oxygen sub-lattice towards cubic symmetry.



For the Y-doped zirconia system, according to Eq. (5.1), two Y<sup>3+</sup> ions substitute for two Zr<sup>4+</sup> ions to create one oxygen vacancy. This pair of yttrium dopants together with the charge compensating oxygen vacancy is considered in these calculations as a bound defect cluster (Y-V-Y). Different configurations of the Y-V-Y defect cluster have been studied by locating the cation defects either in nearest-neighbour (NN) sites or next-nearest-neighbour (NNN) sites (2.2 Å and 4.2 Å, respectively) to the oxygen vacancy. These simple pair clusters showing NN and NNN sites configurations are illustrated in **Figure 5.3**.



**Figure 5.3** Schematic diagrams for the NN and NNN sites of yttrium with respect to the oxygen vacancy. (Zr ●; O ●; O vacancy ○; alternative sites for Y ● )

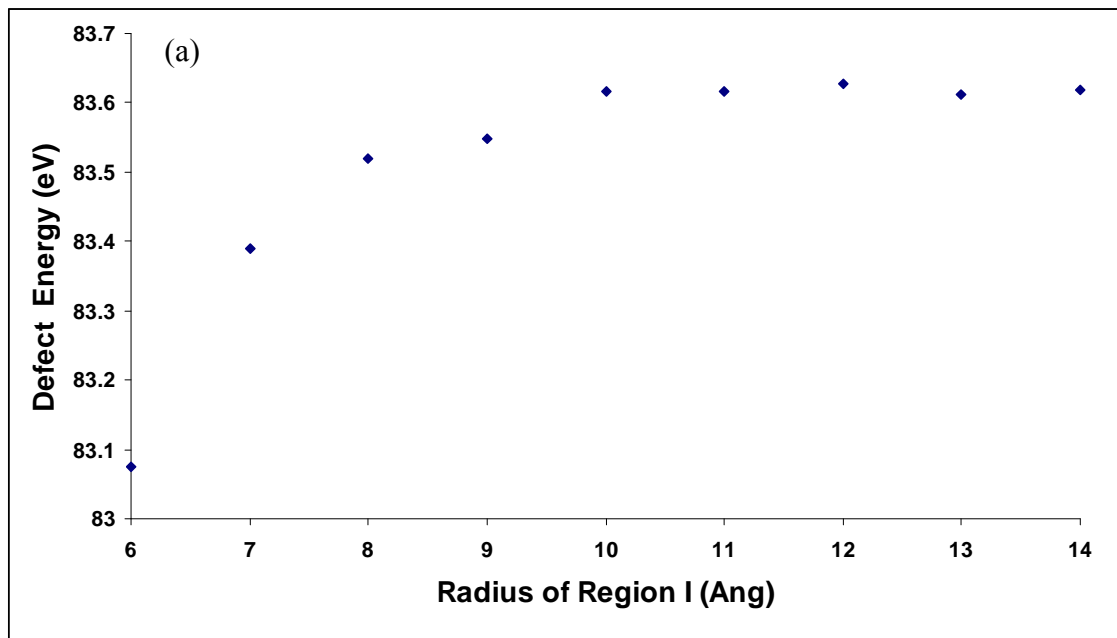


In the following Section 5.1, both Mott-Littleton and supercell simulations have been carried out on the defect configuration of the YSZ systems based on cubic  $\text{ZrO}_2$  structure.

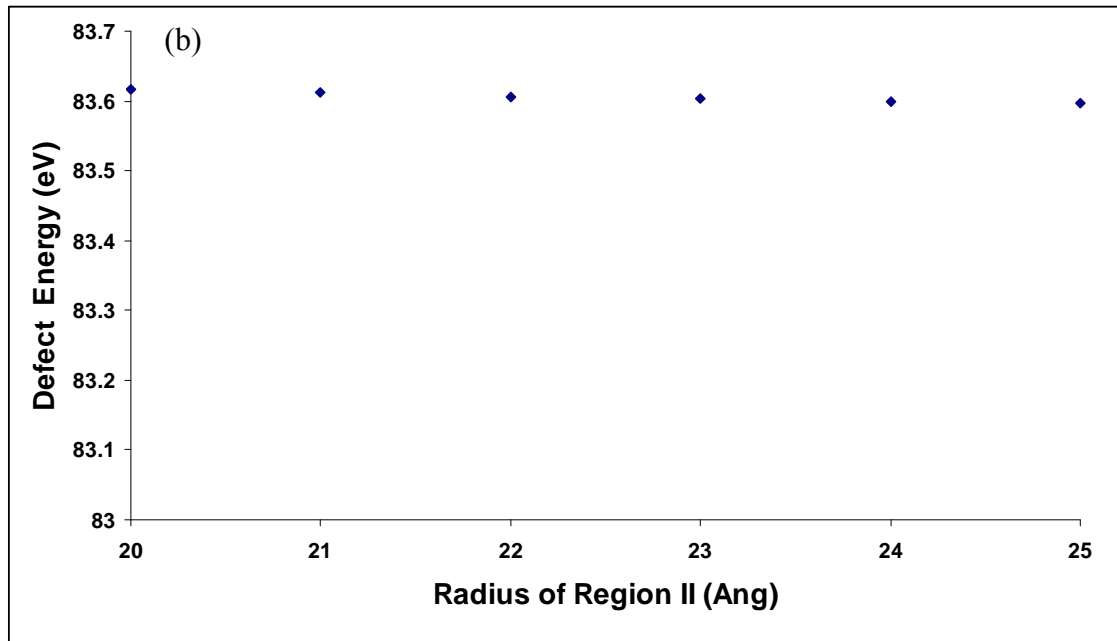
### 5.2.1 Defect Calculations using the Mott-Littleton Method

Calculations representing the infinite dilute case employing the Mott-Littleton approach are based on explicitly relaxing ions within an inner spherical region I surrounding the defect with polarization of the outer region II calculated via a quasi continuum approximation.<sup>[12]</sup> The sizes of region I = (10 Å) and region II = (20 Å) were determined from the convergence of the calculated energy, i.e. the lattice energy changes less than 0.01 eV on expansion. **Figure 5.4** shows the variation of defect energy  $E_{DEF}$  against the radius of region I and II.

**Figure 5.4** Plots of defect energy versus the radii of region I (a) and II (b) in Mott-Littleton calculations. In the defect cluster, two Y were substituted at the NN sites of the oxygen vacancy. (Ang= Å)







In this section, various cluster configurations have been considered in the Mott-Littleton calculations for the infinitely dilute system as presented in **Table 5.4**. The solution energy derived from the Born Haber cycle.

$$E_{sol} = \frac{1}{2} (2E[\text{ZrO}_2] + E_{DEF} - E[\text{Y}_2\text{O}_3]) \quad (5.2)$$

and the binding energy obtained has been estimated from Eq. 4.12 by comparison with the energy of isolated defects, i.e. the substitution of  $\text{Y}^{3+}$  and  $\text{O}^{2-}$  vacancy.

**Table 5.4** summarizes the results of the Mott-Littleton calculations. In particular, the NNN site yttrium-vacancy (Y-V) cluster which has a negative binding energy of -0.33 eV is favored by 0.40 eV with respect to the NN site (Y-V) cluster. The preference for yttrium to occupy the next-nearest-neighbor (NNN) site to the oxygen vacancy generally agrees with early reported experimental observations <sup>[13,14,15]</sup> as well as the previous interatomic study by Khan *et al.* <sup>[16]</sup> and *ab initio* calculations by Stapper *et al.* <sup>[10]</sup> However, for the charge neutral Y-V-Y cluster, the energetically favorable configuration can be identified here as two yttrium next to each other and both occupying the next-nearest neighbour sites to the oxygen vacancy. Such a configuration gives a solution energy of -0.58 eV per yttrium in contrast to the considerably more negative value of -3.1 eV suggested by Khan *et al.* <sup>[16]</sup> The contradiction with the reported solution energies may be due to different values being taken for the lattice energies of the solute; in our case we employ the energy for the cubic structure which



has been fully relaxed using the reported interatomic potentials. We consider our value to be more realistic since the figure from Khan's work would represent a strongly exothermic process.

**Table 5.4** Binding energies and solution energies derived from Mott-Littleton calculations.

Defect	Vo	Y	Y-Vo		Y-Vo-Y cluster					
Config.	Isolated defect		NN	NNN	NN	NNN		NN-NNN		
<b>d<sub>1</sub> (Å)</b>	14.78	34.81	2.195	4.204	2.195	4.204	4.204	2.195	2.195	2.195
<b>d<sub>2</sub> (Å)</b>					2.195	4.204	4.204	4.204	4.204	4.204
<b>d<sub>3</sub> (Å)</b>					3.585	3.585	8.016	3.585	5.07	6.209
<b>d<sub>3</sub><sup>rel</sup> (Å)</b>					3.608	3.608	7.980	3.543	5.118	6.276
<b>E<sub>DEF</sub> (eV)</b>			49.67	49.26	83.62	82.98	83.59	83.45	84.06	84.03
<b>E<sub>bind</sub> (eV) per Y</b>			0.07 (0.18 <sup>a</sup> (-0.10 <sup>b</sup> )	-0.33 (-0.26 <sup>a</sup> ) (-0.44 <sup>b</sup> )						
<b>E<sub>sol</sub> (eV) per Y</b>					-0.26	-0.58	-0.27	-0.34	-0.04	-0.05

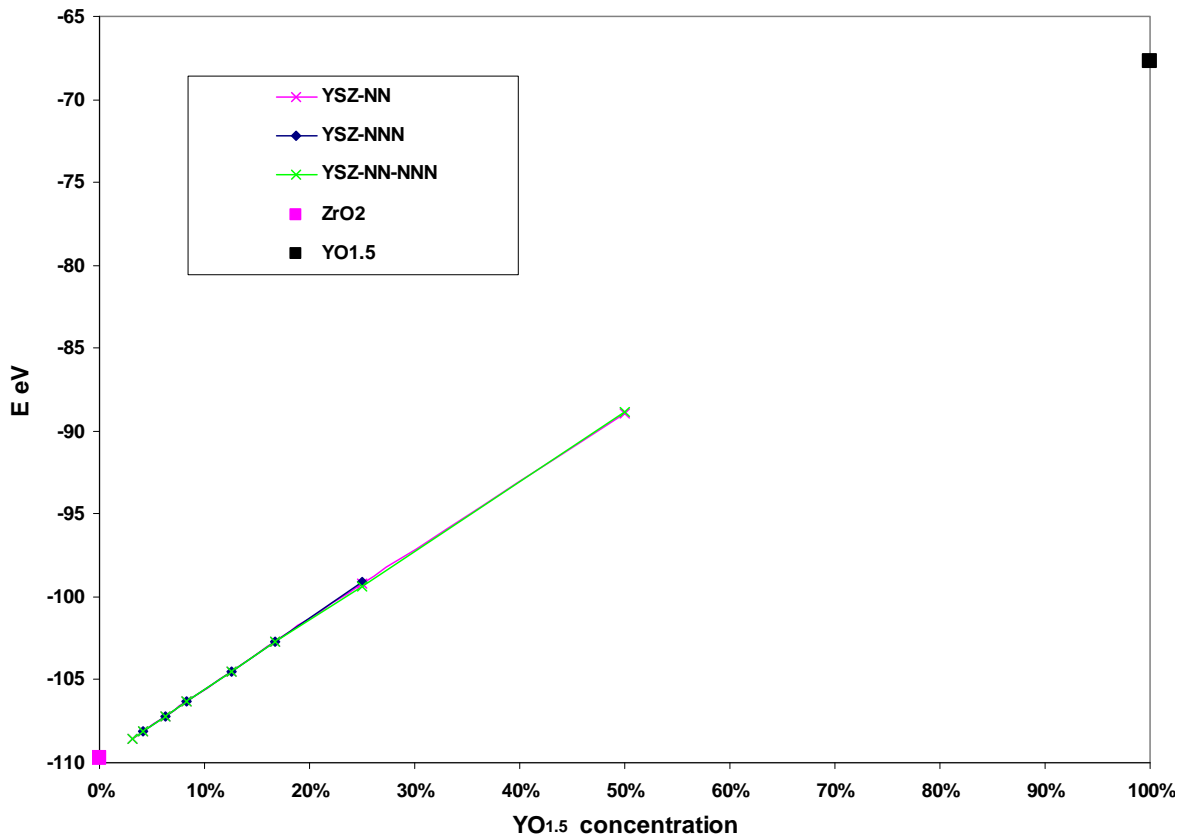
(d<sub>1</sub> and d<sub>2</sub> are the distances between yttrium ions and the center of oxygen vacancy (Y-V); d<sub>3</sub> and d<sub>3</sub><sup>rel</sup> are the distance of two yttrium ions (Y-Y) before and after relaxation in the various configurations of the defect cluster. a and b refer to the calculated binding energy from Ref. [16] and [10])

### 5.2.2 Defect Calculations using the Supercell Approach

In addition to the Mott-Littleton approach, the YSZ systems with varying Y concentrations were investigated by introducing one defect cluster to the cell and extending the unit cell size from a 1x1x1 (Y<sub>2</sub>Zr<sub>2</sub>O<sub>3</sub>, ~50%Y) to a 4x2x2 (Y<sub>2</sub>Zr<sub>62</sub>O<sub>127</sub>, ~3%Y) supercell. Studies of phonon dispersion curves show negative frequencies for the YSZ systems especially those with Y content less than 5% which corresponds experimentally to the monoclinic region in the Y<sub>2</sub>O<sub>3</sub>-ZrO<sub>2</sub> phase diagram.<sup>[17]</sup> **Figure 5.5** plots lattice energy as a function of YO<sub>1.5</sub> concentration. Three series of data are presented by choosing the value for the lowest energy configuration in each series.



According to **Figure 5.5**, there is a clear trend that the lattice energy linearly increases with yttrium doping level. Nevertheless, the lattice energies for YSZ systems with the same yttrium concentration are slightly influenced by the configuration of the defect cluster. The energy differences between NN and NNN configurations are within  $\pm 0.1$  eV per unit cell and there is no consistent pattern as to which configuration is most stable.



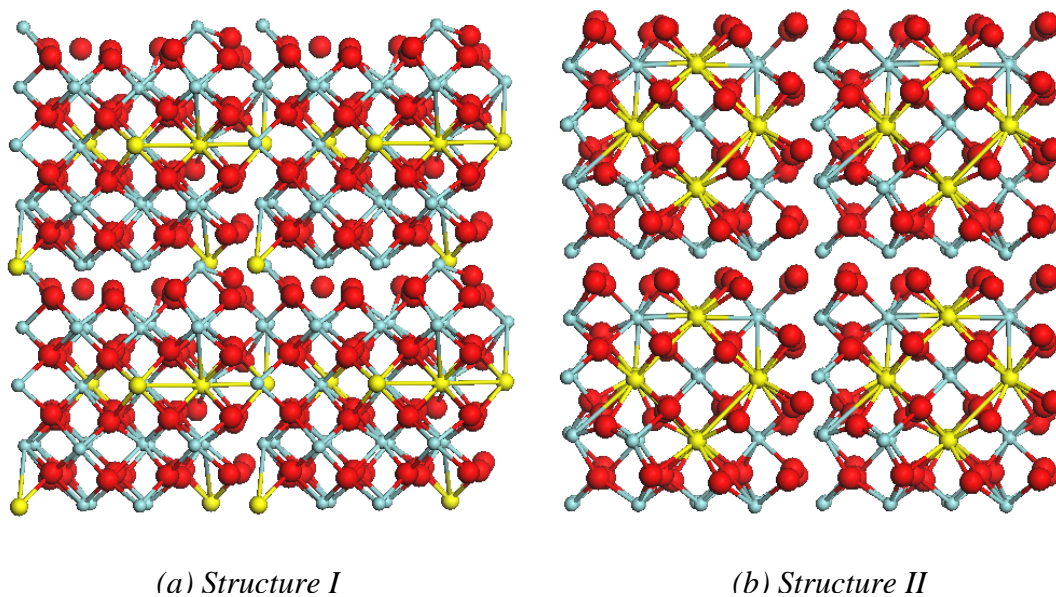
**Figure 5.5** Lattice energy as a function of yttrium concentration.

In order to investigate the experimentally claimed cubic-like structure of YSZ with 8-10 mol %  $Y_2O_3$  concentration,  $2 \times 2 \times 2$  supercells doped with 3 and 4  $Y-V-Y$  defect clusters have been employed equivalent to doping level of 18.75% and 25 % mole  $YO_{1.5}$ . After relaxation, two cubic-like YSZ structures were formed with the unit cell expanded 1%-2% compared to pure  $ZrO_2$  as shown in **Figure 5.6**. The stability of these cubic-like structures has been confirmed by examination of the phonon dispersion curves, which showed no negative frequencies. **Table 5.5** compares the two yttrium doped structures with pure cubic zirconia. Structure-I splits the 6 Y of  $Zr_{26}Y_6O_{61}$  into two groups of 4 and 2 yttrium atoms, and locates these two groups of



dopants alternately with a single  $\text{ZrO}_2$  slab between them. For structure-II, which containing 25 mol%  $\text{YO}_{1.5}$  (**Figure 3-b**), i.e. fully stabilized material, the oxygen vacancies are located in four corner sites of the supercell and yttrium occupies the NNN sites with respect to the oxygen vacancies.

**Figure 5.6** Schematic diagrams for the calculated YSZ cubic-like structures I (a) and II (b). (Zr ●; Y ●; O ●)



**Table 5.5** Comparisons of undoped  $\text{ZrO}_2$  and Y doped  $\text{ZrO}_2$  cubic like structures.

Parameter	2x2x2 $\text{Zr}_{32}\text{O}_{64}$	Structure I $\text{Zr}_{26}\text{Y}_6\text{O}_{61}$	% $\Delta$	Structure II $\text{Zr}_{24}\text{Y}_8\text{O}_{60}$	% $\Delta$
a (Å)	10.14	10.25	1.12	10.33	1.90
b (Å)	10.14	10.27	1.24	10.33	1.87
c (Å)	10.14	10.26	1.18	10.33	1.85
$\alpha$	90°	90.00°	—	90.00°	—
$\beta$	90°	90.04°	0.04	90.00°	—
$\gamma$	90°	90.00°	—	89.69°	-0.15
Lattice Energy Per Atom (eV)	-36.59	-33.98		-33.07	
$E_{\text{sol}}$ (eV) per Y		-0.33		0.15	





### 5.3 Pure Zirconia Surface

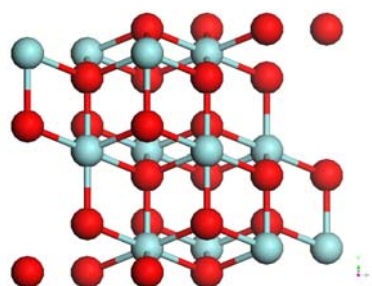
To examine the surface structure of cubic  $\text{ZrO}_2$ , the three low index surfaces (111), (110), and (100) together with the (310) surface were studied, since, according to Balducci *et al.*,<sup>[18]</sup> the (310) surface has a comparable surface energy to that of the (100) surface after relaxation. The simulations were carried out by the MARVIN code using a 1x1 surface repeat. Oxygen (O) terminated faces have been chosen for the calculations, since they were identified as being more stable than Zr or O-O terminations from the electronic structure calculations of Eichler *et al.*<sup>[19]</sup> The dipolar type III (100) surface was reconstructed by removing the dipole moment as in Section 4.1.6. In order to achieve insensitivity to region size, defined in the terms of a surface energy change of less than  $0.01 \text{ J/m}^2$  on expansion of either, the sizes for region I and II required for simulation of the (111) and (110) surfaces were determined to be 6 and 12 unit cells; for the reconstructed (100) surface, 6 and 9, and for the (310) surface 6 and 20 unit cells respectively. All the structures were then relaxed using the Broyden-Fletcher-Goldfarb-Shanno algorithm (BFGS).<sup>[20]</sup>

The calculated surface energies are presented in **Table 5.6**, which clearly predicts that the (111) and (110) surfaces are the most stable for cubic  $\text{ZrO}_2$  with the (111) surface being dominant since the energy is approximately  $1 \text{ J/m}^2$  lower. The reconstructed (100) surface after relaxation is more energetically favoured than before but still less stable than the (111) or (110) surfaces. For the (310) surface, following large displacement of atoms in the top layers (about  $4 \text{ \AA}$ ), the surface energy of the optimized structure becomes comparable to the (100) surface. Our study precisely reproduces the results reported by Balducci *et al.*<sup>[18]</sup> and the order of surface stability for c- $\text{ZrO}_2$ ,  $(111) > (110) > (100) > (310)$ , is in agreement with many previous theoretical studies.<sup>[18-19][21-22]</sup> A comparison of the constructed and relaxed surface structures is displayed in **Figure 5.7**.

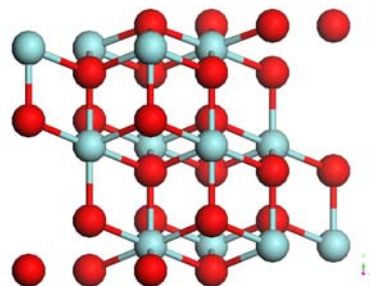


**Figure 5.7** Unrelaxed and relaxed structures of (111), (110), (100), and (310) surfaces. (Lattice sites are colour coded as Zr ; O )

(a) (111) surface

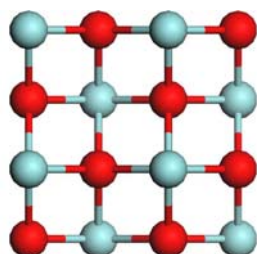


*Unrelaxed*

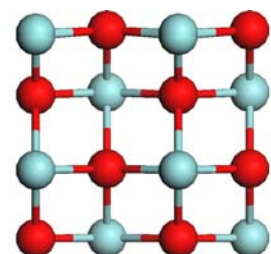


*Relaxed*

(b) (110) surface

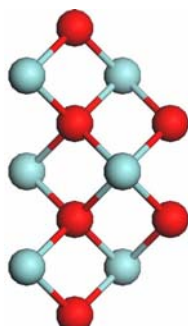


*Unrelaxed*

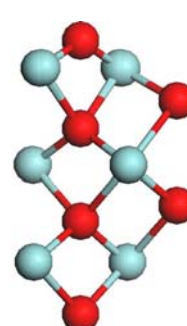


*Relaxed*

(c) Reconstructed (100) surface

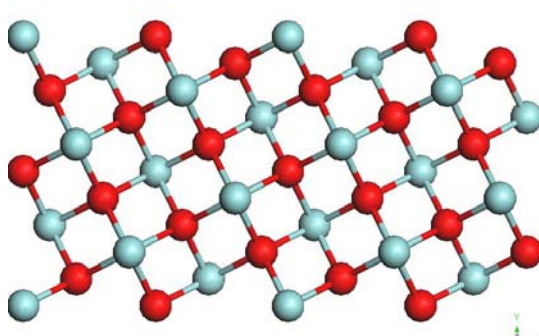


*Unrelaxed*

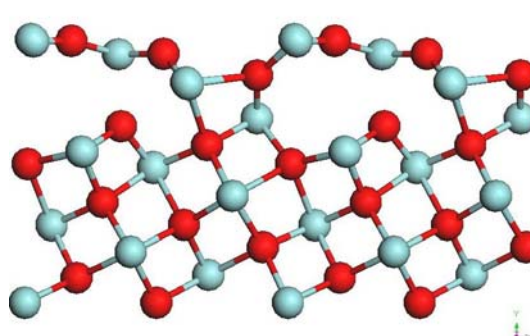


*Relaxed*

(d) (310) surface



*Unrelaxed*



*Relaxed*



**Table 5.6** Calculated surface energies of zirconia by the interatomic potential (IP) approach compared to the previous Hartee-Fork (HF) study.

Miller index	Region I : II (Å)	ZrO <sub>2</sub> ( J/m <sup>2</sup> )		ZrO <sub>2</sub> ( J/m <sup>2</sup> ) (Previous work) HF <sup>[22]</sup>	
		IP			
		Unrelaxed	Relaxed	Unrelaxed	Relaxed
(111)	6:12	1.448	1.210	1.514	1.485
(110)	6:12	3.638	2.147	3.035	2.406
(100)	6:9	10.062	2.704		
(310)	6:20	13.142	2.955		

#### 5.4 Yttrium Segregation on the ZrO<sub>2</sub> Surfaces

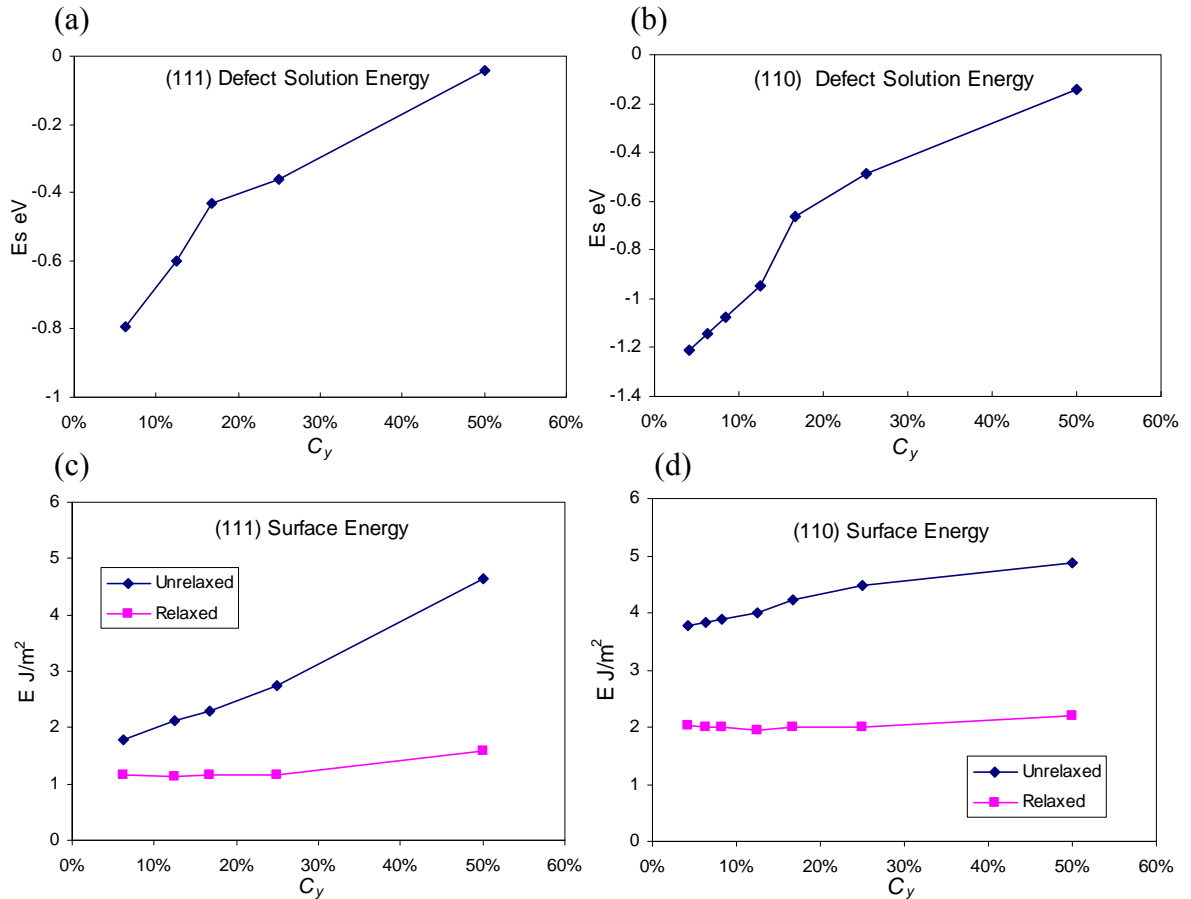
For the YSZ system, the surface energies and yttrium solution energies were calculated as a function of the defect cluster depth and orientation and yttrium concentration at the surface. Two Y atoms and one oxygen vacancy are introduced as a defect cluster (Y-V-Y) in all the surface calculations as well as in the bulk.

This study focused on the two most energetically favorable surfaces of c-ZrO<sub>2</sub>, i.e. the (111) and (110). The solution and surface energies for different yttrium concentrations ( $C_Y$ ) in the outmost surface layer of YSZ system are plotted in **Figure 5.8**. The variation of yttrium concentration ( $C_Y$ ) was achieved by extending the surface repeat unit from (1x1) to (2x3).

Energetically favorable yttrium solution energies were obtained at a Y surface content level of less than 25% for the (111) and (110) surfaces, which accords with the earlier atomistic study of the Ca/ZrO<sub>2</sub> system carried out by Kenway *et al.*, <sup>[23]</sup> who suggested that Ca<sup>2+</sup> cations also have favorable solution energies for the (111)<sub>c</sub> and (110)<sub>c</sub> surfaces for all compositions and that the cations segregate to the surface. For Y doping, compared to the (111) and (110) surfaces of undoped ZrO<sub>2</sub> (**Table 5.4**), the surface energies were reduced slightly over the same yttrium content region which indicates that both these surfaces of c-ZrO<sub>2</sub> can be stabilized by yttrium doping. However, the relative stabilities of the (111) and (110) surfaces do not change.



**Figure 5.8** Plots of Y solution energy and surface energy versus Y concentration for the (111) and (110) surfaces of c-ZrO<sub>2</sub>. NN defect clusters are located in the top layer of the surface and orientated in the X direction (parallel to the surface). ‘(a) (111) surface defect solution energy; (b) (110) surface defect solution energy; (c) (111) surface energy; (d) (110) surface energy.



The results in **Figure 5.8** show that yttrium solution at the surface becomes decreasingly favorable with increasing Y concentration; and indeed, both the defect solution and the surface energies have a strong dependence on the yttrium content in the surface layer of YSZ.

The tendency for yttrium segregation at the (111) and (110) surfaces of c-ZrO<sub>2</sub> was investigated directly by calculating the segregation energy ( $E_{\text{seg}}$ ) and trap energy ( $E_{\text{trap}}$ ).  $E_{\text{seg}}$  is defined as the energy difference between the defect cluster in the bulk crystal ( $E_{\text{bulk}}^{\text{def}}$ ), or at a considerable depth below the surface, and at the surface ( $E_{\text{surf}}^{\text{def}}$ ).



$$E_{\text{seg}} = E_{\text{surf}}^{\text{def}} - E_{\text{bulk}}^{\text{def}} \quad (5.3)$$

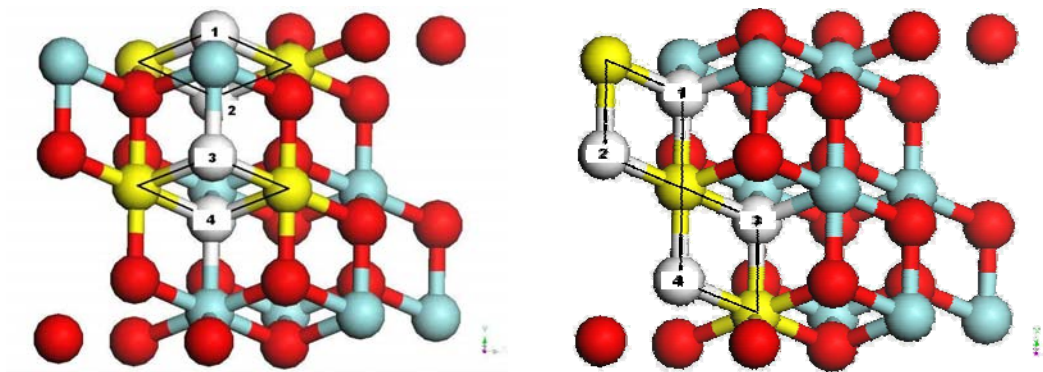
Similarly,  $E_{\text{trap}}$  is defined as the difference between the energy of the defect cluster at the surface ( $E_{\text{surf}}^{\text{def}}$ ) and in the lowest energy site ( $E_{\text{trap}}^{\text{def}}$ )

$$E_{\text{trap}} = E_{\text{trap}}^{\text{def}} - E_{\text{surf}}^{\text{def}} \quad (5.4)$$

A negative value for  $E_{\text{seg}}$  indicates the surface sites are more favorable than the bulk and segregation can occur. The trap energy  $E_{\text{trap}}$  can be zero, which means no trap sites are found, or negative, i.e. there are more stable sites near the surface but not at the surface.

The segregation energy was evaluated by moving the Y-V-Y clusters from the top layer of the surfaces towards the bottom of region I. Both 1x1 and 1x2 surface repeat units were examined. Two series of cluster sets were studied with different defect orientations parallel or perpendicular to the surface, i.e. Y-V-Y along the X and Z directions as displayed in **Figures 5.9** and **5.11**. Yttrium ions are either located at nearest neighbour (NN) or next nearest neighbour (NNN) sites to the oxygen vacancy. The variation of yttrium solution energy versus the depth of these defect clusters from the surface is presented in **Figures 5.10** and **5.12** for the (111) and (110) surfaces respectively.

**Figure 5.9** Schematic representation of the defect cluster moving down from the top of the c-ZrO<sub>2</sub> (111) surface in a sequence of 1, 2, 3, 4...sites. I. Defect cluster orientated along X direction; II. Defect cluster orientated along Z direction. (Zr ●; Y ●; O ●; O vacancy )

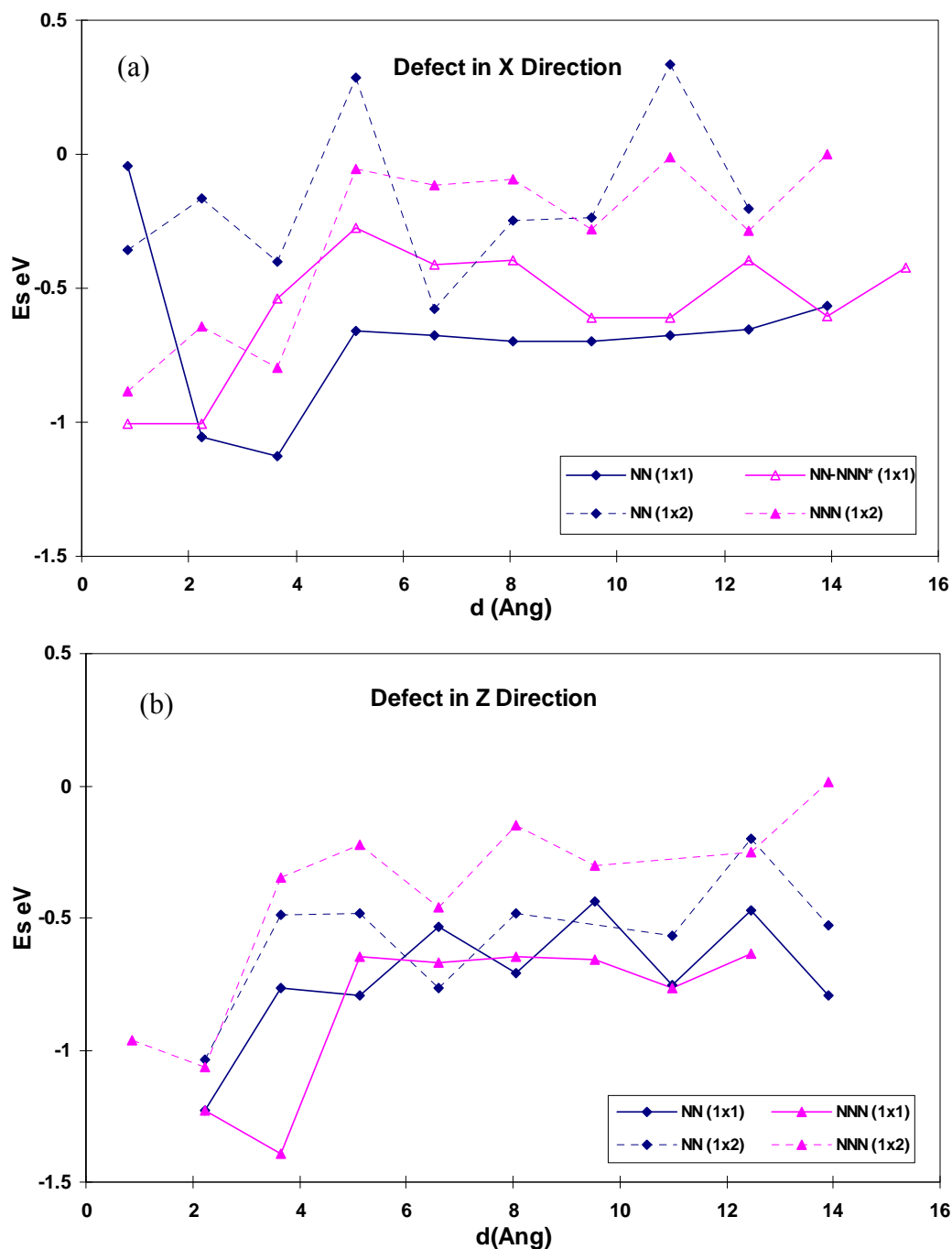


*I. X direction Y-V-Y*

*II. Z direction Y-V-Y*



**Figure 5.10** Defect solution energy  $E_s$  (eV) versus cluster depth  $d$  (Å) for the 1x1 and 1x2 repeat units of the (111) surface. (a) Defect cluster orientated along X direction; and (b) Defect cluster orientated along Z direction. (NN-NNN\* due to 1x1 repeat unit is too small for NNN sites defect cluster along X direction.)



The most significant results for the (111) surface are listed in **Tables 5.7**. In general, for both X and Z orientations of the Y-V-Y cluster, the solution energy no longer depends strongly on cluster orientation at a distances  $\sim 5$  Å or more from the surface (**Figure 5.10**). However, as the cluster approaches the surface, a strong



configurational dependence is apparent. The surfaces with the defect clusters in the Z orientation (**Figure 5.9-II**) possess favorable segregation energies up to -0.7 eV; hence, the defect cluster tends to locate along the  $\langle 100 \rangle$  direction on the  $(111)_c$  surface. An enrichment of yttrium towards the  $(111)$  surface would occur with formation of a higher concentration layer extending over 4~5 Å deep (depth equivalent to four oxygen layers or two O-Zr-O trilayers). The values of  $E_{\text{seg}}$  in **Table 5.7** are mostly negative, which is consistent with the results of the surface energy calculations.

**Table 5.7** Summary of segregation and trap energies for the Y doped  $(111)$  surface of c-ZrO<sub>2</sub>. Segregation depth indicated the depth of the energetically favorable sites for yttrium to the top of the surface.

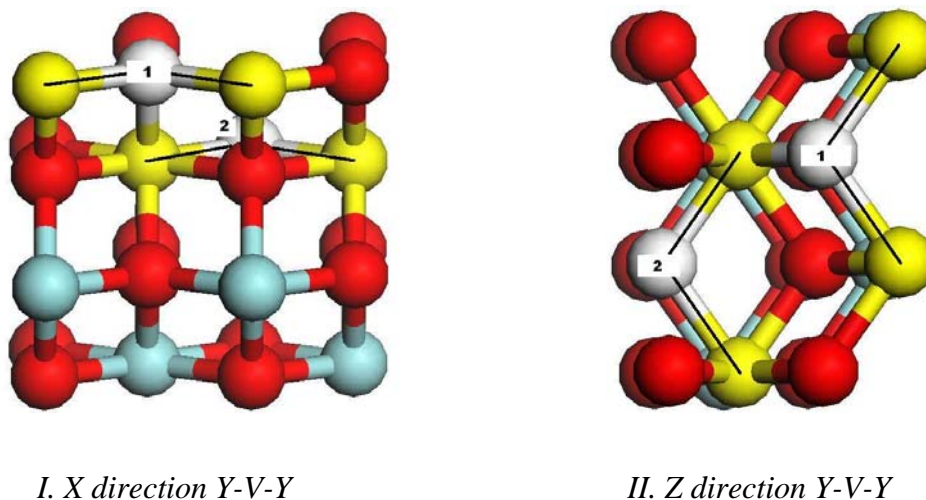
Surface Unit	Defect Orient. (axis)	Defect config.	$E_{\text{seg}}$ per Y (eV)	$E_{\text{trap}}$ per Y (eV)	Segregation depth (Å)
1x1	X	NN	0.7	-1.1	~5
1x1	X	NN-NNN	-0.5	—	3~4
1x2	X	NN	-0.3	—	~5
1x2	X	NNN	-0.7	—	~5
1x1	Z	NN	-0.6	—	3~4
1x1	Z	NNN	-0.6	-0.2	~5
1x2	Z	NN	-0.5	—	3~4
1x2	Z	NNN	-0.7	-0.1	3~4

One notable result in **Table 5.7** concerns the high yttrium concentration level of 50%, i.e. for the 1x1 surface repeat unit with the defect cluster in the X orientation, where the calculations for the NN sites configuration give a positive segregation energy in the outmost layer accompanied by a large energy trap in the subsurface layer. In such a case, the yttrium tends to disperse to the NNN site, so the defect cluster is orientated with the vacancy at the top surface or subsurface (i.e. Z direction). This result suggests that saturation of yttrium has been achieved at the outmost layer with an Y/Zr ratio 1:1 and thus the defect clusters prefer to locate in the 2<sup>nd</sup> and 3<sup>rd</sup> layers of the subsurface. Therefore, from these calculations we can conclude that yttrium



segregates at the (111) surface near the oxygen vacancy sites up to a depth of four oxygen layers (4~5 Å).

**Figure 5.11** Schematic representation of the defect cluster moving from the top of the c-ZrO<sub>2</sub> (110) surface in sequence of 1, 2 ...sites. I. Defect cluster orientated along X direction; II. Defect cluster orientated along Z direction. (Zr ●; Y ●; O ●; O vacancy ○)

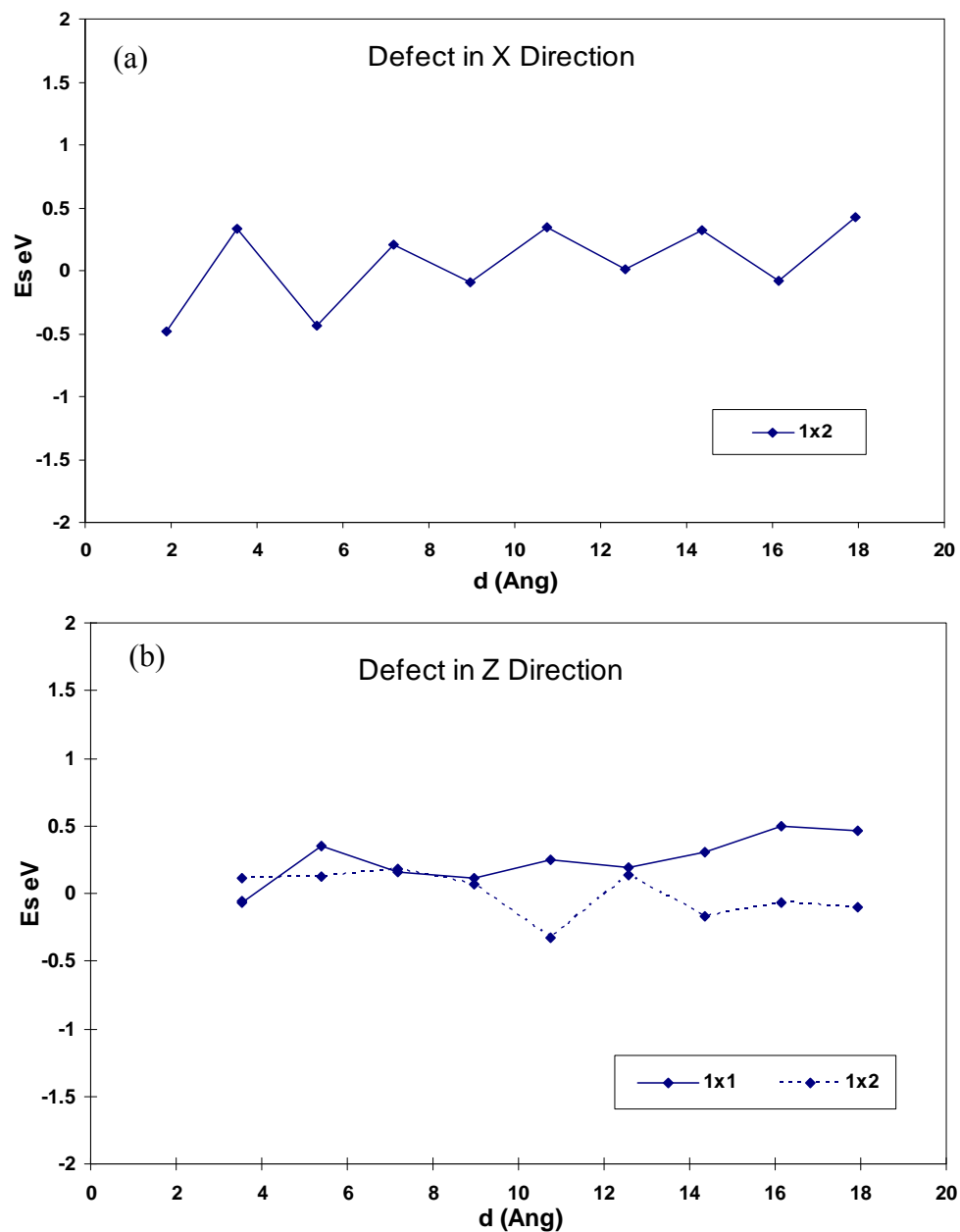


A series of calculations for the less stable (110) surface was performed in a similar manner to those for the (111) surface using the configuration shown as **Figure 5.11**. **Figure 5.12** presents the solution energy as a function of the defect depth using 1x1 and 1x2 surface repeat units. In these models, the NNN defect sites adopt an identical configuration to the NN sites after relaxation. For the X orientation, only the 1x2 repeat can be considered. In this case, with substitution of yttrium at half of the Zr sites at the (110) surface layer, the segregation energy oscillates, and no significant trap energy is observed. Such a variation of solution energy  $E_S$  with defect depth is ascribed to the cluster dipole interacting with the local dipole along the surface. A slightly lower yttrium solution energy is estimated for the outmost layer of the (110) surface for the Y-V-Y cluster in the X orientation. However, there is no strong indication that the yttrium dopants will segregate to the (110) surface ( $0 > E_{seg} > -0.3\text{eV}$ ). Equally, Y solution energies as a function of depth for the Z orientation do not suggest surface segregation. These results from atomistic calculations are consistent with the previous electronic structure study which also indicates little driving force for yttrium



segregation at the (001) surface in  $t\text{-ZrO}_2^{[19]}$  which is equivalent to the (110) surfaces of  $c\text{-ZrO}_2$ .

**Figure 5.12** Plots of defect solution energy  $E_s$  (eV) as a function of defect cluster depth  $d$  (Å) for the 1x1 and 1x2 repeat units of the (110) surfaces. (a) Defect cluster orientated along X direction; and (b) Defect cluster along Z direction.



Overall, from the above results, it is expected that an enrichment of yttrium towards the (111) surface would occur with the formation of a higher concentration layer extending over 4-5 Å (i.e. four layers from the top) and no clear driving force for Y segregation at the (110) surface. This finding is consistent both with previous



calculations for t-ZrO<sub>2</sub> <sup>[19][24]</sup> and c-ZrO<sub>2</sub> <sup>[25]</sup> as well as several experimental observations. <sup>[3][19][26-29]</sup> In particular, the production of an upper limit to the level of Y at the surface is in accordance with the experimental study by Zhu *et al.* which suggested the composition of the outmost surface YSZ is independent of Y concentration in the bulk due to segregation of Y<sub>2</sub>O<sub>3</sub>. <sup>[3]</sup> The accompanying surface segregation of the charge compensating of oxygen anion vacancies will have a substantial effect on surface chemistry.

## 5.5 Conclusions

The atomistic studies reported in this chapter have successfully modelled the bulk cubic phase of ZrO<sub>2</sub> and the (111), (110), (100) and (310) surfaces of c-ZrO<sub>2</sub>. For bulk supercell calculation in the range 9-12 mol% yttria, two stable cubic-like phases were indicated differing in their detailed oxygen arrangement in line with experimental observations. The order of surface stability for c-ZrO<sub>2</sub>: (111)<sub>c</sub> > (110)<sub>c</sub> > (100)<sub>c</sub> > (310)<sub>c</sub> was confirmed by the calculations, i.e. the (111)<sub>c</sub> surface is the dominant surface of undoped c-ZrO<sub>2</sub> in good agreement with previous experimental and theoretical studies.

Doping with yttrium stabilizes the cubic phase ZrO<sub>2</sub> and the energy of the YSZ lattice is found to increase linearly with yttrium concentration in the bulk. According to the Mott-Littleton calculations, yttrium is more stable in the next nearest neighbour (NNN) sites to the vacancy rather than nearest neighbour (NN) sites; in addition, the two yttrium ions tend to be located together. However, the supercell calculations suggest that the dispersion of yttrium with respect to the oxygen vacancy depends on yttria content level and the NN and NNN sites are almost equally favorable.

The energetically favorable (111) and (110) surfaces of pure cubic zirconia can be further stabilized by the yttrium doping. However, doping does not change the relative stabilities of the (111)<sub>c</sub> and (110)<sub>c</sub> surfaces. Yttrium tends to segregate at the top layers (up to 5 Å) of the dominant (111)<sub>c</sub> surface. In contrast, no clear tendency for yttrium segregation of yttrium has been observed on the (110) c surface of YSZ.



The present work, which has been published <sup>[30]</sup> has advanced our understanding of the effect of yttrium doping and the creation of oxygen vacancies in ZrO<sub>2</sub> surfaces. In the next Chapter, an investigation of the electronic structure of ZrO<sub>2</sub> and YSZ surfaces using quantum mechanical methods will be reported.

## References

- 
- [1] M. Yashima, K. Ohtake, M. Kakihana, H. Arashi. and M. J. Yoshimura, *J. Am. Ceram. Soc.* **57**, 17, 1996.
  - [2] M. Yashima, H. Takanhashi, K. Ohtake, T. Hirose, M. Kakihana, H. Arashi and M. J. Yoshimura, *J. Am. Ceram. Soc.* **57**, 289, 1996.
  - [3] J. Zhu, J. G. van Ommen, A. Knoester, L. J. Lefferts, *J. Catal.* **230**, 291, 2005.
  - [4] A. Dwivedi, A. N. Cormack, *Philos. Mag. A.* **61**, 1, 1990.
  - [5] M. Ruhle, and H. Heuher, *Adv. Ceram.* **12**, 14, 1984.
  - [6] C. R. A. Catlow, *J. Chem. Soc., Faraday Trans.* **86**, 1167, 1990.
  - [7] E. V. Stefanovich, A. L. Shluger and C. R. A. Catlow, *Phys. Rev. B* **49**, 11560, 1994.
  - [8] JCPDS pattern No. 42-1164
  - [9] R. Orlando, C. Pisani, and C. Roetti, *Phys. Rev. B* **45**, 592, 1992-II.
  - [10] G. Stapper, and M. Bernasconi, *Phys. Rev. B* **59**, 797, 1999-II.
  - [11] František, *Acta Cryst. B* **40**, 76, 1984.
  - [12] N. Mott, M. Littleton. *Trans. Faraday Soc.* **34**, 485, 1938.
  - [13] P. Li, W. Chen, Penner-Hahn, *Phys. Rev. B.* **48**, 10063, 1993; *J. Am. Ceram. Soc.* **77**, 118, 1994.
  - [14] C. R. A. Catlow, A. V. Chadwick, G. N. Greaves, L. M. Monroney, *J. Am. Ceram. Soc.* **69(3)**, 272, 1986.
  - [15] D. Komyoji, A. Yoshiasa, T. Moriga, S. Emura, F. Kanamaru and K. Koto, *Solid State Ionics* **50**, 291, 1992.
  - [16] M. S. Khan, M. S. Islam, D. R. Bates, *J. Mater. Chem.* **8(10)**, 2299, 1998.
  - [17] M. Yashima, K. Morimoto, N. Ishizawa and M. J. Yoshimura, *J. Am. Ceram. Soc.* **76**, 1745, 1993.



- 
- [18] G. Balducci, J. Kašpar, P. Fornasiero, M. Graziani and M. S. Islam, *J. Phys. Chem. B.* **102**, 557, 1998.
- [19] A. Eichler and G. Kresse *Phys. Rev. B* **69**, 045402, 2004.
- [20] W. H. Press, S. A. Teukolsky, W. T. Vetterling and B. P. Flannery, "*Numerical Recipes*", Cambridge University Press, Cambridge, 2nd edn. 1992.
- [21] C. Morterra, G. Cerrato, L. Ferroni and L. Montanara, *Mat. Chem. and Phys.* **37**, 243, 1994.
- [22] S. Gernard, F. Cora and C. R. A. Catlow, *J. Phys. Chem. B.* **103**, 10158, 1999.
- [23] P. R. Kenway, P.M . Oliver, S.C. Parker, D. C. Sayle, T. X. T. Sayle and J O. T itiloye, *Mol. Simul.* **9**, 83, 1992.
- [24] S. E. Redfern, C. R. Stanek, R.W. Grimes and R.D. Rawlings, *Philo. Magaz. Lett.* **85**, 445, 2005.
- [25] G. Ballabio, M. Bernasconi, F. Pietrucci, and S. Serra, *Phys. Rev. B.* **70**, 075417, 2004.
- [26] A. Bernasik,; K. Kowalski,; A.Sadowski, *J. Phys. Chem. Solids* **63**, 233, 2002.
- [27] A. J. A. Winnubst,; P. J. M. Kroot and A. J. Burggraaf, *J. Phys. Chem. Solids* **44**, 955, 1983.
- [28] M. de Ridder, A.G. Vervoort,; R.G. van Welzenis and H. H. Brongersma, *Sol. State Ionics* **156**, 255, 2003.
- [29] M. de Ridder, R.G. van Welzenis, H. H. Brongersma and U. Kreissig, *Sol. State Ionics* **158**, 67, 2003.
- [30] X. Xia, C. R. A. Catlow and R. Oldman, *Chem. Mater.* **21(15)**, 3576, 2009.



## Chapter 6 Quantum Mechanical Studies of YSZ

*Every observable quantity of a quantum system can be calculated from the density of the system ALONE.*

*-- Hohenberg, Kohn*

In order to gain insight into the electronic properties of YSZ bulk and surfaces, quantum mechanical DFT calculations have been carried out by employing the Vienna *ab initio* simulation package (VASP), which is based on the methodologies summarized in Chapter 4. In this Chapter, the three low pressure phases of pure  $\text{ZrO}_2$  are first reproduced. The defect structure and vacancy formation energy of bulk YSZ are also estimated. Next, the structure of the plane surface (111) and yttrium segregation effects are examined at the quantum mechanical level. In addition, more complicated surface topologies have been studied by building a variety of stepped and cornered models. The electronic structure has been explored using the Bader analysis, charge density maps and the projected density of states.

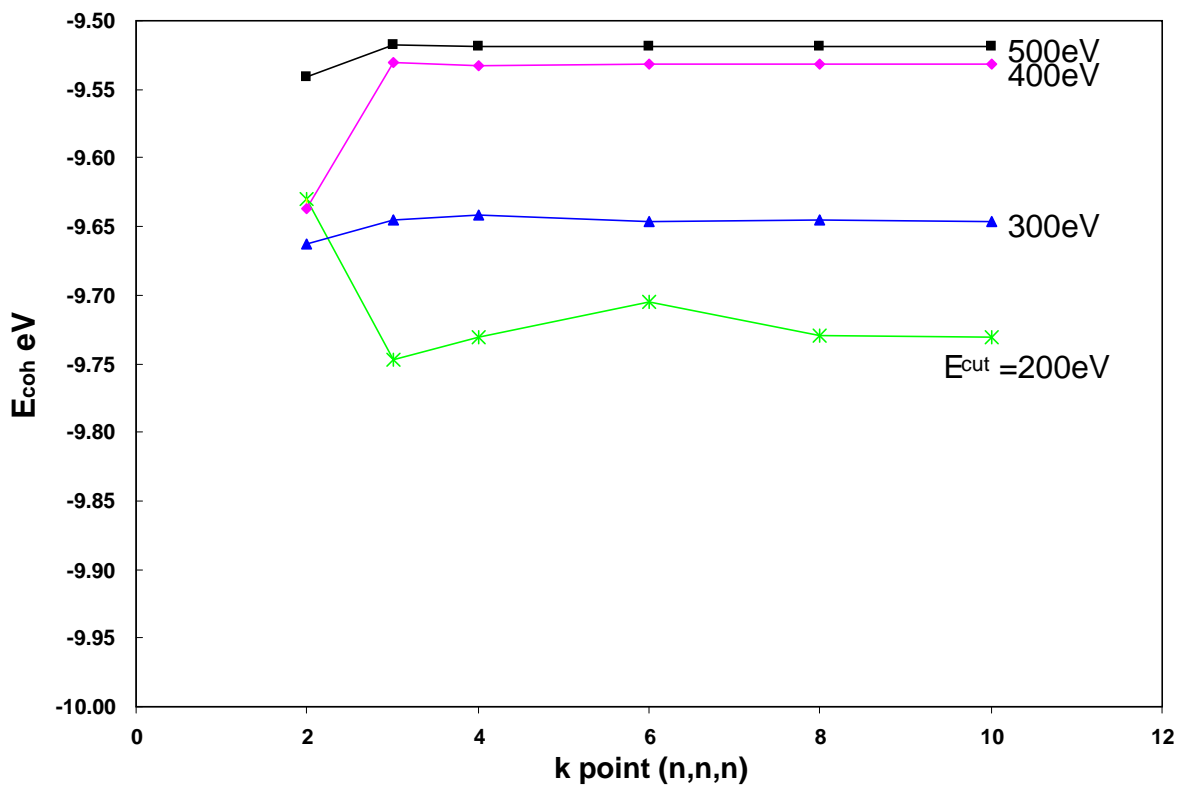
### 6.1 $\text{ZrO}_2$ Phases

Both local density approximation (LDA) and generalized gradient approximation (GGA) calculations have been carried out for the phase study of  $\text{ZrO}_2$ . The core electrons were described with the projector augmented wave (PAW) method of Blöchl<sup>[1]</sup> as implemented in VASP by Kresse and Joubert.<sup>[2]</sup> The  $4p^6 5s^1 4d^3$  electrons for Zr and  $2s^2 2p^4$  for O were treated as valence electrons. The number of plane waves is controlled by a cut-off energy ( $E_{\text{cut}}=500\text{eV}$ ) which is set to be 100eV above the recommended value for the potentials employed to achieve the convergence of the stress tensor. Structural optimizations were performed using a conjugate gradient technique in which the iterative relaxation of atomic positions was stopped when the



forces on the atoms were less than 0.01 eV/ Å. For the geometry optimization, an 8x8x8 mesh of k points was used to sample the reciprocal space. The cohesive energy convergence has been examined with respect to the number of k point and plane wave cut-off energy as shown in **Figure 6.1**. At the chosen kinetic energy cut-off (500eV) and k-point mesh (8x8x8), the k-point integration errors are estimated to be less than 1 meV/atom and the Pulay stresses <sup>[3]</sup> are also negligible. All the structure calculations presented in this chapter have been performed spin restricted since the previous studies of solids with predominantly (80%) ionic bonding character indicated little effect when freedom for spatial variations in the spin density were included. <sup>[4, 5, 6, 7]</sup>

**Figure 6.1** The cohesive energy (per atom) convergence of c-ZrO<sub>2</sub> with respect to the number of k point (n, n, n) (n=2, 3, 4...) and plane wave cutoff ( $E_{\text{cut}}=200\sim 500\text{eV}$ ).





**Table 6.1** 0K equilibrium geometry and cohesive energy per unit cell for the three phases of  $\text{ZrO}_2$ . (a [8], b [9] and c [10] for lattice parameter; d [11] and e [12] for energy difference)

	LDA	GGA	GULP	Expt.
<b>m-ZrO<sub>2</sub></b>				
a(Å)	5.127	5.198		5.234 <sup>a</sup> 5.150 <sup>b</sup>
b/a	1.004	1.013		1.007 <sup>a</sup> 1.012 <sup>b</sup>
c/a	1.023	1.029		1.031 <sup>a</sup> 1.032 <sup>b</sup>
V <sub>eq</sub> (Å <sup>3</sup> )	34.60	36.12		35.22 <sup>a</sup>
E <sub>coh</sub> (eV) per unit cell	-31.07	-28.70		
E <sub>m</sub> -E <sub>t</sub> (eV)	-0.05	-0.09		-0.06 <sup>d</sup>
<b>t-ZrO<sub>2</sub></b>				
a=b	3.584	3.628	3.588	3.605 <sup>a</sup>
c/a	1.435	1.442	1.454	1.437 <sup>a</sup>
d <sub>z</sub>	0.042	0.046	0.061	0.065 <sup>c</sup>
V <sub>eq</sub> (Å <sup>3</sup> )	33.03	34.44	33.76	33.66 <sup>a</sup>
E <sub>coh</sub> (eV) per unit cell	-31.02	-28.61		
E <sub>t</sub> -E <sub>c</sub> (eV)	-0.04	-0.05		-0.057 <sup>e</sup>
<b>c-ZrO<sub>2</sub></b>				
a=b=c	5.085	5.13	5.076	5.086 <sup>a</sup>
V <sub>eq</sub> (Å <sup>3</sup> )	32.58	33.74	32.69	32.89 <sup>a</sup>
E <sub>coh</sub> (eV) per unit cell	-30.98	-28.56		

From the results in **Table 6.1**, it can be seen the three low pressure phases of pure  $\text{ZrO}_2$  were successfully reproduced by VASP code in good agreement with the experimental observations and in contrast to the interatomic potential based calculations in Chapter 5 where the monoclinic phase minimised as an orthorhombic structure. In general, the GGA approach predicted higher cohesive energies comparing with LDA results. The non-local exchange-correlation effects cause an increase of the cohesive energy of around 8% for all the  $\text{ZrO}_2$  phases in the GGA. The LDA tends to slightly underestimate the lattice parameters, while the GGA expands the lattice.



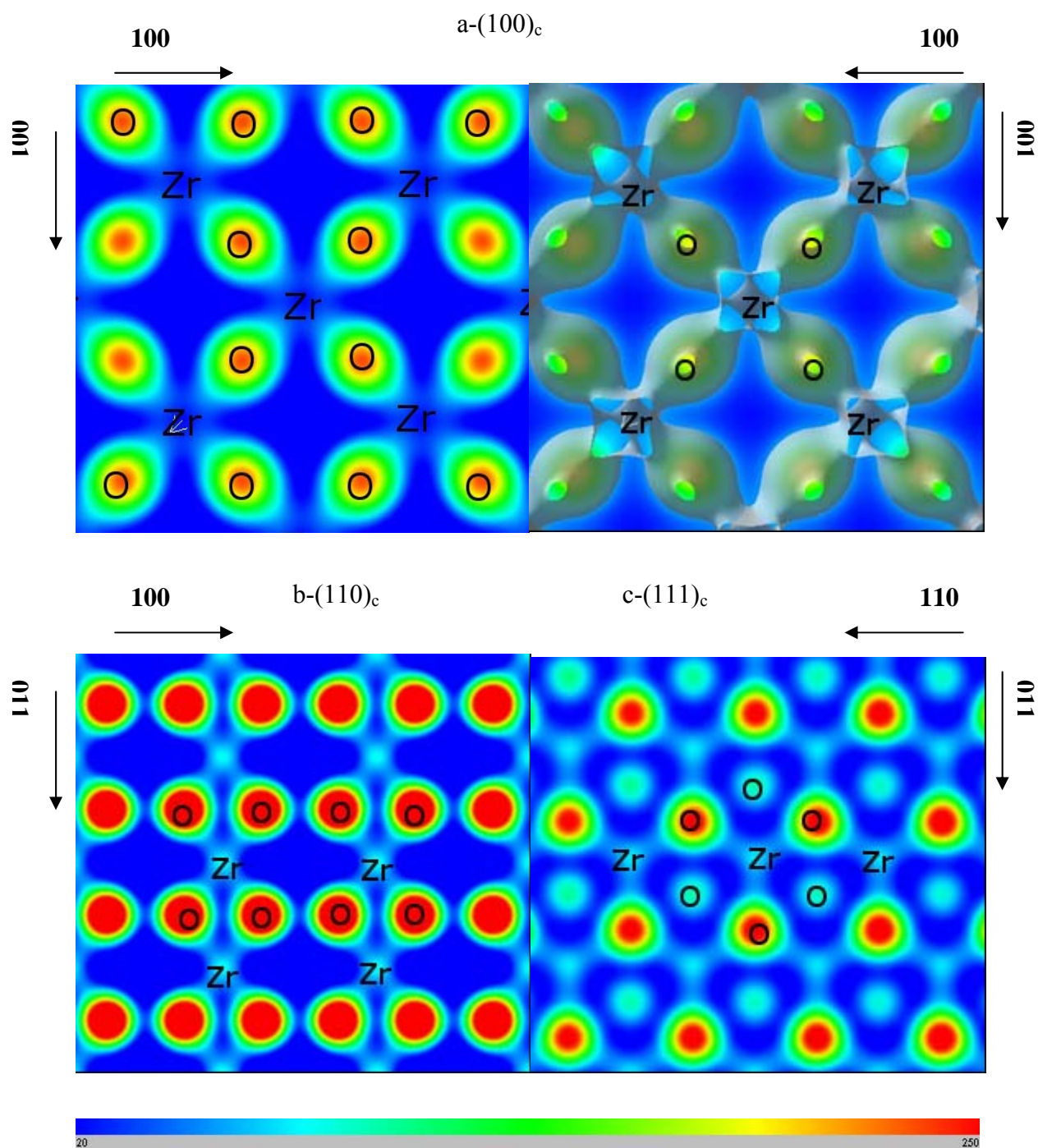
However, considering the structure variations from cubic, the GGA provides better values of  $c/a$ ,  $b/c$ , and  $d_z$  when compared to the experimental results (with here  $d_z$  being the displacement of oxygen along the  $X_2^-$  mode in  $t\text{-ZrO}_2$  with respect to the ideal fluorite positions, in units of  $c$ ). In addition, the energy difference,  $E_m - E_t$  and  $E_t - E_c$ , which refer to the adiabatic structural energy differences (eV per  $\text{ZrO}_2$  unit) for the low-pressure  $\text{ZrO}_2$  phases obtained by GGA calculations, are also very close to experiment and the thermal energy estimated from the phase transition temperatures as  $E_m - E_t = k (T_{t-c} - T_{m-t})/2 = 0.112\text{eV}$  and  $E_m - E_c = kT_{t-c}/2 = -0.052\text{eV}$ . Overall, the relative energetic stability of these three phases has been confirmed to be monoclinic  $>$  tetragonal  $>$  cubic for both the LDA and GGA approaches. For the following quantum mechanical calculations, the electron exchange and correlation were only treated within the GGA approach.

To study the electronic structure of these three phases, charge density maps have been presented in **Figure 6.2**. A comparison of the charge density maps (i)a-  $(100)_c$  and (ii)  $c\text{-(}110\text{)}_t$ , (i)  $b\text{-(}110\text{)}_c$  and (ii)  $a\text{-(}001\text{)}_t$ , which are plotted equivalently for cubic and tetragonal structures, show that the displacement of oxygen atoms has distorted the electronic distribution between the zirconium and oxygen atoms along  $\langle 001 \rangle$  direction. The charge density map of the  $(101)_t$  tetragonal plane, which corresponds to the  $(111)_c$  cubic plane (**Figure 6.2** (ii)-b and (i)-c, correspondingly) suggests the interaction between zirconium with the upper layer oxygen (in lighter colour) is relatively weaker than that with the lower layer oxygen, and hence the displacement of oxygen atoms leads to half the Zr-O bonds becoming weaker and the other half stronger. For the monoclinic structure of  $\text{ZrO}_2$ , the symmetry of the charge density has been significantly changed and adopts the pattern shown in **Figure 6.2** (iii). The oxygen atoms around Zr are redistributed to reduce the coordination number from 8 to 7, i.e. four fold by oxygen in the  $(110)_m$  plane and three fold by oxygen in the  $(111)_m$  plane, and a stronger directionality of the Zr-O bond comparing to the cubic phase can be observed on the electronic density maps.



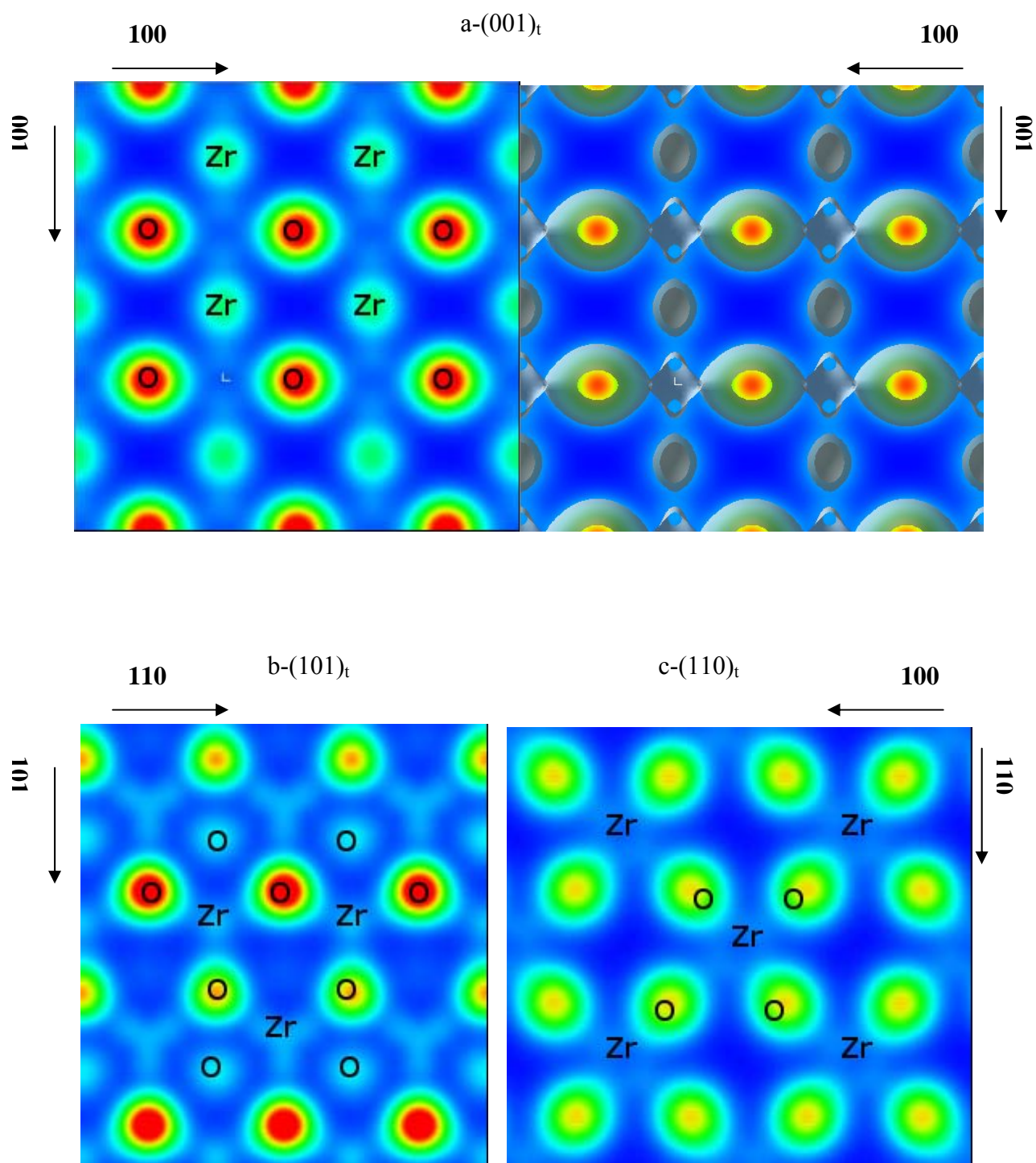
**Figure 6.2** Charge density for zirconia phases at equilibrium lattice parameters: (i) cubic (ii) tetragonal and (iii) monoclinic.  $(001)_t$  corresponds to  $(110)_c$ ,  $(101)_t$  to  $(111)_c$  and  $(110)_t$  to  $(100)_c$ . Isosurfaces are taken at 20 eV for the (100) planes (a Left).

(i) Cubic



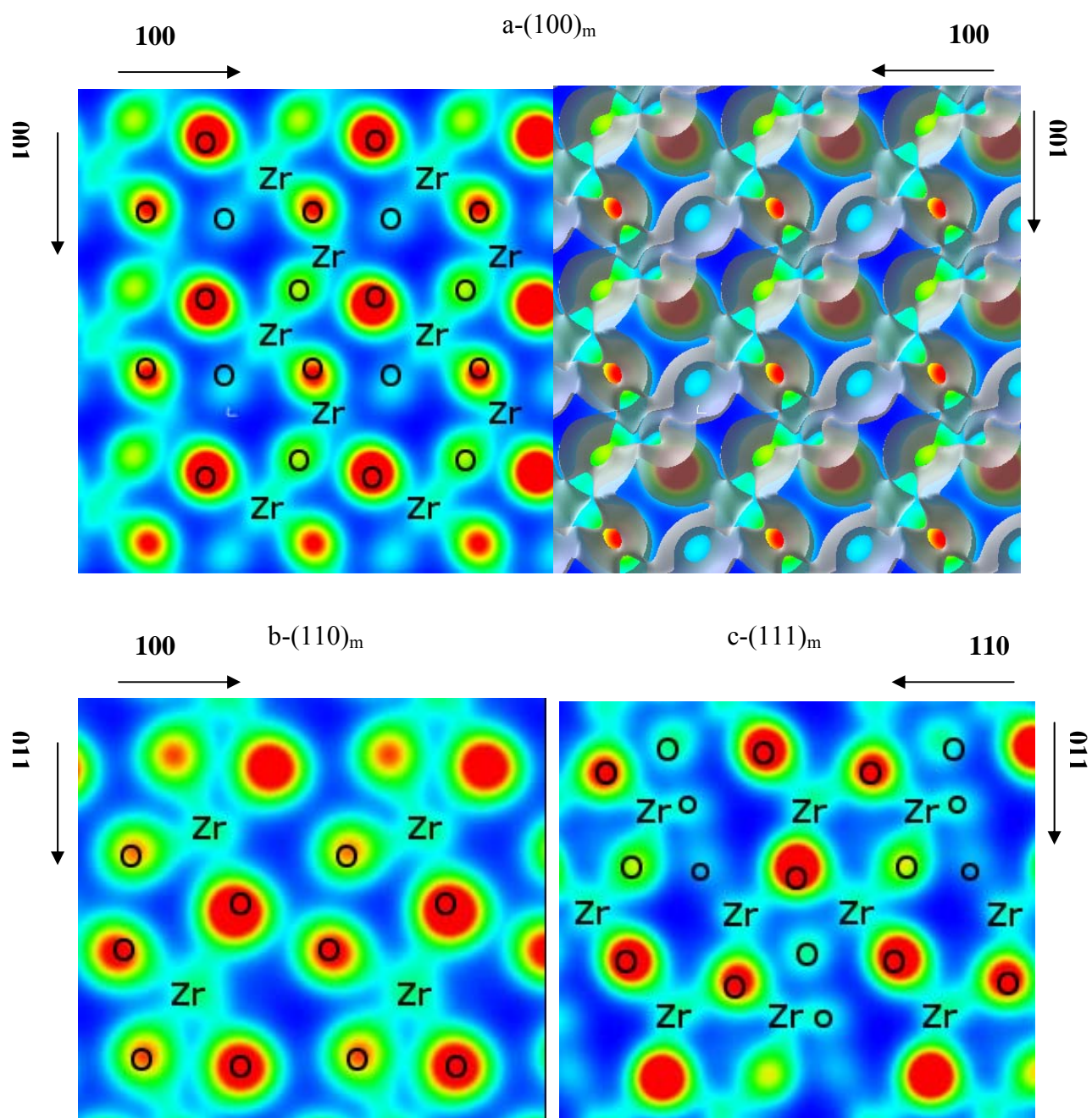


(ii) Tetragonal





(iii) Monoclinic



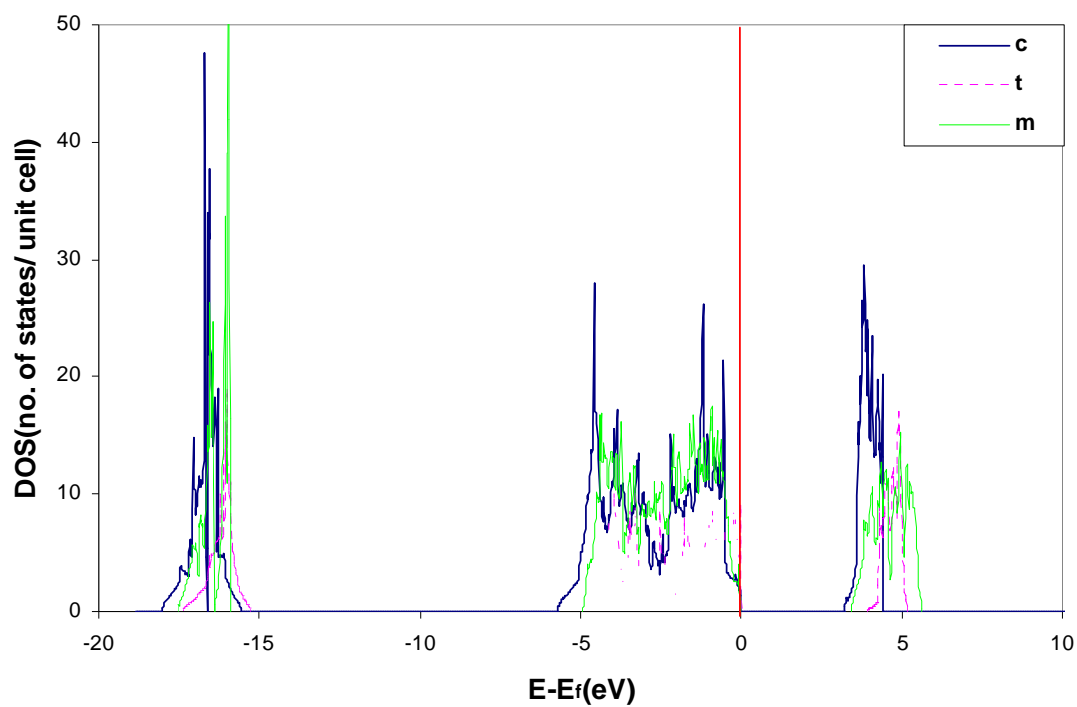
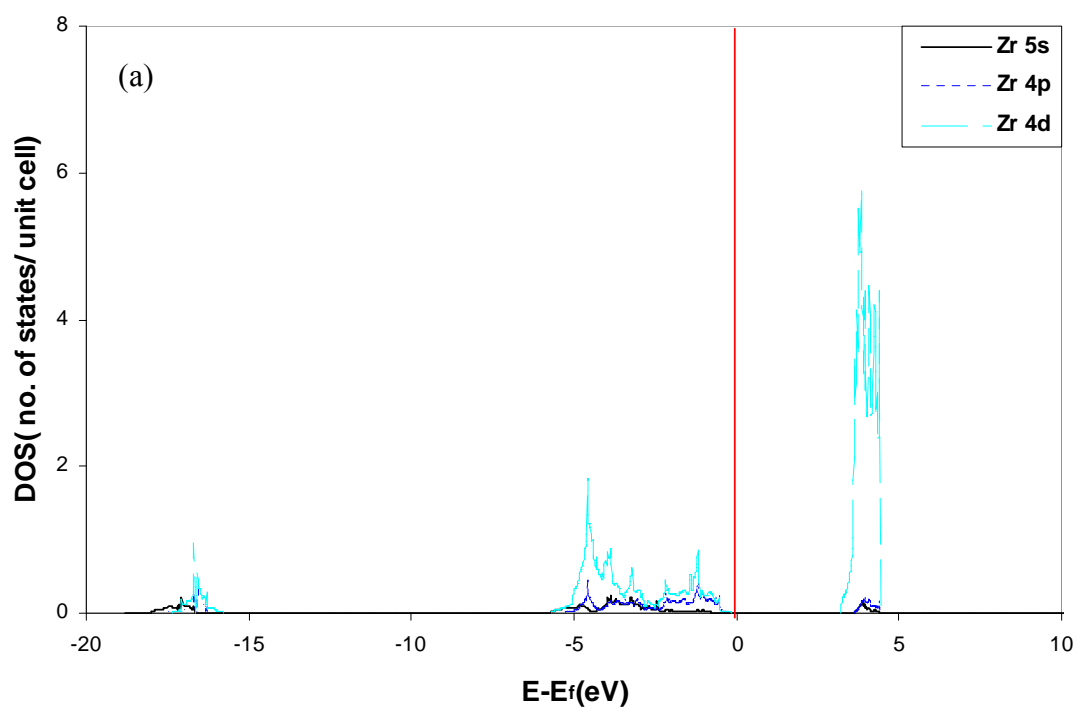


According to the Bader charge analysis of the GGA results, the charge for Zr atoms has been reduced from +3.48e in the cubic phase to +3.26e in the tetragonal phase, while the average charge on oxygen increases from -1.74e to -1.63e. In the monoclinic phase, the average Bader charges are evaluated to be +3.32e for Zr and -1.69e for O.

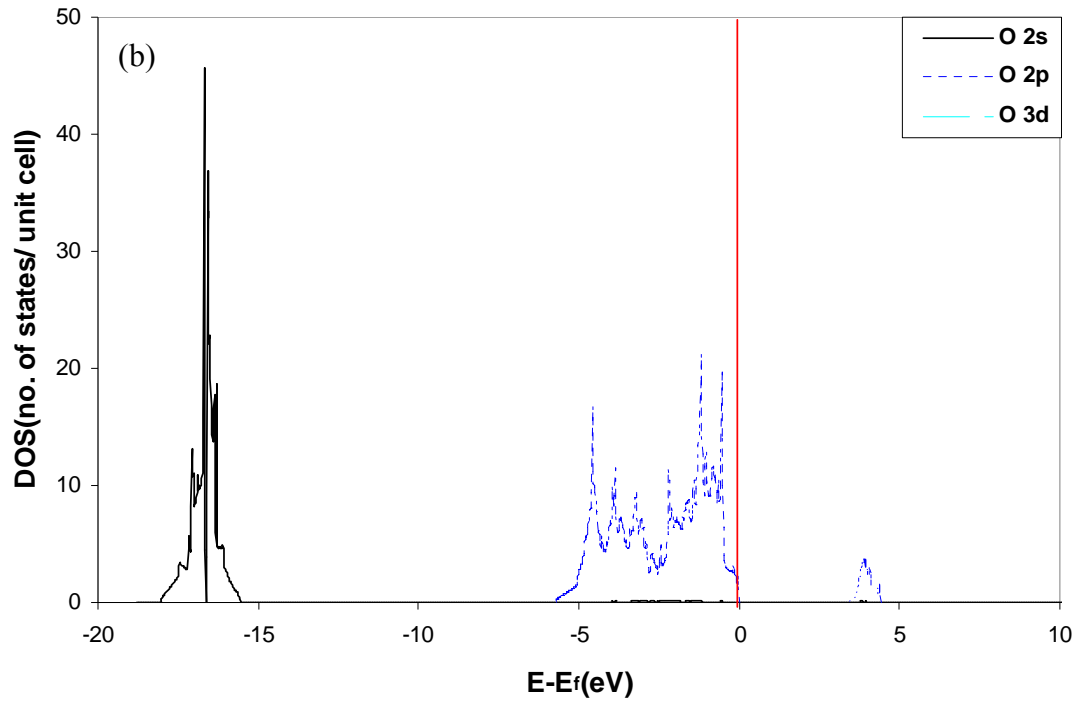
The electronic densities of state (DOS) for the three polymorphs have also been calculated with VASP using GGA schemes. **Figure 6.3** and **6.4** present the total and partial DOS obtained from these phases, in which the Fermi level has been shifted to 0 eV. The total DOS are all similar and are composed of two valence bands: the lower energy narrow band lies at about -17 eV with O 2s character and the upper energy broad band lies between -7 eV and 0 eV with O 2p character separated by an energy gap from the conduction band of Zr 4d character as seen from the analysis of the partial densities of states in **Figure 6.4**. This is in very good agreement with previous theoretical studies <sup>[13]</sup> and also with valence band X-ray photoemission spectra experiments by French *et al.* <sup>[14]</sup> who report a narrow O 2s band peaked at -19 eV and a broader O 2p band which extends binding energy from of -7 eV to 0 for the zirconia phases. In particular, comparing to the DOS of c-ZrO<sub>2</sub>, the populations of Zr 4d band have been reduced for the tetragonal and monoclinic phases, which is considered in relation to the stronger covalency of Zr-O bond in lower symmetry structures. <sup>[15]</sup>

Also, as observed experimentally, an insulating feature for zirconia phases has been indentified. The calculated band gaps are 3.22, 3.94, and 3.43 eV for the cubic, tetragonal and monoclinic phases, respectively. These values are lower than the experiment results. According to the previous study by electron energy loss spectroscopy (EELS), <sup>[16]</sup> the band gap is 4.6 eV for the cubic zirconia, and 4.2 eV for the tetragonal and monoclinic phases while ultraviolet absorption (VUV) reflectance, <sup>[14]</sup> which tends to overestimate the magnitude of the band gaps, gives values of 6.1, 5.78 and 5.83 eV for the same sequence. However, the theoretical calculations of the band gaps display some discrepancies with experimental data since DFT theory is strictly valid for the ground state properties only and usually gives poor band gaps.



**Figure 6.3** Total density of state (DOS) of cubic, tetragonal and monoclinic zirconia.**Figure 6.4** Partial DOS for Zr (a) and O (b) in cubic zirconia.





## 6.2 Defect Structure and Oxygen Vacancy Formation

In this section, the formation of oxygen vacancies has been studied by removing one neutral oxygen atom from a supercell of  $\text{ZrO}_2$  and optimizing all the atom coordinates, keeping the cell parameters fixed. The vacancy formation energy ( $V_{\text{FE}}$ ) is defined in Eq. 6.1 as the energy required to remove one oxygen atom from the bulk to form half an oxygen molecule:

$$V_{\text{FE}} = \frac{1}{2} E [\text{O}_2] + E [\text{Zr}_n\text{O}_{2n-1}] - E [(\text{ZrO}_2)_n] \quad (6.1)$$

where the  $E [\text{Zr}_n\text{O}_{2n-1}]$  is calculated from VASP for cubic  $\text{ZrO}_2$  and  $E [(\text{ZrO}_2)_n]$  is the cohesive energy of cubic  $\text{ZrO}_2$  shown in **Table 6.1**, and  $n$  is the number of formula units in the supercell. The energy of the  $\text{O}_2$  (i.e.  $E [\text{O}_2]$ ) molecule was obtained from the previous study by VASP calculations utilizing the same oxygen PAW potential. The equilibrium bond distance of the  $\text{O}_2$  molecule has been found to be 1.235 Å (compared with the experimental value of 1.207 Å).<sup>[17]</sup> At the equilibrium distance, a spin triplet solution for  $\text{O}_2$  was obtained corresponding to the energy of -9.83 eV.

For cubic  $\text{ZrO}_2$ , the  $V_{\text{FE}}$  required to remove one of eight oxygen anions in the unit cell is 5.92 eV. In the case of the monoclinic phase, the two types of four and threefold



coordinated oxygen anions have been considered separately as  $V_4$  and  $V_3$ , and their corresponding formation energy are calculated to be 5.99 and 5.91 eV, respectively. However, the vacancy formation energy is also related to the vacancy concentration in the bulk structure. A lower vacancy concentration could slightly reduce the vacancy formation energy as shown in **Table 6.2**. The electronic structure associated with vacancy formation will be discussed in detail for the surface study in section 6.4.

**Table 6.2** Oxygen vacancy formation energy  $V_{FE}$  for cubic and monoclinic  $ZrO_2$ .

<b>Vacancy Fraction</b>	<b>c-<math>ZrO_2</math> <math>V_{FE}</math> eV</b>	<b>m-<math>ZrO_2</math> <math>V_{FE}</math> eV</b>
1/8	5.92	5.99 ( $V_4$ ); 5.91 ( $V_3$ )
1/16	5.91	
1/32	5.90	

The yttrium doped  $ZrO_2$  structure has been modelled by inducing one Y-V-Y defect cluster to the  $ZrO_2$  supercell, in which the Y cation dopants are located at the NN site to the oxygen vacancy. The lattice parameter and energy of the calculated structures are listed in **Table 6.3**. The pure yttria structure has also been studied by GGA-PAW approach. The lattice parameter of the cubic cell  $Y_2O_3$  is calculated to be  $a=b=c=10.69$  Å. As for c- $ZrO_2$ , the GGA calculations slightly expended the lattice compared to the results from IP calculations in section 5.1, however, from both the approaches, the differences of lattice parameters and ion coordinates are all within 1% of the experiment data.

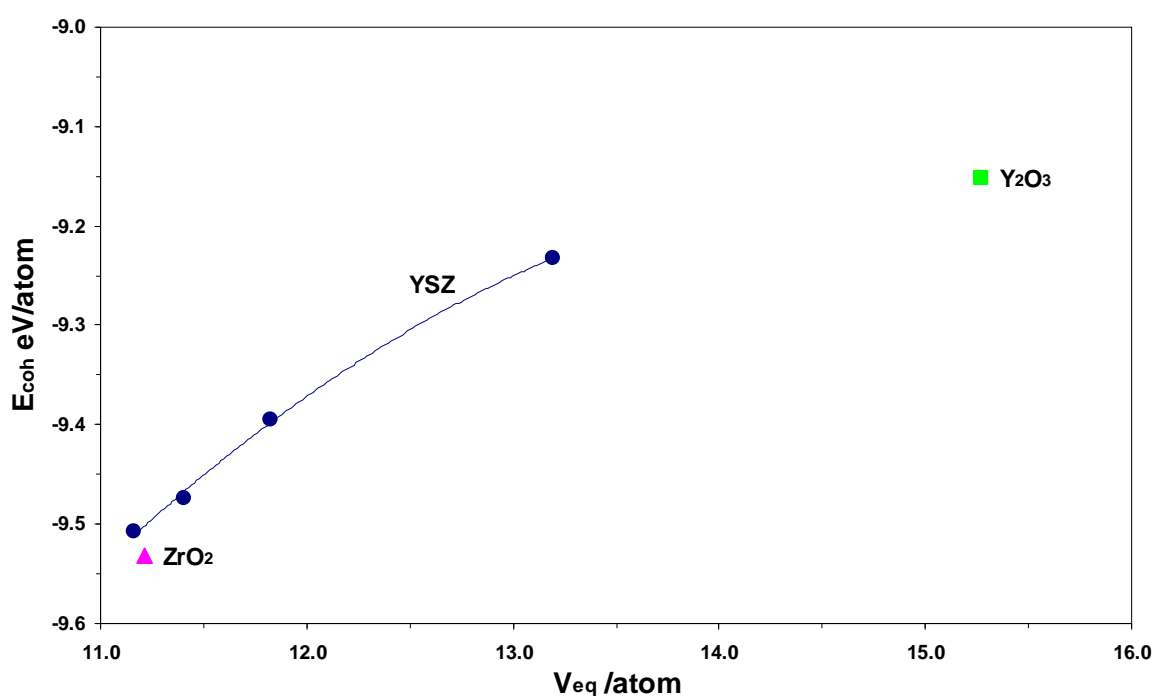
The cohesive energy of the calculated YSZ system is plotted as a function of the average volume per atom as displayed in **Figure 6.5**, according to which, the energy increases almost linearly with the average volume as well as the yttria concentration. It can be concluded that the  $ZrO_2$  lattice expands while doping with the larger unit cell size yttria. The calculated solution energy increases with yttrium concentration in YSZ systems.



**Table 6.3** Calculated geometry and energy for YSZ systems with NN sites defect configuration, i.e. two yttriums located in nearest neighbour sites to the oxygen vacancy. The  $\text{Y}_2\text{Zr}_2\text{O}_7$ ,  $\text{Y}_2\text{Zr}_6\text{O}_{15}$ ,  $\text{Y}_2\text{Zr}_{14}\text{O}_{31}$  and  $\text{Y}_2\text{Zr}_{30}\text{O}_{63}$  structure are derived from  $1\times 1\times 1$ ,  $2\times 1\times 1$ ,  $2\times 2\times 1$  and  $2\times 2\times 2$  supercell of  $\text{ZrO}_2$ , respectively.

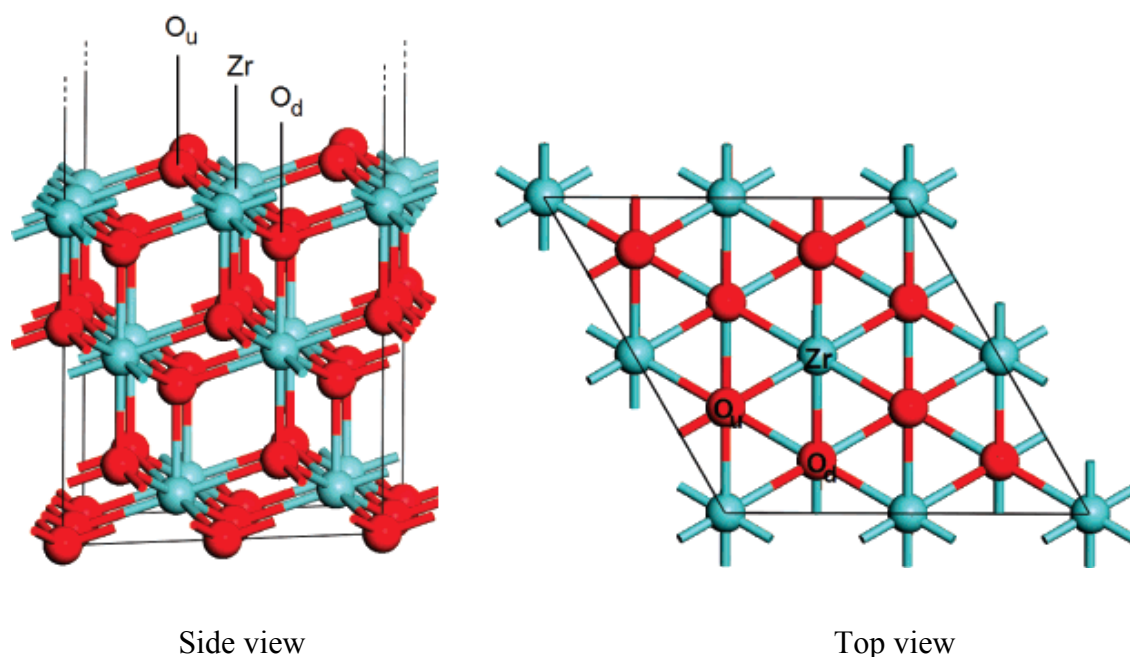
Structures	$\text{Y}_2\text{O}_3$ (100% Y)	$\text{Y}_2\text{Zr}_2\text{O}_7$ (50% Y)	$\text{Y}_2\text{Zr}_6\text{O}_{15}$ (33.3% Y)	$\text{Y}_2\text{Zr}_{14}\text{O}_{31}$ (12.5% Y)	$\text{Y}_2\text{Zr}_{30}\text{O}_{63}$ (6.25% Y)
Model size ( $\text{ZrO}_2$ unit)	$2\times 2\times 2$	$1\times 1\times 1$	$2\times 1\times 1$	$2\times 2\times 1$	$2\times 2\times 2$
a(Å)	10.689	5.325	10.247	10.224	10.197
b(Å)	10.689	5.228	5.145	10.224	10.197
c(Å)	10.689	5.228	5.16	5.123	10.200
$V_{\text{eq}}$ (Å <sup>3</sup> ) per atom	15.26	13.12	11.82	11.39	11.19
$E_{\text{coh}}$ (eV) per atom	-9.15	-9.23	-9.41	-9.47	-9.50
$E_{\text{sol}}$ (eV)		0.67	0.34	0.22	-0.03

**Figure 6.5** Cohesive energy (eV) as a function of volume (Å<sup>3</sup>) of YSZ systems. The energy and volume are calculated per atom.





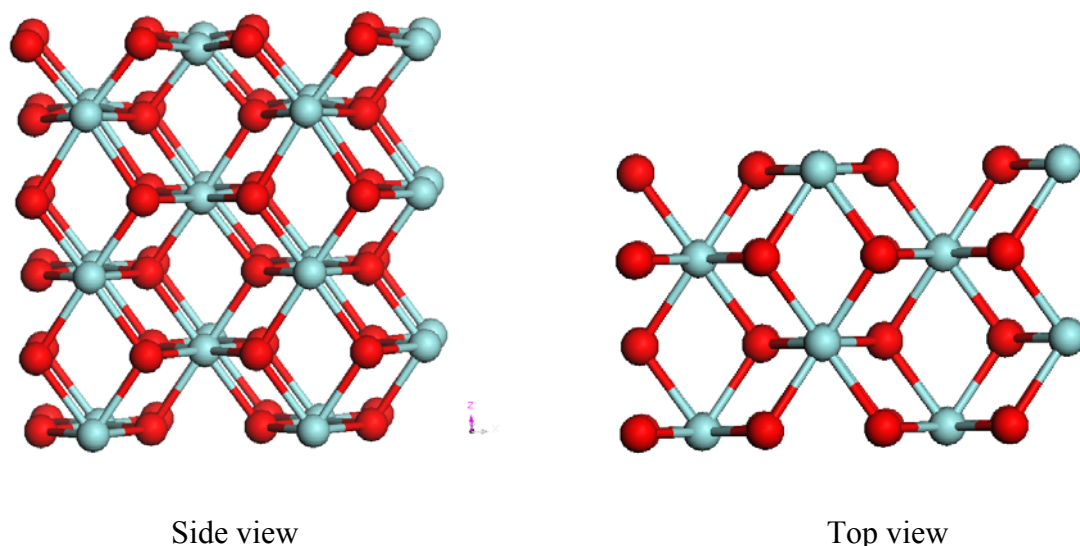
### 6.3 Plane $\text{ZrO}_2$ Surfaces



**Figure 6.6** (a) side view and (b) plan view of the O-terminated  $\text{ZrO}_2$  (111) surface. Red and blue spheres correspond to oxygen and zirconium atoms respectively.  $\text{O}_u$  and  $\text{O}_d$  refers to the upper most and subsurface oxygen.

The (111) plane surface of cubic  $\text{ZrO}_2$  has been simulated with the periodic model, where a repeated slab is used to represent the surface (**Figure 6.6**). This model consists oxygen-terminated slabs separated from each other by a vacuum gap (a separation of 15 Å has been chosen to minimize the interaction between slabs) and containing nine atomic layers (three O-Zr-O trilayers) in the direction perpendicular to the surface which is sufficient to achieve energy convergence (less than 0.01 eV energy change). Parallel to the surface, the supercell consists of a 2x2 array of hexagonal surface unit cells. Each unit cell contains one  $\text{ZrO}_2$  unit at the surface, and therefore, the three-layer simulation supercell contains 36 atoms in total, with four oxygen ions at each surface. In all of the calculations, the positions of the four atomic layers at the bottom of the slab were kept fixed at the relaxed bulk positions, while the first five layers of the top face, which is the surface under investigation, were fully relaxed. The details are discussed elsewhere in a previous study <sup>[18]</sup>. Similarly, the (110) surface has also been studied by a periodic model containing 6 layers of O-Zr-O with 72 atoms ( $\text{Zr}_{24}\text{O}_{48}$ ) as display in **Figure 6.7**.





**Figure 6.7** (a) side view and (b) plan view of the O-terminated  $\text{ZrO}_2$  (110) surface. Red and blue spheres correspond to oxygen and zirconium atoms respectively.

As in the VASP calculation of bulk  $\text{ZrO}_2$ , electron-ion interactions are described using the projector augmented wave method with plane waves up to a cutoff energy of 500eV. Generalized gradient functional (GGA) is employed. The Brillouin zone of the surfaces cells was sampled using a  $3 \times 3 \times 1$  Monkhorst Pack K-point mesh. Structure relaxation by the conjugate gradient method achieves energy convergence with the forces acting on the atoms of less than  $0.01 \text{ eV}/\text{\AA}$ . The calculated results after surface relaxation are displayed in **Table 6.4**.

For the (111) surface of c- $\text{ZrO}_2$ , the relaxation increased the top Zr-O bond distance by  $\sim 0.2 \text{ \AA}$ , which was accompanied by a small reduction in the interplanar Zr-O distance between the two outermost  $\text{ZrO}_2$  trilayers. The surface energy for the (111) surface of cubic  $\text{ZrO}_2$  is calculated to be  $1.02 \text{ J m}^{-2}$  for the surface model with 3 trilayers (nine atomic layers). On increasing the slab depth from 3 to 5 trilayers, this energy converges to within  $0.01 \text{ J m}^{-2}$  of the above value. The surface calculations reproduce the results of previous DFT calculations<sup>[17]</sup> and give a typically higher surface energy for semicovalent zirconia than other fluorite-type structures e.g. values of  $0.39 \text{ J m}^{-2}$  for  $\text{CaF}_2$  with more ionic character<sup>[19]</sup> and  $0.45 \text{ J m}^{-2}$  for  $\text{CeO}_2$ .<sup>[20]</sup>



**Table 6.4** Relaxation of the Zr-O interplanar distances compare to the bulk value (2.221 Å and 2.198 Å from GGA and IP calculations respectively) for the slab models of the ZrO<sub>2</sub> (111) O terminated surfaces.

Surface Trilayer		111				110		
		IP	DFT-GGA			IP	DFT-GGA	
			N=3	N=4	N=5		N=6	
I O-Zr-O (Å)	$\Delta d(O_u-Zr_I)$ $\Delta d(Zr_I-O_d)$	-0.019 +0.003	0.019 $\pm 0.004$	0.019 $\pm 0.004$	0.019 $\pm 0.004$	$\Delta d(O_I-Zr)$	-0.072	-0.011
Interplanar (Å)	$\Delta d(O_d-Zr_{II})$	-0.040	-0.041	-0.059	-0.059	$\Delta d(Zr-O_{II})$	-0.187	-0.135
II O-Zr-O (Å)	$\Delta d(O_u-Zr_{II})$ $\Delta d(Zr_{II}-O_d)$	+0.005 +0.001	+0.005 -0.005	+0.002 -0.001	+0.002 -0.001	$\Delta d(O_{II}-Zr)$	-0.110	0.00
Interplanar (Å)	$\Delta d(O_d-Zr_{III})$	+0.003	Fixed	0.011	0.013	$\Delta d(Zr-O_{III})$	+0.107	+0.119
III O-Zr-O (Å)	$\Delta d(O_u-Zr)$ $\Delta d(Zr-O_d)$	0.00 Fixed	Fixed	0.001 -0.006	$\pm 0.002$ -0.001	$\Delta d(O_{III}-Zr)$	-0.008	-0.001
Interplanar (Å)	$\Delta d(O_d-Zr)$			Fixed	0.009	$\Delta d(Zr-O_{IV})$	-0.043	-0.049
VI O-Zr-O (Å)	$\Delta d(O_u-Zr)$ $\Delta d(Zr-O_d)$			Fixed	+0.002 -0.004	$\Delta d(O_{IV}-Zr)$	0.004	-0.001
Interplanar (Å)	$\Delta d(O_d-Zr)$				Fixed	$\Delta d(Zr-O_V)$	0.024	0.028
V O-Zr-O (Å)					Fixed	$\Delta d(Zr-O_{VI})$	-0.002	0.0
Interplanar (Å)							-0.011	0.010
VI O-Zr-O (Å)							-0.001	Fixed

(O<sub>u</sub> and O<sub>d</sub> refer to the uppermost and lower oxygen in each trilayers. Zr<sub>I</sub>, Zr<sub>II</sub> etc refer to the Zr ions in the successive trilayer as a function of depth. The interplanar distance is the distance between successive Zr ions).

The relaxation of the (110) surface tends to reduce the interplanar Zr-O distance of the outmost layer and increase the spacing for the next layer correspondingly. A higher surface energy of 1.69 Jm<sup>-2</sup> is obtained for the (110) surface. In general, the values of surface energy obtained from DFT calculations are lower than that from the



interatomic potential (IP) approach in Chapter 5. However, according to both IP and DFT approaches, the dominance of (111) surface has been confirmed for cubic  $\text{ZrO}_2$ . This result may be attributable to the Zr atoms in the top layer of the (111) surface having a higher coordination number of 7 (the same as in monoclinic phase) compared to 6 in the (110) plane. The surface stability with respect to Zr coordination number will be further discussed for more complicated topological surfaces in section 6.5.

## 6.4 Defects on Plane (111) Surfaces

In order to study the effect of defects on the surface, the formations of isolated oxygen vacancies and oxygen vacancies compensated by yttrium dopants have been modelled separately. The subsequent calculations in this section were carried out on the relaxed plane surface with a 500eV energy cutoff and  $3 \times 3 \times 1$   $k$ -point meshes.

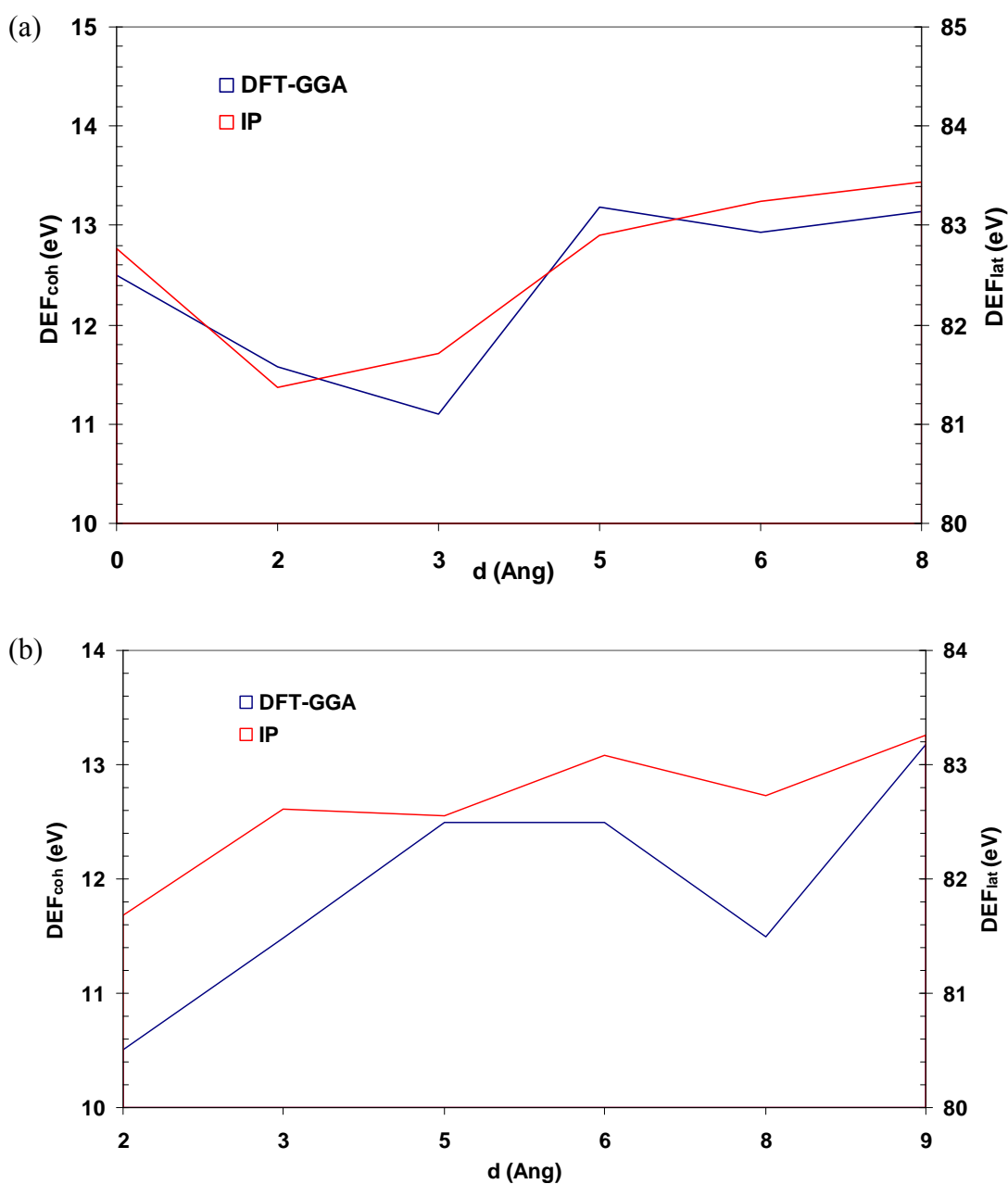
For oxygen vacancy formation, a neutral oxygen atom is moved from the top of the plane surface with  $2 \times 2$  arrays of the  $\text{ZrO}_2$  unit cell thus creating an oxygen reduction of 25% on the outermost layer. In this case, the required energy for oxygen vacancy formation on the surface is estimated to be 5.83 eV, less than the value ( $\sim 5.9$  eV) needed in the bulk. This lower vacancy formation energy suggests that oxygen removal is facilitated on the (111) surface of  $\text{ZrO}_2$ . The (110) surface has also been modelled with respect to vacancy formation. A much lower energy of 4.43 eV is found for the removal of one oxygen atom corresponding to an oxygen deficiency of 12.5% on the outmost layer.

The calculations for yttrium doping were carried out on the (111) surface with  $2 \times 2$  arrays of the  $\text{ZrO}_2$  unit cell and a depth of five O-Zr-O trilayer. 10 mol% of  $\text{YO}_{1.5}$  were substituted in this surface slab of  $\text{Zr}_{20}\text{O}_{40}$  (i.e.  $\text{Y}_2\text{Zr}_{18}\text{O}_{39}$  formation) by positioning defect clusters of Y-V-Y in a configuration either parallel or perpendicular to the surface, denoted as the X and Z orientations respectively. Only the nearest neighbour sites (NN) to the oxygen vacancy have been considered for yttrium cation dopants in this QM study, since the second (next) nearest neighbour configurations (NNN) are more complicated to model and also the previous interatomic potential modelling in Chapter 5 has suggested there is little energy difference compared to NN configurations. As displayed in **Figure 5.9** for IP calculations, two series of X and Z



orientated Y-V-Y defect clusters are moved from the top to the bottom of the (111) surface and calculated separately. The depth of the defect is denoted by the centre of the defect cluster i.e. the oxygen vacancy site.

**Figure 6.8** Comparison of yttrium segregation for the (111) surface from DFT-GGA and IP calculations. (a) NN sites defect cluster in X orientation, (b) NN sites defect cluster in Z orientation.





The defect formation energy, which is defined here as the total energy difference between the doped and pure surface of c-  $\text{ZrO}_2$ , has been plotted versus the depth of the defect cluster for the (111) surface in **Figure 6.8**. In order to compare with the DFT results, the same defect model of five O-Zr-O trilayers has also been calculated by the interatomic potential (IP) method using the GULP code. Note that, although similar calculations have been run in Chapter 5, the models used are not exactly the same due to the two region slab model employed in the previous calculations. Despite the different energetic terms, cohesive energy and lattice energy, calculated by the QM and IP methods, the variations may be compared as we note a similar trend in the change of energy with depth in both approaches as shown in **Figure 6.8**. Lower defect formation energies have been obtained for the outermost and subsurface defect sites compare to the bulk, which provide a driving force for yttrium segregation to the (111) surface. The segregation depth is calculated to be  $\sim 4$  Å. The good agreement of results from IP calculations with theoretical quantum mechanical studies demonstrates that the IP method can be an efficient tool in defect studies of plane surfaces for systems like c- $\text{ZrO}_2$ . However, the results from different method do show discrepancies in details. Notably, for the defect at a depth of 3 Å, the IP method tends to give a higher defect energy which may be caused by a smaller structural relaxation of the layer near the phase boundary formed by yttria segregation.

## 6.5 Topologically Complex Surfaces

The calculations represented so far have given detailed information on the plane (111) and (110) surfaces, but information on surfaces with more complicated topologies is still lacking. The modelling of such topological surfaces allows investigation of the effect of low-coordinated surface sites which may be important in catalysis while preserving the chemical stoichiometry and also has importance in the study of nonstoichiometric nanoparticles.<sup>[21, 22]</sup> In this section, the DFT calculations were carried out to elucidate the role of topological irregularities such as steps, corners and reverse corners. Note that the stability of different surface topologies are compared in terms of average cohesive energy per unit cell  $\text{ZrO}_2$  instead of using surface energies since the definition of surface area becomes ambiguous for a rough surface.



### 6.5.1 Step Models

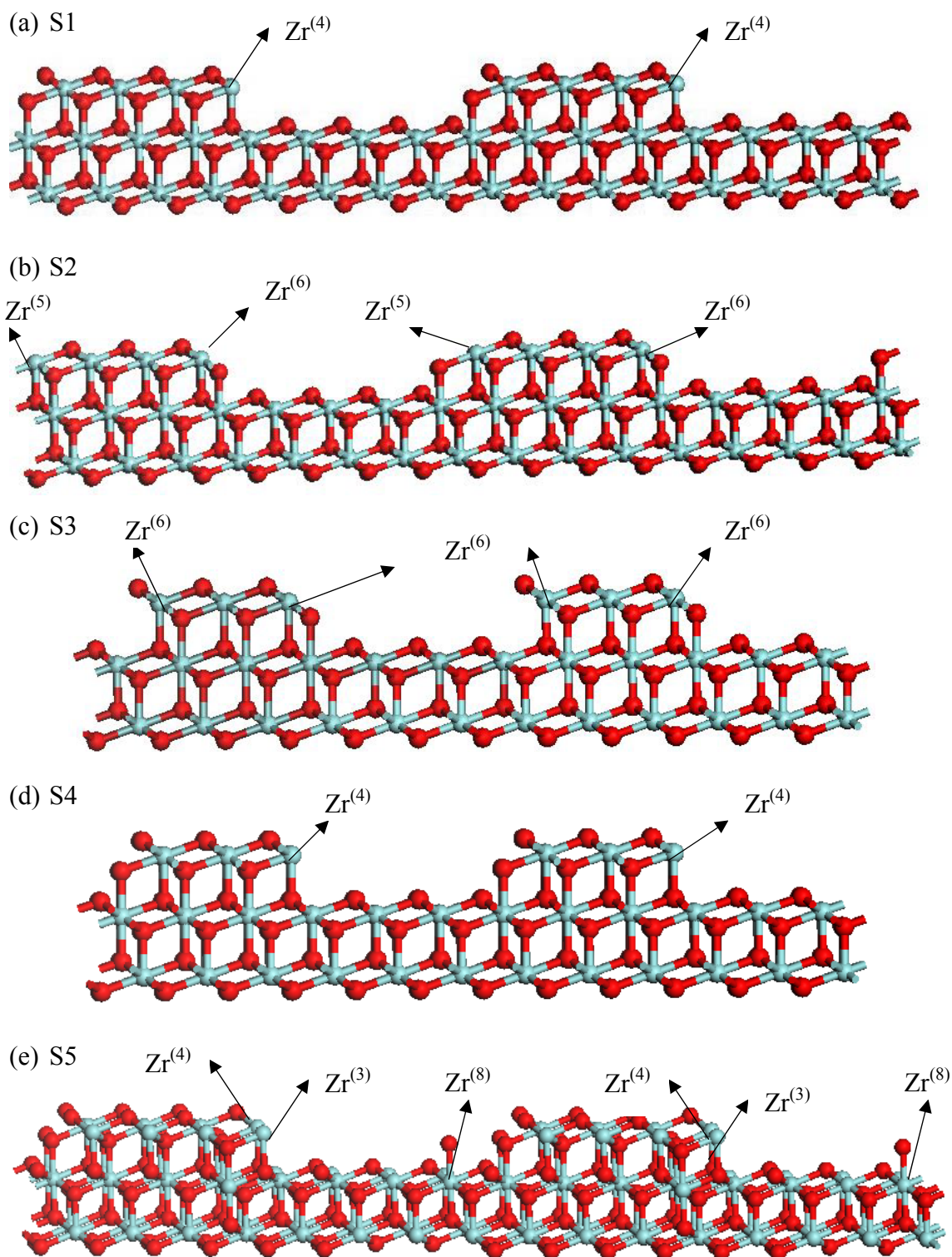
As in Section 6.4, periodic slab models containing up to nine atomic layers were constructed for the perfect, O-terminated,  $\text{ZrO}_2$  (111) surface with a vacuum width of  $\sim 15$  Å between the neighbouring interleaved slabs. A variety of terrace and step-containing models have been considered following the strategy outlined in previous work on  $\text{CeO}_2$ .<sup>[23]</sup>

In order to examine the electronic structure of low-coordinated sites, but without introducing any nonstoichiometry at the same time, different possible stoichiometric stepped slab surface models were built starting with the planar  $\text{ZrO}_2$  oxygen terminated (111) surface. The first step model **S1** (**Figure 6.9-a**), referred to as  $\text{Zr}_{20}\text{O}_{40}$ , is generated from the  $8 \times 1$  supercell by removing 4 rows from the topmost three layers resulting in a surface which is perpendicular to the  $\langle 111 \rangle$  direction and with (1-10) Miller indexes. Thus one 4 coordinated Zr is created at the edge site. In a similar way, model **S2** also corresponds to  $\text{Zr}_{20}\text{O}_{40}$  ( $8 \times 1$ ) and is derived from **S1** by moving O atoms on the top of the step to the opposite side of the step on the lower terrace sites. This procedure results in two different surfaces without a single set of Miller indexes and two Zr atoms at the edge sites which are 6 and 5 coordinated, respectively, as shown in **Figure 6.9-b**. The third model, **S3** ( $\text{Zr}_{15}\text{O}_{30}$ ), is derived from a  $6 \times 1$  unit cell by taking out 3 rows from the top three layers (O-Zr-O) which are perpendicular to the (1-10) Miller indexes, and corresponds to (-211) or (11-2) Miller planes (**Figure 6.9-c**). It should be noted that this (-211) type surface is nonpolar and thus stable, but less so than (111) or (110). As in **S2**, the **S3** model also has two lower coordinated Zr ions on each side of (111) terrace and both are 6 co-ordinated, but the terrace in **S3** is smaller which means a larger proportion of unsaturated Zr. The **S4** model (**Figure 6.9-d**) is derived from **S3** by moving one O atom of the step to its opposite side thereby creating one 4 coordinated Zr in the corresponding  $\text{Zr}_{15}\text{O}_{30}$  slab. The **S5** model is derived from **S1** by doubling the supercell size to  $8 \times 2$  and removing half of the O atoms on the step sites to the lower terrace layer in such a way that each of the oxygen vacancies thus created is separated from its neighbour in the row by one O atom (**Figure 6.9-e**). One of the 4 coordinated Zr at the edge sites of the upper terrace reduces therefore to 3 fold while for another Zr on the lower terrace co-ordination by



oxygen is increased from 7 to 8. In such a way, **S5** model preserves stoichiometry equivalent to  $\text{Zr}_{40}\text{O}_{80}$  (see **Table 6.5**).

**Figure 6.9** Step slab models of the  $\text{ZrO}_2$  (111) surface (Side View). (a) **S1**:  $(8 \times 1)$ , unit cell  $\text{Zr}_{20}\text{O}_{40}$ ; (b) **S2**:  $(8 \times 1)$ , unit cell  $\text{Zr}_{20}\text{O}_{40}$ ; (c) **S3**:  $(6 \times 1)$ , unit cell  $\text{Zr}_{15}\text{O}_{30}$ ; (d) **S4**:  $(6 \times 1)$ , unit cell  $\text{Zr}_{15}\text{O}_{30}$ ; (e) **S5**:  $(8 \times 2)$ , unit cell  $\text{Zr}_{40}\text{O}_{80}$ .





**Table 6.5** Formulae and Zr occupancy with respect to different coordination number sites for the constructed step models.

Model	Formula	Zr Occupancy (coordination no.)					
		Zr(8)	Zr(7)	Zr(6)	Zr(5)	Zr(4)	Zr(3)
<b>S1</b>	Zr <sub>20</sub> O <sub>40</sub>	4	15			1	
<b>S2</b>	Zr <sub>20</sub> O <sub>40</sub>	5	13	1	1		
<b>S3</b>	Zr <sub>15</sub> O <sub>30</sub>	3	10	2			
<b>S4</b>	Zr <sub>15</sub> O <sub>30</sub>	3	11			1	
<b>S5</b>	Zr <sub>40</sub> O <sub>80</sub>	9	29			1	1

Interatomic potential calculations using the GULP code were first performed to examine the stabilities of the above surfaces. Then DFT calculations employing the GGA (PW91) approach were carried out with the VASP code to investigate their electronic structure and energy. The six upper atomic layers are fully relaxed in these five stepped slab models. Net charges on relevant atoms were calculated using the topologic Bader analysis from the GGA density which properly takes into account the changes in atomic volume accompanying a change in oxidation state.<sup>[24-25]</sup>

**Table 6.6** Calculated lattice energy and cohesive energy per ZrO<sub>2</sub> calculated at the interatomic potential and DFT-GGA level respectively.

System	ZrO <sub>2</sub>		CeO <sub>2</sub>
Method	IP	DFT(GGA)	DFT(GGA+U)
	E <sub>lat</sub> /unit cell (eV)	E <sub>coh</sub> /unit cell (eV)	E <sub>coh</sub> /unit cell (eV)
S1	-109.65	-27.88	-24.68
S2	-109.83	-27.94	-24.61
<b>S3</b>	<u>-109.85</u>	<b><u>-27.98</u></b>	<u>-24.73</u>
S4	-109.73	-27.67	-24.47
S5	-109.74	-27.66	-24.14

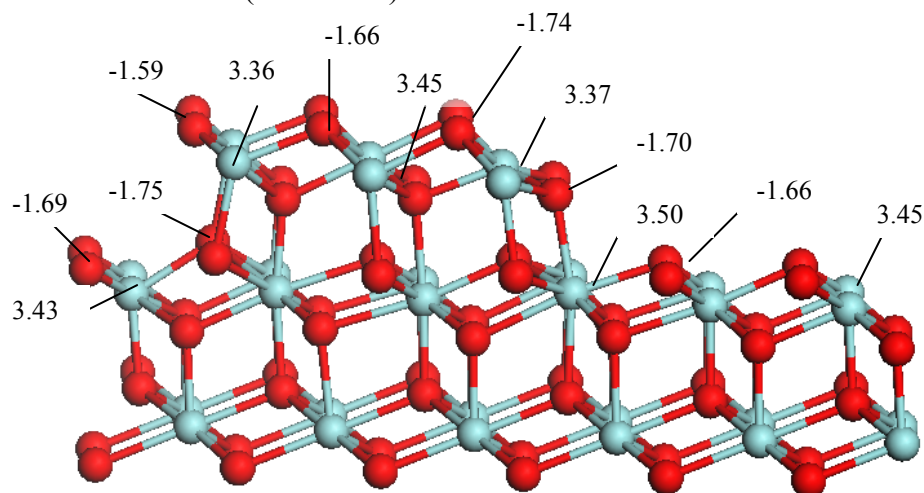
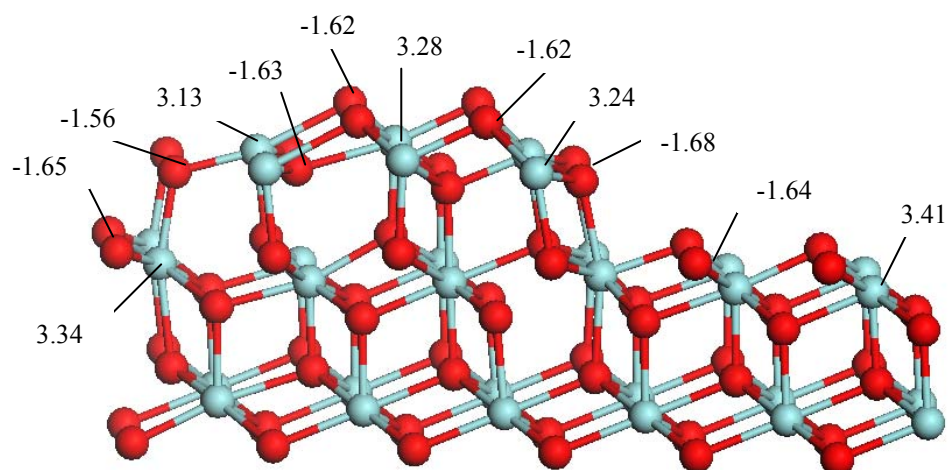


**Table 6.6** lists the results of the calculations which are compared with those for a previous CeO<sub>2</sub> study <sup>[22]</sup>. Among all the models tested, the **S3** step tends to achieve the most stable structure with little distortion of the initial step model, this is also the most stable step model suggested for CeO<sub>2</sub>. **S2** is the next most stable surface with an energy increase of less than 0.01 eV per unit cell. **S1**, **S4** and **S5** appear to have relatively large relaxations and greater cohesive (and lattice) energy. In particular, since classical IP calculations have limited tolerance to bond breaking and reformation, the energy convergence of the less stable step models can only be achieved with relatively large forces remaining on the atoms. However, from both IP and DFT calculations, the energy differences of these models are small.

Considering the coordination of Zr atoms at the edge sites (**Table 6.5**), there is a clear trend that the model preserving 6 coordinated Zr<sup>(6)</sup> atoms (i.e. **S3**) is more stable than that with Zr<sup>(5)</sup> (**S2**), Zr<sup>(4)</sup> (**S4**) and Zr<sup>(3)</sup> (**S5**) in sequence. And in the cases of **S1** and **S4**, which both have Zr<sup>(4)</sup> atoms, the one with a larger surface area and a smaller Zr<sup>(4)</sup> occupancy is more stable. By comparing the energy differences of these models, the existence of significantly reduced coordinations for the Zr atom (i.e. 4 or 3 coordinated) increases the instability of the step model, while the Zr atoms with less reduced coordination are more energetically favourable at the edge sites as in **S2** and **S3**.

The optimized structures of these two stable step surfaces **S3** and **S2** are analyzed in **Figure 6.10**. In the **S3** surface, the topologic Bader charge of Zr atoms on the step plane corresponding to a (-211) Miller index is only slightly lower than on the (111) terrace sites, and as high as in the (1-10) Miller indexes (the opposite side of the terrace). In the **S2** surface, the Bader charges of Zr on both sides of the terrace have been more significantly reduced, i.e. 3.24e and 3.13e, respectively. Therefore, the more stable model (**S3**) preserves higher charged Zr atoms at the surface sites.



**Figure 6.10** Bader charge analysis on the relaxed stepped surfaces **S3** (a) and **S2** (b).(a) Relaxed **S3** surface (Side View)(b) Relaxed **S2** surface (Side View)

### 6.5.2 Corner Model

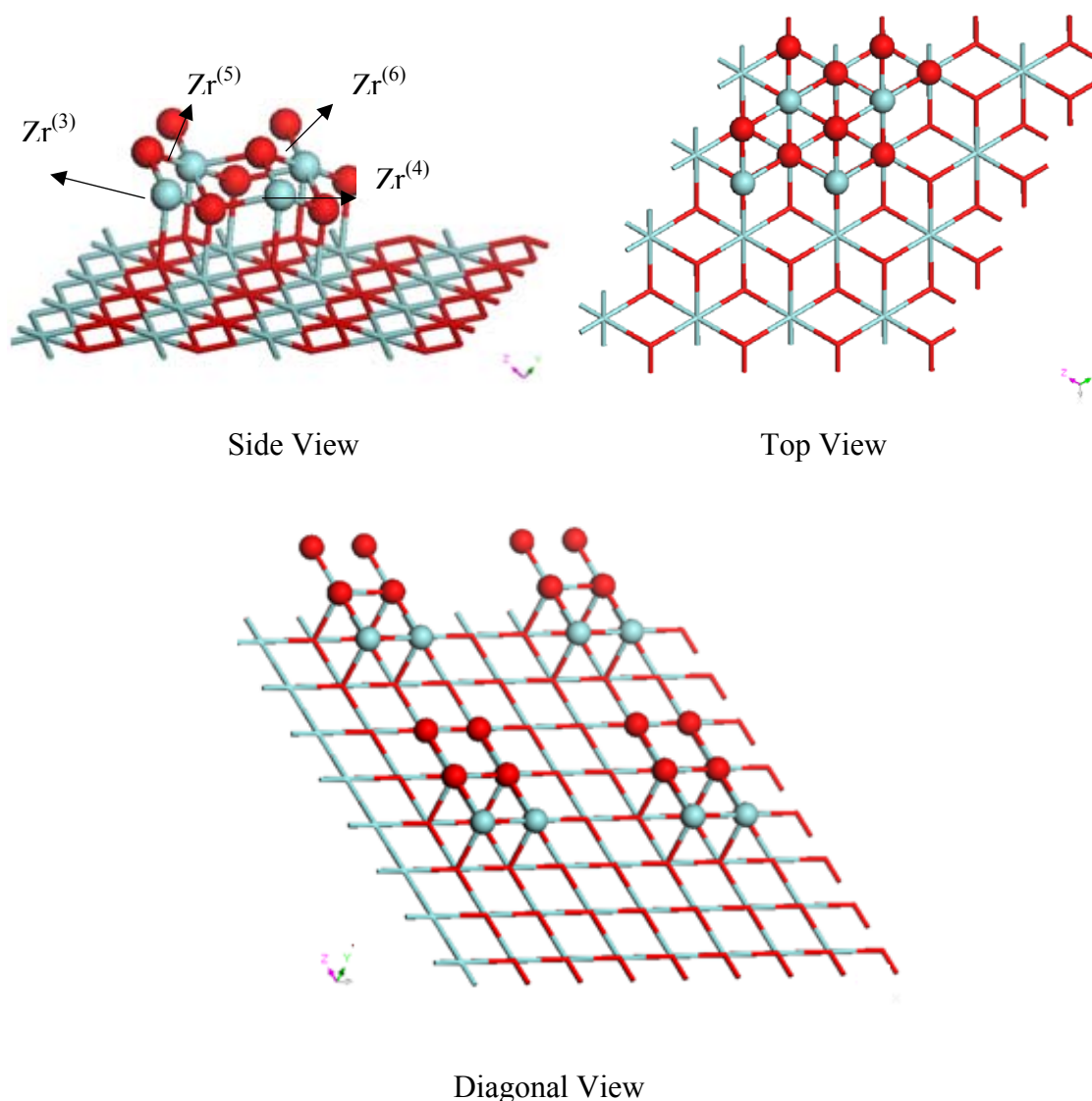
In this section, the cornered surface of pure  $\text{ZrO}_2$  is investigated by employing models corresponding to corners and kinks as shown in **Figure 6.11**. The models are derived from a  $4 \times 4$  supercell where six atomic layers were employed to form the periodic slab with an interval vacuum gap of  $\sim 15 \text{ \AA}$  width. The corner is generated by taking off half of the top trilayer along the (11-2) plane and then moving another half of the resulting  $4 \times 2$  supercell along the perpendicular (1-10) direction (**Figure 6.11-a**). Thus only a  $2 \times 2$  supercell remains on the top trilayer. In such a way, a higher coordination number for Zr atoms at the corner sites can be achieved as in the step model **S3**. The four Zr at



the corner sites are reduced to 6, 5, 4 and 3 coordination by oxygen, respectively. The reverse corner is formed by removing a 2x2 supercell from the top trilayers which is complementary to the corner model as displayed in **Figure 6.11-b**. The constructed kink model (reverse corner) preserves four  $\text{Zr}^{(6)}$  ions at the two edge sides of the terrace along (11-2) plane. On the perpendicular terrace of (1-10) plane,  $\text{Zr}^{(5)}$  and  $\text{Zr}^{(4)}$  are created at one edge site while two  $\text{Zr}^{(6)}$  are located in the opposite edge side. The two reverse corner site Zr ions are 7 and 6 coordinated by oxygen respectively.

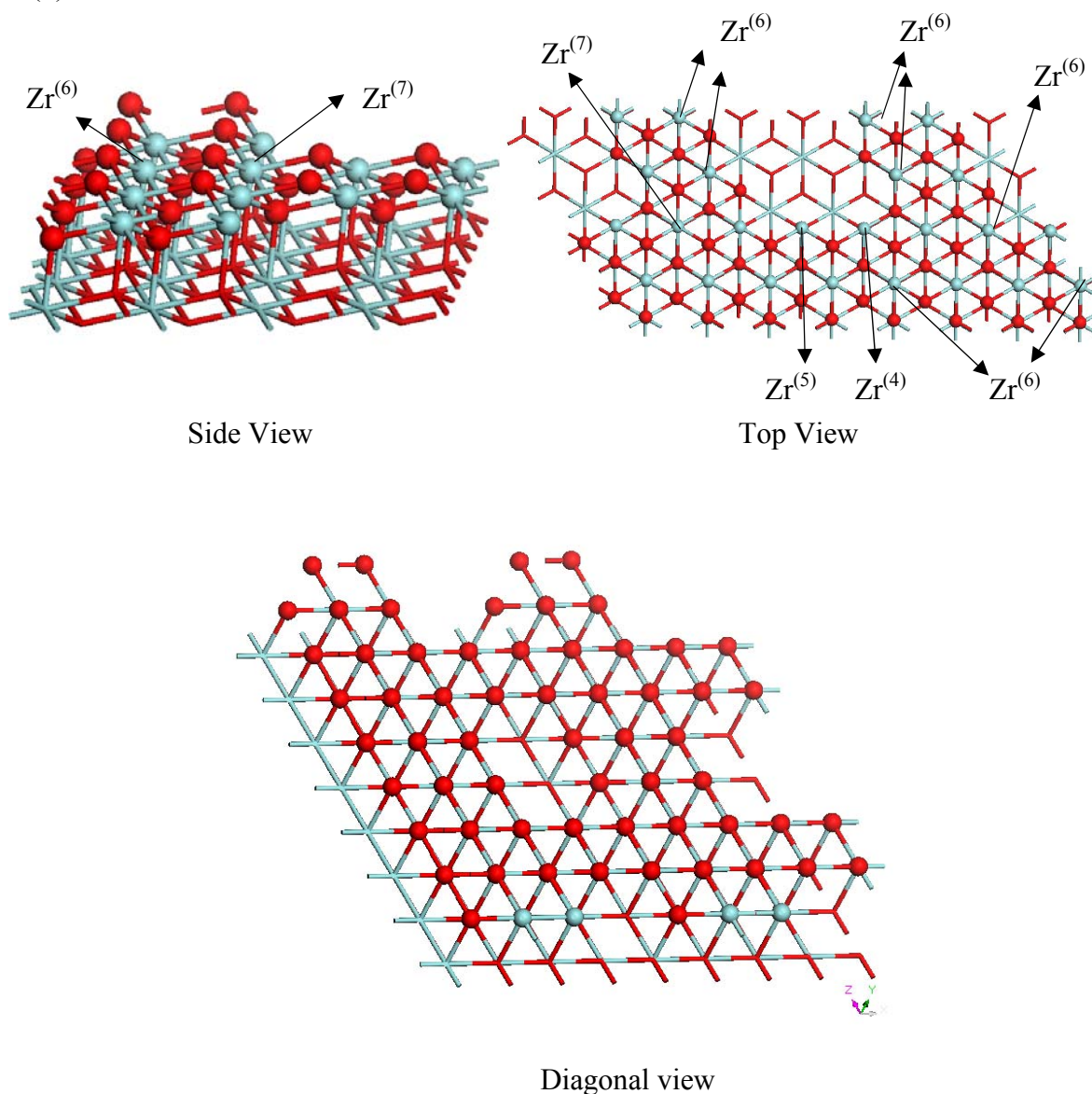
**Figure 6.11** Schematic views of the corner (a) and reverse corner (b) models for the (111) surface of  $\text{ZrO}_2$ . (Side View and Top View)

(a) Corner Model C1





(b) Kink Model C2



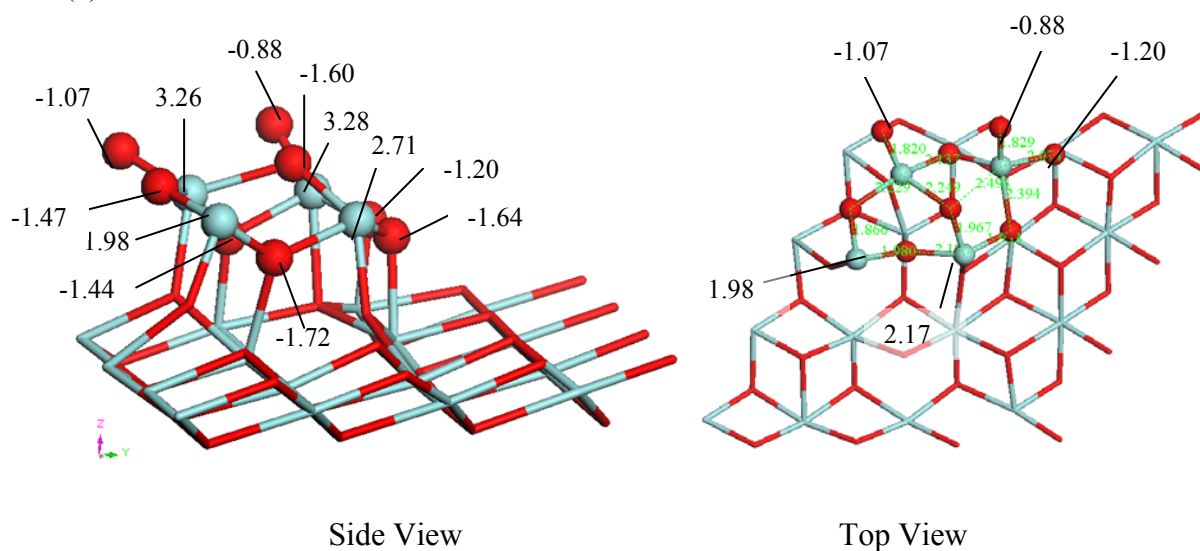
After optimization, the kink model **C2** is calculated to be the more energetically favourable than the corner model **C1** (see **Table 6.7**), which can be explained by the appearance of lower coordinated (charged) Zr atoms in the corner sites. The Bader charge analyses of the relaxed corner and reverse corner structures are illustrated in **Figure 6.12**. For the corner model **C1** (**Figure 6.12-a**), two highly bond unsaturated Zr ions with the Bader charge of +2.71e and +1.98e have been found at the corner sites, while two oxygen atoms in the opposite side, each one bonded to only one Zr atom (different in each case and with charges 3.28e and 3.26e), have dramatically increased their charges to around -1e. In contrast, Zr ions at the edge sites of the kink are much less reduced after extensive structure relaxation and correspondingly, no



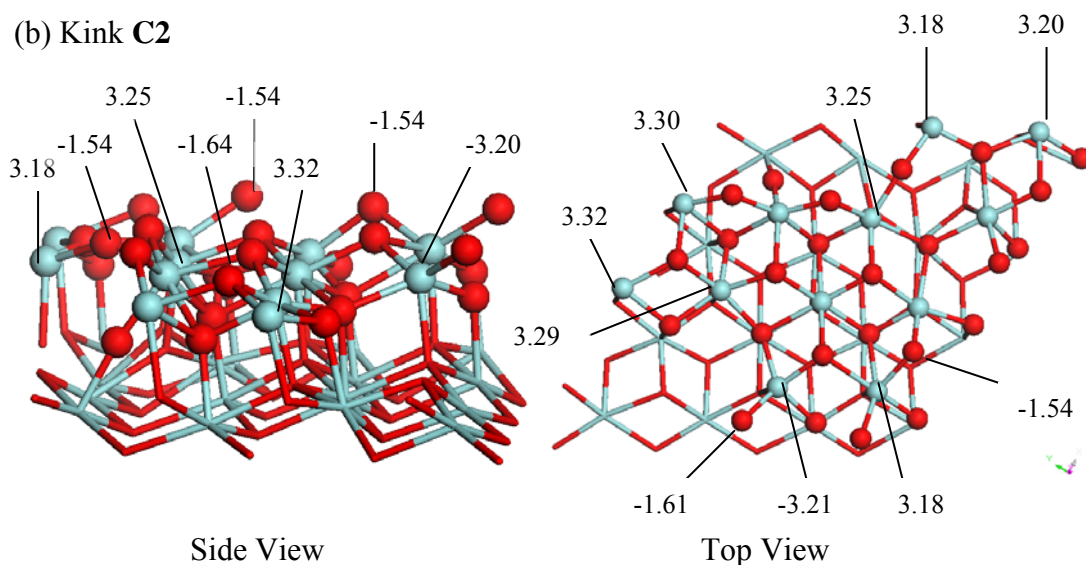
significant increments of topological Bader charge have been found for the top layer oxygen anions. In the kink model **C2**, the Bader charges on the four 6 coordinated Zr ion are about +3.30e while the 5 and 4 coordinated Zr ions are charged in a value around +3.20e. The topological charges on two reverse corner Zr ions are +3.25 and +3.28 respectively.

**Figure 6.12** Optimized corner models of the  $\text{ZrO}_2$  (111) surface showing selected interatomic distances (dashed lines) and topological (Bader) charges (solid lines). (a) Corner; (b) Kink. (Side View and Top View)

(a) Corner **C1**



(b) Kink **C2**





**Table 6.7** Calculated cohesive energy per  $\text{ZrO}_2$  and average Zr coordination number of topological surfaces. The average coordination number is calculated for Zr atoms in the top layer.

Model	Corner <b>C1</b>	Kink <b>C2</b>	Step <b>S3</b>	Plane	Plane
Surface	(111)	(111)	(111)	(111)	(110)
Formula	$\text{Zr}_{20}\text{O}_{40}$	$\text{Zr}_{28}\text{O}_{56}$	$\text{Zr}_{15}\text{O}_{30}$	$\text{Zr}_{12}\text{O}_{24}$	$\text{Zr}_{24}\text{O}_{48}$
Zr coordination (average)	4.5	6	6.3	7	6
$E_{\text{coh}}(\text{eV})$ /unit cell	-26.84	-27.67	-27.99	-28.12	-27.93

The calculated energies of different topological surfaces have been summarized with respect to average Zr coordination numbers as shown in **Table 6.7**. For all the tested models of the (111) surface, the stability is reduced with the average Zr coordination number in a sequence of plane > step > kink > corner. This finding is consistent with the previous study of zeolite plane surfaces, which proposed that the most stable surface cuts through the least number of bonds.<sup>[26]</sup> The step model, **S3**, for the (111) surface is even more energetically favourable than the (110) plane surface. However, although the kink model **C2** has the same average coordination number for Zr atoms at top layer as the (110) surface, the calculated energy suggest it is less stable than this surface model due to the presence of lower coordination  $\text{Zr}^{(5)}$  and  $\text{Zr}^{(4)}$  ions. Indeed, the lower stability of the corner models could also possibly be an artefact of the use of a thinner slab compared to the 6 layer slab employed for (110) plane, the feasibility of calculation with a thicker slab were prohibitively expensive. The relatively stable plane and step (111) surfaces will be used for the next stage of the study involving oxygen adsorption.

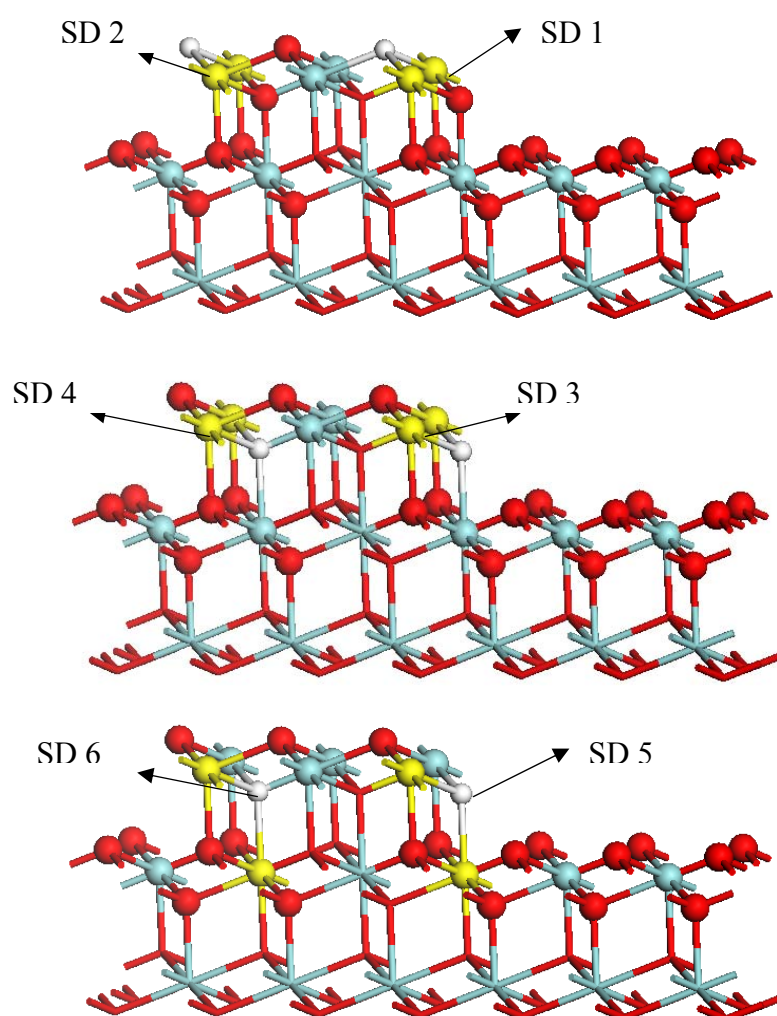
### 6.5.3 Defect Sites on Stepped Surfaces

As concluded in above section, the **S3** step model is only slightly less stable than the (111) plane surface for c- $\text{ZrO}_2$ . In order to generate a realistic model for the study of



oxygen adsorption on YSZ step surface, the most stable defect sites for oxygen vacancies and yttrium dopants in the step have been identified by creating a model (formula  $\text{Y}_2\text{Zr}_{28}\text{O}_{59}$ ) derived from the **S3** stepped surface (as discussed in section 6.5.1). The Y-V-Y cluster has been located at six different defect sites involving two sides of the (111) terrace and both the upper and lower edge oxygen vacancies sites as displayed in **Figure 6.13**.

**Figure 6.13** Stepped surface models for YSZ (Side View). (Zr ●; Y ●; O ●; O vacancy ○)



The calculated energies of optimised YSZ step structures are listed in **Table 6.8**. According to which, the defect site **SD5** with the oxygen vacancies located in the lower edge sites and the Y-V-Y defect cluster lying along  $\langle 100 \rangle$  direction is the most stable configuration. The average cohesive energy of **SD5** step is 0.19 eV higher than the bulk value derived from -9.50 eV per atom for  $\text{Y}_2\text{Zr}_{32}\text{O}_{63}$ , and closer to the value



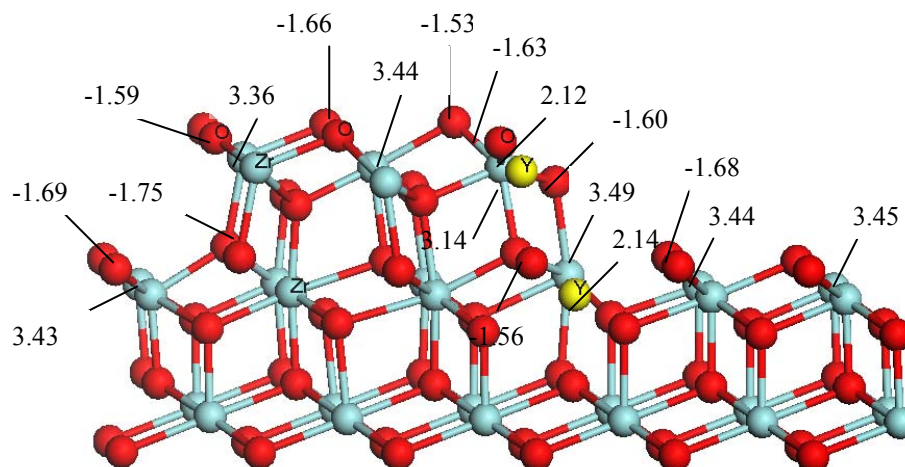
obtained for the yttrium segregated (111) surface of -9.41 eV for the  $\text{Y}_2\text{Zr}_{18}\text{O}_{39}$  surface with the same defect configuration but a higher yttrium concentration of 10%. This planar surface is also the most stable surface structure of YSZ found from the yttrium surface segregation study in section 6.4)

**Table 6.8** Cohesive energy of stepped (111) surfaces of yttria-stabilized zirconia ( $\text{Y}_2\text{Zr}_{28}\text{O}_{59}$ ).

$\text{Y}_2\text{Zr}_{28}\text{O}_{59}$	<b>SD1</b>	<b>SD2</b>	<b>SD3</b>	<b>SD4</b>	<b>SD5</b>	<b>SD 6</b>
$E_{\text{tot}}$ (eV)	-827.88	-827.47	-827.01	-827.60	<b><u>-828.36</u></b>	-827.77
$E_{\text{coh}}$ (eV) per atom	-9.30	-9.30	-9.29	9.30	<b><u>-9.31</u></b>	-9.30

The topological charge analysis of the **SD5** stepped surface is shown in **Figure 6.14**. The co-existence of yttrium and oxygen vacancy decrease the Bader charges of the Zr cations on the neighbouring edge sites to a value of +3.14e.

**Figure 6.14** Bader charge analysis on the relaxed step of the YSZ (111) surface. (Side View)



The **SD5** model with the most energetically favourable defect configuration on the step surface will be used for the  $\text{O}_2$  dissociation study in Chapter 8.



## 6.6 Conclusions

The quantum mechanical simulations in this chapter have reproduced the three low pressure phase of zirconia with the correct order of stability which is monoclinic > tetragonal > cubic and energy difference for two phase transition of  $E_m - E_t = 0.05 - 0.09 \text{ eV}$  and  $E_t - E_c = 0.04 - 0.05 \text{ eV}$  in good agreement with available experimental data.

The effects of oxygen vacancy formation and yttria doping have been investigated for both the bulk and surfaces of YSZ. The oxygen vacancy formation energies for the (111) and (110) surface have been found to be 5.83 and 4.43 eV, respectively, which is lower than the energy value of  $\sim 5.9 \text{ eV}$  calculated for the bulk structures.

Yttrium segregation has been studied for the most stable surface of c-ZrO<sub>2</sub> (111) by DFT-GGA calculations. The results suggest yttrium enrichment at the top layers up to a depth of  $\sim 4 \text{ \AA}$ , in agreement with the results of the interatomic potential based calculations present in chapter 5.

Based on the dominant (111) surface of c-ZrO<sub>2</sub>, a variety of stepped and cornered models have been designed with increasing topological complexity. The relative stability of these models, which has been calculated to be plane > step > kink > corner, and the stability varies monotonically with the coordination number of Zr at the surface sites; a lower coordination state of Zr corresponds to a higher energy of the system. In addition, for the most stable stepped (111) surface, the energetically favorable defect sites of yttrium and oxygen vacancy have been indentified. In all cases, the most stable plane and stepped pure and Y doped surface have been selected to serve as basis for further adsorption studies in succeeding chapters.



## Reference

- 
- [1] P. E. Blochl, *Phys. Rev. B* **50**, 17953, **1994**.
  - [2] G. Kresse, D. Joubert, *Phys. Rev. B* **59**, 1758, 1999.
  - [3] G. P. Francis and M. C. Payne, *J. Physics-Condensed Matter*. **2**, 4395, 1990.
  - [4] N. I. Medvedeva, V. P. Zhukov, M. Ya. Khodos and V. A. Gubanov, *Phys. Status Solidi. B* **160**, 517, 1990.
  - [5] L. Soriano, M. Abbate, J. Faber, C. Morant, and J. M. Sanz, *Solid State Commun.* **93**, 659, 1995; L. Soriano, M. Abbate, J. C. Fuggle, M. A. Jimenez, J. M. Sanz, C. Mythen, and H. A. Padmore, *ibid.* **87**, 699, 1993.
  - [6] M. Morinaga, H. Adachi, and M. Tsukada, *J. Phys. Chem. Solids* **44**, 301, 1983.
  - [7] J. M. Sanz, A. R. González-Elipse, A. Fernández, D. Leinen, L. Galán, A. Stampfl, and A. M. Bradshaw, *Surf. Sci.* **307/309**, 848, 1994.
  - [8] C. J. Howard, R. J. Hill, and B. E. Reichert, *Acta Crystallogr. Sect. B: Struct. Sci.* **44**, 116, 1988.
  - [9] C. T. Lynch, *"Handbook of Materials Science"*, CRC Press, Cleveland, **I**, 330, 1974.
  - [10] G. Teufer, *Acta Crystallogr.* **15**, 1187, 1962.
  - [11] H. J. F. Jansen, *Phys. Rev. B* **43**, 7267, 1991.
  - [12] R. J. Ackermann, E. G. Rauh, and C. A. Alexander, *High Temp. Sci.* **7**, 304, 1975.
  - [13] G. Jomard, T. Petit, A. Pasturel, L. Magaud, G. Kresse and J. Hafner *Phys. Rev. B* **59**, 4044, 1999
  - [14] R. H. French, S. J. Glass, F. S. Ohuchi, Y. N. Xu, and W. Ching, *Phys. Rev. B* **49**, 5133, 1994
  - [15] E. V. Stefanovich, A. L. Shluger and C. R. A. Catlow, *Phys. Rev. B* **49**, 5133, 1994.
  - [16] D. W. McComb, *Phys. Rev. B* **54**, 7094, 1996.
  - [17] R. Grau-Crespo, I. de P. R. Moreira, F. Illas, N. H. de Leeuwac and C. R. A. J. *Mater. Chem.* **16**, 1943, 2006.
  - [18] Ricardo Grau-Crespo, Norge Cruz Hernández, Javier F. Sanz, and Nora H. de Leeuw, *J. Phys. Chem. C* **111**, 10448, 2007.



- [19] N. H. de Leeuw, J. A. Purton, S. C. Parker, G. W. Watson and G. Kresse, *Surf. Sci.* **9**, 452, 2000.
- [20] Y. Jiang, J. B. Adams, M. J. van Schilfgaarde, *Chem. Phys.* **123**, 064701, **2005**.
- [21] C. Loschen, S. T. Bromley, K. M. Neyman, and F. Illas *Phys. Chem. Chem. Phys.* **11**, 10142, 2007.
- [22] C. Loschen, A. Migani, S. T. Bromley, F. Illas and K. M. Neyman *Phys. Chem. Chem. Phys.* **10**, 5730, 2008.
- [23] M. M. Brande, C. Loschen, K. M. Neyman and F. Illas, **112**, 17643, 2008.
- [24] R. F. W. Bader, P. M. Beddall, *J. Chem. Phys.* **56**, 3320, 1972.
- [25] R. F. W. Bader, "*Atoms in Molecules – A Quantum Theory*", Clarendon Press; Oxford, 1994.
- [26] Manisha Mistry, "The surface structure and growth of natural zeolite." *Phd. Thesis*, University College London 2005.



## Chapter 7 Quantum Mechanical Studies of Oxygen Adsorption

*Everything is happening, happening to one.*

-- "The garden of forking paths" Jorge Luis Borges

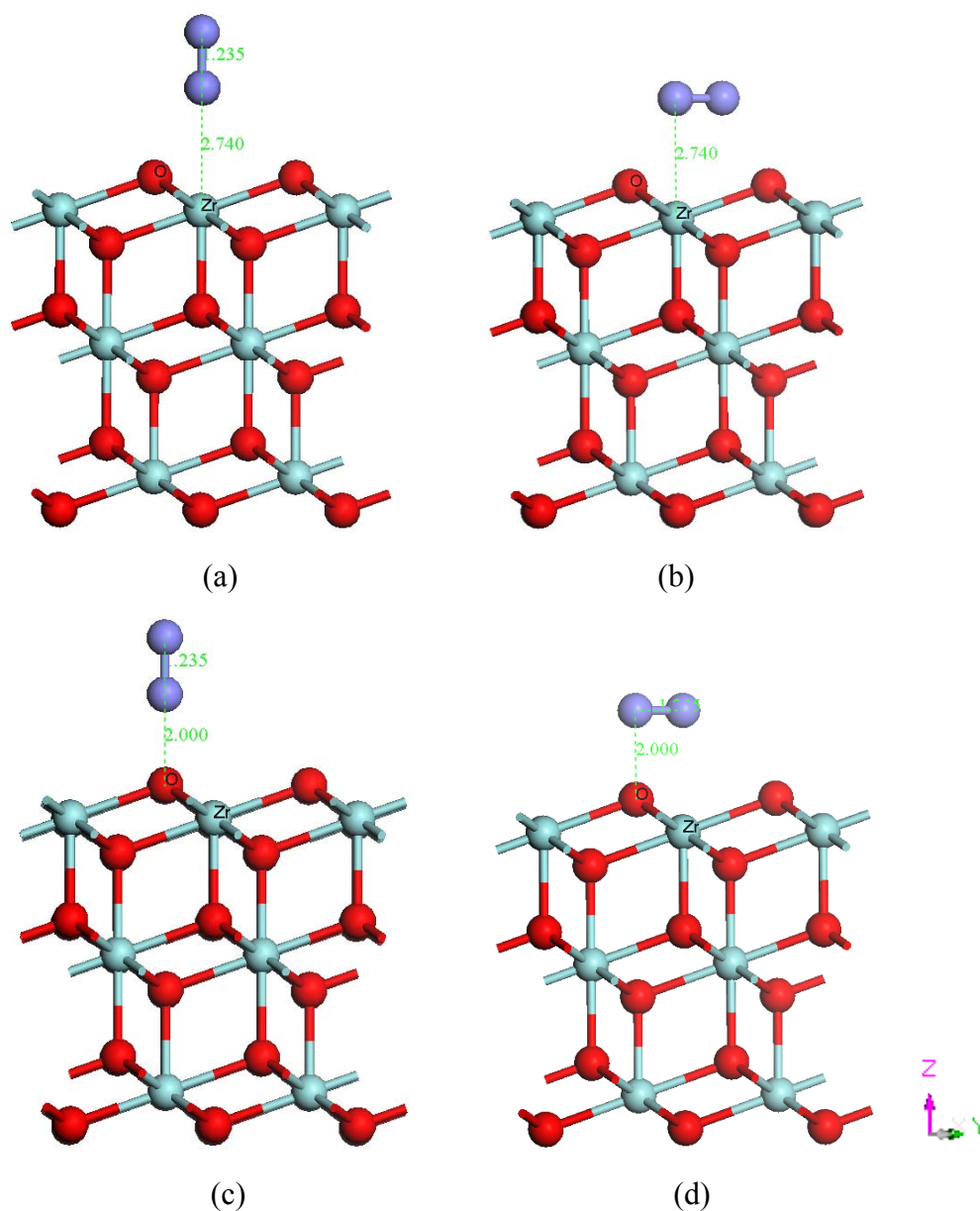
Quantum mechanical simulation can provide a powerful approach to studying the electronic structure and energy states of reaction intermediates as well as the bulk and surface of  $\text{ZrO}_2$  as discussed in the last chapter and thus allow insight into catalytic mechanisms on specific crystallographic surfaces and defect sites such as oxygen vacancies. This information is of vital importance in understanding the activity of catalytic materials, but is difficult to obtain by experimental measurements alone. In this chapter, density functional theory calculations utilizing the VASP code have been applied to explore the interaction between molecular oxygen and the dominant (111) surface of pure and yttria stabilized zirconia. According to the calculated energetic results and structure geometry, the probable reaction pathways for  $\text{O}_2$  dissociation were predicted in relation to the defect configuration of the substrate model. A perspective of the oxygen adsorption states on the (111) plane surface has been provided by the analysis of density of states (DOS), topological Bader charges and spin magnetization.

### 7.1 $\text{O}_2$ Adsorption on the Plane (111) Surface of Pure $\text{ZrO}_2$

Based on the oxygen terminated (111) surface model with a thickness of three trilayer as developed in Chapter 6,  $\text{O}_2$  adsorption on pure  $\text{ZrO}_2$  has been studied with respect to the molecular orientation and adsorption sites. The  $2 \times 2$  arrays of hexagonal surface unit cells containing 4 Zr and 4 upper sites O provides an  $\text{O}_2$  coverage of  $1/8$  ML. In order to find the minimum energy configuration for the adsorption, different initial geometries were generated. Two possible adsorption sites on the top of the surface, i.e.



over Zr or O atoms have been investigated as in **Figure 7.1**. The orientation of the O<sub>2</sub> molecule approaching the surface was examined by relaxing the O<sub>2</sub> molecule initially either parallel or perpendicular to the (111) surface of ZrO<sub>2</sub> (i.e. horizontally and vertically orientated O<sub>2</sub>) at distances of 2.0 Å above the surface oxygen (substantially larger than equilibrium O-O bond length of 1.235 Å in O<sub>2</sub>) or 2.7 Å above surface Zr (again larger than equilibrium Zr-O bond length of 2.221 Å in ZrO<sub>2</sub>), as shown in **Figure 7.1**.



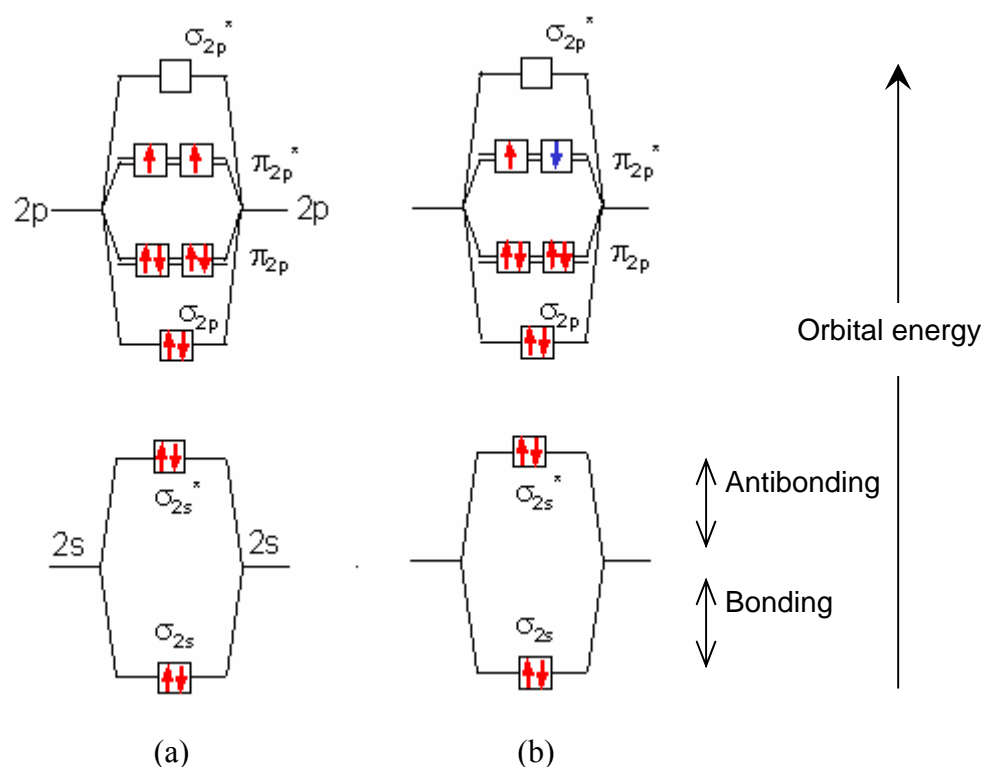
**Figure 7.1** The models for O<sub>2</sub> approaching the (111) surface of ZrO<sub>2</sub> (Side view): O<sub>2</sub> above surface Zr site in vertical orientation (a) and horizontal orientation (b); O<sub>2</sub> above surface O site in vertical orientation (c) and horizontal orientation (d).



The DFT calculations were carried out by VASP code employing the PAW-GGA method with a plane wave cut-off of 500eV and 3x3x1  $k$ -point mesh, whereas for the final single-point runs for the calculation of the electronic density of states, a denser mesh of 5x5x1 points was employed. The iterative relaxation of atomic positions was stopped when the forces on the atoms were less than 0.01eV/Å. All following calculations for oxygen adsorbed systems were performed at a spin polarized level. The influence of spin polarization is discussed below.

### 7.1.1 Spin Polarization

Spin polarization effect must be considered for a system containing species with non-zero spin such as O<sub>2</sub>. The spin configurations for the O<sub>2</sub> molecule adsorbed on the ZrO<sub>2</sub> surface have been studied in terms of “triplet” and “singlet” state as shown in **Figure 7.2**.



**Figure 7.2** Schemes of electronic structure of the homonuclear oxygen molecule with triplet (a) and singlet (b) spin configurations.

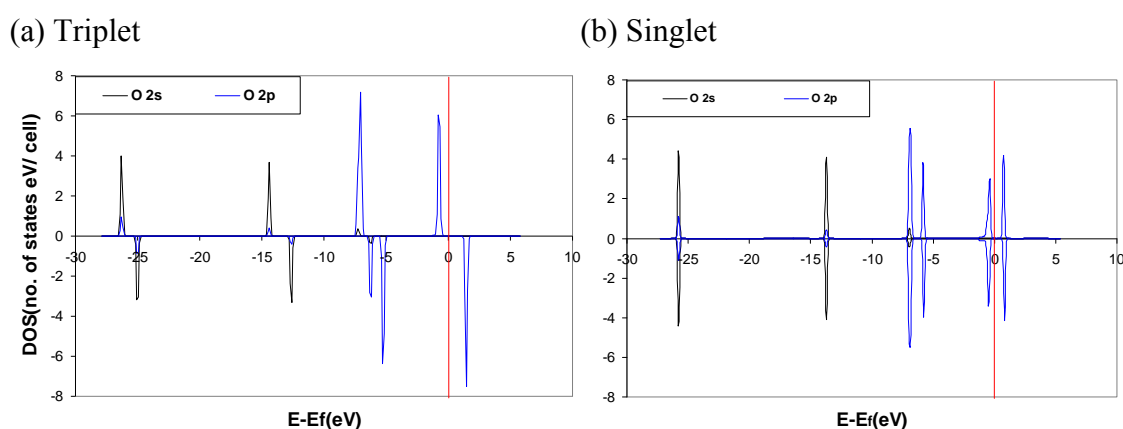
The calculations show as expected, that in the ZrO<sub>2</sub>-O<sub>2</sub> system, the triplet state is lower in energy than the singlet state by 0.45eV. Spin polarization has also been estimated



for the  $\text{ZrO}_2$  system, only a very tiny energy difference of  $0.4 \times 10^{-5}$  eV found between the spin polarised and unpolarised  $\text{ZrO}_2$  (111) surface that was studied in Chapter 6. Thus, the total energy difference of the  $\text{ZrO}_2\text{-O}_2$  system is therefore, as anticipated, mainly due to the spin polarization effect of  $\text{O}_2$ .

The DOS for the neutral oxygen atoms of  $\text{O}_2$  with triplet and singlet spin configuration are presented in **Figure 7.3**. The singlet spin configuration adopts a symmetric DOS pattern with two O 2s peaks at a lower energy level and four O 2p peaks at a higher energy level. In contrast, for the oxygen atom of triplet  $\text{O}_2$ , the spin-down peaks have been shifted to a higher energy level than the spin-up and an unpaired spin-up peak of O 2p appears at around -6 eV. The diversity of spin-up and spin-down peaks indicates a non-zero magnetic dipole moment has been introduced by the two single electrons of  $\pi_{2p}$  orbital with a ferromagnetic spin configuration.

**Figure 7.3** Density of state for neutral oxygen atoms of the undissociated  $\text{O}_2$  molecule with triplet (a) and singlet (b) spin configurations.



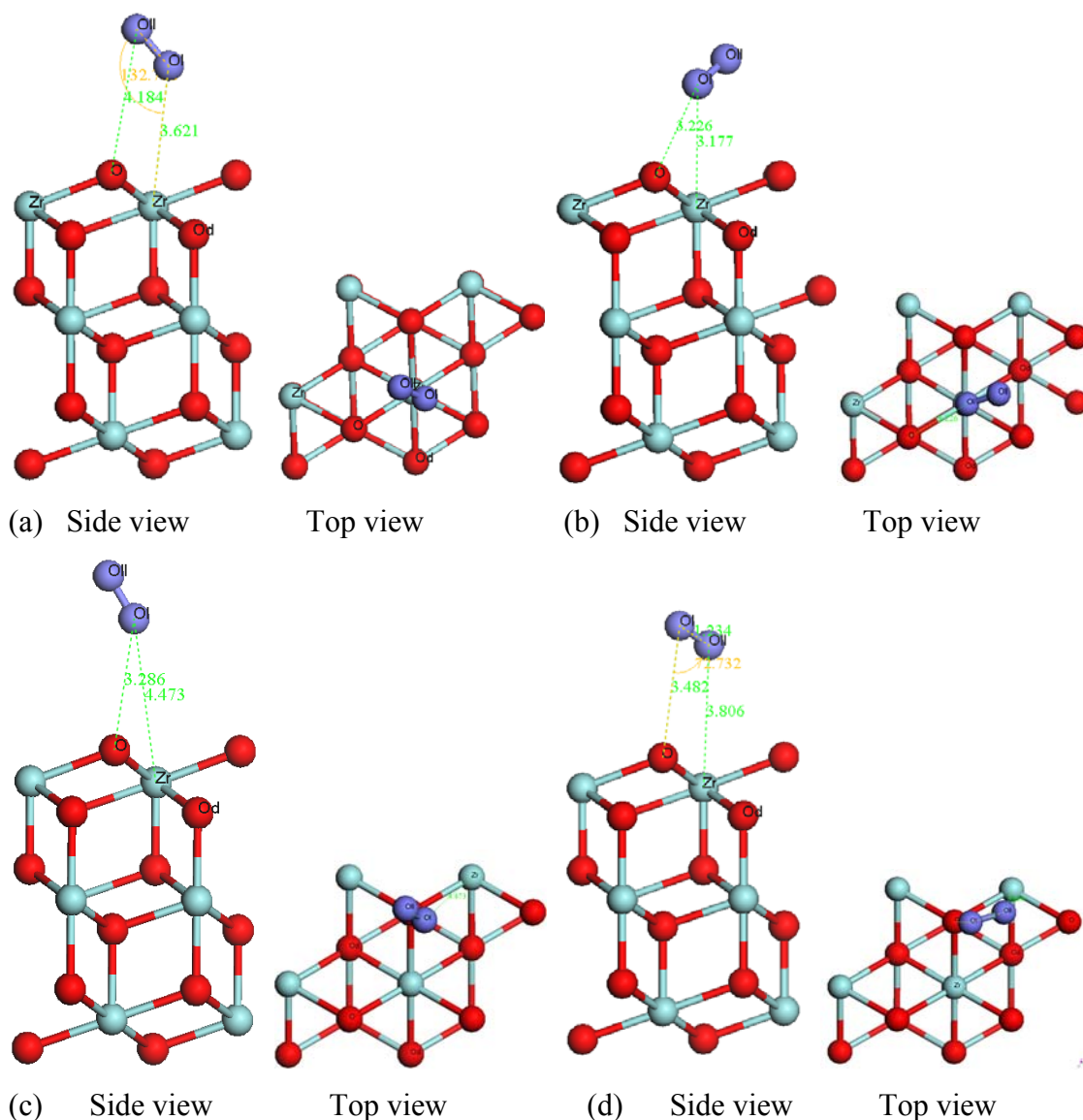
In addition to the triplet  $\text{O}_2$  molecule, the superoxy  $\text{O}_2^-$  and radical  $\text{O}^-$  with one singly electron also have non-zero spin. The peroxy  $\text{O}_2^{2-}$  and lattice anion  $\text{O}^{2-}$  are singlet species. The spin polarization effects of oxygen species are studied in the subsequent calculations investigating their adsorption states.



### 7.1.2 Adsorption Sites

The effect of  $O_2$  adsorption sites and orientations are compared in the following section. **Table 7.1** lists the main geometric and energetic results obtained from the initial models (**Figure 7.1**) and the corresponding relaxed structures are presented in **Figure 7.4**. The adsorption energy  $E_{ads}$  in **Table 7.1** is derived by comparing the energy difference of the  $O_2$  adsorbed system  $E_{tot}$  and the pure  $ZrO_2$  surface  $E[ZrO_2]$  plus an isolated  $O_2$  molecule with  $E[O_2]$  of 9.826 eV, i.e.  $E_{ads} = E_{tot} - E[ZrO_2] - E[O_2]$ .

**Figure 7.4** The optimised adsorption sites of  $O_2$  on the (111) surface of pure  $ZrO_2$  (Side View and Top View). (a), (b), (c) and (d) are the relaxed structures for the corresponding models in **Figure 7.1**.





**Table 7.1** Geometric and energetic results for O<sub>2</sub> adsorption on the pure ZrO<sub>2</sub> (111) surface. O<sub>I</sub> and O<sub>II</sub> represent the two atoms in undissociated O<sub>2</sub>, O<sub>I</sub> relates to the end of molecule close to the surface site.

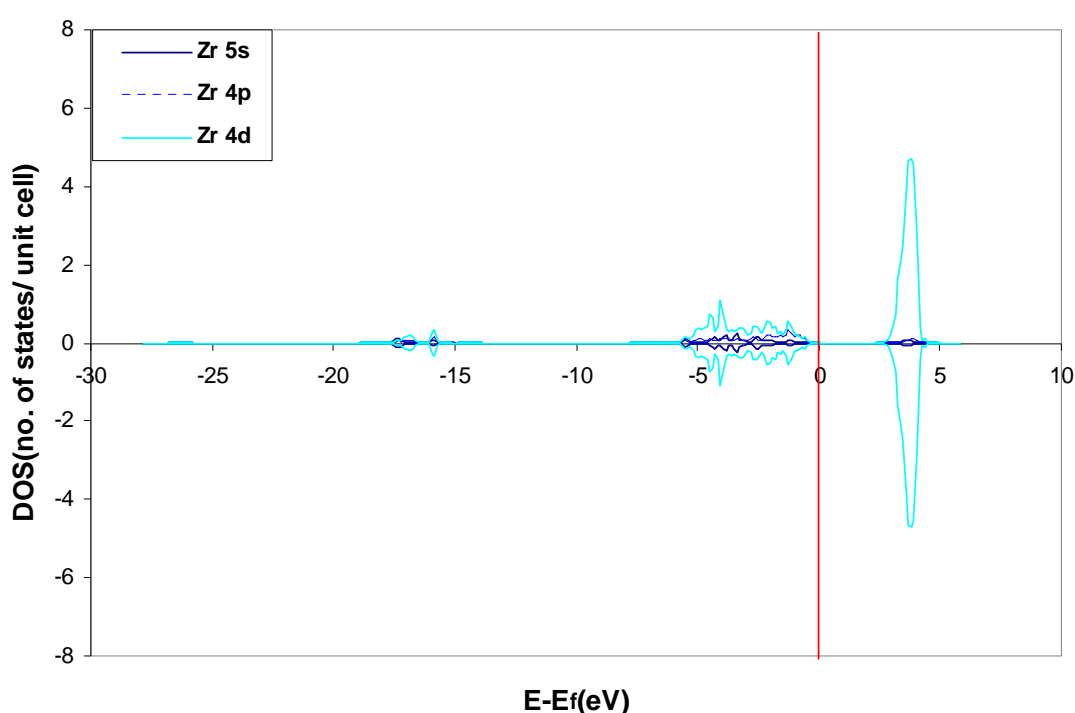
O <sub>2</sub> -Zr <sub>12</sub> O <sub>24</sub>	a	b	c	d
d(O <sub>I</sub> -O <sub>II</sub> ) Å	1.233	1.234	1.234	1.234
d(O <sub>I</sub> -Zr) Å	3.642	3.177	4.473	4.574
d(O <sub>I</sub> -O) Å	3.621	3.226	3.286	3.482
d(O <sub>II</sub> -Zr) Å	4.549	3.967	5.547	3.806
d(O <sub>II</sub> -O) Å	4.184	4.408	4.310	3.331
<O <sub>II</sub> O <sub>I</sub> Zr	132.763°	121.695°	146.758°	45.170°
<O <sub>II</sub> O <sub>I</sub> O	107.664°	160.461°	140.433°	72.732°
E <sub>tot</sub> eV	-347.346	-347.343	-347.331	-347.343
E[ZrO <sub>2</sub> ] eV	-337.486	-337.486	-337.486	-337.486
ΔE eV	-9.859	-9.857	-9.845	-9.857
E <sub>ads</sub> eV	<b>-0.033</b>	-0.031	-0.019	-0.031

The calculated results show that configuration (a) in **Figure 7.4**, where the O<sub>2</sub> molecule adsorbs at the Zr site on the surface with the O-O bond almost parallel the Zr-O bond of the surface ZrO<sub>2</sub>, is most stable, although configurations (b) and (d) are very close in energy. The absorption distance between O<sub>2</sub> and the surface Zr ion is shown to be 3.62 Å with <O<sub>II</sub>O<sub>I</sub>Zr angle of 132.8°. The adsorption energy varies for other optimised configurations of O<sub>2</sub> adsorption. Adsorption is slightly exothermic releasing 3.18 kJ for per mole O<sub>2</sub>. The O<sub>I</sub>-O<sub>II</sub> bond length of the adsorbate remains at the original equilibrium bond distance of the O<sub>2</sub> molecule. The charge states have been analysed by examining the topological Bader charge, which is negligible on the adsorbate. In all cases, the sum of charges on O<sub>I</sub>-O<sub>II</sub> is calculated to be around -0.01e, while the topological charge on the adsorption site Zr remains as +3.45e, suggesting a very slightly interaction between the O<sub>2</sub> and surface atoms. It can therefore be concluded that only weak physisorption of O<sub>2</sub> occurs on the oxygen terminated (111) surface of pure ZrO<sub>2</sub>, although we note that the physisorption energy might be underestimated since DFT method do not take dispersion effect (van der waals interactions) into account properly.<sup>[1]</sup>



The DOS of two oxygen atoms of the O<sub>2</sub> adsorbate are shown in **Figure 7.3** (a) for the triplet spin configuration. The partial DOS for Zr ion at the adsorption sites has been sketched for the most stable O<sub>2</sub> orientation, (a), in **Figure 7.5**. In comparison with **Figure 6.4-b** in Chapter 6 for c-ZrO<sub>2</sub> bulk, 4d character is retained for the surface Zr cation. Little change can be identified except that the density peak in the upper band around 4 eV has been slightly reduced.

**Figure 7.5** Partial density of states for Zr adsorption sites on the outmost layer of the (111) surface.

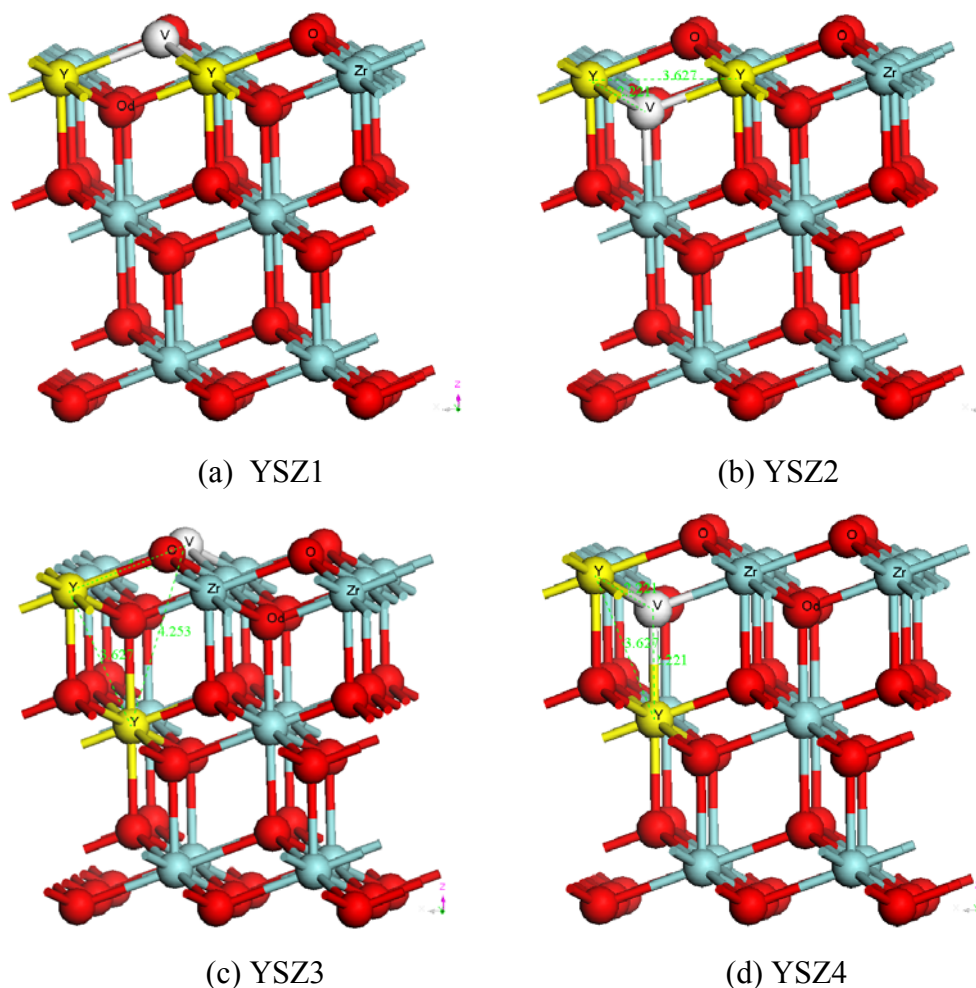


## 7.2 O<sub>2</sub> Adsorption on the Plane (111) Surface of YSZ

In the case of O<sub>2</sub> adsorption on the yttrium doped zirconia surface, the defect configurations as well as the compositions of the surface must be considered. Four YSZ surfaces with different defect configurations denote as YSZ1, 2, 3 and 4 in **Figure 7.6**, were constructed as substrate models for oxygen adsorption. For all these surface models, the two Y are located in the nearest neighbour sites to each other lying in either the  $\langle 110 \rangle$  direction (X) or  $\langle 100 \rangle$  direction (Z) while in the YSZ2 and 4, the oxygen vacancies are shifted from the outer most layers of YSZ1 and 3 to the subsurface. The YSZ composition in the trilayer slab is set to be  $\sim 8\%$  mol of Y<sub>2</sub>O<sub>3</sub>, i.e.



as which concentration we would expect the cubic phase to be stable. However, the yttrium content in the outmost layer of the surface varies in each case from 1/4 to 1/2 (i.e. 1/2 for the X direction defect in models YSZ1 and YSZ2 and 1/4 for the Z direction defect in YSZ3 and YSZ4). Two initial orientations of  $O_2$ , horizontal (H) and vertical (V), have been investigated as in the pure  $ZrO_2$  surface. The coverage of  $O_2$  on the (111) surface is also 1/8 ML.



**Figure 7.6** Models of the Y-V-Y defect sites on the (111) surface of YSZ. (a)YSZ1: Oxygen vacancy at the outmost layer, two NN sites Y along the X direction; (b) YSZ2: Oxygen vacancy in the subsurface layer, two Y along the X direction; (c) YSZ3: Oxygen vacancy at the outmost layer, two NNN sites Y along the Z direction; (d) YSZ4: Oxygen vacancy at the subsurface layer, two NN sites Y along the Z direction.



**Table 7.2** Calculation results for oxygen adsorption on the (111) surface of YSZ.

$\text{Y}_2\text{Zr}_{10}\text{O}_{23}$ / $\text{O}_2$	(a) YSZ1		(b) YSZ2		(c) YSZ3		(d) YSZ4	
	V	H	V	H	V	H	V	H
$\angle \text{ZrO}_\text{I}\text{Y}$	87.061°	87.486°	41.222°	117.794°	53.082°	47.931°	52.379°	61.669°
$\angle \text{ZrO}_\text{II}\text{Y}$	63.061°	77.595°	35.105°	121.811°	43.057°	37.610°	40.508°	46.160°
$d(\text{Y}-\text{O}_\text{I}) \text{ \AA}$	2.670	2.990	3.932	3.756	4.547	4.914	3.899	4.118
$d(\text{Zr}-\text{O}_\text{I})$ $\text{ \AA}$	2.910	2.534	5.662	3.855	3.340	3.598	4.398	2.244
$d(\text{O}-\text{O}) \text{ \AA}$	1.275	1.303	1.235	1.425 ( $\text{O}_\text{I}-\text{O}_\text{II}$ ) 1.526 ( $\text{O}_\text{I}-\text{O}$ )	1.235	1.235	1.235	1.324 ( $\text{O}_\text{I}-\text{O}_\text{II}$ ) 1.759 ( $\text{O}_\text{I}-\text{O}$ )
<b>Etot eV</b>	-335.660	-335.734	-335.805	-334.830	-336.497	<u>-336.537</u>	-336.479	-335.427
<b>E<sub>YSZ</sub> eV</b>	-325.466	-325.466	-325.956	-325.956	-326.617	-326.617	-326.685	-326.685
<b><math>\Delta E</math> eV</b>	-10.195	-10.269	-9.850	-8.874	-9.880	-9.920	-9.794	-8.742
<b>E<sub>ads</sub> eV</b>	-0.369	<u>-0.443</u>	-0.024	+0.948	-0.054	-0.094	+0.033	+1.084
<b>Oxygen species</b>	$\text{O}^{-0.32}$ $-\text{O}^{-0.02}$	$\text{O}^{-0.18}$ $-\text{O}^{-0.12}$	$\text{O}^{-0.05}$ $-\text{O}^{+0.03}$	$\text{O}^{-0.57}$ $-\text{O}^{0.19}$ $-\text{O}^{-0.88}$	$\text{O}^{-0.03}$ $-\text{O}^{-0.01}$	$\text{O}^{-0.13}$ $-\text{O}^{-0.07}$	$\text{O}^{-0.02}$ $-\text{O}^{+0.01}$	$\text{O}^{-0.48}$ $-\text{O}^{0.17}$ $-\text{O}^{-1.13}$



### 7.2.1 Geometries and Energies

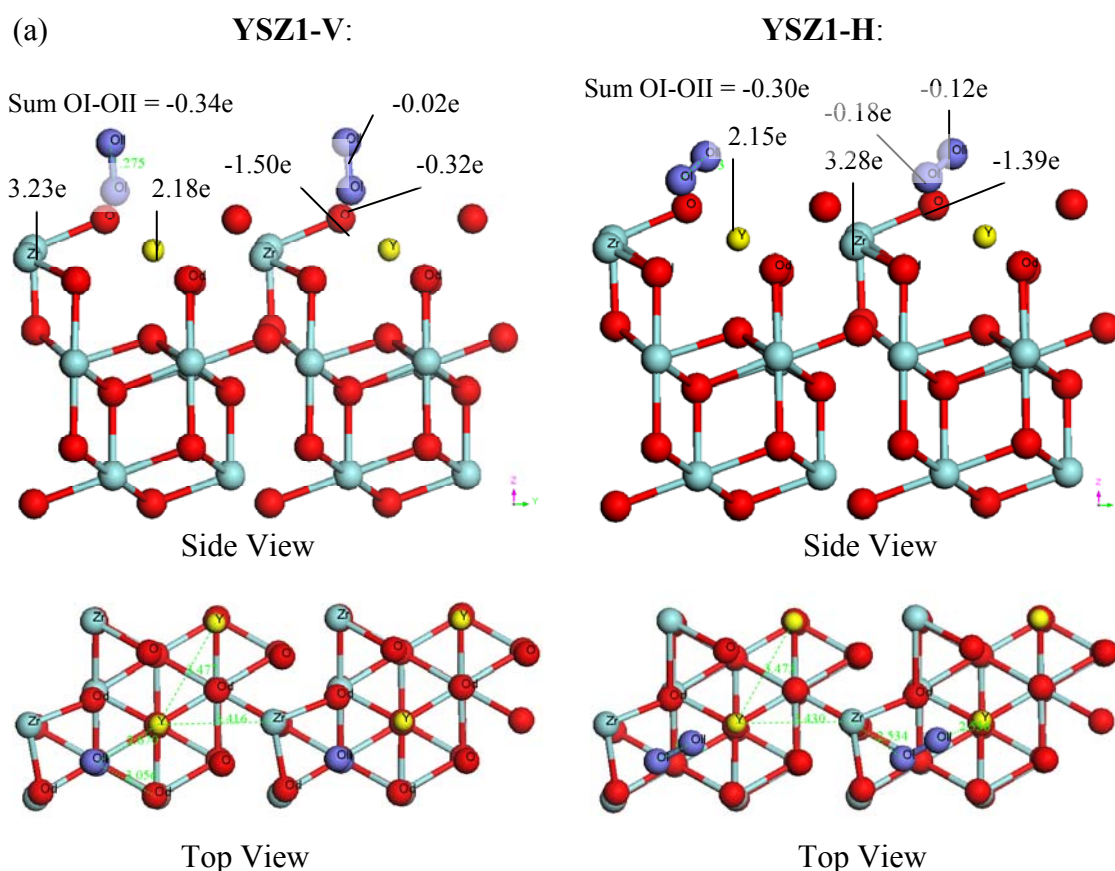
The optimised structures for the different YSZ-O<sub>2</sub> adsorption systems are presented in **Figure 7.7**. The geometries and energies are summarized in **Table 7.2**. As discussed in Chapters 5 and 6, the most stable location of the Y-V-Y defect cluster is with a subsurface oxygen vacancy and the two nearest neighbour yttrium lying in  $\langle 100 \rangle$  direction as in the YSZ4 model (**Figure 7.7-d**). In the case of the O<sub>2</sub> adsorption, a metastable state would form due to its strong interaction with outmost layer oxygen on YSZ4, which gives a positive adsorption energy and increases the total energy of the system. The defect model YSZ3 (**Figure 7.7-c**) with outmost layer oxygen vacancies represents the lowest total energy of YSZ-O<sub>2</sub> system. However, since little change in the oxygen molecule bond length has been found and the O<sub>2</sub> adsorption energy for the YSZ3 surface is as low as for the pure ZrO<sub>2</sub> surface, only very weak physisorption occurs on the substrate. In contrast, for the defect structure YSZ1 (**Figure 7.7-a**), in which both oxygen vacancies and yttrium dopants are located in the outmost layer of the (111) surface, the O-O bond of O<sub>2</sub> molecule, is stretched to 1.303 Å with an energy release of 0.443eV (-42.7 kJ/mol). Such a configuration results in far more exothermic O<sub>2</sub> adsorption than on the surface of pure ZrO<sub>2</sub> (3.18 kJ/mol). The Bader charges on the two oxygen atoms of the adsorbate are calculated to be -0.12e and -0.18e for the energetically favoured orientation of O<sub>2</sub> (as in **Figure 7.7-a** YSZ1-H).

In all cases, if the O<sub>2</sub> molecule approaches horizontally, there is a greater interaction with the YSZ surface. For structures YSZ2 and YSZ4 with subsurface oxygen vacancies, positive values of the adsorption energy (92.0 kJ/mol and 104.6 kJ/mol, respectively) indicate an local minimum (metastable state) can be achieved when the adsorbed oxygen pair aligns at a shallow angle to the (111) surface as illustrated in **Figure 7.7** (b) YSZ2-H and (d) YSZ4-H. The O-O bonds have been extended to 1.425 Å and 1.324 Å respectively. For system b-H, the stretched O<sub>2</sub> molecules relax towards the bridging oxygen sites on the (111) surface and form triatomic oxygen species. The distance between the bridging site oxygen and the nearest adsorbed oxygen O<sub>I</sub> is 1.526 Å. The Bader charges on O<sub>I</sub>, O<sub>II</sub> and bridging O are calculated to be -0.19e, -0.57e and -0.88e, respectively. For YSZ4-H, when one oxygen atom of O<sub>2</sub> moves closer to the bridging oxygen ( $d(\text{O}_I\text{-O})=1.759\text{Å}$ ), the other oxygen atom shift towards the



neighbouring Zr site and become stabilised at a distance of 2.244 Å, which is only slightly larger than the equilibrium Zr-O bond distance of 2.221 Å in the ZrO<sub>2</sub> lattice. The topological charges on the triatomic species are -0.17e, -0.48e and -1.13e in YSZ4-H. Since the O-O bond distances of the adsorbed species significantly increase in YSZ2-H and 4-H, these two configurations are considered as metastable states for O<sub>2</sub> dissociation on the substrate surfaces. However, when an O<sub>2</sub> molecule approaches the surface in a vertical orientation, it is slightly pushed away by the surface oxygen. The lower adsorption energies given by YSZ2-V and YSZ4-V indicate that weak physisorption of O<sub>2</sub> is more energetically favourable on the models with subsurface oxygen vacancies.

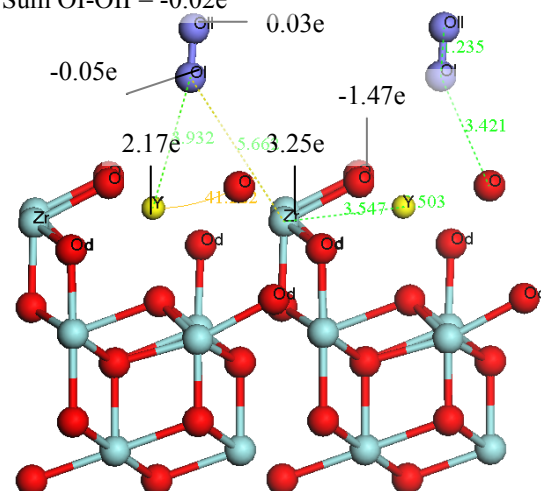
**Figure 7.7** O<sub>2</sub> adsorption on the (111) surfaces of YSZ with four different defect configurations: (a) YSZ1, (b) YSZ2, (c) YSZ3 and (d) YSZ4; and two different orientation: (V) Relaxed structure for vertically approaching O<sub>2</sub> (H) Relaxed structure for horizontally approaching O<sub>2</sub> (see **Table.7.1**). Both Side View and Top View are presented for the structures. Bader charge (solid line), atomic distance (dash line).



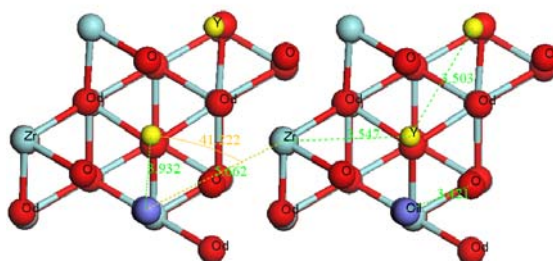


(b) **YSZ2-V:**

Sum OI-OII = -0.02e



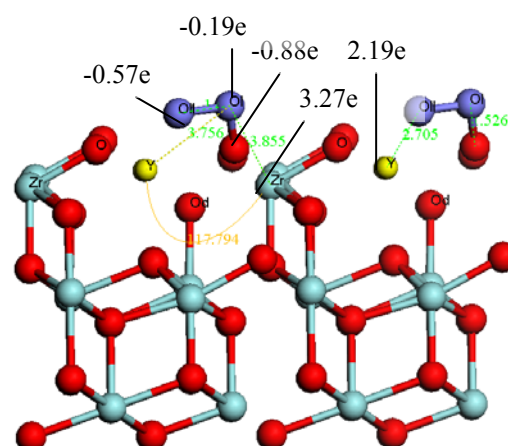
Side View



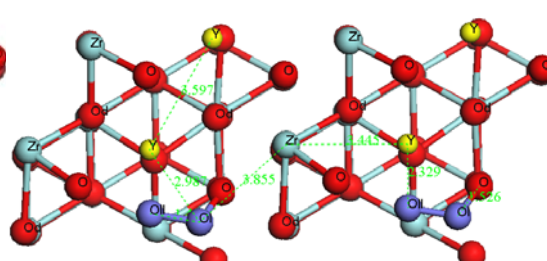
Top View

**YSZ2-H:**

Sum OI-OII = -0.76e



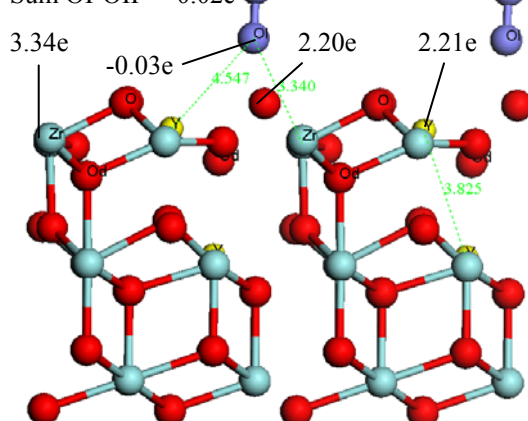
Side View



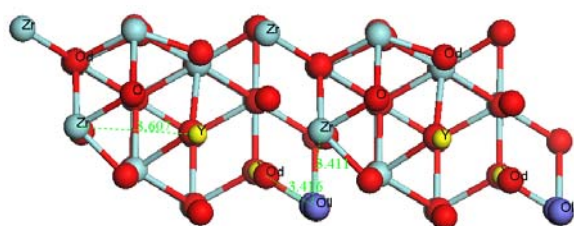
Top View

(c) **YSZ3-V:**

Sum OI-OII = -0.02e



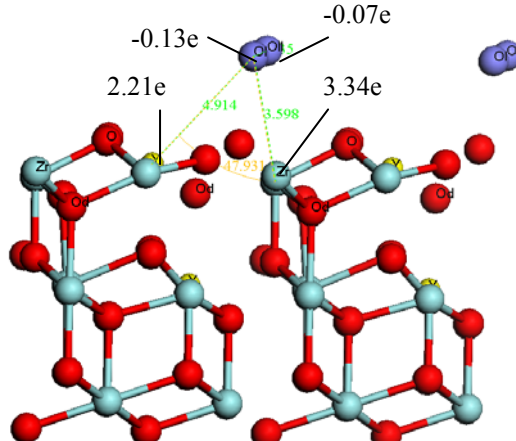
Side View



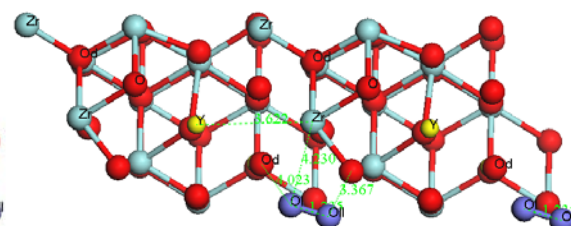
Top View

**YSZ3-H:**

Sum OI-OII = -0.20e

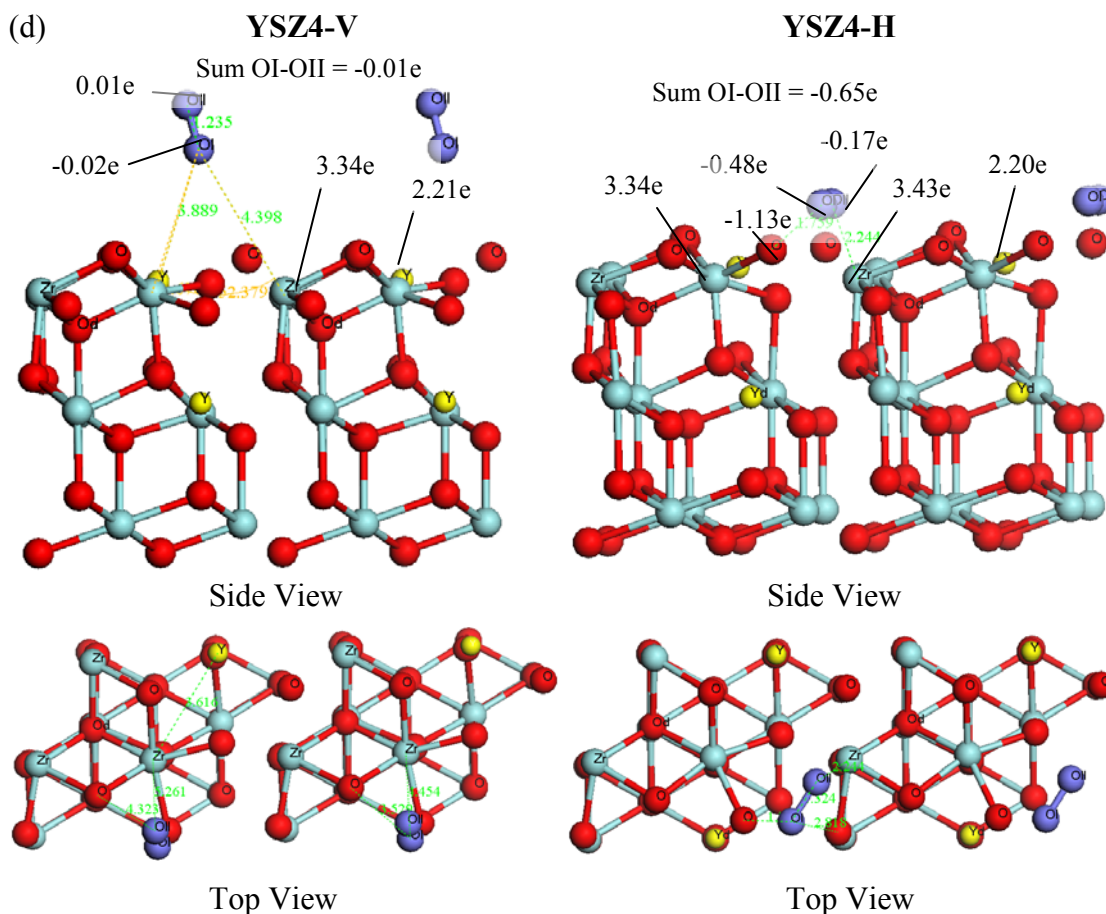


Side View



Top View





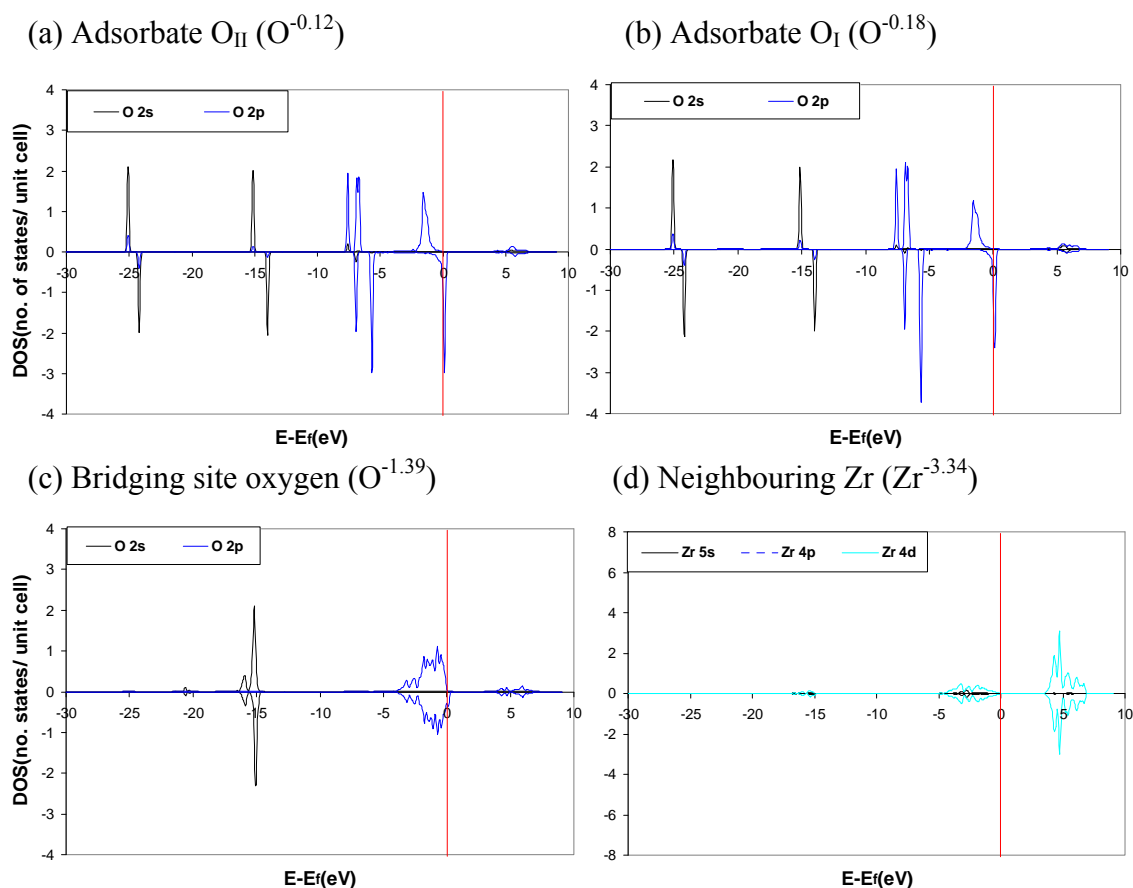
By comparing the results for the substrate models in **Figure 7.6**, oxygen vacancies in the outermost surface layer contribute to attracting the  $O_2$  molecule while the subsurface oxygen vacancies could relax the surrounding lattice oxygens towards the vacancy sites and influence the adsorbed molecule by stretching or polarizing the O-O bond. The yttrium next to oxygen vacancies in the top layer, i.e. defect structure (a) YSZ1 also enhance the adsorption resulting in polarised dioxygen pairs and an increase in the topological charge on the  $O_2$  molecule. The yttrium dopant in the subsurface site, which is further from the oxygen vacancy, has little contribution on the adsorption of molecular  $O_2$ . In relation to  $O_2$  orientation shown in **Figure 7.7**, the molecule tends to deviate a slightly from with parallel orientation at the adsorption site above the oxygen vacancy on the (111) surface of YSZ which leads to a more uniformly distributed topological charge on the two oxygen atoms compared with the vertical orientation for the  $O_2$ . The resulting configuration increases the coordination of the neighbour site Zr ion, which is 6 fold coordinated by oxygen anions on the YSZ1 substrate.



## 7.2.2 Density of States

For the slightly polarized oxygen molecular in the cases of YSZ2-V, and more energetically favourable YSZ3-V, YSZ3-H and YSZ4-V, the partial DOS for oxygen atoms suggest triplet spin as shown in **Figure 7.3** (a). In contrast, the more stretched oxygen molecules are investigated in this section to identify their oxygen states. The partial DOS for oxygen adsorption on the optimised YSZ1-H, YSZ2-H and YSZ4-H systems are presented in **Figures 7.8, 7.9** and **7.10**, respectively. The DOS pattern for the adsorbed oxygen atom on YSZ1-V is similar to YSZ1-H.

**Figure 7.8** Partial density of states for the adsorbed oxygen molecule on model YSZ1-H: OII (a) OI, (b), bridging site O (c), and neighbour site Zr (d).

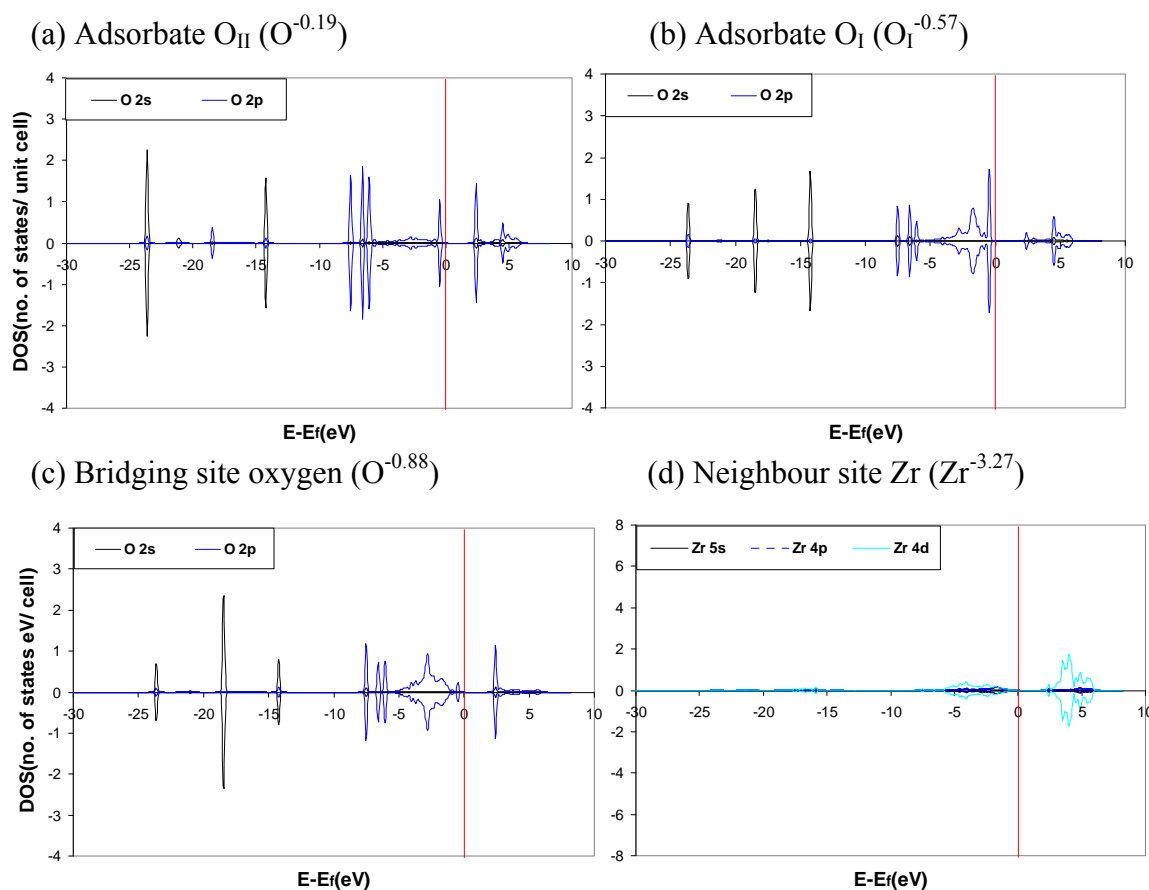


**Figure 7.8** shows that for YSZ1-H, the partial DOS for the two oxygen atoms of the adsorbate retain the polarization effect of molecular  $O_2$ . However, the O 2p “up” peak at -6.6 eV splits into two separate peaks and the magnetic moment on the dioxygen pairs is reduced owing to occupancy of the partially filled  $\pi_{2p}$  orbital of the oxygen



molecule. In the case of the substrate ions, the partial DOS for the bridging oxygen anion on the outmost surface shows slightly polarised O 2s peaks with lower intensity at around -15eV compared to the typical 2s character for the lattice oxygen anion  $O^{2-}$  (**Figure 6.4-a**). For the neighbouring site Zr, the intensity of 4d valence band at around 4eV is significantly reduced which may be caused by the stronger covalent character of Zr-O bond. Thus, charge density has been redistributed between the substrate Zr cation and the adsorbate. The oxygen pairs with a small topological charge (0.3 in sum) and a reduced magnetic moment may be considered superoxide like and denoted as  $O_2^{\alpha-}$  ( $0 < \alpha < 1$ ).

**Figure 7.9** Partial density of states for adsorbed oxygen molecule on model YSZ2-H: OII (a) OI (b), bridging site O (c) and neighbour site Zr (d).

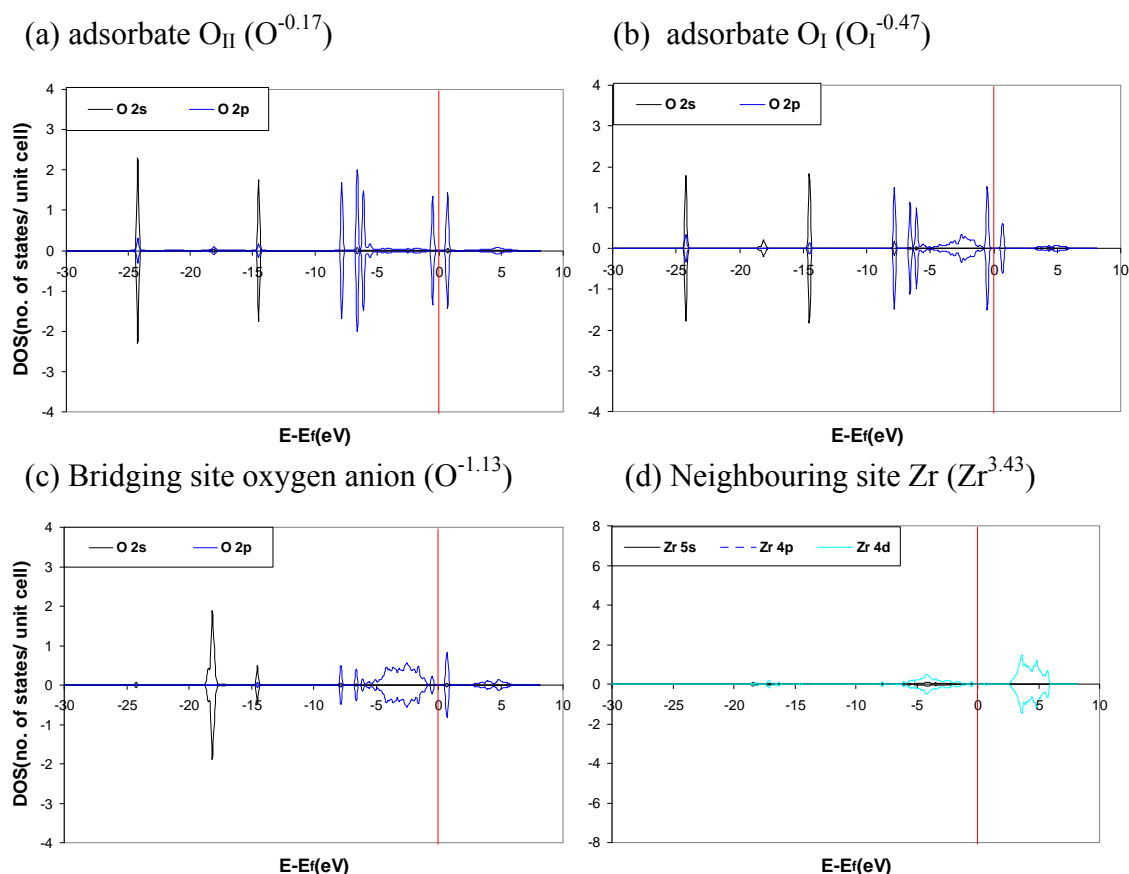


For YSZ2-H, the O<sub>II</sub> oxygen atom of the adsorbed O<sub>2</sub> retains the 2s character of a neutral oxygen atom, but the 2p character changes significantly with multiple peaks as shown in **Figure 7.9-a**, while the O<sub>I</sub> oxygen atom changes both its 2p and 2s characters as in **Figure 7.9-b**; and both of the oxygen atoms have zero spin. A comparable DOS



pattern to  $O_I$  is presented by the bridging site oxygen  $O^{-0.88}$  (**Figure 7.9-c**) which suggests strong overlapping of the O 2s orbital at -17 eV and indicates charge transfer between the adsorbate and substrate oxygen ions. For the neighbouring site Zr in **Figure 7.9-d**, the 4d peak at around 4 eV has also been dramatically reduced and replaced by a broader valence band lying between 3 and 6 eV. Therefore, the strong interaction between the  $O_2$  molecule and substrate surface of YSZ2-H leads to charge redistribution between the adsorbate and the bridging oxygen resulting in a triatomic oxygen species  $O_3^\beta$  ( $1 < \beta < 2$ ) with a non-magnetic spin like peroxide.

**Figure 7.10** Partial density of states for the adsorbed oxygen molecule on model YSZ4-H: OII (a), OI (b), bridging site O (c), neighbouring site Zr (d).



In **Figure 7.10** relating to  $O_2$  adsorption on the YSZ4 surface with H orientation, both the oxygen atoms of the adsorbate species have zero spin (**Figure 7.10-c**). The partial DOS for the bridging site oxygen (**Figure 7.10-c**) is similar to the singlet surface oxygen anion but shows a slight overlapping of the O 2p valence band with the  $O_I$  atom of the adsorbate species. The change in the DOS for oxygen ions suggests that



charge transfer occurs between the adsorbed oxygen species and bridging oxygen ions at the surface sites. The diamagnetic oxygen species formed can be identified as peroxide. Moreover, in **Figure 7.10-d**, for the nearest neighbour Zr site, the Zr 4d valence band is also reduced and lies between 3-6 eV. The net topological charge is +3.43e, close to the value of +3.48e for the 8-fold coordinated lattice Zr cation.

In conclusion, the adsorption of oxygen molecules is energetically most favourable in the case of the YSZ model with both the oxygen vacancy and yttrium cation defects exposed on the outmost surface. The resulting superoxo-like species  $O_2^{\alpha-}$  ( $0 < \alpha < 1$ ) adsorb at the oxygen vacancy sites with a shallow angle to the (111) surface. In the case of subsurface defects, peroxo-like species in form of triatomic  $O_3^{\beta-}$  ( $1 < \beta < 2$ ) can also occur, which, however, requires an adsorption energy of  $\sim 1$  eV. There is evidence for charge transfer between the adsorbed molecule and the bridging oxygen.

In the further investigation of  $O_2$  dissociative adsorption reported in the following Section 7.3, only defect structures YSZ1 and YSZ3 with oxygen vacancies at the outermost layer of the (111) surface have been considered. These two models, YSZ1 gives the lowest adsorption energy for  $O_2$  but is less stable since the Y content reaches the saturation limit as discussed in Chapter 5; while, YSZ3 with the two yttriums in the  $\langle 100 \rangle$  direction (Z) reduces the yttrium content level in the outermost layer by half and thus is more stable. However, subsurface oxygen vacancies can also be exposed at the step surface for oxygen adsorption, and such models will be studied in Chapter 8.

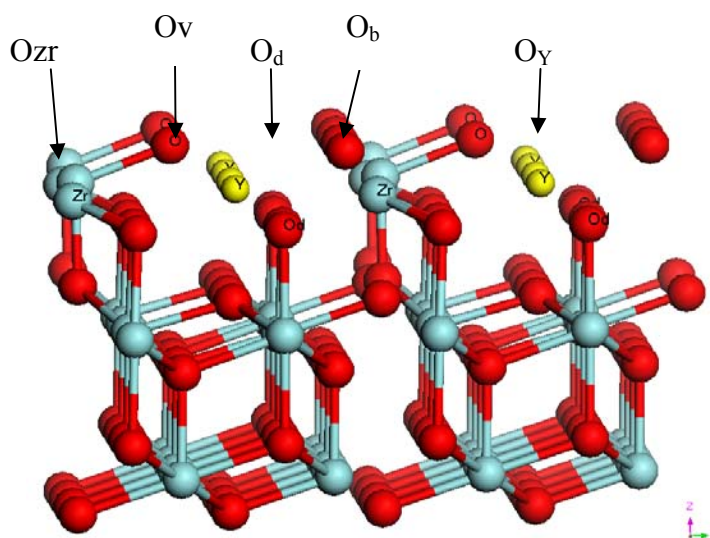
### 7.3 $O_2$ Dissociation on the Plane (111) Surface of YSZ

The study of  $O_2$  adsorption has suggested that molecular oxygen tends to be adsorbed non-dissociatively with some stretching of the O-O bond. In order to elucidate how feasible homolysis of  $O_2$  is at the surface, the mechanism and energies of dissociation of  $O_2$  over the yttria stabilized (111)  $ZrO_2$  surface, models YSZ1 and 3 are investigated here.

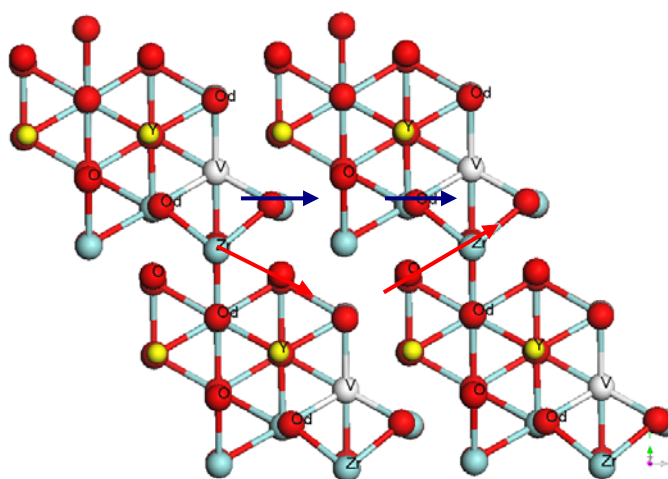


### 7.3.1 O<sub>2</sub> Dissociation on the YSZ1 Surface Model

**Figure 7.11** Schematic views of the dissociation process on the (111) surface of YSZ1: (a) Side View and (b) Top View. Ov is the dissociation site above oxygen vacancy in the top layer; Ob site is above the bridging oxygen; Od above the subsurface oxygen; Ozr and O<sub>Y</sub> are the dissociation sites above Zr and Y cations in the topmost layer.



(a) Side View



(b) Top View

Dissociation route 1 (blue arrow); Dissociation route 2 (red arrow).

The stoichiometric surface model of YSZ1 is formed by substituting one row of Zr with Y cations and removing half of the bridging site oxygen anion in the top layer of the ZrO<sub>2</sub> (111) surface. The dissociation of molecular oxygen was modelled by



encapsulation of an oxygen atom in the vacancy and location of the second monoatom at a neighbouring atom. **Figure 7.11** shows a schematic view of the possible oxygen dissociation sites on the YSZ1 surface. All the non-equivalent adsorption sites in the six rows exposed at the surface have been considered. The resulting formation energies for different configurations are listed in **Table 7.3**. The position of the dissociated oxygen atom above each surface site after relaxation is presented in **Figure 7.12**.

**Table 7.3** Calculation results for oxygen dissociation on the YSZ1 surface.

Adatom	superoxo <sup>a</sup> - Y	superoxo- O <sub>b</sub>	superoxo- O <sub>d</sub>	diss <sup>b</sup> -Zr	Int <sup>c</sup> -V <sub>O</sub>
d (Zr-O) Å	2.523	2.993	2.563	2.162	3.584
d (Y-O) Å	2.535	2.710	2.541		4.927
d (O-O <sub>v</sub> ) Å	1.303	1.289	1.274	2.244	
E <sub>tot</sub> eV	-335.734	-335.620	-335.518	-333.557	-660.966 (-330.483)
E <sub>YSZ</sub> eV	-325.466	-325.466	-325.446	-325.446	-650.892 (-325.446)
E <sub>ads</sub> eV	<u>-0.442</u>	-0.327	-0.246	1.715	-0.248 (-0.124)
Oxygen Species	O <sup>-0.34</sup> -O <sup>-0.18</sup>	O <sup>-0.40</sup> -O <sup>-0.01</sup>	O <sup>-0.32</sup> -O <sup>0.14</sup>	O <sup>-0.46</sup> (O <sup>-1.22</sup> )	O <sup>-1.44</sup> (O <sup>-1.38</sup> )

<sup>a</sup>superoxo-Y, O<sub>b</sub> and O<sub>d</sub> designate superoxide species on different adsorption sites derived for the dissociated O atom and a neighbour surface oxygen;

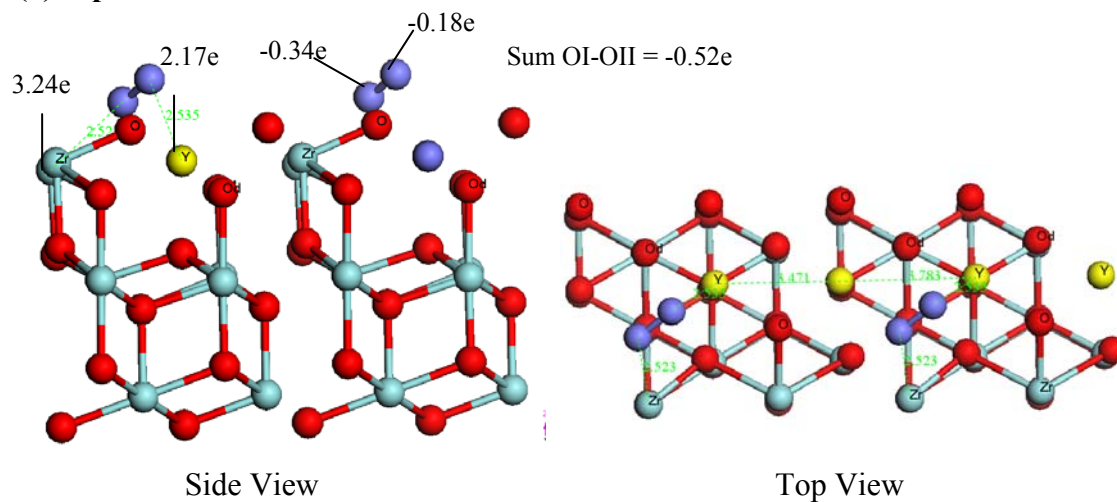
<sup>b</sup>diss-Zr represents an dissociated adatom O at surface Zr site;

<sup>c</sup>int-V<sub>O</sub> represents an oxidised YSZ surface with dissociated O in the oxygen vacancy.

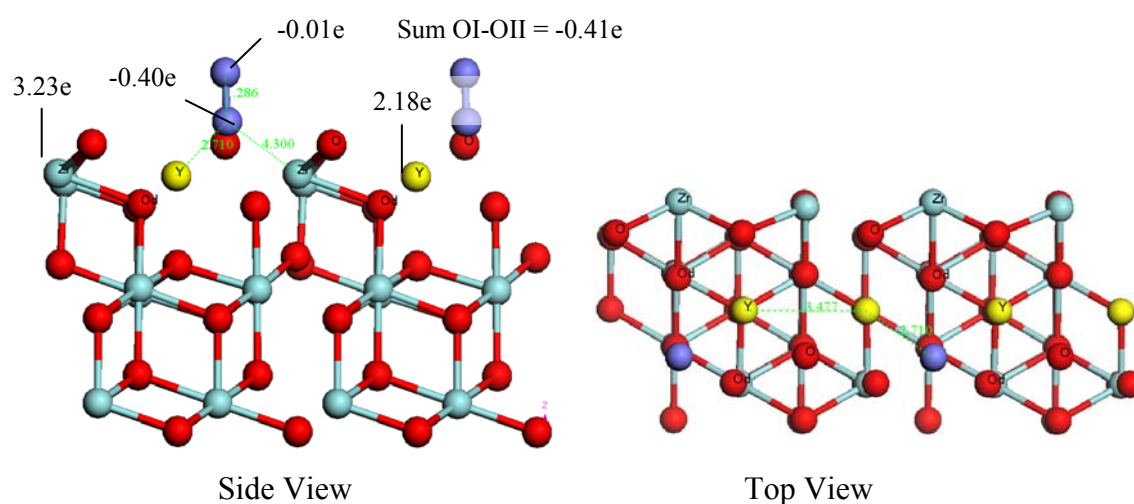


**Figure 7.12** The optimised structure of O adsorbed above different sites at the (111) surface of YSZ1 (see Table 7.3). Bader charge (solid line); atomic distance (dash line).

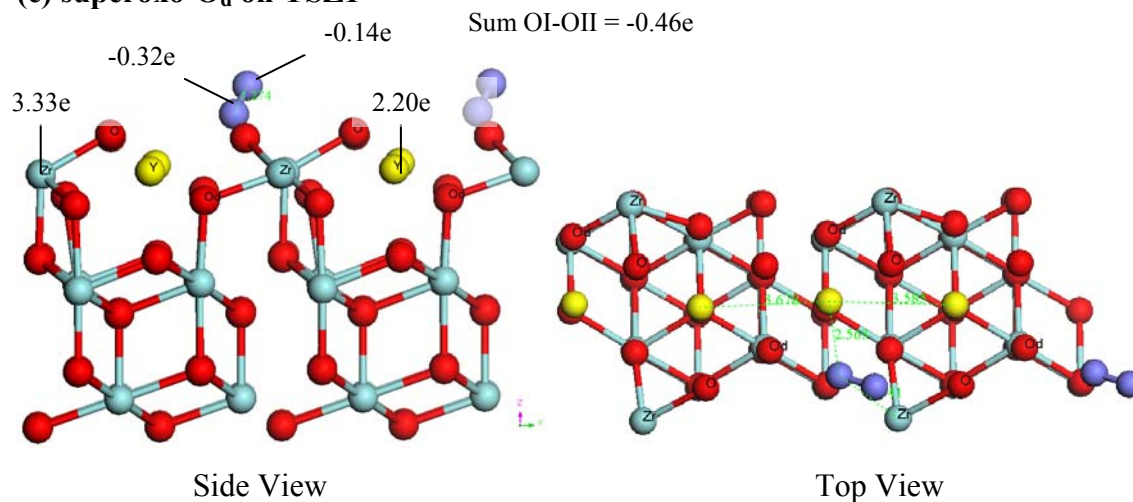
**(a) superoxo-Y on YSZ1**



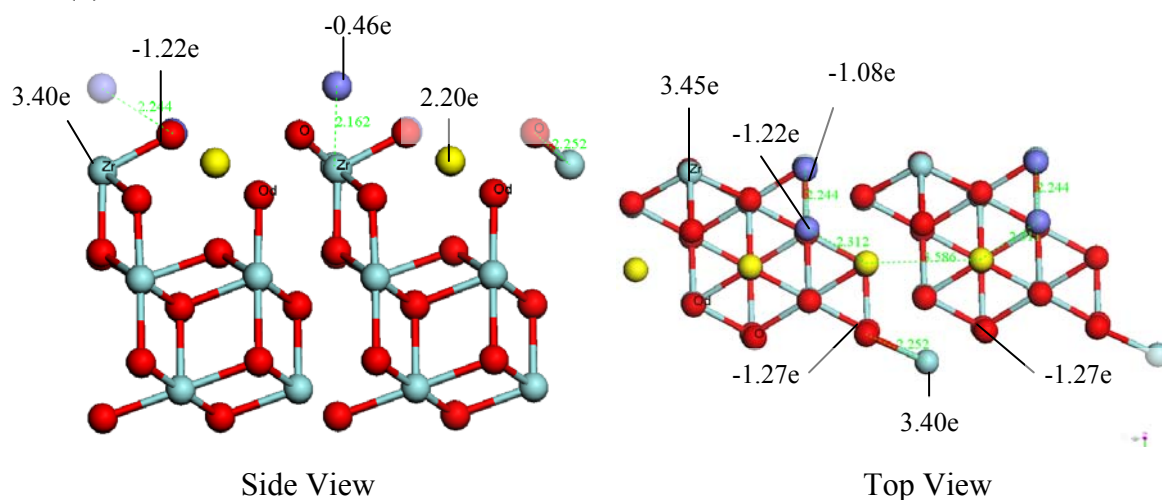
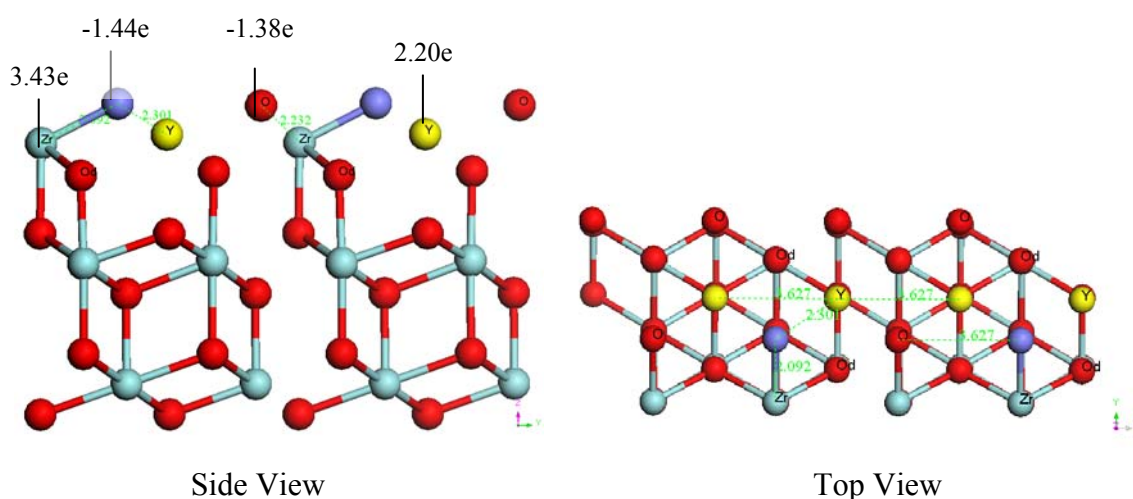
**(b) superoxo-O<sub>b</sub> on YSZ1**



**(c) superoxo-O<sub>d</sub> on YSZ1**





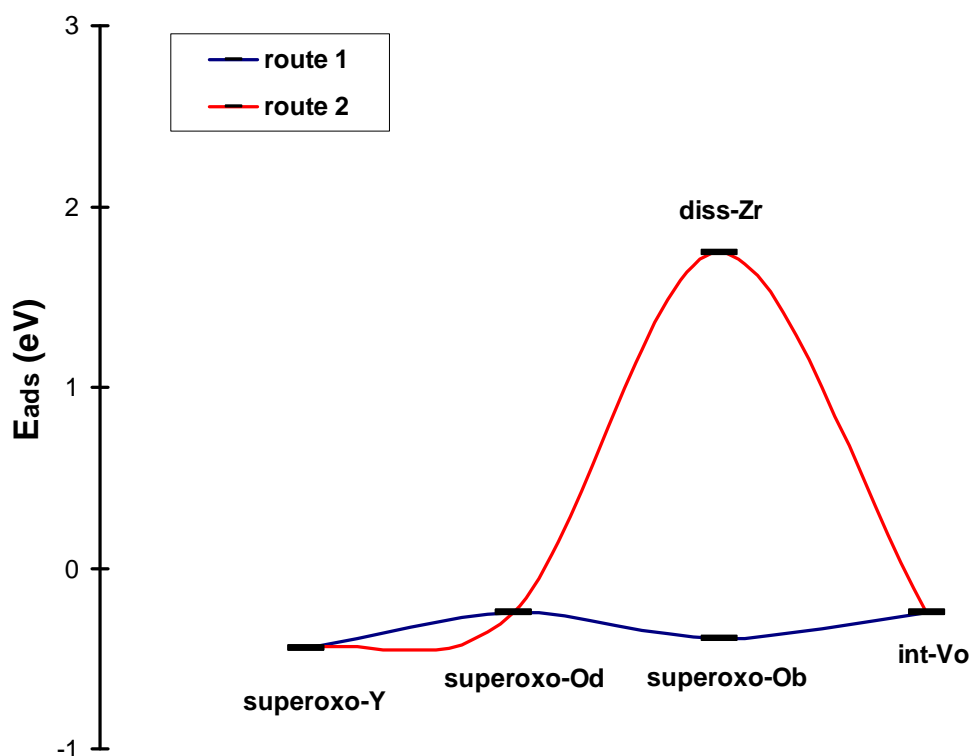
**(d) diss-Zr on YSZ1****(e) int- $V_O$  on YSZ1**

According to the results of calculations, several intermediates and products were obtained after structure relaxation. The oxygen atoms above Y and  $O_d$  (i.e. oxygen atom in the subsurface layer) are not in the stable locations. These adatoms tend to move towards the bridging oxygen sites and bond with the top oxygen with bond lengths of 1.30 Å and 1.29 Å (see **Figure 7.12-a** and c). However, apart from the bridging oxygen sites (**Figure 7.12-b**), the Zr cation in the top layer can also serve to trap oxygen atoms. One dissociated oxygen atom adsorbs above this Zr cation at a distance of 2.16 Å and its Bader charge is -0.46e; the other dissociated oxygen atom encapsulates in the vacancy site and has a Bader charge of -1.22e (**Figure 7.12-d**). The energy required for adsorption of the oxygen atom at the Zr cation site is 1.72 eV, i.e. 166.10 kJ/mol. In the case where the two oxygen atoms occupy the two outermost oxygen vacancy sites  $V_O$ , which gives an oxidized YSZ surface as product and the



surface site Zr ions are 7-fold by oxygen anions in the adopted structure. The adsorption energy is calculated to be a negative value of -0.25 eV (**Figure 7.12-d**). The two possible routes for oxygen dissociation can be summarized as illustrated in **Figure 7.13**.

**Figure 7.13** Potential energy profile of intermediate states for O<sub>2</sub> dissociation on the YSZ1 surface. Note that: the energy profiles present here and after are only a guide to the eye for the adsorption energy changes with the oxygen dissociation/adsorption sites (see **Figure 7.12**).

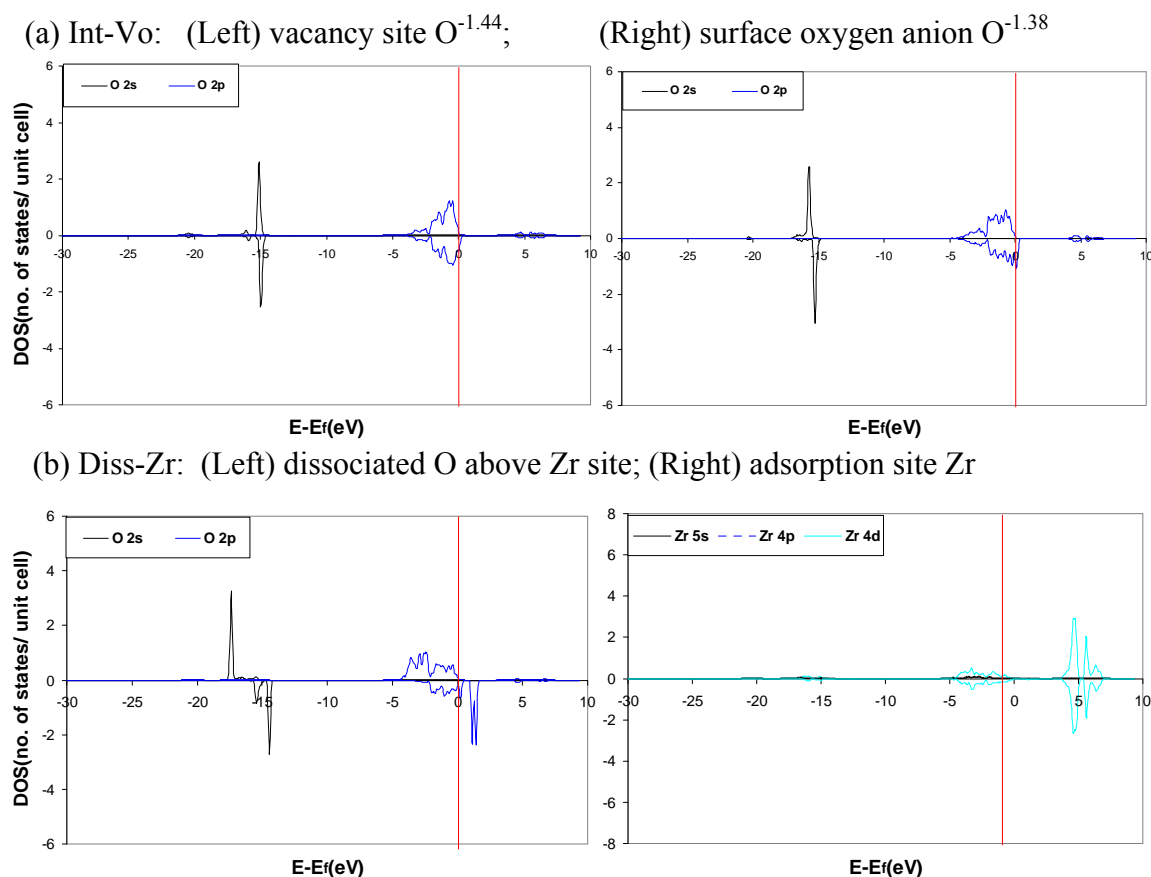


Route 1 involves one of the adatom oxygens bonding with the top site oxygen to form an oxygen pair, which has been denoted as O<sub>2</sub><sup>α-</sup>, where α is less than unity. The DOS pattern of this oxygen pair is shown in **Figure 7.8** and corresponds to a superoxy species. By rolling through the surface oxygen along the energy profile in **Figure 7.13**, i.e. the locations given in **Figure 7.13-a, b and c**, the oxygen atom can be finally delivered to another vacancy site so breaking the O-O bond and forming an O<sup>-1.44</sup> on the oxidized surface (**Figure 7.12-e**), which suggests the dissociated oxygen atom is stabilised as surface oxygen anion O<sup>2-</sup>. However, the DOS for the surface oxygen ions possess a small but non-zero spin as shown in **Figure 7.14-a**. On such an oxidised surface, charges have been redistributed among the oxygen ions which are surrounding the 8-fold Zr formed on the outermost surface.



In Route 2, after adsorption of the oxygen molecule in the vacancy site, the O-O bond is stretched towards the metal sites, and subsequently, one of the oxygens is dissociated to the top Zr cation site. The energy profile of route II is also shown in **Figure 7.13** and represents transport between the sites shown in **Figure 12-a, d** and finally e. The resulting adatom  $O^{-0.46}$  forms a triangle with two neighbouring surface oxygen ( $O^{-1.27}$ ) with distances of 2.244 and 2.492 Å. The Bader charge on these two neighbouring site oxygens is reduced to -1.27eV. The DOS pattern of the dissociated oxygen atom shown in **Figure 7.14-b** can be distinguished from both the neutral O atom in  $O_2$  and a lattice anion  $O^{2-}$ . The dissociated atom shows two 4p peaks at around 1eV, which indicates unpaired “down” spin electrons in O 2p orbital. The resulting magnetic moment is calculated to be 1.18 (Bohr magnetons). However, the partial DOS of the outmost layer Zr cation 8-fold by oxygen atoms has 4d character as the lattice Zr, so no charge transfer between the Zr and dissociated oxygen atoms can be identified here. The adsorbed species is denoted as  $O^{a-}$ . In general, route 1 is a process with a very low barrier, while route 2 has an energy barrier of ~2eV.

**Figure 7.14** Density of states for  $O_2$  dissociation into oxygen vacancy sites (a) and above Zr site (b) on YSZ1.

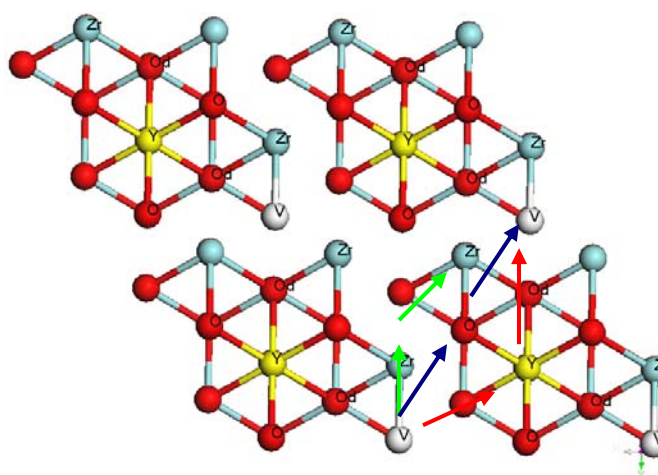
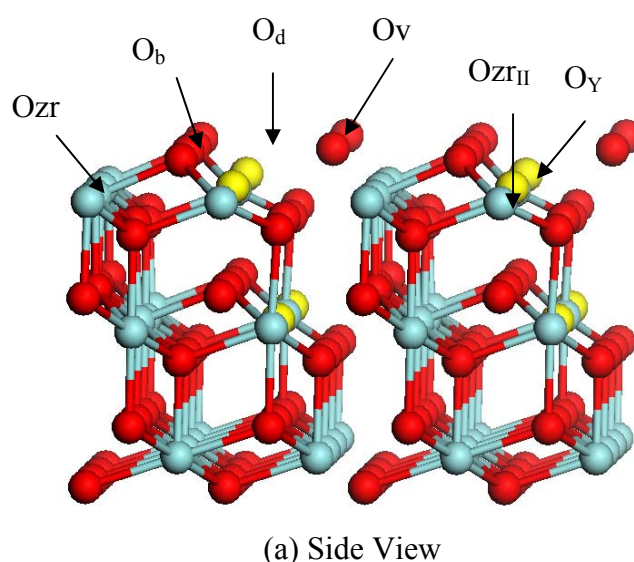




### 7.3.2 O<sub>2</sub> Dissociation on the YSZ3 Surface Model

Since the high yttrium concentration on the top layer of YSZ1 leads to a less stable surface, oxygen dissociation has also been studied on the YSZ3 surface which reduces the yttrium content on the outmost layer by half. **Figure 7.15** presents a schematic view of the non-equivalent dissociation sites on six periodic rows of the YSZ3 surface. The geometric and energetic results of the optimised structures are summarised in **Table 7.4** and displayed in **Figure 7.16**.

**Figure 7.15** Schematic views of the oxygen dissociation process on the YSZ3 surface: (a) Side View and (b) Top View. Ov is the dissociation site above oxygen vacancy in the top layer; Ob above the bridging oxygen; Od above the subsurface oxygen; O<sub>Zr</sub>, O<sub>ZrII</sub> and O<sub>Y</sub> are the non-equivalent sites above Zr and Y cations in the topmost layer.





**Table 7.4** Calculation results for oxygen dissociation on the YSZ3 surface.

Adatom	<sup>a</sup> mol-O	mol-O <sub>d</sub>	<sup>b</sup> superoxo-Y	superoxo-Zr	superoxo-ZrII	<sup>d</sup> diss-V <sub>O</sub>
d (Zr-O) Å	4.203	3.180	2.898	2.441	2.430	2.424
d (Y-O) Å	3.666	4.181	2.682	2.830	2.955	
d (O-O <sub>v</sub> ) Å	1.237	1.236	1.263	1.302	5.982	
E <sub>tot</sub> eV	-336.793	-336.545	-335.564	-335.828	-335.813	-660.398 (-330.199)
E <sub>YSZ</sub> eV	-326.617	-326.617	-326.617	-326.617	-326.617	-653.234 (-326.617)
E <sub>ads</sub> eV	-0.350	-0.102	0.879	0.615	0.630	2.662 (-1.331)
Oxygen species	O <sup>-0.02</sup> -O	O <sup>-0.05</sup> -O	O <sup>-0.17</sup> -O <sup>-0.09</sup>	O <sup>-0.32</sup> -O <sup>-0.24</sup>	O <sup>-0.25</sup> ; (O <sup>-0.28</sup> )	O <sup>-1.08</sup>

<sup>a</sup>mol-O, O<sub>d</sub> designate the reformed molecular O<sub>2</sub> from the initial dissociated state O and a neighbour site oxygen on the surface;

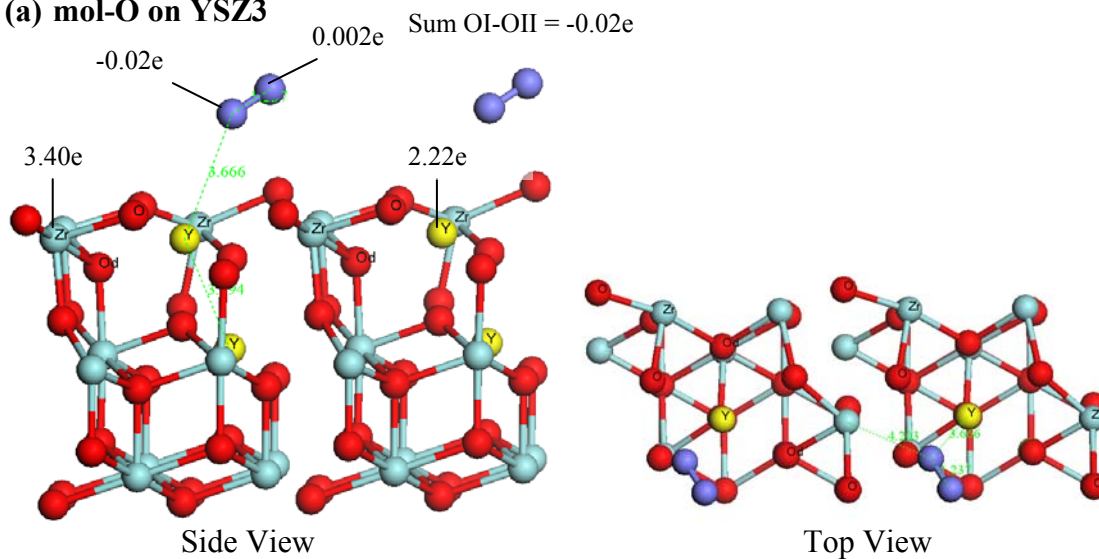
<sup>b</sup>superoxo-Y, Zr, ZrII designate superoxide species adsorbed either close to the neighbour Y or Zr sites.

<sup>c</sup>diss-V<sub>O</sub> represents an dissociated adatom O above the oxygen vacancy site.

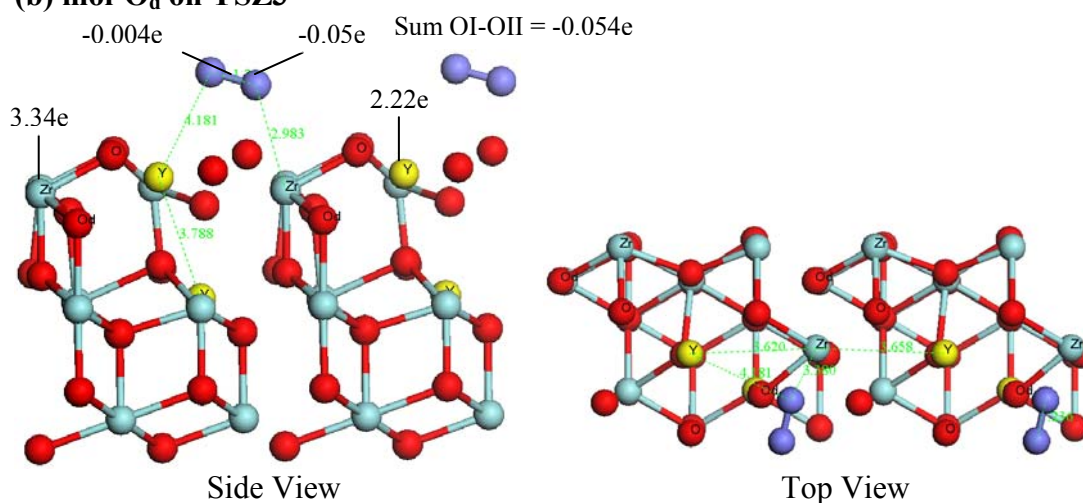


**Figure 7.16** The optimised structures of O above different sites at the (111) surface of YSZ3 surface (see **Table 7.4**). Bader charge (solid line); atomic distance (dash line).

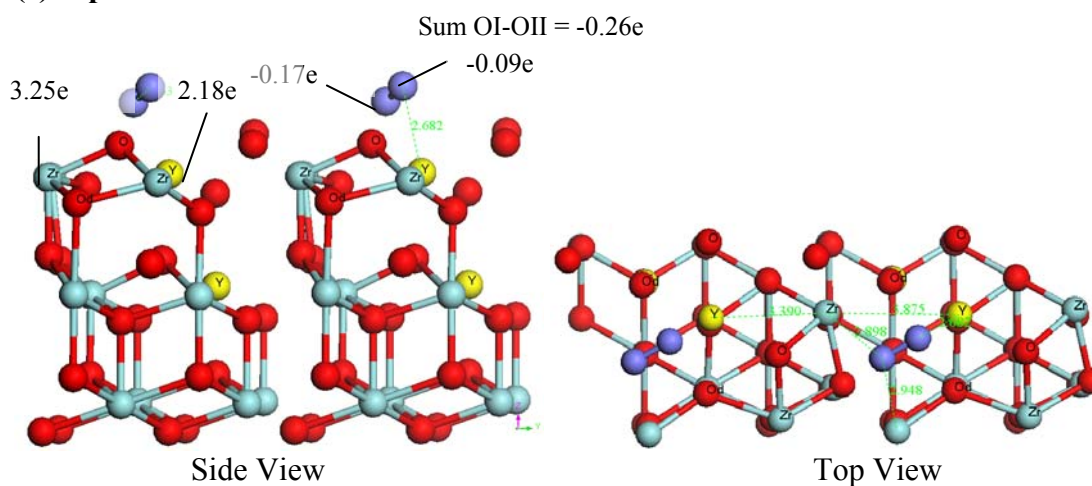
**(a) mol-O on YSZ3**



**(b) mol-O<sub>d</sub> on YSZ3**



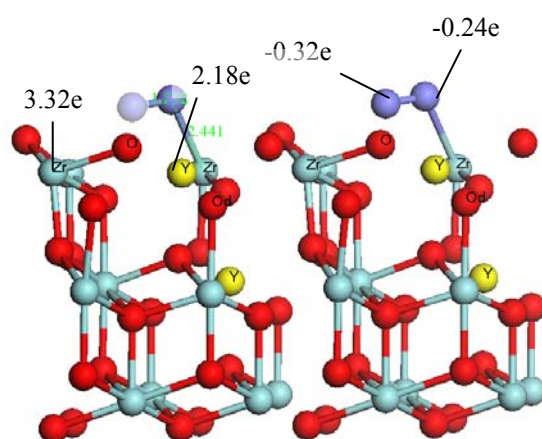
**(c) superoxo-Y on YSZ3**



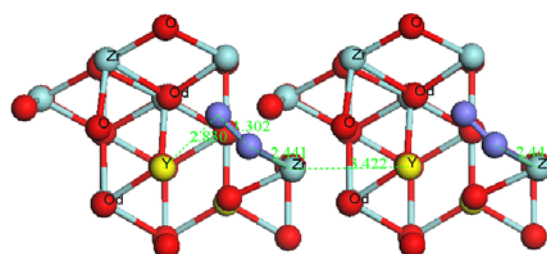


**(d) superoxo-Zr on YSZ3**

Sum OI-OII = -0.56e



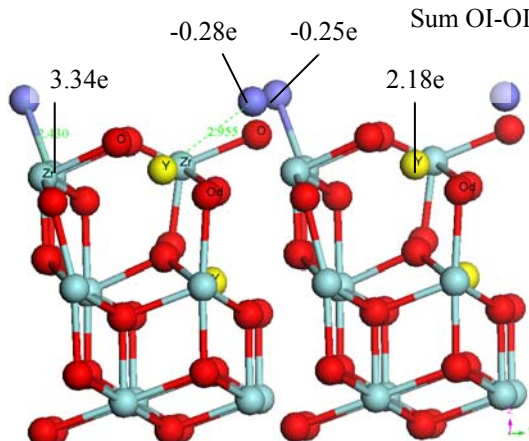
Side View



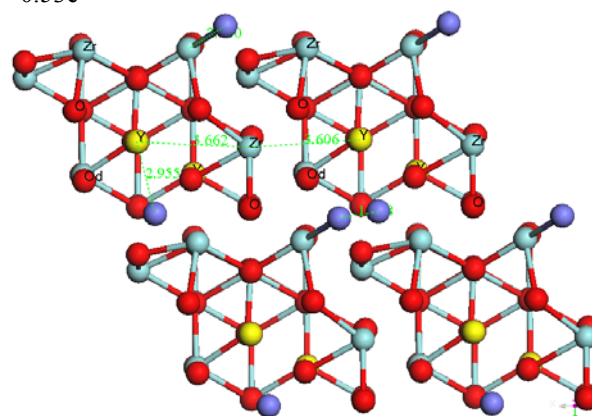
Top View

**(e) superoxo-ZrII on YSZ3**

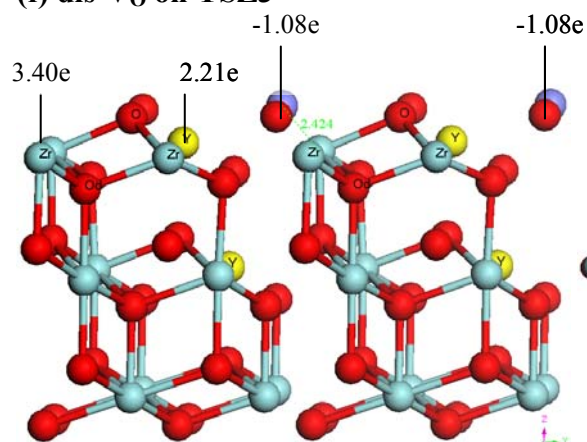
Sum OI-OII = -0.53e



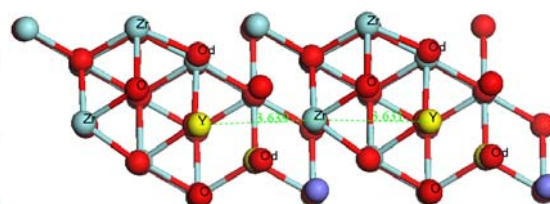
Side View



Top View

**(f) dis-V<sub>O</sub> on YSZ3**

Side View



Top View



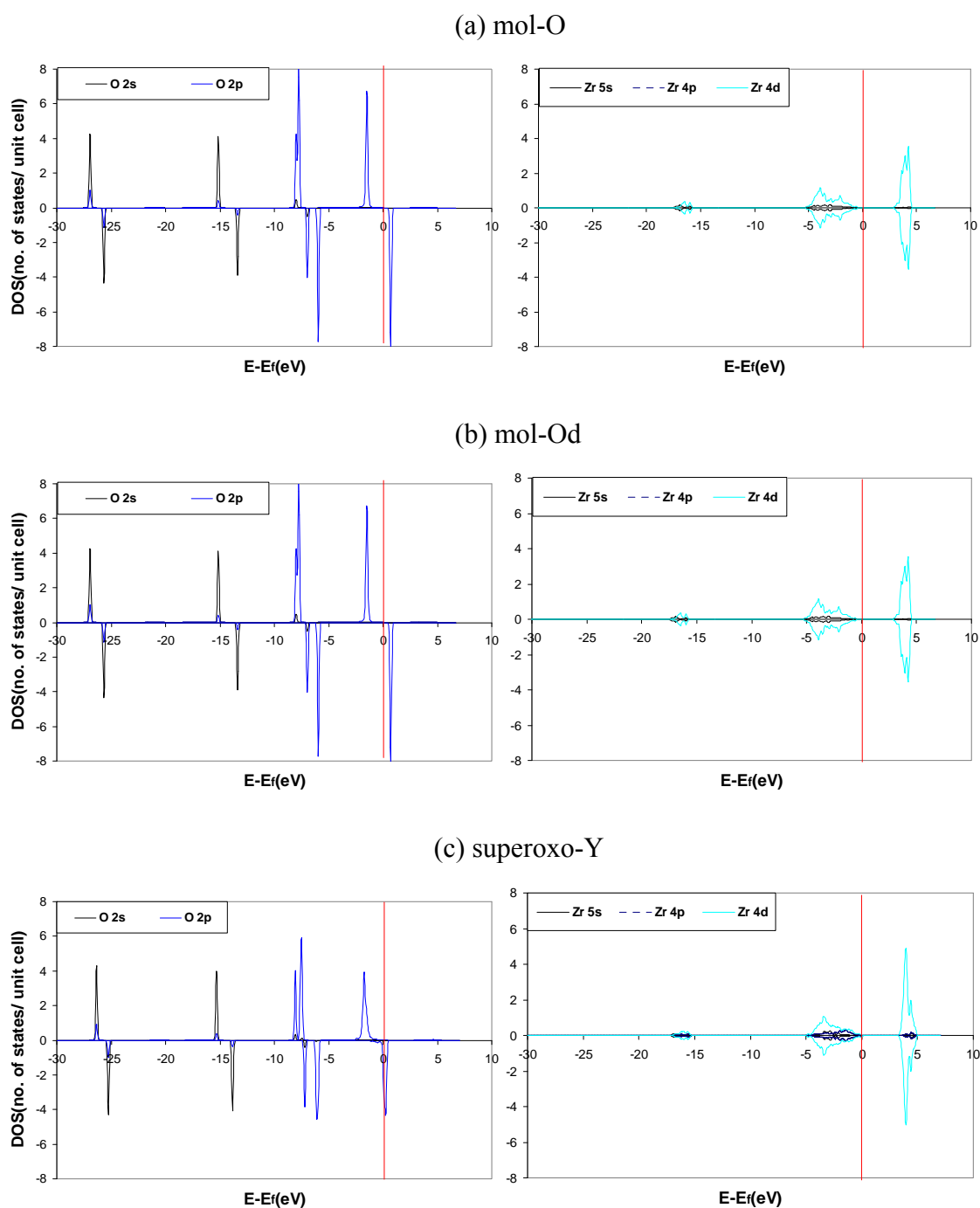
After structure relaxation, the oxygen atoms above the oxygen sites tend to bond with the surface oxygen and reform the O<sub>2</sub> molecule with little change of the O-O bond distance. The adsorption of molecular O<sub>2</sub> (mol-Ob and mol-Od) on the YSZ3 surface is an exothermic process, which can release an energy of 0.35 eV at the most stable adsorption site above an oxygen vacancy (**Figure 7.16-a**). The oxygen monoatoms above the metal sites also interact with surface oxygen anions to form oxygen pairs, which lie between yttrium and zirconia cation sites, with stretched O-O bonds. Three different configurations can be adopted with the dioxygen pairs inclined to either the Y or Zr (ZrII) cation (see **Figure 7.16-c, d and e**). The adsorption site for the most energetically favourable configuration of the superoxide like species is above the Zr cation at a distance of 2.44 Å (**Figure 7.16-e**) and involves a positive adsorption energy of 0.62 eV, i.e. ~1eV higher than in the YSZ1 surface. The dissociation of O<sub>2</sub> into surface oxygen vacancy sites is also less favourable on YSZ3 than YSZ1. The resulting oxygen species O<sup>-1.08</sup> tends to adsorb slightly above the vacancy site and requires a dissociation energy as large as 2.66 eV (**Figure 7.16-e**).

The DOS for adsorbate and substrate atoms are shown as shown in **Figure 7.17**. For ml-O and ml-Od, the partial DOS patterns in **Figure 7.17-a and b** are the same as for the neutral oxygen atoms in molecular O<sub>2</sub> and hence physisorption of slightly polarised O<sub>2</sub> occurs on the corresponding sites shown in **Figure 7.16-a and b**. In the case of superoxo-Y (**Figure 7.16-c**), the charge density is also uniformly distributed on the two oxygen atoms of the dioxygen species with non-zero spin, but the O 2p spin-up peak at -7.7 eV for O<sub>2</sub> splits into two distinguishable peaks, while the O 2p peak near Fermi level is reduced to a lower density of state. The topological charge on the neighbour also has been reduced to 3.25. Compared to the partial DOS for superoxo-Y, two extra O 2p peaks can be observed for superoxo-Zr, i.e. the spin-up peaks of O 2p at the lower energy state around 7 eV and further split into three peaks, and the spin-down peak above the Fermi level separates into two adjacent peaks (**Figure 7.17-d**). Such a DOS pattern remains for superoxo-ZrII (**Figure 7.17-e**). Thus, the superoxo-Y, Zr and ZrII are considered as intermediate state of molecular O<sub>2</sub> and superoxy species O<sub>2</sub><sup>-</sup> and can be denoted as O<sub>2</sub><sup>α-</sup>. The partial DOS for the adatom oxygen of diss-V<sub>o</sub> in **Figure 7.17-f**, which is distinguishable from the non-magnetic lattice O<sup>2-</sup> anion, shows a O 2p spin-down peak just above the Fermi level, while a reduced O 2s up peak lies at



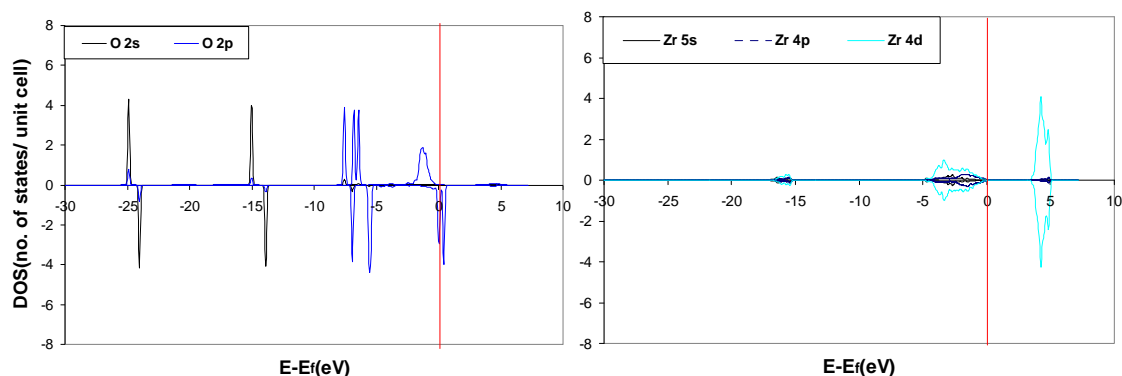
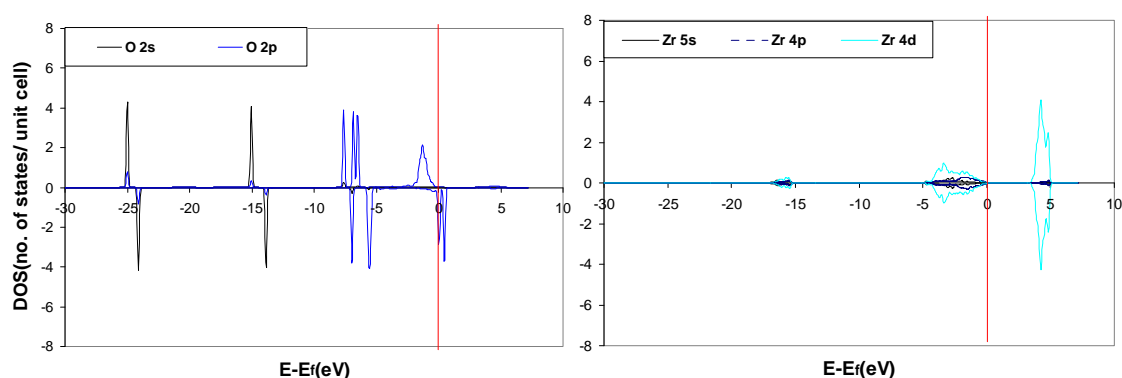
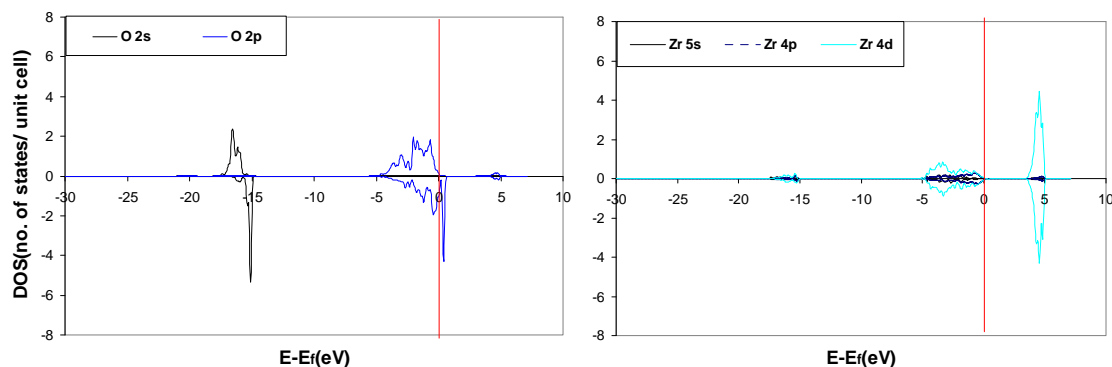
-17 eV. The spin polarization effect remains on the adopted surface with two dissociated oxygen atoms. Thus, the oxygen species adsorbed above vacancies sites is considered in relation to doublet oxygen species  $O^-$  with one single electron.

**Figure 7.17** Partial DOS for adsorbed oxygen species (left) and the neighbour site Zr (right) on YSZ3. mol-O(a), Od (b), superoxo-Y(c), Zr (d) Zr<sub>II</sub> (e) and diss-Vo (f).





(d) superoxo-Zr

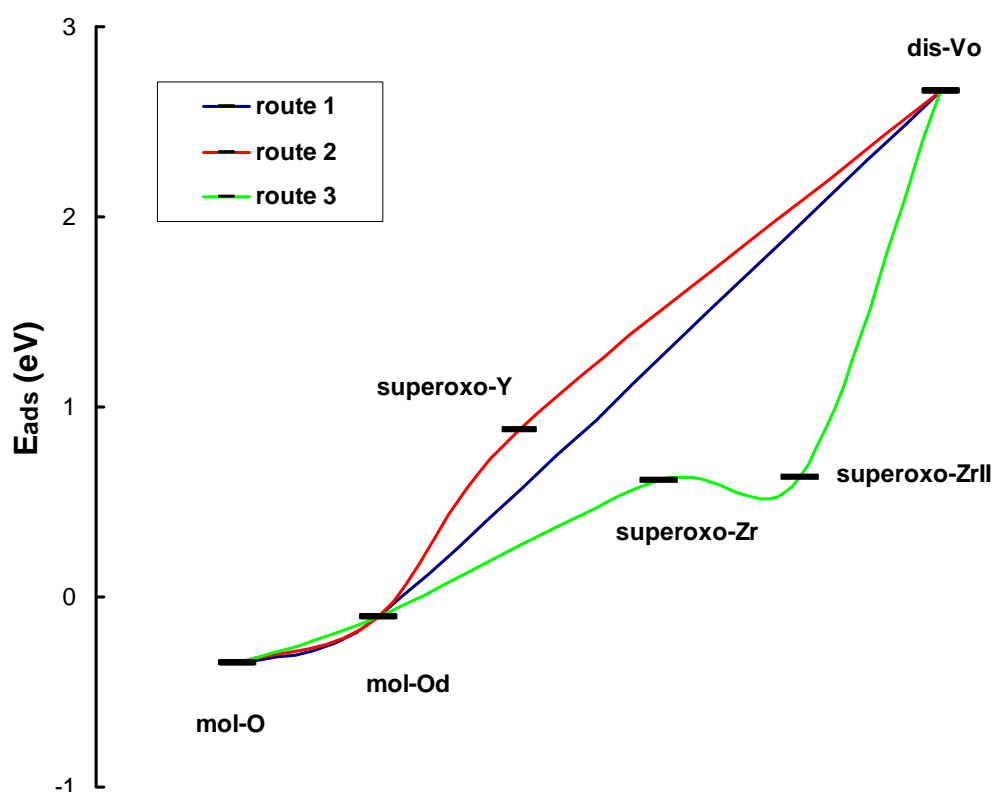
(e) superoxo-Zr<sub>II</sub>(f) diss-Vo (lattice O<sup>-1.08</sup>)

In summary, three routes for the dissociation of O<sub>2</sub> can be envisaged as in **Figure 7.18**. Route 1, O<sub>2</sub> migrates through the bridging site oxygen and dissociates into the oxygen vacancies creating 2O<sup>-</sup> at the outmost layer of the surface. This route needs to overcome energy barrier of 2.66 eV. The energy profile for route 1 is shown in **Figure 7.18** and depicted in **Figure 7.16-a, b** and **f**. Route 2, dissociation involves intermediates in the form of superoxo like species O<sub>2</sub><sup>α-</sup>, formed between the metal sites and inclined to the yttrium defect site. The energy profile for route 2 in **Figure 7.18** represents migration between the sites in **Figure 7.16-a, b, c** and **f**. Alternatively, in



route 3, and two superoxo-like species can form by moving the  $O_2^{\alpha-}$  toward the Zr cation and subsequently the O-O bond breaks, two dissociated oxygen atom oxygen occupying the oxygen vacancy sites. The energy profile for route 3 in **Figure 7.18** represents passage between the sites in **Figure 7.16**-a, b, d, e and f.

**Figure 7.18** Potential energy profile of intermediate states for  $O_2$  dissociation on the YSZ3 surface. The lines denote the potential energy changes with oxygen dissociation/adsorption sites in each case. The corresponding dissociation/adsorption sites are shown in **Figure 7.16**.



#### 7.4 Adsorption States of Oxygen on the YSZ (111) Plane Surface

The Bader charge analysis indicated that several oxygen species such as  $O^{-0.34}-O^{-0.18}$ ,  $O^{-0.17}-O^{-0.59}-O^{-0.88}$ ,  $O^{-0.28}$ ,  $O^{-0.46}$ ,  $O^{-1.08}$ ,  $O^{-1.44}$  have been identified by the modelling study. These species can be categorized as diatomic  $O_2^{\delta-}$  ( $0 \sim \delta < 1$ ),  $O_2^{\alpha-}$  ( $\alpha < 1$ ), triatomic  $O_3^{\beta-}$  ( $1 < \beta < 2$ ) and monoatomic  $O^{\alpha-}$  and  $O^{\beta-}$  in relation to  $O_2$ ,  $O_2^-$ ,  $O_2^{2-}$ ,  $O^-$  and  $O^{2-}$  correspondingly. **Table 7.5** summarizes the adsorption energies of these adsorbed oxygen species on the (111) surface of YSZ with different defect structures.



**Table 7.5** Adsorption energies of adsorbed oxygen species on the (111) surface of YSZ with different defect configurations ( $\delta$ ,  $\alpha$  and  $\beta$  denote the topological Bader charges on the oxygen species increasing from 0 to 2,  $0 \sim \delta < 1$ ;  $0 < \alpha < 1$ ;  $1 < \beta < 2$ .  $\mu$  is the magnetic moment on oxygen atoms).

Category	Substrate	Oxygen species	d(O-O) Å	Magnetization (x)		Adsorption energy $E_{\text{ads}}$ kJ/mol
				$\mu_{\text{OI}}$	$\mu_{\text{OII}}$	
$\text{O}_2^{\delta-}$	YSZ-4	$\text{O}^{-0.02}-\text{O}^{+0.01}$	1.23	0.79	0.83	+3.18
	YSZ-3	$\text{O}^{-0.05}-\text{O}^{+0.03}$	1.24	0.80	0.81	-2.32
	YSZ-2	$\text{O}^{-0.03}-\text{O}^{-0.01}$	1.24	0.81	0.81	-5.21
	YSZ-3	$\text{O}^{-0.13}-\text{O}^{-0.07}$	1.24			-9.07
	YSZ-3	$\text{O}^{-0.05}-\text{O}$	1.24	0.79	0.82	-9.84
	YSZ-3	$\text{O}^{-0.02}-\text{O}$	1.24			-33.77
	YSZ-1	$\text{O}^{-0.32}-\text{O}^{0.14}$	1.27	0.51	0.76	-23.37
$\text{O}_2^{\alpha-}$	YSZ-1	$\text{O}^{-0.18}-\text{O}^{-0.34}$	1.30	0.50	0.62	-44.75
	YSZ-1	$\text{O}^{-0.32}-\text{O}^{-0.02}$	1.28			-42.70
	YSZ-1	$\text{O}^{-0.40}-\text{O}^{-0.01}$	1.29			-31.55
	YSZ-3	$\text{O}^{-0.17}-\text{O}^{-0.09}$	1.26	0.68	0.71	+84.81
	YSZ-3	$\text{O}^{-0.32}-\text{O}^{-0.24}$	1.30	0.58	0.56	+59.34
	YSZ-3	$\text{O}^{-0.25}-\text{O}^{-0.28}$	1.30			+60.68
	YSZ-3	$\text{O}^{-0.57}-\text{O}^{-0.19}-\text{O}^{-0.88}$	1.43 (1.53)	0.00	0.00	+91.66
$\text{O}_3^{\beta-}$	YSZ-4	$\text{O}^{-0.48}-\text{O}^{-0.17}-\text{O}^{-1.13}$	1.32 (1.76)	0.00	0.00	+104.59
	YSZ-1	$\text{O}^{-0.46};$ $\text{O}^{-1.22}(\text{O}^{-1.27})$	2.24	1.21		+166.10
$\text{O}^{\alpha-}$				0.40	(0.36)	
	YSZ-3	$\text{O}^{-1.08};$ $(\text{O}^{-1.60})$		0.56		+128.42 per atom
	YSZ-1	$\text{O}^{-1.44};$ $(\text{O}^{-1.38})$		0.27		12.01 per atom
$\text{O}^{\beta-}$				0.27		



Regarding to the defect configuration, the high concentrations of yttrium and oxygen vacancies at the outermost layer in the YSZ-1 model, which reaches the segregation limit defined in Chapter 5, lead to a less saturated state for the Zr cations at the surface, i.e. the average oxygen coordination number (C.N.) for metal cations in the outermost layer of YSZ-1 is less than 6 compared to 7 in the pure  $\text{ZrO}_2$  surface. On the substrate of YSZ-1, charged oxygen species  $\text{O}_2^{\alpha-}$  ( $0 < \alpha < 1$ ) rather than neutral  $\text{O}_2$  molecules tend to be adsorbed on the surface in an orientation lying between the Zr and Y cations. The dissociated oxygen monoatoms of  $\text{O}_2$  prefers to occupy the oxygen vacancy sites and are stabilised as  $\text{O}^{\beta-}$  ( $1 < \beta < 2$ ), in which case, the coordination number of surface Zr cations increase to 7 as in the most stable (111) surface. This process leads to an oxidised YSZ surface and an energy release of -24.02 kJ for per mole  $\text{O}_2$  dissociation. Adsorption of the less reduced  $\text{O}^{\alpha-}$  species above Zr site is energetically unfavourable and the charge density has been redistributed among surrounding oxygen ions. Therefore, the order of stability for oxygen species on the YSZ-1 surface is  $\text{O}_2^{\alpha-} > \text{O}^{\beta-} > \text{O}^{\alpha-}$  corresponding to  $\text{O}_2^- > \text{O}^{2-} > \text{O}^-$ .

On the most stable substrate, YSZ-3, the yttrium concentration at the upper surface is reduced by half compared to YSZ-1 and a higher saturation state of Zr and Y cations can be adopted in the top layer. The slightly polarised  $\text{O}_2$  molecule (i.e.  $\text{O}_2^{\delta}$ ) is the most favourable absorbate. The formation of super-oxide like species  $\text{O}_2^{\alpha-}$  requires a relatively higher energy of around 60 kJ per mol and dissociated oxygen atoms are very unlikely to occur as  $\text{O}^{\beta-}$  ( $1 < \beta < 2$ ) ions at oxygen vacancy sites. Hence, the order of stability is  $\text{O}_2^{\delta} > \text{O}_2^{\alpha-} > \text{O}^{\beta-}$  i.e.  $\text{O}_2 > \text{O}_2^- > \text{O}^{2-}$  on YSZ-3.

For the YSZ-2 and YSZ-4 structures with subsurface oxygen vacancies,  $\text{O}_2$  moves towards the vacancy at lower surface sites to adsorb as neutral molecules or alternatively, to form triatomic species with the upper surface site oxygen. In this case, the charge density is redistributed and requires a relatively high formation energy  $\sim 1\text{eV}$ . A diamagnetic spin configuration has been adopted for the resulting oxygen species of  $\text{O}_3^{\beta-}$ , which is considered in relation to peroxide  $\text{O}_2^{2-}$ . The relative stabilities of oxygen species are  $\text{O}_2 > \text{O}_3^{\beta-}$  i.e.  $\text{O}_2 > \text{O}_2^{2-}$ .



Overall, the adsorption state of oxygen species depends on the defect configuration of the substrate YSZ surface. The highly segregated yttrium surface containing lower saturation Zr cations (less stable) tends to attract higher charged oxygen species. In contrast, the surfaces with lower yttrium concentrations tend to adsorb neutral  $O_2$  and the formation of the charged oxygen species is an endothermic process. In general, the adsorption of strongly reduced monoatomic oxygen species involves higher adsorption energy than the dioxygen species. The most stable adsorption states of oxygen species are generated by reaching the bond saturation state for the lower co-ordinated Zr ions at the YSZ surface sites. The calculated O-O bond distances of diatomic species  $O_2^{\delta-}$ ,  $O_2^{\alpha-}$  and triatomic  $O_3^{\beta-}$  are in accordance with the experimental values of bond lengths for  $O_2$ ,  $O_2^-$  and  $O_2^{2-}$  respectively. [2-5] The negative charges on the adsorbed oxygen species are compensated by charge density redistribution of the surrounding surface oxygen ions, since the topological Bader charge on the under coordinated Zr ions only slightly changes after adsorption.

The role of defect and lower co-ordinated Zr cations will be further discussed on the step surface in the next Chapter.

## References

- 
- [1] S. Kristyán and P. Pulay, *Chem. Phys. Lett.* **229**, 175, 1994.
  - [2] *Interatomic Distance*, Chemical Society Special Publication No.11, p. S8. London, 1958.
  - [3] D. G. Tuck, *J. Inorg. Nucl. Chem.* **26**, 1525, 1964.
  - [4] D. H. Templeton and C. H. Dauben, *J. Acta. Cryst.* **8**, 579, 1955.
  - [5] S. C. Abrahams and J. Kalanas, *Acta Cryst.* **7**, 838, 1954.



## Chapter 8 Role of Active Sites Topology on O<sub>2</sub> Adsorption

*You've got to go out on a limb sometimes because that's where the fruit is.*

*--Will Rogers (1879-1935)*

In this chapter, DFT calculations have been carried out on the stepped (111) surface to elucidate the role of active site topology for O<sub>2</sub> adsorption. As discussed in Chapter 6, most stable step models **S3** and **SD5** are used as step surfaces for ZrO<sub>2</sub> and YSZ respectively. We propose dissociation mechanism for O<sub>2</sub> for the different adsorption sites; the intermediates and products are categorized according to their Bader charges and further indentified by the analysis of their DOS patterns.

### 8.1 O<sub>2</sub> Adsorption on the Stepped (111) Surfaces

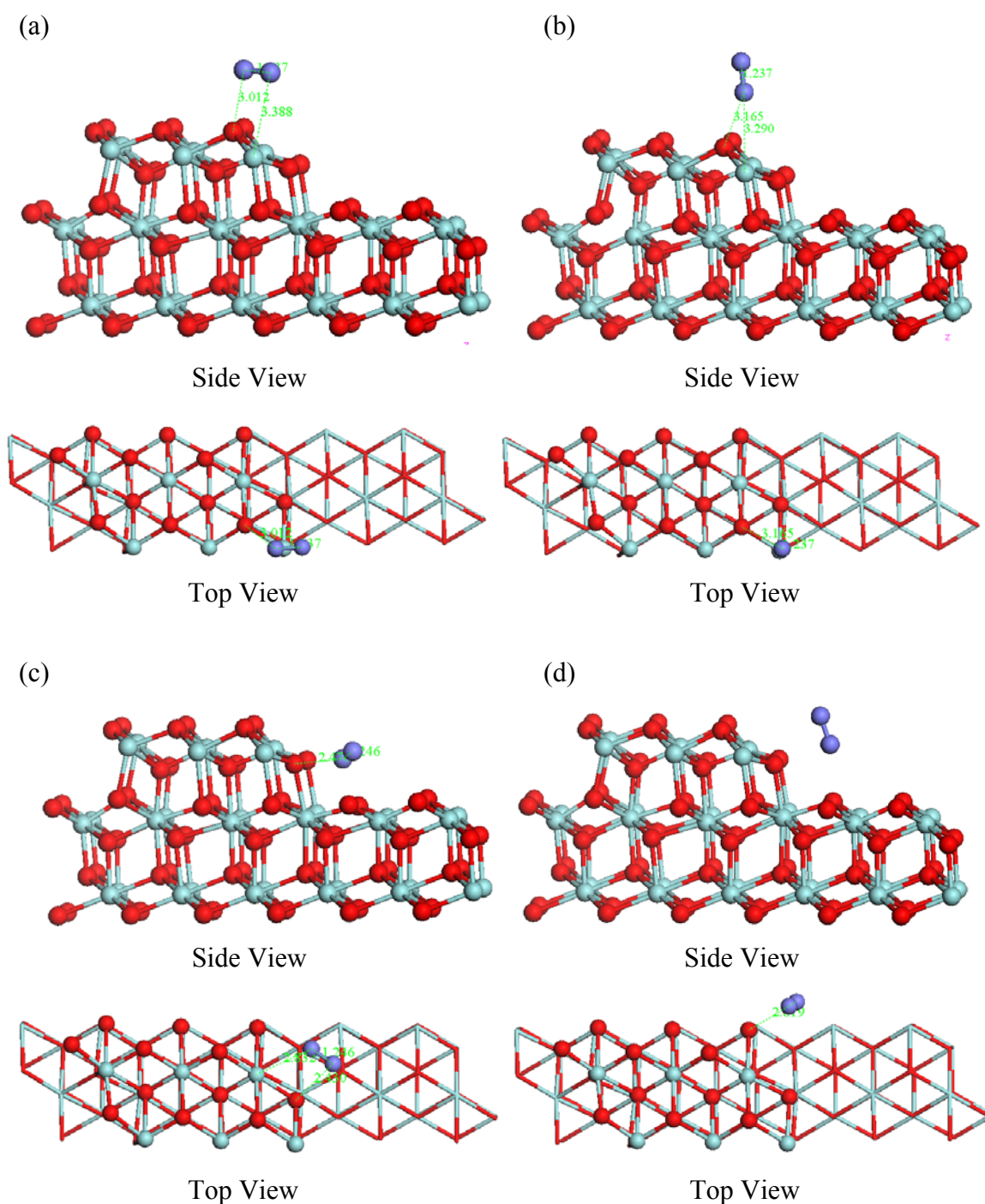
As for the plane surface, O<sub>2</sub> adsorption has been studied here by modelling different orientations of the oxygen molecule at the edge of stepped pure ZrO<sub>2</sub> and YSZ surfaces. The O<sub>2</sub> molecules are all located at the edge side, which involves Zr ions with low coordination numbers, i.e. 6 fold Zr<sup>(6)</sup> ions for the pure step model **S3** and 5 fold Zr<sup>(5)</sup> ions for the yttrium doped step model **SD5**.

#### 8.1.1 O<sub>2</sub> Adsorption on the Step Edge Sites of Pure ZrO<sub>2</sub>

In this section, adsorption is modelled with four different initial orientations of O<sub>2</sub>, i.e. either parallel or perpendicular to the upper and lower terraces of the stepped (111) surface: (a) O<sub>2</sub> parallel to upper terrace, (b) O<sub>2</sub> perpendicular to the upper terrace (c) O<sub>2</sub> parallel to lower terrace and (d) O<sub>2</sub> perpendicular to the lower terrace. The optimised structures for the correspondingly adsorption process on pure ZrO<sub>2</sub> are presented in **Figure 8.1**. The calculated energies are listed in **Table 8.1**.



**Figure 8.1** O<sub>2</sub> adsorption on the pure ZrO<sub>2</sub> stepped (111) surface with O<sub>2</sub> (a) parallel and (b) perpendicular to the upper terrace and (c) parallel and (d) perpendicular to the lower terrace (Side View and Top View). Atomic distance (dash line).





**Table 8.1** Calculated energies and Bader charge analysis for O<sub>2</sub> adsorption on the stepped surface (111) of pure zirconia.

O <sub>2</sub> / Zr <sub>30</sub> O <sub>60</sub>	Upper terrace		Lower terrace	
	a	b	c	d
d(O-O) Å	1.237	1.237	1.246	1.2347
E <sub>ads</sub> eV	-0.045	-0.108	+1.035	+0.060
E <sub>TOT</sub> eV	-849.523	-849.586	-848.443	-849.41
Oxygen species	O-O <sup>-0.04</sup>	O <sup>+0.07</sup> -O <sup>-0.09</sup>	O <sup>-0.04</sup> -O <sup>-0.23</sup>	O <sup>+0.01</sup> -O <sup>-0.05</sup>

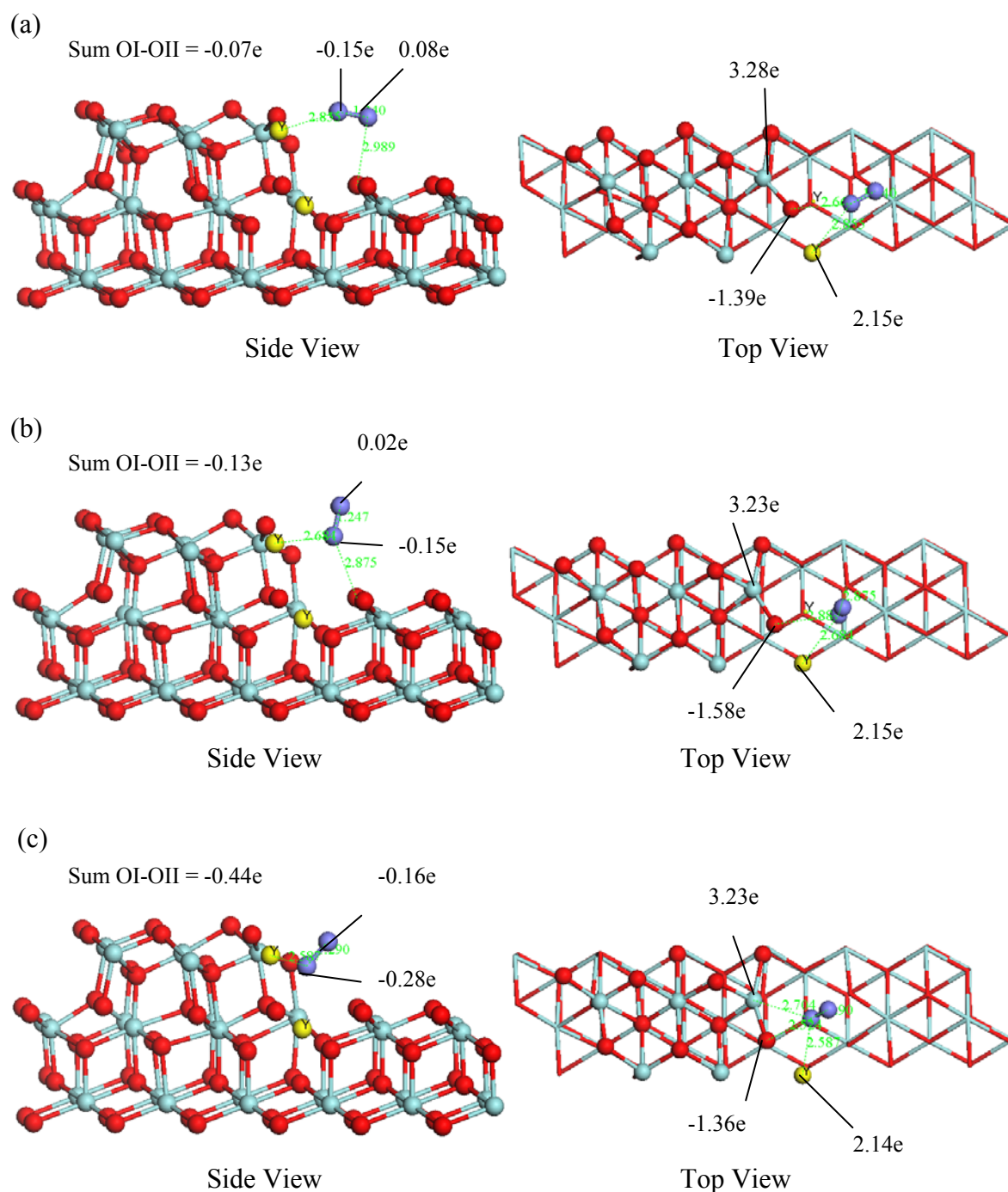
The results in **Table 8.1**-a, b and d, show that the adsorbed oxygen species has a small topological charge, i.e. less than -0.04e in total and retains the equilibrium O-O bond distance and triplet spin configuration of O<sub>2</sub>. The O<sub>2</sub> molecules are slightly polarized and denoted as O<sub>2</sub><sup>δ-</sup> (δ~0). The calculation results also suggest that the O<sub>2</sub> molecule tends to adsorb at the edge sites of the upper terrace and favoured by the vertical orientation as shown in **Figure 8.1**-b. The adsorption energy is as small as -0.102 eV (i.e. -9.84 kJ/ mol). In contrast, O<sub>2</sub> has little tendency to adsorb at the edge site of the lower terrace, especially, for the horizontally approaching O<sub>2</sub>. The O-O bond can be stretched thus resembling a superoxide like species; however, it only occurs by overcoming an energy barrier of 1eV (**Figure 8.1**-c). This relatively high adsorption energy is considered due to Zr ions at the edge sites of the lower terrace are bond saturated as in the cubic ZrO<sub>2</sub> bulk (i.e. 8-fold).

### 8.1.2 O<sub>2</sub> Adsorption on the Edge Sites of YSZ Step

On the YSZ step, three initial orientations of the oxygen molecule have been investigated: (a) O<sub>2</sub> parallel to the (111) surface; (b) O<sub>2</sub> perpendicular to the (111) step surface; (c) O<sub>2</sub> perpendicular to the edge facet along (11-2) plane. The corresponding optimized structures for the adsorption process are presented in **Figure 8.2** and the calculated energies in **Table 8.2**.



**Figure 8.2** O<sub>2</sub> adsorption on the SD5 stepped surface model of YSZ with O<sub>2</sub> orientation: (a) parallel and (b) perpendicular to the (111) surface and (c) perpendicular to the edge facet along (11-2) plane (Side View and Top View). Bader charges (solid line), atomic distance (dash line).





**Table 8.2** Calculate energies and Bader charge analysis for O<sub>2</sub> adsorption on the stepped (111) surface of YSZ.

O <sub>2</sub> /Y <sub>2</sub> Zr <sub>18</sub> O <sub>59</sub>	H	V	T
d(O-O) Å	1.240	1.247	1.281
E <sub>TOT</sub> eV	-838.565	-838.382	-838.240
E <sub>ads</sub> eV	-0.376	-0.193	-0.051
Oxygen species	O <sup>+0.08</sup> -O <sup>-0.15</sup>	O <sup>+0.02</sup> -O <sup>-0.10</sup>	O <sup>-0.16</sup> -O <sup>-0.28</sup>

The O<sub>2</sub> orientation parallel to the (111) surface and perpendicular to the edge facet of the (11-2) plane as in **Figure 8.2** (a) is the most energetically favourable for adsorption. The O-O bond length of the polarised O<sub>2</sub> has been stretched to 1.24 Å with an energy release of 0.38 eV (i.e. -36.28 kJ/mol). The topological charge on this edge site Zr cation increases from +3.14e to +3.28e (comparable to the value of +3.26 in tetragonal ZrO<sub>2</sub>). However, if one oxygen atom of the oxygen pair is turned toward the vacancy site (**Figure 8.2-c**), the adsorption energy increases to a value of -0.05 eV. The adsorbed oxygen species is superoxide-like O<sub>2</sub><sup>α-</sup> (0<α<1). In general, the 5-fold coordinated Zr ion at the edge facet of **SD5** is more likely to adsorb charged oxygen pairs compared to the 6 fold Zr ions of the pure ZrO<sub>2</sub> step model **S3**. The dissociation of O<sub>2</sub> will be discussed in the following section.

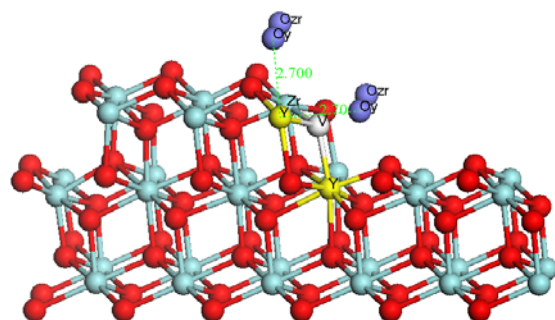
## 8.2 O<sub>2</sub> Dissociation on the Stepped (111) Surface of YSZ

In order to investigate the O<sub>2</sub> dissociation process on the stepped surface, two series of calculations have been carried out corresponding to the dissociation routes via cation and oxygen anion sites. As in the study of the plane YSZ surfaces, we can consider two oxygens from the dissociated O<sub>2</sub> molecule, one fills the oxygen vacancy site at the edge and the other oxygen is located above the neighbouring metal cation, oxygen anion or oxygen vacancy sites with an initial distance ~2.5 Å (larger than the equilibrium Zr-O bond distance in ZrO<sub>2</sub> lattice). **Figure 8.3** illustrates the possible dissociation sites on the stepped surface model of YSZ.

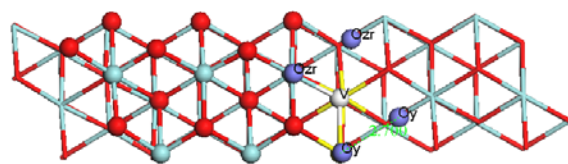


**Figure 8.3** Schematic views of the possible O<sub>2</sub> dissociation sites on the stepped (111) surface of YSZ: (a) metal cations sites and (b) oxygen and oxygen vacancy sites (Side View and Top View).

(a) Dissociation sites on metal cations

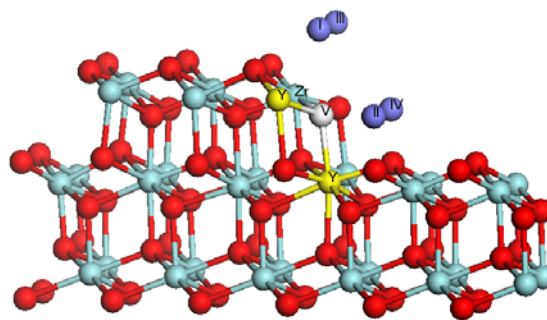


Side View

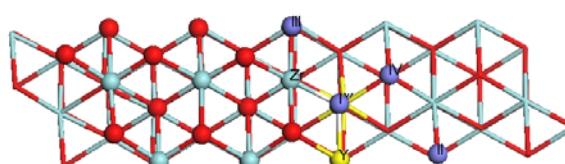


Top View

(b) Dissociation sites on oxygen anions



Side View



Top View

After structural relaxation, dissociated oxygen atoms may move relatively far from the initial dissociation site and bond with neighbouring site oxygens to form oxygen pairs. The derived oxygen species with different charge states and orientations at the stable adsorption sites are listed in **Table 8.3** and depicted in **Figure 8.4**. The important adsorbed species are designated as superoxo-OI, superoxo-OII, superoxo-OIII, superoxo-Y, diss-Zr and int-Vo.



**Table 8.3** Calculated geometries and energies for oxygen dissociation on the stepped (111) surface of YSZ.

$O_2/$ $Y_2Zr_{18}O_{59}$	superoxo-OI	superoxo-OII	superoxo-Y	superoxo-OIII	diss-Zr	int- $V_O$
<b>d (Y-<math>O_{ad}</math>) Å</b>	2.858	4.270	2.511	3.497	2.892	2.292
<b>d (Zr-<math>O_{ad}</math>) Å</b>	2.475	3.436	2.352	2.239	2.174	2.082
<b>d (<math>O_{ad}</math>-<math>O_b</math>) Å</b>	2.603	<u>1.288</u>	2.820	<u>1.354</u>	2.179	2.597
<b>d (<math>O_{ad}</math>-<math>O_v</math>) Å</b>	<u>1.281</u>	2.771	<u>1.301</u>	3.167	3.493	3.363
<b><math>E_{TOT}</math> eV</b>	-838.307	-838.256	-838.545	-838.922	-836.587	-833.220 (-1666.440)
<b><math>E_{ads}</math> eV</b>	-0.118	-0.067	-0.356	<u>-0.733</u>	1.602	0.112 (0.056)
<b>Oxygen species</b>	$O^{-0.02}$ $-O^{-0.39}$	$O^{-0.03}$ $-O^{-0.46}$	$O^{-0.26}$ $-O^{-0.35}$	<u><math>O^{-0.41}</math> <math>-O^{-0.50}</math></u>	$O^{-0.60}$ ; ( $O^{-1.11}$ ) <sub>sur</sub>	$O^{-1.24}$ ( $O^{-1.42}$ ) <sub>sur</sub>

<sup>a</sup>superoxo-OI, OII, OIII, and Y designate superoxide species on different adsorption sites derived for the dissociated O atom and a neighbour surface oxygen;

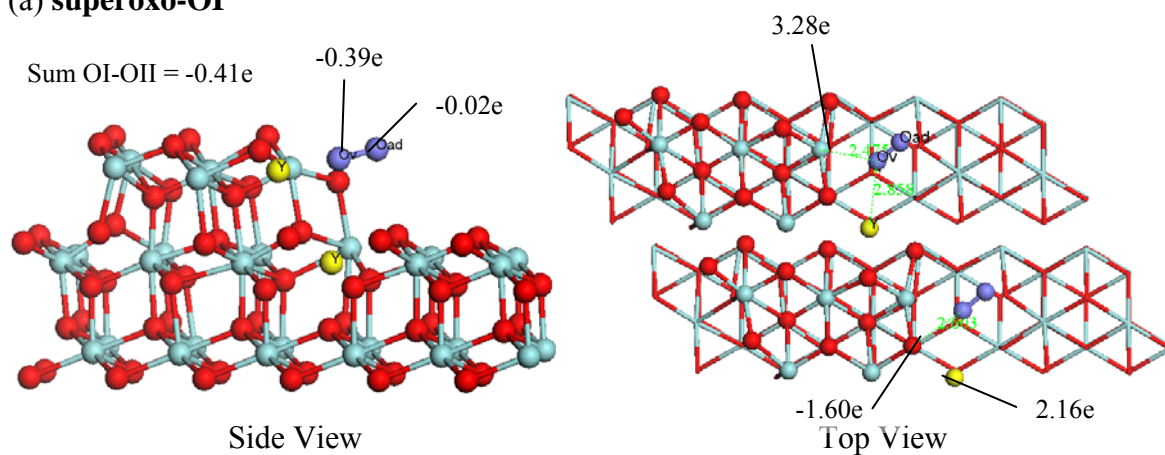
<sup>b</sup>diss-Zr represents an dissociated adatom O at the edge site Zr;

<sup>c</sup>int- $V_O$  represents an oxidised step surface with dissociated O in the oxygen vacancy at the edge site.

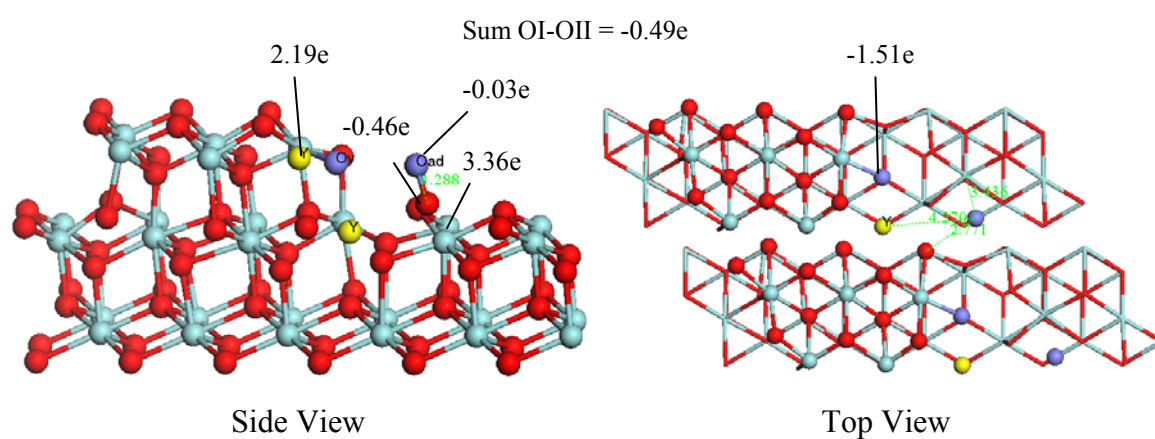


**Figure 8.4** The optimized structures of O<sub>2</sub> dissociation sites on the stepped (111) YSZ surface (see **Table 8.3**). Side View (Left); Top View (Right); Bader charge (solid line); distance between ions (dash line).

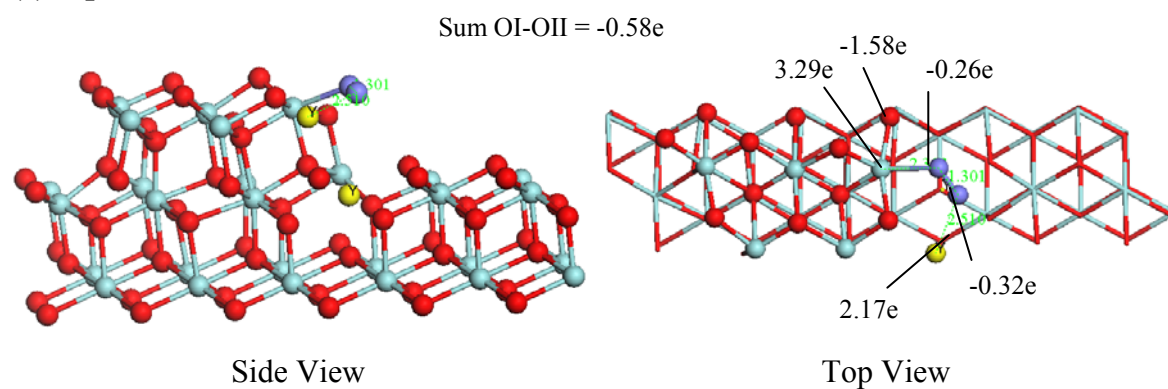
(a) **superoxo-OI**



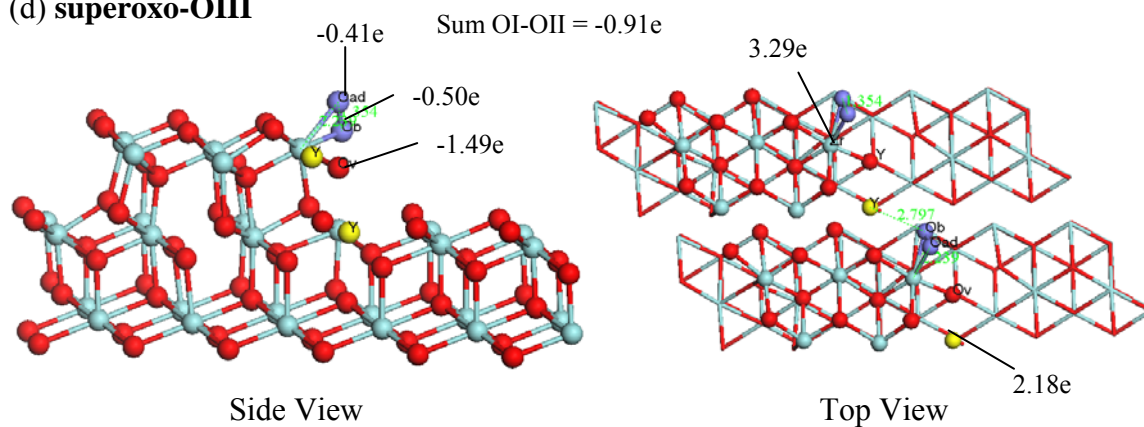
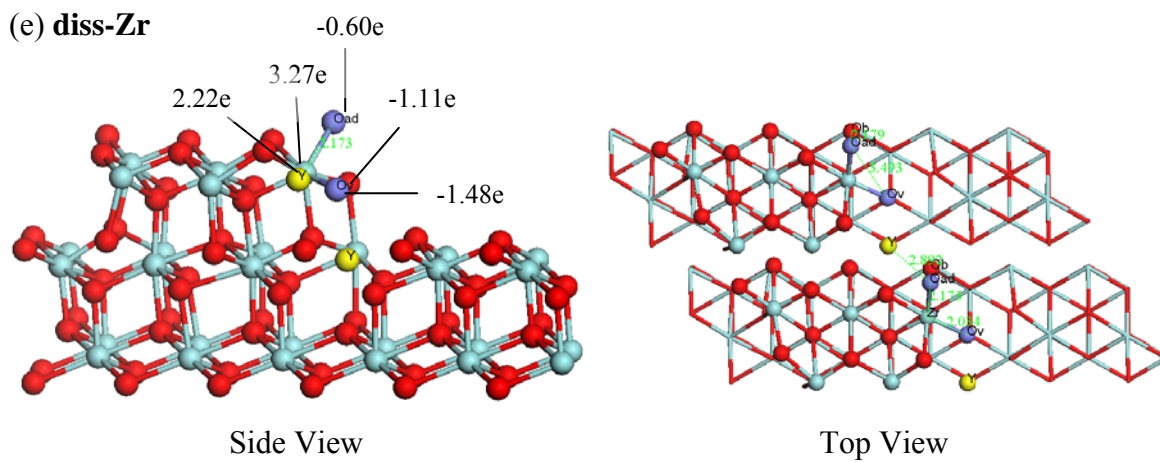
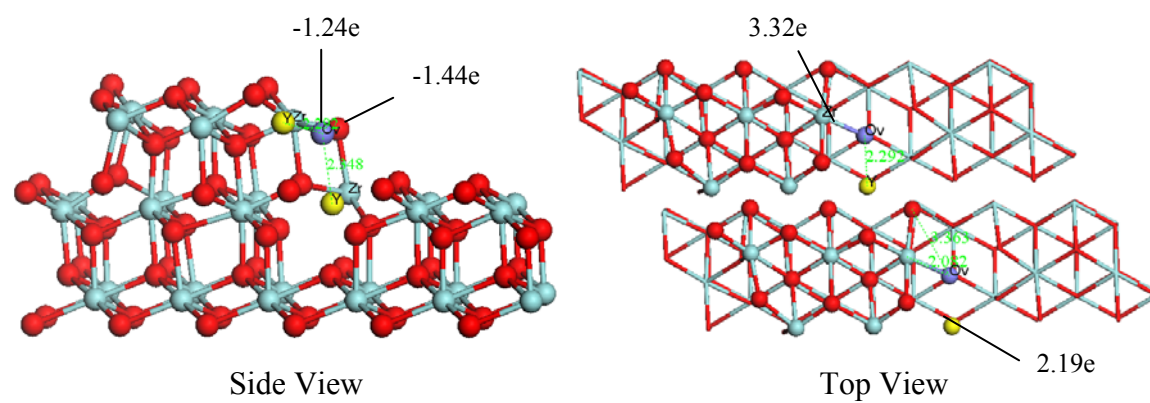
(b) **superoxo-OII**



(c) **superoxo-Y**





(d) **superoxo-OIII**(e) **diss-Zr**(f) **int-Vo**

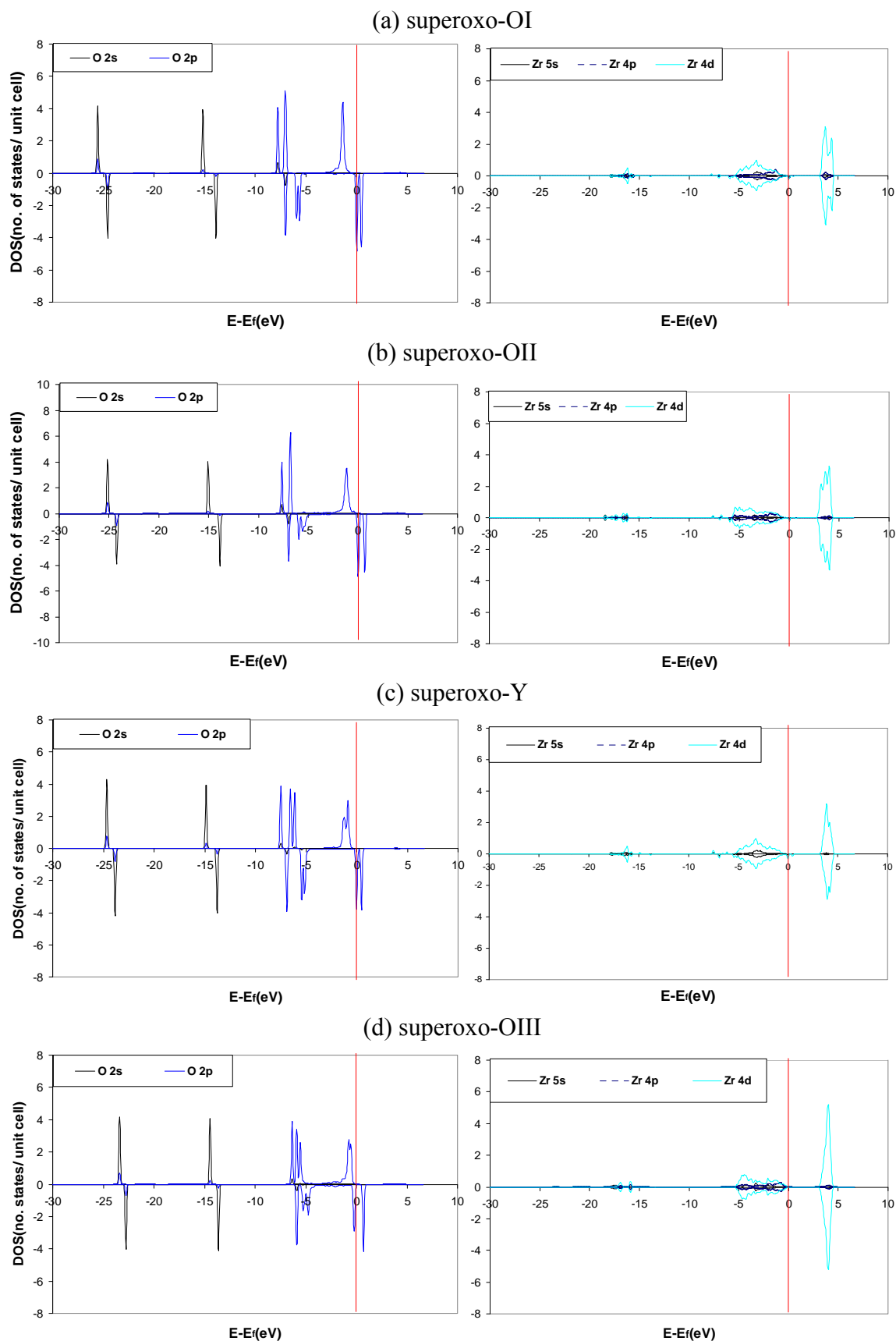


For the reformed dioxygen pairs, the orientation parallel to the edge facet (**Figure 8.4-c**) is favoured rather than that perpendicular to the edge side (**Figure 8.4-a**) or lower terrace (**Figure 8.4-b**) with an energy release of 34.35 kJ/mol. However, the most stable adsorption site for oxygen pairs is as shown in **Figure 8.4-d**. In this case, one of the oxygen adatom bonds with both the edge site Zr and bridging oxygen ions at a distance of 1.354 Å and 2.239 Å respectively (compared to the equilibrium bond distance of 1.235 Å for O<sub>2</sub> and 2.221 Å for lattice ZrO<sub>2</sub>). The other dissociated oxygen atom from the O<sub>2</sub> molecule fills the oxygen vacancy sites and thus the coordination number of the edge site Zr cation is increased from 5 to 7 as in the plane (111) surface. This process is strongly exothermic and gives an adsorption energy of -70.72 kJ/mol. The sum of the Bader charges on the reformed oxygen pair (O<sup>-0.41</sup>-O<sup>-0.50</sup>) is around -1e.

**Figure 8.5** compares the DOS for the four superoxide-like species: superoxo-OI, superoxo-OII, superoxo-OIII and superoxo-Y. The partial DOS for the adsorbed oxygen pairs exhibit multiple O 2p peaks, all of which suggest non-zero spin but with a reduced magnetic moment on the more stable oxygen species. In addition, the partial DOS pattern of the edge site Zr ions is also influenced by different orientations of the adsorbed oxygen pairs. For superoxo-OIII, which is the most energetically favourable oxygen species on the **SD5** step surface, the spin polarization effects are significantly reduced as shown by the small energy deviation of the up and down-spin. The DOS pattern is almost symmetric below the Fermi level, and an extra O 2p peak appears at just above the Fermi level. Accordingly, the 4d valence band of the adsorption site Zr cation (7-fold) gives a sharper peak at around 4eV. Therefore, the superoxo-OIII adsorbate is considered as an dissociation intermediate relate to peroxide O<sub>2</sub><sup>2-</sup> or 2O<sup>-</sup>, and the stronger spin polarised superoxo-OI, superoxo-OII and superoxo-Y species are indentified as superoxide. The calculated O-O bond lengths of these dioxygen pairs are in agreement with the earlier experiment data for superoxide O<sub>2</sub><sup>-</sup> and peroxide O<sub>2</sub><sup>2-</sup>, [1-2] and also in accord with a very recent study of oxide species by electronic structure calculations employing B1LYP method. [3]



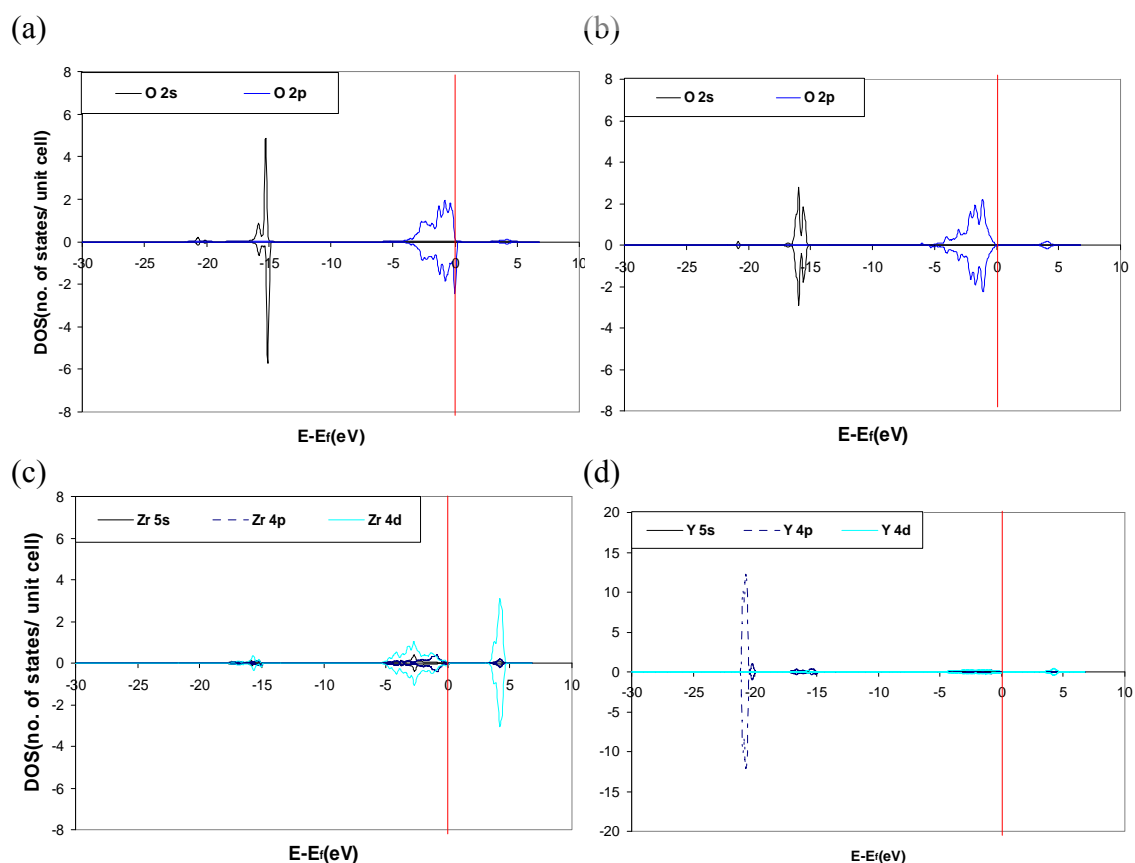
**Figure 8.5** Partial DOS for oxygen for dioxygen species (left) and adsorption site Zr ion (right). (a) superoxo-OI (b) superoxo-OII (c) superoxo-Y and (d) superoxo-OIII.





For the dissociated oxygen species, adsorption above terrace oxygen or metal ions is energetically unfavourable leading to the formation of  $O^{\alpha-}$  ( $\alpha < 1$ ) species and corresponding to a high dissociation energy of 130.54 kJ/mol. The oxygen atom is more stable when compensating the edge side oxygen vacancy site, in which case, 6-fold Zr and Y cations can be adopted at the edge site of **SD5** as in the pure  $ZrO_2$  step **S3**. The required dissociation energy is calculated to be 10.83 kJ for per mole  $O_2$ . According to the partial DOS for int-Vo in **Figure 8.6**, the edge site oxygens can all be indentified as lattice oxygen anions  $O^{2-}$ . Compared to the original bare **SD5** surface, the topological charge of the Zr cation at the edge sites increases from +3.14e to +3.32e (the same as in 7-fold Zr in the monoclinic structure). The partial DOS also exhibit a sharper Zr 4d peak above the Femi level in **Figure 8.6-c**, while the intensity of Y 4p peaks slightly reduce in **Figure 8.7-d**. Therefore, the local charge at the oxidized edge side has been redistributed in the step surface of int-Vo.

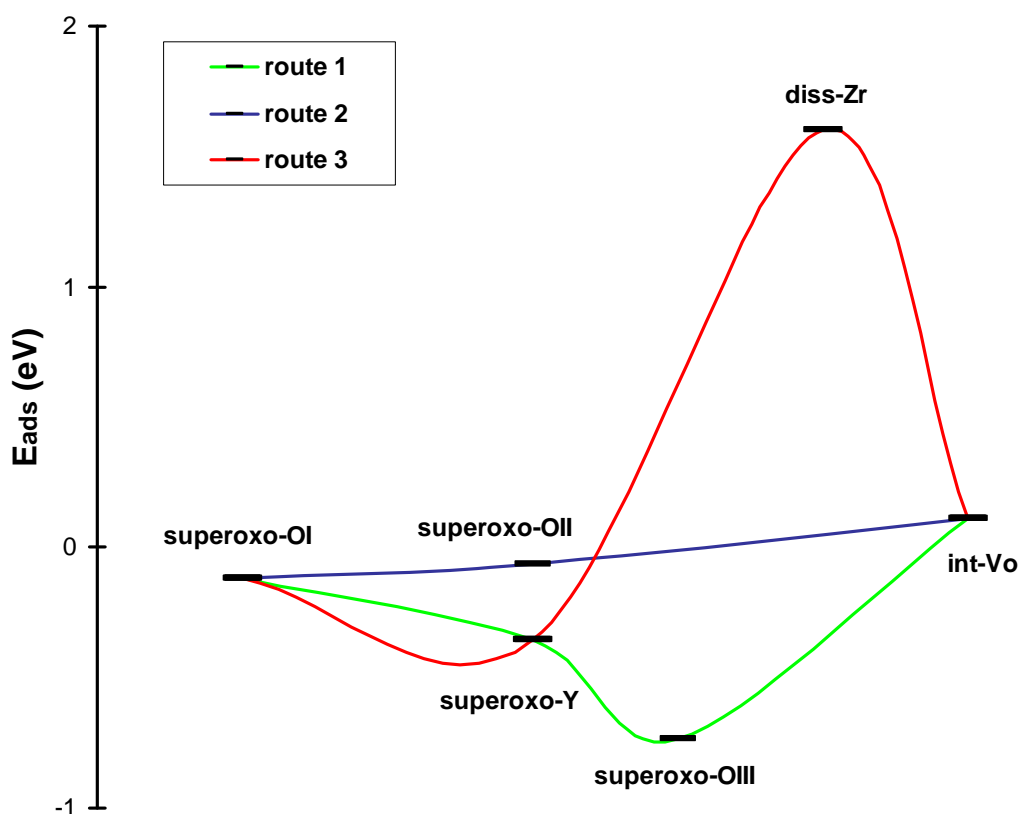
**Figure 8.6** Partial DOS for the dissociated oxygen atom and edge site metal ions of int-Vo on the SD5 step surface of YSZ. (a) dissociated oxygen atom in oxygen vacancy site; (b) bridging site oxygen on the edge side; (c) edge site Zr and (d) Y ions.





The overall oxygen dissociation pathways on the **SD5** step surface are illustrated in **Figure 8.7**. In route 1,  $O_2$  dissociates through the bridging site oxygen at the edge side; the energy profile for route 1 represent transport between the sites in **Figure 8.4**-a, c, d and f. In route 2,  $O_2$  dissociates via the neighbouring oxygen site on the lower terrace as depicted in **Figure 8.4**-b and in route 3,  $O_2$  dissociates above edge site Zr cation (**Figure 8.4**-e). Consistent with the findings for the plane (111) surface of YSZ, route 1,  $O_2$  dissociation via the bridging site oxygen at the edge side is the most energetically favourable route. This route is an exothermic process involving the formation of superoxide like species ( $O^{-0.41}$ - $O^{-0.50}$ ). There is a very small energy increase for Route 2, where  $O_2$  dissociates through the neighbouring oxygen on the lower terrace site. Route 3 is strongly endothermic since it involves an unstable intermediate  $O^{\alpha-}$  ( $\alpha < 1$ ) absorbed above the Zr cation at the edge site. The final product of oxygen dissociation via all routes is an oxidized step surface almost as stable as the initial substrate **SD5**.

**Figure 8.7** Energy profile for  $O_2$  dissociation on the stepped YSZ (111) surface of SD5. The route lines denote the potential energy changes with oxygen dissociation/adsorption sites (see **Figure 8.4**).





### 8.3 Oxygen Adsorption States on the Stepped Surface of YSZ

In contrast to oxygen dissociation on the plane surface, the under coordinated Zr ions on the step surface serves to lower the energy barrier by producing strongly reduced oxygen pairs i.e. peroxide like  $O^{-0.41}-O^{-0.50}$  on **SD5**, and hence the dissociation process as well as  $O_2$  absorption can be facilitated. **Table 8.4** lists the oxygen species which have been found from the calculation of  $O_2$  adsorption and dissociation on the step surface.

**Table 8.4** Adsorption energies of adsorbed oxygen species on the stepped (111) surface. ( $\delta$ ,  $\alpha$  and  $\beta$  denote the topological Bader charge  $0 \sim \delta < 1$ ;  $0 < \alpha < 1$ ;  $1 < \beta < 2$ )

Category	Substrate	Oxygen species	d(O-O) Å	Magnetization (x)		$E_{ads}$ kJ/mol
				$\mu_{OI}$	$\mu_{OII}$	
$O_2^{\delta-}$	S3	$O^{+0.01}-O^{-0.05}$	1.23	0.83	0.80	+5.79
	S3	$O-O^{-0.04}$	1.24	0.82	0.80	-4.34
	S3	$O^{+0.07}-O^{-0.09}$	1.24	0.84	0.79	-10.42
$O_2^{\alpha-}$	S3	$O^{-0.04}-O^{-0.23}$	1.25	0.77	0.57	99.82
	SD3	$O^{+0.08}-O^{-0.15}$	1.24	0.83	0.73	-36.28
	SD3	$O^{+0.02}-O^{-0.10}$	1.25	0.81	0.71	-18.62
	SD3	$O^{-0.02}-O^{-0.39}$	1.28	0.76	0.48	-11.38
	SD3	$O^{-0.03}-O^{-0.46}$	1.29	0.73	0.42	-6.46
	SD3	$O^{-0.26}-O^{-0.35}$	1.30	0.53	0.51	-34.35
	SD3	$O^{-0.41}-O^{-0.50}$	1.35	0.42	0.40	<u>-70.72</u>
$O^{\alpha-}$	SD3	$O^{-0.60};$	2.18	1.06		65.27
		$(O^{-1.11})$		0.53		per ion
$O^{\beta-}$	SD3	$O^{-1.24};$	2.60	0.23		5.41
		$(O^{-1.42})$		(0.14)		per ion



According to **Table 8.4**, the pure step surface **S3** tends to adsorb slightly polarised  $\text{O}_2^{\delta-}$  ( $\delta \sim 0$ ) at the edge sites 6-fold Zr cations. On the Y doped step surface **SD5**, the more strongly charged dioxygen pairs  $\text{O}_2^{\alpha-}$  are present as the most favourable adsorbate at the low coordinate Zr site (5-fold). For dissociated oxygen monoatoms,  $\text{O}^{\beta-}$  (i.e.  $\text{O}^{2-}$ ), adsorption at the edge vacancy sites is more favourable than  $\text{O}^{\alpha-}$  adsorbed above the Zr cation. Therefore, the charged dioxygen pairs are more stable than the oxygen atoms, and the formation of highly reduced  $\text{O}^{\beta-}$  at vacancy sites is preferred as the  $\text{O}_2$  dissociation product rather than  $\text{O}^{\alpha-}$ . The order of stability is  $\text{O}_2^{\alpha-} > \text{O}^{\beta-} > \text{O}^{\alpha-}$ .

Comparing results in this Chapter with those obtained for the plane surface, we can draw a general conclusion that the existence of lower coordinated Zr cations facilitates the oxygen reduction on the YSZ step surface. More strongly reduced oxygen species tend to adsorb at the less stable surface comprising unsaturated Zr cations. The most stable oxygen adsorption state on the substrate is generated to adopt a higher coordination number of the Zr cations at the edge sites. However, we have not calculated the exact activation energy which rather suggested the transition path and this will be topic for our future work.

## References

- 
- [1] D. G. Tuck, *J. Inorg. Nucl. Chem.* **26**, 1525, 1964.
  - [2] F. Feher, I. von Welucki and G. Dost, *Ber. Chem. Disch. fes.* **86**, 1429, 1953.
  - [3] E. L. Uzunova, Hans Mikosch, and G. St. Nikolov, *J. Chem. Phys.* **128**, 094307, 2008.



## Chapter 9 Conclusions

*We are to admit no more causes of natural things than such as are both true and sufficient to explain their appearances. Therefore, to the same natural effects we must, so far as possible, assign the same causes.*

*-- Sir Isaac Newton*

The thrust of the computational work in this thesis has been to investigate the defect chemistry of the important catalytic material yttria stabilised zirconia (YSZ) system in order to identify oxygen states on the surface during high temperature oxidation catalysis and demonstrate the relationship between the defect dispersion and O<sub>2</sub> adsorption. Both interatomic potential and quantum mechanical approaches have been applied to study the bulk and surface defect structures of YSZ. The electronic structure of the ZrO<sub>2</sub> phases and the charge densities of adsorbed oxygen species were calculated and analysed by quantum mechanical methods based on density functional theory. Overall, the conclusions can be summarised regarding three aspects: (i) the structural stability of the bulk phases, and the plane and topological surfaces for stoichiometric ZrO<sub>2</sub>; (ii) the bulk dispersion and surface segregation of defects in the YSZ system; and (iii) the oxygen states on the surface of pure and yttrium doped ZrO<sub>2</sub> during O<sub>2</sub> adsorption and dissociation.

### 9.1 Structural Stability of Zirconia

The structures of the three low pressure phases, cubic, tetragonal and monoclinic, of zirconia have been reproduced precisely with the correct order of stability by quantum mechanical simulations and the monoclinic structure was demonstrated as the lowest energy phase, in contrast to the orthorhombic structure predicted by the interatomic



potential method. According to the electronic structure and charge density analysis, the covalent contribution to the Zr-O bonding in zirconia (indicated by the increase of bond directionality and reduction in the population of the Zr 4d) is more pronounced for the monoclinic phase with a lower symmetry and coordination number, which leads to inaccuracies in the IP approach based on an ionic model. The monoclinic structure with lower coordination number corresponds to stronger covalency (smaller ionicity) in accordance with the Phillips-van Vechten-Levine scheme of ionicity.

For the surface studies, the three low index surfaces, (111), (110) and (100), as well as the (310) surface of c-ZrO<sub>2</sub> were simulated by the IP approach. The order of surface stability for c-ZrO<sub>2</sub> is shown to be: (111)<sub>c</sub> > (110)<sub>c</sub> > (100)<sub>c</sub> > (310)<sub>c</sub>. The dominance of the (111)<sub>c</sub> surface was also confirmed by DFT calculations. In addition, based on the (111)<sub>c</sub> surface, two sets of step and corner models with topological irregularities were investigated by quantum mechanical technique. An interesting trend was found relating to the Zr coordination number (CN): the stability reduces with the CN of the Zr ions at the topological sites of the corresponding surface structure with the order: plane > step > kink > corner. Therefore, the average Zr coordination number can be used as a criterion to estimate the relative stability of different ZrO<sub>2</sub> surfaces either plane or with topological complexity.

## 9.2 Bulk Dispersion and Surface Segregation of Defects in YSZ

Doping with yttrium stabilizes the cubic phase of ZrO<sub>2</sub>, while expanding the lattice volume. The energy of the YSZ lattice is found to increase linearly with the yttrium concentration in the bulk. Consistent with experimental observation of the t" and c phases, two stable cubic-like YSZ structures differing in their detailed oxygen arrangement have been identified in the range 9-12 mol% yttria content by interatomic potential calculations.

Regarding defect dispersion in the YSZ bulk, two different approaches—super-cell and Mott-Littleton methods—have been applied for IP simulations. The results of Mott-Littleton calculations for a dilute system indicate that: (i) yttrium is more stable in the next nearest neighbour (NNN) sites to the vacancy rather than nearest neighbour (NN) sites, and (ii) two yttrium atoms tend to be located together with the nearest neighbour



separation. The supercell calculations for systems containing higher amounts of  $\text{Y}_2\text{O}_3$  suggest that the NN and NNN sites to oxygen vacancy are almost equally favourable for yttrium dopant but the preferential defect configuration depends on the yttria content level in each case.

For YSZ surfaces, the energetically favourable (111) and (110) surfaces of pure cubic zirconia are further stabilized by yttria doping, but the relative stability of the two surfaces is unchanged. In addition, yttrium (with an oxygen vacancy) tends to segregate to the top layers (up to 4-5 Å) of the dominant (111)<sub>c</sub> surface of YSZ and saturation of yttrium at the outmost layer is achieved with a maximum Y/Zr ratio of 1:1, which is around the maximum solubility of yttrium in  $\text{ZrO}_2$  bulk. The yttrium saturation at the outer layer of (111) surface may relate to the formation of a second phase. In contrast, no clear tendency for yttrium segregation has been demonstrated for the (110)<sub>c</sub> surface of YSZ. Good agreement of the yttrium segregation tendency has been achieved between the interatomic potential and quantum mechanical studies which prove the IP method can serve as an efficient tool for defect studies of c- $\text{ZrO}_2$ .

The segregation effect of yttrium suggests the composition of the outermost surface of YSZ is independent of yttria concentration in the bulk, which could lead to phase partitioning of understabilised YSZ.

### 9.3 Adsorption of Oxygen

The adsorption states of oxygen have been identified on the plane and stepped (111) surfaces of pure and yttrium stabilised zirconia by DFT-GGA calculations. Various adsorbates including monatomic, diatomic, and triatomic oxygen species were obtained on different substrates and can be categorized as  $\text{O}_2^\delta$  ( $0 \sim \delta < 1$ ),  $\text{O}_2^{\alpha\cdot}$  and  $\text{O}^{\alpha\cdot}$  ( $0 < \alpha < 1$ ),  $\text{O}_3^{\beta\cdot}$  and  $\text{O}^{\beta\cdot}$  ( $1 < \beta < 2$ ). These categories of oxygen species are considered in relation to the oxygen molecule, superoxide ion, radical monoxide, peroxide and lattice oxygen anion in experimental observation, respectively.

For the (111) plane surface of pure c- $\text{ZrO}_2$ , there is weak physisorption of  $\text{O}_2$  molecule. This process is a slightly exothermic releasing 3.2 kJ/mol. The details of the



adsorption of oxygen on the YSZ surface depend on the precise defect configuration of particular sites and the yttrium composition at the outermost layer.

More specifically, in the case of a substrate with high yttrium content level, (i.e. the segregation limit of yttrium at the outmost surface has been reached), which has been modelled as YSZ1, we find that:

- Charged oxygen pairs  $O_2^{\alpha-}$  ( $0 < \alpha < 1$ ) rather than the neutral  $O_2$  molecule tend to be adsorbed at the oxygen vacancy sites in an orientation lying between the Zr and Y cations and with a shallow angle to the surface.
- An oxidised YSZ surface, with  $O^{\beta-}$  ( $1 < \beta < 2$ ) occupying the surface vacancy sites, can be formed by releasing an energy of -24 kJ/mol. The electron density of the surrounding oxygen ions is redistributed to compensate the charge on the 7 coordinated Zr in the outer layer of the (111) surface.
- Adsorption of monatomic  $O^{\alpha-}$  species above the Zr site is energetically unfavourable.
- The order of stability for oxygen species is  $O_2^{\alpha-} > O^{\beta-} > O^{\alpha-}$  corresponding approximately to  $O_2^- > O^{2-} > O^-$ .

In the case of a substrate with low yttrium content level, (i.e. below the saturation limit for segregation at the outermost surface), which has been modelled as YSZ3, we find that:

- The slightly polarised  $O_2$  molecule denoted as  $O_2^{\delta-}$  ( $0 \sim \delta < 1$ ) is the most favourable adsorbate.
- The formation of superoxide like species  $O_2^{\alpha-}$  ( $0 < \alpha < 1$ ) with stretched O-O bonds requires a relatively higher energy of ~60 kJ per mole.
- The strongly reduced monoatomic oxygen species  $O^{\beta-}$  ( $1 < \beta < 2$ ) is very unlikely to occur as ions at oxygen vacancy sites since there is a very high dissociation barrier of 256.84 kJ for per mole  $O_2$ .
- The relative preference for oxygen adsorption states is  $O_2^{\delta-} > O_2^{\alpha-} > O^{\beta-}$  i.e. approximately corresponding to  $O_2 > O_2^- > O^{2-}$ .



In the cases where there is an oxygen vacancy in the immediate subsurface (models YSZ2 and YSZ4), the  $O_2$  molecule is also the most favoured oxygen adsorbate species. However, charged triatomic species ( $O_3^{\beta-}$ ) can be formed by requiring relatively high formation energies around 96.8 kJ/ mol. In the latter cases, a strong interaction between the adsorbed oxygen pair and the upper surface site oxygen is suggested by the observed charge redistribution.

For the stepped YSZ (111) surface, yttrium pairs tend to locate in the  $\langle 100 \rangle$  direction as in the plane surface. In the corresponding model of the YSZ step SD5, the subsurface oxygen vacancies as well as the low coordinated Zr ions (5 fold) can be exposed as sites for  $O_2$  adsorption. In particular, we find that:

- Compared to the plane YSZ (111) surface, the highly unsaturated Zr ions on the step surface serve to lower the dissociation energy barrier by producing strongly reduced oxygen pairs such as  $O^{-0.41}-O^{-0.50}$  as an intermediate, which show only a slight spin magnetization effect.
- To adopt the most stable oxygen adsorption state, the coordination number of Zr ions at the edge site increases to 7 on oxidation. This process is strongly exothermic releasing an energy of -70.7 kJ/mol.
- The oxidised surface producing 6 coordinated Zr ions at the edge site can be achieved by filling oxygen vacancies with the  $O^{\beta-}$  (i. e.  $O^{2-}$ ). However, the formation of such a non-stoichiometric step surface is less favoured compared to the adsorption process creating 7 fold Zr ions at edge sites. The adsorption energy of  $O^{\beta-}$  is estimated to be a small positive value of 5.41 eV per ion. The less reduced monoatomic oxygen  $O^{\alpha-}$  can only occur through a much higher energy adsorption process.
- Hence, the order of stability for the adsorbed oxygen species is given as  $O_2^{\alpha-} > O^{\beta-} > O^{\alpha-}$ , corresponding approximately to  $O_2^- > O^{2-} > O^-$ .

Overall, the oxygen adsorption state on the surface depends on the local defect configuration as well as surface irregularities. There is a general trend exists with respect to Zr coordination number: the more strongly reduced oxygen species (higher topological charges) tend to occur at substrate sites containing lower coordinated Zr ions. The most stable adsorption configuration is formed by redistribution of charge



density among the surrounding oxygen ions with therefore an increase in the Zr coordination as in the ground state  $\text{ZrO}_2$ . However, despite different charge states for the oxygen species in relation to surface topology and composition, the dioxygen pair is more stable than the dissociated monoatomic oxygen atoms.

The oxygen adsorbed YSZ surfaces can be considered as “non-stoichiometric” structures with an excess of oxygen. The preference for different oxygen adsorption states, which is estimated in terms of adsorption energy, i.e. the formation energy of the adsorption system, could also denote the stability of the corresponding non-stoichiometric surface. Therefore, Zr coordination number as a criterion for structure stability can also be applied to non-stoichiometric YSZ surfaces.



## Outline of Future Work

To further understand oxygen adsorption on YSZ surface, issues for the next stage of modelling would include aspects of surface topology and calculation methodology; in particular, the following issues need to be addressed:

- Since the nature of the oxygen adsorption species appears to depend on the degree of bond unsaturation of the Zr ions exposed at the substrate surface, it will be necessary to test this concept further by modelling adsorption on the cornered and kinked YSZ surfaces.
- In order to understand further the oxygen dissociation process, the relevant saddle points, which act as the bottlenecks for a particular barrier-crossing event on the minimum energy paths (MEPs) need to be calculated. Such saddle points can be identified by using computational modelling techniques such as nudged elastic band (NEB) and the string methods.
- The accuracy of QM calculation depends on the extent of electronic localization, including band gaps and magnetic coupling constants which are important factors for modelling oxygen adsorption on  $\text{ZrO}_2$  and YSZ surfaces. However, DFT tends to underestimate the band gaps and spin population. Therefore, it is intended to improve the calculations for oxygen adsorption by employing hybrid functional method such as B3LYP.

In addition to direct partial oxidation of methane by oxygen, two other routes to syngas are of interest: steam and dry ( $\text{CO}_2$ ) reforming. Therefore, it would be worthwhile to develop an understanding of the adsorption behaviour of  $\text{H}_2\text{O}$  and  $\text{CO}_2$  on YSZ surfaces. Of wider catalytic importance, adsorption of  $\text{N}_2\text{O}$  would also be of considerable interest.



## **Acknowledgements**

I would like to record my gratitude to University College London for the special Funding and to Prof. Richard Catlow for the research opportunity provided and for his inspiring supervision, kindness and patience. I am pleased to have the honour and felicity of being his student.

I owe countless thanks to Prof. Richard Oldman. More than a great supervisor on science, he is also a sincere friend and English language tutor. My gratitude to him is beyond words.

I am grateful to Drs Ricardo Grau-Crespo, Alexei Sokol, Scott Woodley and Aron Walsh for their helpful discussions and expert advice. I am also indebted to Dr. Saira Khan for her previous work on Perovskites, which benefited me a lot. Thanks also due all the members of Materials Chemistry Group for their encouragement and support throughout my Ph.D.

Acknowledgement to the computer power provided by the UCL clusters and HECTor funded by EPSRC.

*At last, as an epilogue, "no scientific truth is born anew", ideas in science are collective rather than individual creations. Thanks to all the great forerunners who have enlightened this research field. If there is any finding here, it is due to them, any mistake is mine. Even a false point in the everlasting optimization of research is worth all the effort I have made, since scientific understanding is built on refutability.*